Fractional Modelling of Rechargeable Batteries

A thesis

submitted in fulfilment

of the requirements for the Degree

of

Doctor of Philosophy in Engineering (Electronics)

at

The University of Waikato

by

Rahat Hasan

THE UNIVERSITY OF
WAIKATO
Te Whare Wānanga o Waikato

2021

Abstract

To develop a compact battery model, many authors begin by measuring the impedance of a battery over a frequency range of interest. Most of the models in the literature are either Thevenin-style or Randles' model consisting of one or two RC networks and sometimes a Warburg element. These models are usually based on frequency range that stretches to only 1 mHz. This explains why they require several parameters to accurately reproduce the measured impedance data.

In most applications, a battery goes through a charge/discharge cycle daily or even longer. Therefore, it seems logical to measure the impedance of the cell at frequencies reciprocal of period of charge. This corresponds to approximately 11.6 μHZ or lower. The impedance data at lower frequencies shows that any rechargeable battery can be simply modelled with a constant phase element in series with a resistor.

Based on this observation, an equivalent circuit model and a mathematical model were proposed in this study. Similar to Randles' model presented in 1947, the proposed models do not contain a source or any purely reactive element. The models were then fitted to the measured impedance data of both lithium-ion and nickel-metal hydride cells, the linear region of the charge-voltage curve, and the transient recovery tail that results from a step-change in load current.

Acknowledgements

The author is grateful to:

Professor Jonathan Scott for advice, guidance, whiteboard discussions, proof-reading and problem-solving techniques.

Dr. Nihal Kularatna for instruction and support.

Tracey Morgan for continuous encouragement throughout the studies.

Faculty of Science and Engineering for all the equipment and supplies.

Daniel Blair for moral support.

Contents

List of Figures

Chapter 1

Introduction

In recent years, environmental issues such as global warming have become a major problem around the world. According to a Pew Global Attitude survey, 23 of 25 countries realise the importance of protecting the environment even at the expense of economic growth and job losses [1]. Majorities in France, Japan, Spain, and Germany consider that global warming is a serious problem. The current energy economy heavily relies on fossil fuels with the global demand expected to increase many fold in the coming years. It is well known that increased consumption of fossil fuels to meet the global energy demand is impelling global warming to a dangerous level. Furthermore, the supply of fossil fuels is finite and will soon become economically inaccessible.

This concern drives the search for alternative energy sources such as solar, wind, and water which are clean and renewable in nature. However, it should be noted that such renewable energy sources may not be available during times of peak demand. For example, wind energy can only be harnessed when the weather is windy and solar energy when it is sunny. The solution is a storage system such as rechargeable batteries. They allow the storage of renewable energy in the form of chemical energy and transform them back to electrical energy when required. In engineering, batteries are considered as the nucleus of an electrical system and play a very important role in providing access to clean, safe, and economical electrical services. Ram Ramachander from Social

Innovation Business, at Hitachi Europe describes the significance of battery storage better in [2]:

> "It serves a dual purpose. Firstly, it facilitates the integration of intermittent renewable energy sources, whilst simultaneously opening the door to generating income for prosumers. The dual purpose of battery storage is driving mass-market adoption of residential storage beyond 2020. By 2025, we can expect residential storage to be an integrated and essential component of all renewable energy projects."

1.1 Welcome to the era of rechargeable batteries

Over the past decade, the energy storage industry has revolutionised towards an obvious inflection point of cheap, reliable and scalable technology. At the beginning of 2010, batteries mostly powered mobile phones and laptops and by the end of 2020, they were powering vehicles and houses. This surge in battery application drove their price down to the point where they became economically viable for electric cars and renewable energy storage. According to CNBC [3], UBS approximates that the costs of energy storage will decrease by 66-80% over the next few decades and the global industry will grow up to US$ 426 billion. Battery University in [4] also mentioned that the demand for both primary and secondary cells increased to 7.7 percent annually which is equivalent to USD 120 billion in 2019. An overview of the revenue contributions (reproduced from [5]) by various batteries is shown in figure 1.1. This increase in demand was mainly impelled by laptops and mobile phones.

The lithium battery has seen the most increase in demand in recent years among other batteries [4]. Battery manufacturers are now producing over one billion rechargeable lithium-ion cells a year to meet consumers' demand. Figure 1.2 obtained from World Economic Forum shows how the demand for

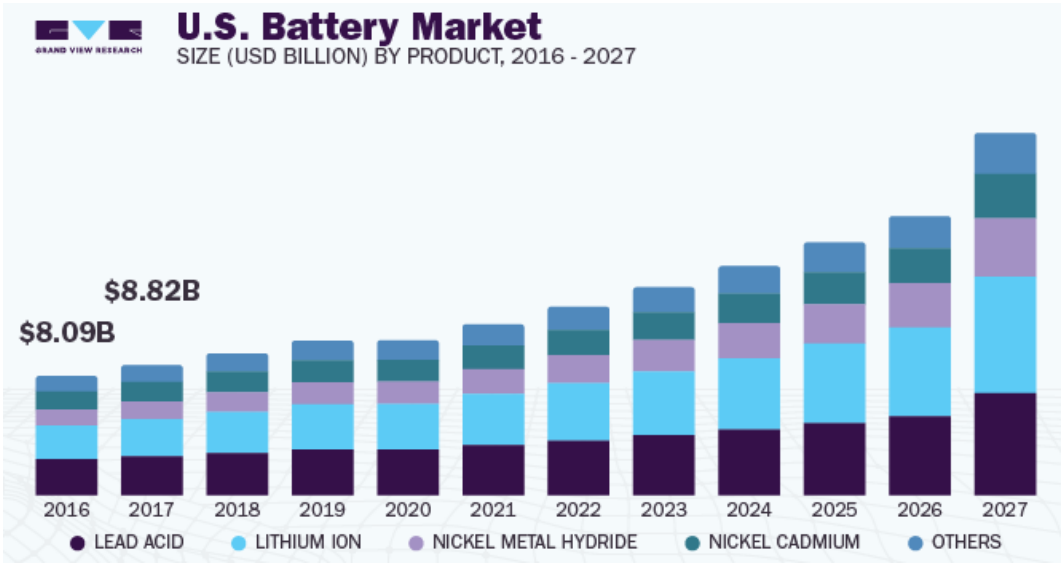

Figure 1.1: An overview of the revenue contributions by various batteries. [5].

lithium-ion cells has increased over the last decade [6]. The adoption of lithium technology in electric vehicles mainly drives this sudden demand for lithium-ion batteries. In the past, Tesla was the only company to commercialise battery-operated vehicles. Now, almost all automakers offer at least a hybrid model or a fully electric car. For example, Ford recently revealed an 11 billion dollar plan to manufacture 40 new electric and hybrid models by the end of 2022, and Volkswagen plans to develop 70 new models by 2028 [3].

Demand for cheaper and high-performance batteries is not limited to the electric car space. With the decline in solar panel prices and the introduction of "rent a roof scheme", more and more consumers are encouraged to change to renewable energy to power their homes. Figure 1.3 depicts the increase in demand for rechargeable batteries in the residential space. Along with SunRun, Tesla is now offering solar and storage solutions with its Powerwall battery [3].

1.2 Motivation of this work

Because of this recent growth in battery demand, everyone is now searching for the "perfect" battery model. A battery model that can give insight into

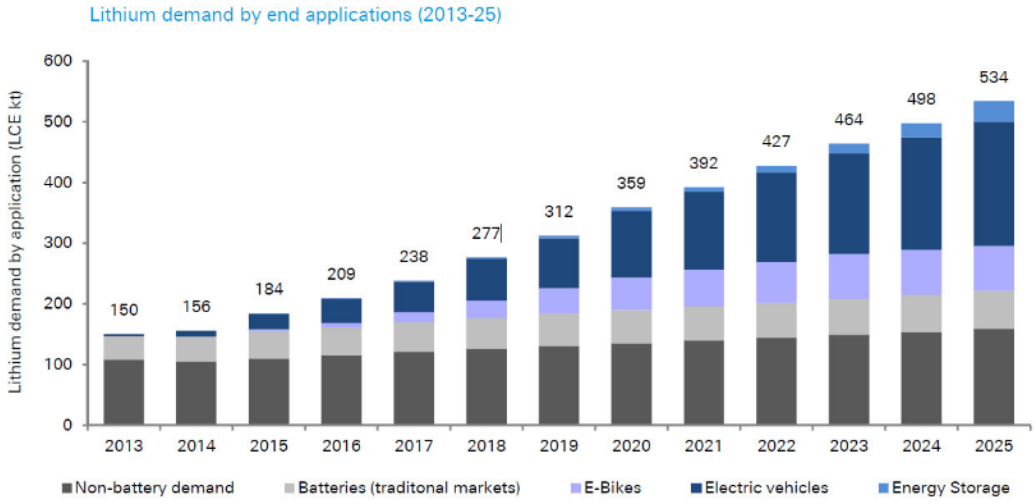

Figure 1.2: Increase in Global demand for lithium-ion batteries [6].

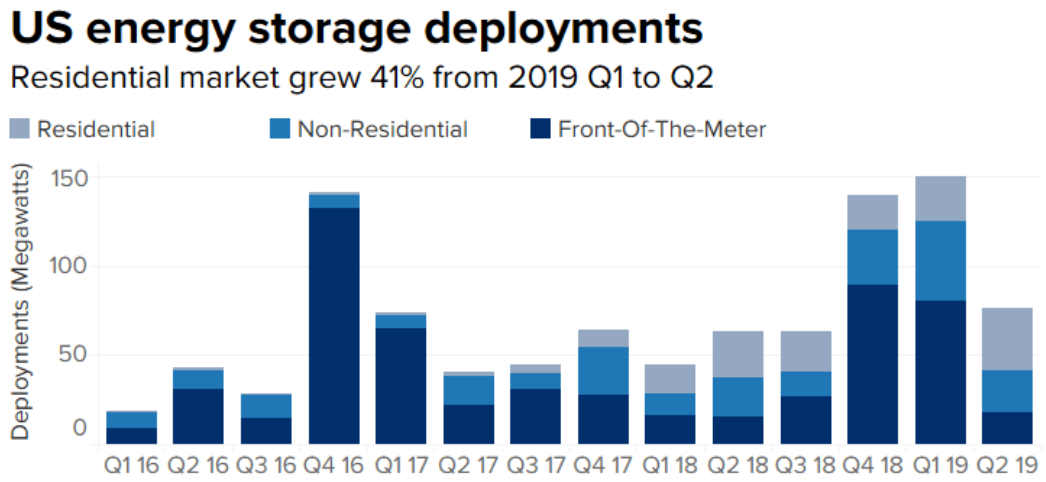

Figure 1.3: Increase in demand for rechargeable batteries in the residential space [3].

electrochemical cell characteristics, mainly the state of charge and state of health. The literature review conducted during this work revealed that there are thousands of papers with the phrase "battery modelling" in the Institute of Electrical and Electronics Engineers (IEEE) stable alone and many more can be found in other journals.

The most commonly mentioned battery model is the Thevenin first-order RC model [7]. However, this model can only characterise the capacitance between the parallel plates and the resistance between the plate and the electrolyte of the cell. In search of better accuracy, some researchers looked into a second-order RC model containing two extra degrees of freedom [8]. This new model now can characterise the mass transport effects as well as the double layer effect. Min Chen et al. [9] presents a more comprehensive equivalent circuit model that captures the transient runtime and state of charge/I-V characteristics of cell but requires six parameters. Upon investigating all RC type models, it was realised that these models are not theoretically appropriate for modelling the transient runtime characteristics of a cell. The author of this work applied the improved version of Swingler's algorithm as described in Chapter 3 [10] to come to this conclusion.

Recently, many researchers have been exploring the idea of modelling rechargeable cells with a fractional element, first introduced by Randles in 1947 [11]. In that paper, Randles chose to investigate rapid electrode reactions with an equivalent-circuit model that does not contain any voltage source. The model only contained a series resistor and a RC network. One of the capacitors in the model, Cl is what is normally referred to as a "parasitic capacitor" in the electronic world and is only visible in the impedance plot at higher frequencies. The other capacitor, Cr is a fractional element with an angle fixed at 45 degrees. This type of element is referred to as a Warburg element in [12]. At low frequencies, the basic form of the model is of a Warburg element in series with a resistor. Analysis of the electrochemical behaviour of rechargeable cells via A.C. impedance measurement shows that Randles' model with no voltage

source can also be implemented in rechargeable batteries, with the exception of Warburg's element been replaced with a constant phase element.

Attention was then drawn to the work conducted by Scott (author's chief supervisor). Scott and Single proposed a model containing a constant phase element; a series resistance and two diode-memristor branches to characterise the impedance characteristics of electrode-electrolyte interface [13]. Most importantly, the paper presented a step-by-step procedure on how to build a fractional element equivalent in a compact simulator with a finite RC series network. This technique was built upon Morrison's work proposed in [14]. Later, a similar model was introduced in [15] for implantable electrodes but one that lacks memristors. Further work on electrodes was conducted by Scott et al. where it was shown that the decay curve generated by neural implant electrodes can only be reproduced in simulation with n-way split constant phase element [16] . These findings laid the foundation for the development of an equivalent battery model that can predict the transient runtime, impedance and charge-voltage characteristics of rechargeable cells with fewer degrees of freedom.

1.3 Statement of originality

The author of this work declares that this work is his original work except where otherwise acknowledged.

1.4 List of publications

1.4.1 Research papers

The co-authorship forms for the published paper is provided in appendix A.

- Chapter 3: Hasan, R., & Scott, J. B., "Application of Swingler's Method for Analysis of Multicomponent Exponentials with Special Attention to Non-equispaced Data", *In 2016 IEEE 12th International Colloquium on*

Signal Processing & Its Applications (CSPA), 4-6 March 2016, Melaysia (pp. 12–15). Washington, DC, USA: IEEE. https://doi.org/10.1109/CSPA.2016.7515794.

- Chapter 3: Hasan, R., & Scott, J. B., "Fractional behaviour of rechargeable batteries", *In Proceedings of the 2016 Electronics New Zealand Conference*, November 17-18, 2016, Wellington, New Zealand (pp. 111–114). Hamilton, New Zealand: Electronics New Zealand Inc.

- Chapter 4: Hasan, R. & Scott, J. B., "Letter to the Editor Re 'Fractional Modeling and SOC Estimation of Lithium-ion Battery'", *IEEE Caa Journal of Automatica Sinica*, 2018, 5(2), 644–644, https://doi.org/10.1109/JAS.2017.7510853.

- Chapter 4: Hasan, R., & Scott, J. B., "Comments on 'State of Charge-Dependent Polynomial Equivalent Circuit Modeling for Electrochemical Impedance Spectroscopy of Lithium-Ion Batteries'", *IEEE Transactions on Power Electronics*, 2019, 1–1, https://doi.org/10.1109/tpel.2019.2938508.

- Chapter 5: Scott, J. B., & Hasan, R., "New results for battery impedance at very low frequencies", *IEEE Access*, 2019, 7, pp. 106924–106929, https://doi.org/10.1109/ACCESS.2019.2932094.

- Chapter 5: Hasan, R., & Scott, J. B., "Impedance measurement of batteries under load", *2019 IEEE International Instrumentation and Measurement Technology Conference*, 2019, Auckland, New Zealand.

- Chapter 6: Hasan, R., & Scott, J. B., "Measurement for fractional characteristic of lithium batteries", *2019 IEEE International Instrumentation and Measurement Technology Conference*, 2019, Auckland, New Zealand.

- Chapter 7: Hasan, R., & Scott, J. B., "Extending randles's battery model to predict impedance, charge-voltage, and runtime characteris-

tics", *IEEE Access*, 2020, vol 8, pp. 1–8, https://doi.org/10.1109/access.2020.2992771.

1.4.2 Patent

A copy of the patent application is provided in appendix B.

- J. Scott, P. Single, R. Hasan, "Battery performance assessment method and apparatus", US 15/930,989, 26 November 2020.

1.5 Thesis outline

This thesis contains 8 chapters, including the introduction and the conclusion. The chapter, the background, introduces readers to the different types of rechargeable batteries, their characteristics and all the existing models proposed in the past to predict these characteristics. The background section also discusses why these models are not suitable for rechargeable cells and the recent approaches adopted by researchers to obtain better accuracy.

Chapter 3 presents two published papers where the first one is built upon the original work by Swingler. The paper proposes a tutorial on how to apply Swingler's algorithm to extract multi-exponential components present in a transient curve with non-equispaced data. It was shown that the modified version of Swingler's algorithm can identify the time constant at least 25% more accurately than the original Swingler's algorithm.

The second paper demonstrates an application of the improved version of Swingler's algorithm to extract multi-exponential components present in the measured recovery voltage waveform of a 900mAh, nickel-metal hydride battery. The result produced no evidence of exponential functions. This discovery proved that RC models are theoretically inappropriate for modelling rechargeable batteries and inspired us to look at existing fractional models.

Chapter 4 of this thesis is composed of two correction papers. The literature review of papers containing fractional models revealed that some authors used

incorrect transfer function equation to model a lithium-ion cell, whereas others created unjustified degree of freedom to obtain a "good fit" with their fractional models.

Knowing that reliable impedance measurement is critical to modelling rechargeable cells, and in the past models for implantable electrodes were developed in a similar fashion [13], the impedance of nickel-metal hydride and lithium-ion cells was measured using Solartron 1260. The frequency response was measured at unusually low frequencies because many batteries in appliances are charged daily, corresponding to a frequency of approximately 11.6 μHz. This is surprising that reference [17], now 20 years old, appears to be the only reference in arguing that impedance measurement down to 1 μHz may be important, but only presents data down to 6.8 μHz and the manuscript does not mention how this data was obtained.

Since the data obtained from Solartron at low frequencies was unreliable, robust methods of measuring on-load and off-load impedance of non-linear components at extremely low frequencies were proposed in Chapter 5. Both methods showed excellent agreement when compared with measurements obtained from two different hardware set-up and were very different from data obtained from Solartron 1260A. Armed with this new method of measuring complex impedance of rechargeable cells, the frequency response of a nickel-metal hydride and lithium-ion cell was measured. The findings concluded that at high frequencies, rechargeable batteries behave like a pure resistor, but reflect features of a fractional capacitor or constant phase element as the frequency gets lower. Such properties of batteries were not historically known.

Based on this observation, first a mathematical model containing only 3 parameters was proposed for a rechargeable battery in chapter 6. The mathematical model predicts the linear region of the charge-voltage curve of a 800mAh, 14500 lithium-ion cell with an accuracy of 0.5%. Realising that mathematical model has no physical justification and cannot be simulated in a compact simulator, later in chapter 7, a compact, equivalent circuit model was presented

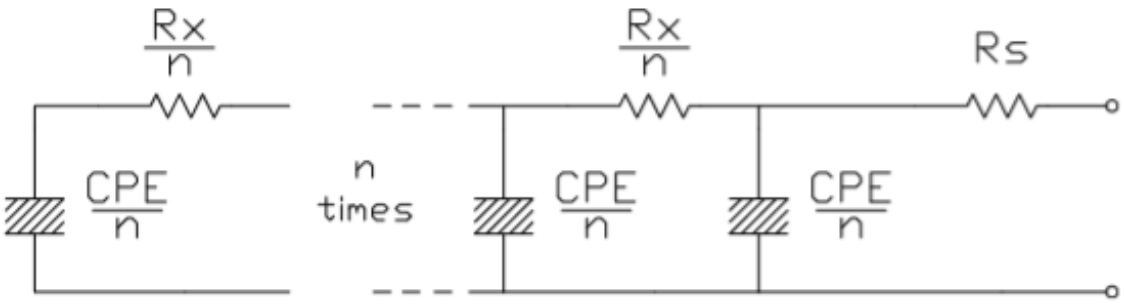

Figure 1.4: Equivalent circuit model for rechargeable cells with n-way split CPE and series resistance. The model requires four parameters and has no voltage or current source. [18].

that uses neither a voltage or current source. The model includes a series resistor and a n-way split constant phase element as shown in figure 1.4. The split constant phase element model perfectly fit the measured impedance data of both nickel-metal hydride and lithium-ion cells. When fitted to the transient runtime characteristics, the split model managed to predict the transient recovery tail with only 3% error. The model also predicted the linear region of the charge-voltage curve with less than 1% error. Chapter 8 gives important conclusions.

Chapter 2

Background

2.1 Rechargeable batteries

2.1.1 Origin of batteries

The concept of a battery may have existed well before the discovery of electricity in the 1740s. However, the idea of the battery emerged from experiments conducted by Luigi Galvani in 1789 when he noticed involuntary movements in frog legs when in contact with two different pieces of metals [19]. Later, Volta contributed to the creation of the first wet chemistry battery which is now known as the Voltaic Pile. Although Volta's batteries could source stable current, they would only last for a short period due to electrolyte leaks and high internal resistance. The Voltaic Pile was later improved by the British chemist John Frederic Daniell, now called the Daniell Cell [20].

2.1.2 Anatomy of batteries

The current working model of the battery consists of one or more electrochemical cells that transform chemical energy into electricity. This working concept is common across all electrochemical cells. According to [21], each terminal of the cell is connected to a conductive material called electrodes. The ions are stored in the negative terminal, also known as the anode. The cathode, on the other hand, is the positive terminal where the ions travel to after they pass

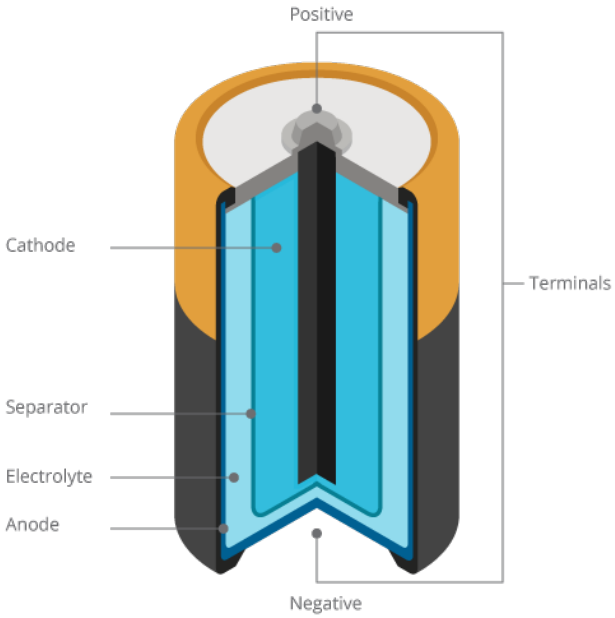

Figure 2.1: Basic anatomy of an electrochemical cell reproduced from [21].

through the device. The electrolyte resides in between the electrodes and allows ions to flow from the anode to the cathode. In most cases, the electrolyte is a neutral solution that is either a liquid or a gel-like substance. Figure 2.1 depicts a basic anatomy of an electrochemical cell.

2.1.3 Types of rechargeable batteries

There are two main types of cells: primary and secondary. The main distinction between the two is that primary cells are not rechargeable, whereas secondary cells can be recharged with a battery charger. In the market, there are now five main different types of secondary batteries [22]. Table 2.2 summarises the characteristics of commonly used secondary batteries.

Nickel Cadmium(NiCd): NiCd batteries have a relatively low energy density compared to the others. They are mostly used where longevity, high discharge rate, and affordable price are important. Although they are not the most environment friendly, applications of NiCd cells are seen in biomedical equipment and power tools [22].

Nickel-Metal Hydride(NiMH): NiMHs are much higher in energy den-

Specifications	Lead Acid	NiCd	NiMH	Li-ion		
				Cobalt	Manganese	Phosphate
Specific energy density (Wh/kg)	30–50	45–80	60–120	150–190	100–135	90–120
Internal resistance[1] (mΩ)	<100 12V pack	100–200 6V pack	200–300 6V pack	150–300 7.2V	25–75[2] per cell	25–50[2] per cell
Cycle life[4] (80% discharge)	200–300	1000[3]	300–500[3]	500–1,000	500–1,000	1,000–2,000
Fast-charge time	8–16h	1h typical	2–4h	2–4h	1h or less	1h or less
Overcharge tolerance	High	Moderate	Low	Low. Cannot tolerate trickle charge		
Self-discharge/ month (room temp)	5%	20%[5]	30%[5]	<10%[6]		
Cell voltage (nominal)	2V	1.2V[7]	1.2V[7]	3.6V[8]	3.8V[8]	3.3V
Charge cutoff voltage (V/cell)	2.40 Float 2.25	Full charge detection by voltage signature		4.20		3.60
Discharge cutoff voltage (V/cell, 1C)	1.75	1.00		2.50 – 3.00		2.80
Peak load current Best result	5C[9] 0.2C	20C 1C	5C 0.5C	>3C <1C	>30C <10C	>30C <10C
Charge temperature	–20 to 50°C	0 to 45°C		0 to 45°C[10]		
Discharge temperature	–20 to 50°C	–20 to 65°C		–20 to 60°C		
Maintenance requirement	3–6 months[11] (topping chg.)	30–60 days (discharge)	60–90 days (discharge)	Not required		
Safety requirements	Thermally stable	Thermally stable, fuse protection common		Protection circuit mandatory[12]		
In use since	Late 1800s	1950	1990	1991	1996	1999

Figure 2.2: Characteristics of commonly used secondary batteries [23].

sity compared to NiCd but have a lower life cycle. They are environment friendly and are commonly seen in cellular devices and laptops [22].

Lead Acid: In terms of low-cost, lead-acid batteries are the cheapest. Although heavy, lead-acid cells are durable and have a high discharge rate. Applications of such batteries are common in hospital equipment, emergency lighting, cars, and uninterruptible power supply systems [22].

Lithum Ion (Li-ion): Li-ion batteries are the most widely used battery system. They are often used where high discharge rate and portability is necessary. Disadvantages of Li-ion cells are the aging effect and requirement of a protection circuit. Some applications are mobile phones and notebooks [22].

2.2 Understanding battery characteristics

The recent growth in battery demand has attracted many researchers to investigate different cell characteristics. Understanding these cell characteristics is important since they give consumers a good insight into the performance of the battery. Some of the important characteristics are discussed below.

2.2.1 Battery Capacity

The term "battery capacity" is defined as the amount of charge stored in a cell and is dependent on the active mass material within the cell [24]. In other words, it is a measure of the maximum amount of energy a battery can source under certain conditions. Figure 2.3 portrays the charge/discharge cell capacity curve of a single 800mAh lithium-ion cell.

One of the main factors that influence the rated battery capacity is the rates at which a cell is being charged and discharged. If a cell is discharged rapidly with a high discharge current, the amount of energy sourced from the battery will be lower than the rated value. On the other hand, a low discharge current will increase the amount of energy one can extract from the battery [24].

External and internal temperature of a cell can also alter the battery ca-

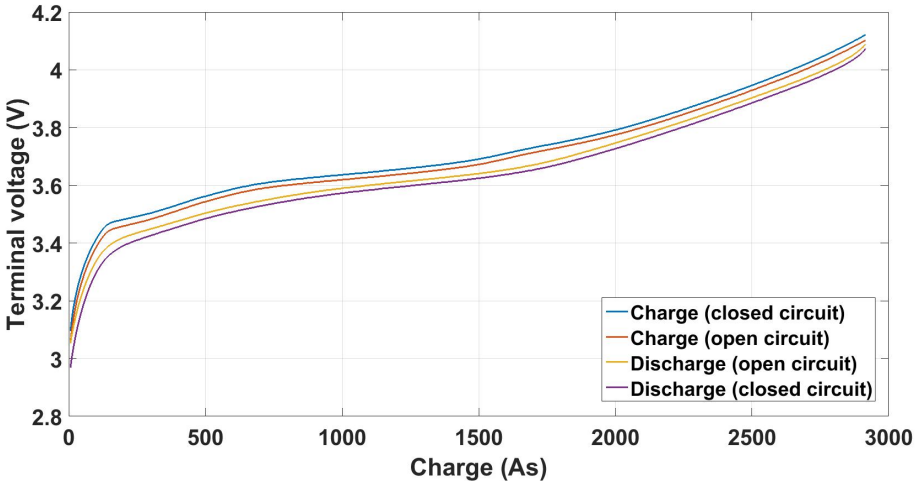

Figure 2.3: Charge/discharge capacity curve of single 800mAh lithium-ion cell. [25]

pacity. The battery capacity is known to increase at higher temperatures, however, elevating the temperature will decrease the lifetime of the cell. Age and history of a cell are other factors that can also affect its capacity [24].

2.2.2 Battery State of Charge

State of charge (SoC) of a battery is defined as a ratio of the amount of energy available in the cell to the rated battery capacity [26]. In layman's term, it is a measure of how full or empty a battery is. There are a few ways to measure this as mentioned in. One simple way of finding the SoC is to measure the terminal voltage of the cell. However, this method produces inaccurate results because variables such as cell materials and temperature influence the terminal voltage. Such a method also yields erroneous results when the cell under test is subjected to charge/discharge current. The current stimuli distorts the terminal voltage and the true SoC of the cell is no longer reflected.

To obtain the true SoC, the cell is required to rest in the open-circuit state for at least 2-3 hours; most battery manufacturers suggest 24 hours of resting period for a lead-acid battery. This makes it difficult to measure the SoC of a battery in active use.

Coulomb counting is another method used to approximate SoC by monitor-

Approximate state-of-charge	Average specific gravity	Open circuit voltage			
		2V	6V	8V	12V
100%	1.265	2.10	6.32	8.43	12.65
75%	1.225	2.08	6.22	8.30	12.45
50%	1.190	2.04	6.12	8.16	12.24
25%	1.155	2.01	6.03	8.04	12.06
0%	1.120	1.98	5.95	7.72	11.89

Figure 2.4: The BCI readings for a typical starter battery. [26]

ing the charge/discharge current and is commonly used in laptops and mobile devices. An alternative to the Coulomb counting method is a hydrometer but the application is only limited to flooded lead-acid batteries. It measures the change in SoC from the change in electrolyte density [26]. The Battery Council International (BCI) readings for a typical starter battery is shown in table 2.4.

2.2.3 Battery Efficiency

Battery efficiency is an important aspect in cell characteristics and is often summarised using coulombic, energy and voltage efficiencies. The coulombic efficiency can be defined as a ratio of the amount of charges flowing into a cell during charging to the amount of charges available during discharge. Coulombic efficiency can be quite high, normally around 95%, and the loss is usually attributed to redox reactions. The energy efficiency of a cell correlates to the charge and discharge C-rate and is generally lower in number compared to the coulombic efficiency. The C-rate is a measure of the rate at which a battery is depleted [27].

The voltage efficiency, on the other hand, is determined from the terminal voltage difference of the cell during the charging and discharging period. This means that a battery whose terminal voltage changes proportionally with the SoC will have low voltage efficiency in comparison to one whose voltage remains constant [27].

2.2.4 Battery State of Health

The state of health (SoH) of a battery is a measure of the general condition and performance of a cell compared to its ideal state. Factors that can affect the SOH of a cell are internal resistance, self-discharge, voltage and charge acceptance. Since it is a subjective measure, the SoH is considered as an estimate rather than a measurement. There are a few ways one can estimate this; the main one being the impedance and conductance testing. In several cases, other cell parameters are also included to derive a more accurate estimation [28].

An alternative approach to impedance and conductance testing is to approximate the SoH from the usage history of the cell. However, estimating the SoH from the number of charge-discharge cycles is not an accurate measure since this does not take into consideration other factors that contribute to the aging of the cell [28].

2.3 Impedance measurement

2.3.1 Importance of impedance measurement

Impedance is a measure of the total opposition of a circuit when subjected to an alternating current at a particular frequency. Since impedance is a complex quantity, it contains a real part and an imaginary part and is often expressed as [29]:

$$Z = R + jX \tag{2.1}$$

where R is the real number and X is the imaginary number. Such measurements give insight into the internal state of a cell such as chemical properties and mechanical design.

In most cases, state of charge (SoC) and state of health (SoH) are of the main interest to many researchers. In the IEEE stable alone, there are thousands of research papers with the phrase “battery state of charge” and “bat-

tery state of health" [30–36, 39–48]. Many authors consider battery models to understand these cell characteristics and the parameters of these models are usually based on the impedance measurement of the cell.

References [30–35] all measured the complex impedance of a cell to estimate either the SoC or SoH. The author of [30] measured the impedance of lithium-ion cells to 0.1mHz and proposed a first-order RC model with Lyapunov-based adaptation law to estimate the SOC and SOH of the cell. [31] investigates the health condition of a 18650, Li-ion cell where the parameters of an RC model were extracted from the EIS plot ranging from 0.1-400 Hz. Similar practice was also seen in [32–35] where the frequency response of the cell was measured using online methods to identify parameters of proposed models which is then used to monitor the SOC in EV applications. References [36], however, uses the measured complex impedance data to determine the integral temperature of lithium-ion batteries.

2.3.2 Existing impedance measurement tools

Since impedance is an important parameter used to characterise cell behaviour, it is crucial to measure it as accurately as possible. There exist several instruments that can claim to make such measurements. Manufacturers such as Solartron [29], Hioki [37], and Zurich [38] make instruments that can measure complex impedance to low frequencies. These instruments all measure impedance using the I-V method where a sinewave signal is applied to the device under test and the voltage and current waveforms are measured. Figure 2.5 shows how most impedance analysers observe the current and voltage response of a device under test.

Some researchers have developed their own impedance analyser. References [39, 41] propose a low-cost Electrochemical Impedance Spectroscopy system which stops at 0.1Hz. They use a similar Discrete Fourier Transform approach to that presented in this thesis, but their system is narrower in focus and less generally applicable. Other references describe power converters that

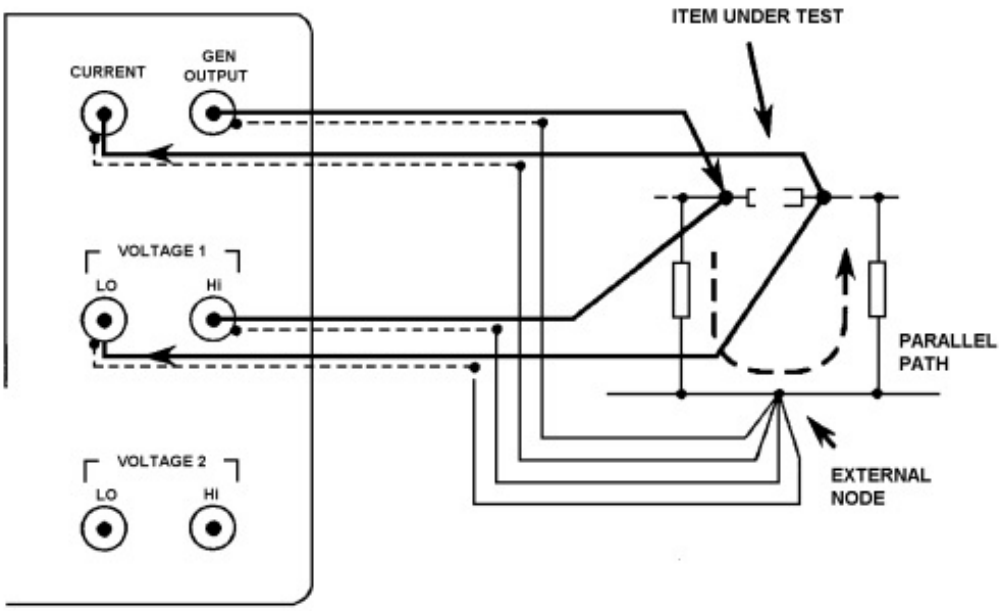

Figure 2.5: Connections to measure the current and voltage during measurement by Solartron 1260A [29].

indirectly measure battery impedance at frequencies as low as 100 mHz [42,43]. References [44, 45] managed to measure both the output impedance and the transient response of power sources; however, the frequency range is only limited to around 100 Hz. References [46–48] propose an online impedance measurement system which measures complex battery impedance at the higher end of the frequency spectrum.

2.3.3 What we thought was a good investment

Impedance measurements at extremely low frequencies–10 μHz and even lower–reveal interesting behaviour of even small cells. Figure 2.6 depicts the measured complex impedance reproduced from [49] for a single 55123, 1850mAh NiMH cell. It can be speculated from this simple curve that the magnitude of the impedance at higher frequencies resembles that of a pure resistor, but the characteristics of a fractional capacitor at frequencies below 100 μHz, based on the straight-line behaviour appearing at frequencies below 300 μHz. Without the data at the lowest edge of this plot, the characteristic of the battery

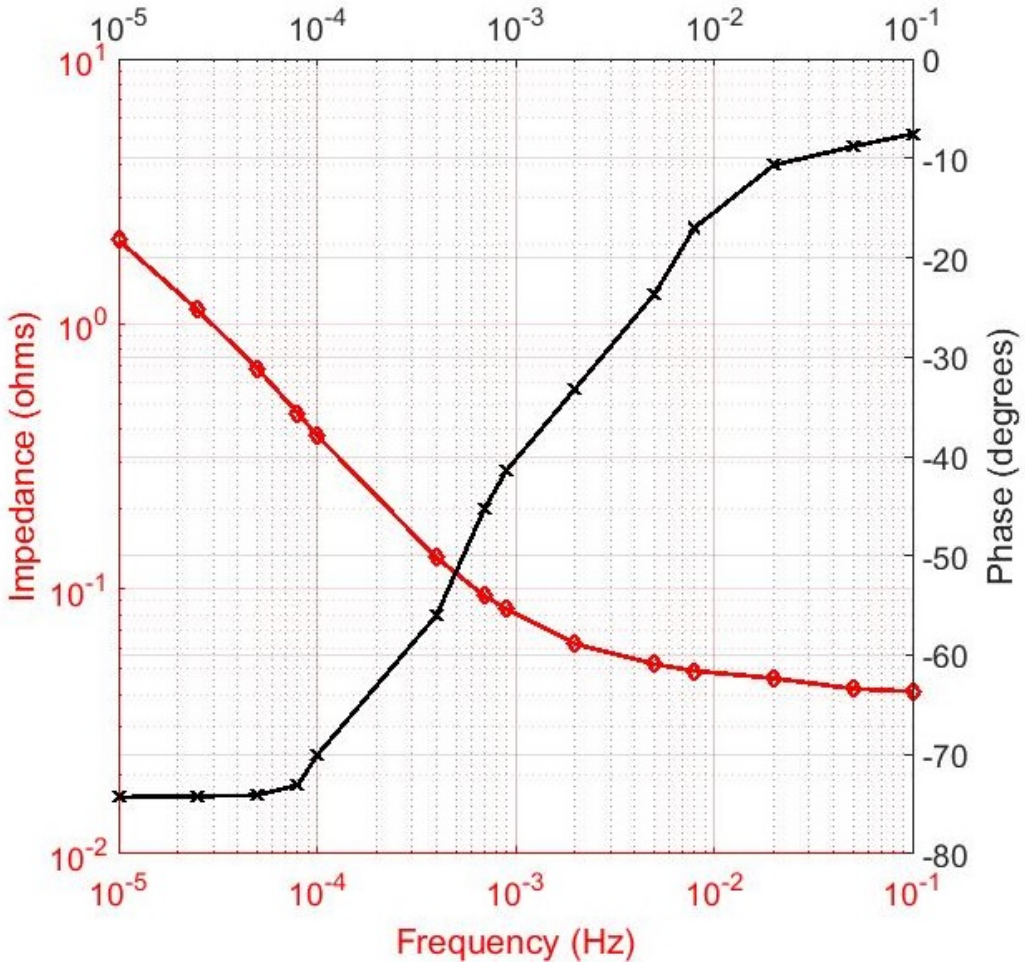

Figure 2.6: Measured impedance and phase for a single 55123, 1850mAh NiMH cell. [49]

cannot be inferred properly. Such observations drive researchers to look for instruments that reach ever-lower frequencies, but few impedance analysers are available that reach frequencies this low.

Although in many manuscripts the instrument used to obtain impedance measurement is not stated, the impedance measurement is often limited to 1 mHz. One instrument, Solartron is specifically mentioned in several manuscripts that claim to reach 10 μHz, e.g. [50, 51]. Trusting that Solartron 1260A can measure the impedance of batteries down to 10μHz, the University of Waikato purchased one. David MacCallum in [52] explains the attempt to measure the impedance of an implantable electrode using the impedance analyser. The thesis mentions that the impedance analyser successfully measured the impedance of an electrolyte capacitor at very low frequencies. However, when repeated with an implantable electrode, the measured data showed significant variation at frequencies below 300 Hz. The cause of the variation was not attributed to noise since the instrument failed to produce any variation with an electrolytic capacitor. The author then repeatedly measured the implantable electrode with Solartron 1260A in a Faraday Shielded room to eliminate any external or internal electromagnetic interference. The variation in data remained unchanged. This concluded that Solartron 1260A is unsuitable for measuring the characteristics of implantable electrodes.

The suitability of Solartron in measuring rechargeable batteries was later tested with a single 55123 NiMH and 14500 Li-ion cells. Interested to know why the impedance analyser produces erroneous impedance data with wet chemistries, the voltage and current waveforms sourced from the Solartron were observed with two Agilent 34401A digital multimeters. The connections are shown in Figure 2.7. The selected stimulus level maintained the fluctuation of the cell state of charge to within 10% at 10 mHz. Figure 2.8 shows the captured current and voltage waveforms at 10 mHz.

The figure clearly shows that the voltage waveform across the cell drifted downward, while the current waveform remains unaffected. We attribute this

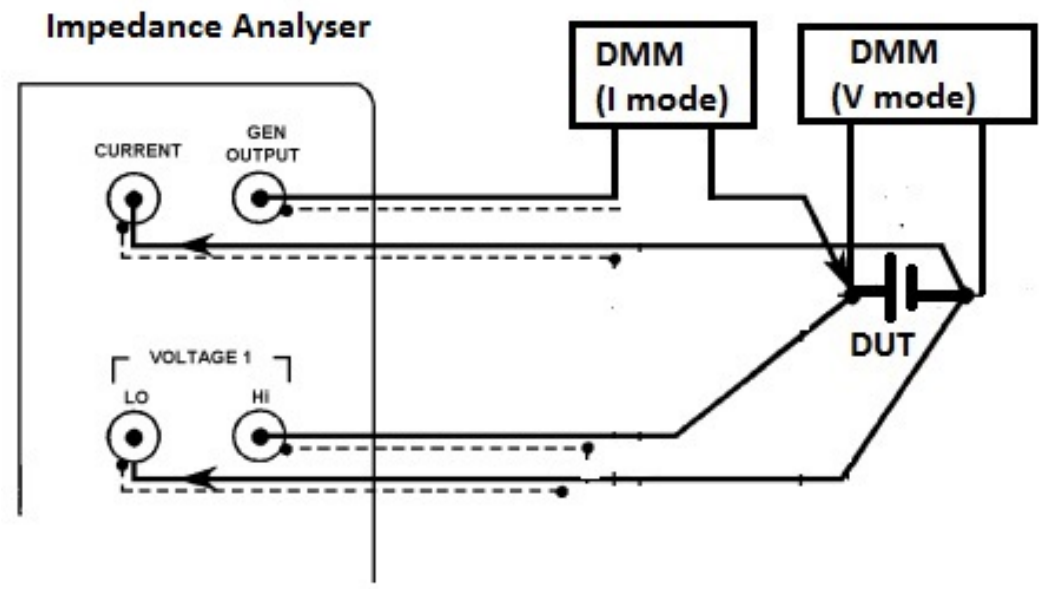

Figure 2.7: The set-up used to observe the current and voltage waveforms across a device under test (DUT).

downward drift to change in internal battery temperature while the battery was cycled during impedance measurement. Since it is impossible to know how Solartron measures impedance, it was speculated that the impedance analyser may use a discrete Fourier Transform to calculate the impedance. This might explain the inaccuracy in the impedance measurement since Fourier Transform expects signals to be continuous and produces corrupted results where the endpoints of a signal do not meet.

Another possible reason behind the impedance analyser producing erroneous data is the distortion of the signal at low frequencies. Figure 2.9 shows the distorted voltage signal. The cause of this distortion is attributed to a mechanism where excess charge delivered is safely dissipated as the cell approaches full charge. This mechanism occurs just before the capacity of the cell reaches the last few percent, especially in higher current. This explains the need to control the magnitude of the stimulus and also to stay away from the ends of the charging curve.

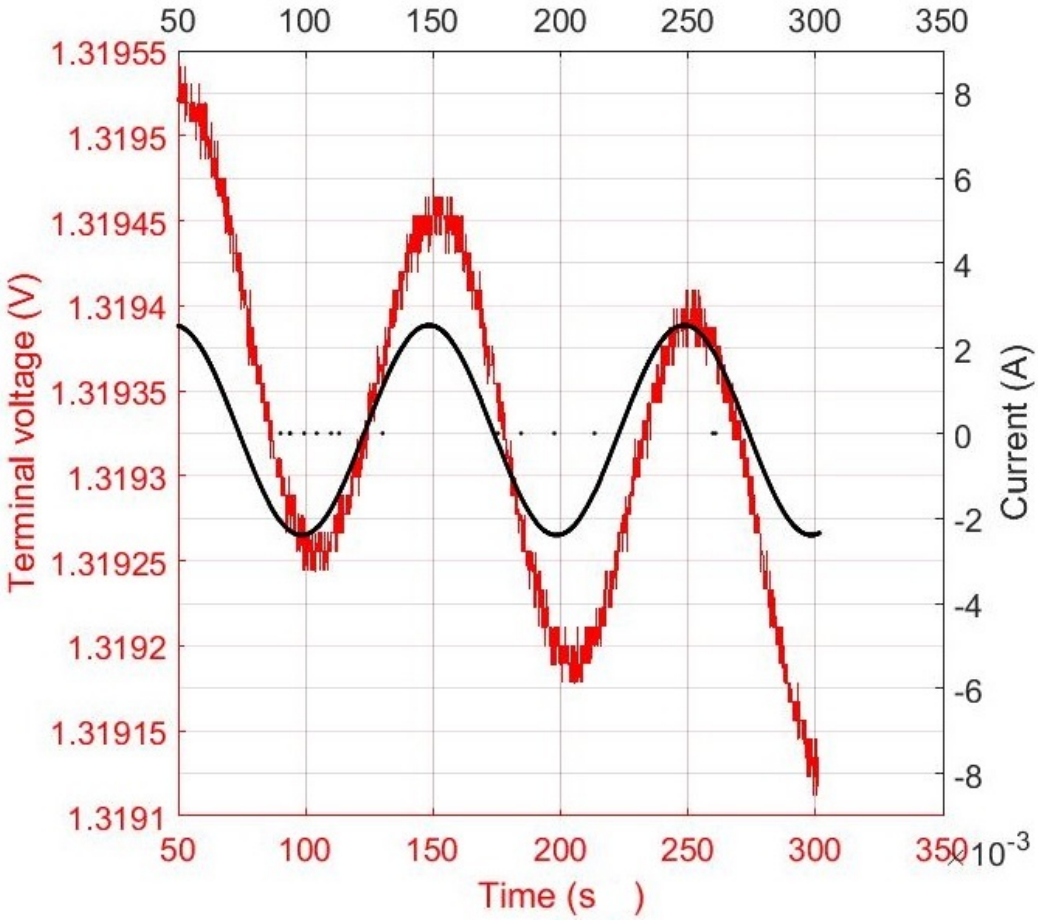

Figure 2.8: Current and voltage waveforms captured at 10 mHz.

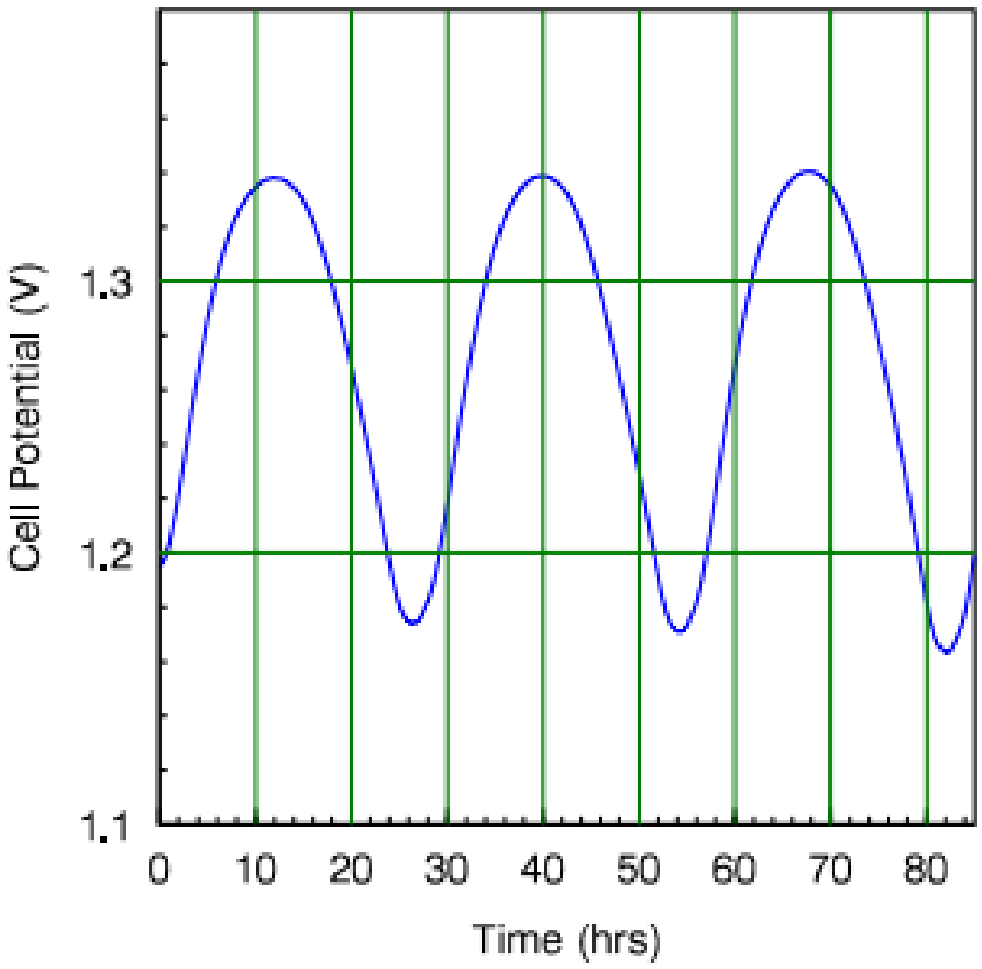

Figure 2.9: Distorted voltage waveforms captured at 10 μHz across a single NiMH cell.

2.4 Traditional RC battery models

A common practice to predict electrochemical cell characteristics is to develop a compact, equivalent circuit model for batteries based on impedance measurement [53–55]. According to [9], there exist several battery models with varying degrees of complexity. These models give insight into cell design, performance estimation, circuit simulation, etc.

Compact circuit models are utilised to improve the physical design of cells [56–58]. They describe the basic mechanism for generating power and are used to link design parameters to cell information such as terminal voltage, current, concentration distribution, etc. Sometimes these models can be complex and involve complicated numerical algorithms and specific cell information.

Some authors [59–61] propose a mathematical model rather than an equivalent circuit model. For example, [60] presented a stochastic battery model that matched to the equivalent circuit model of the battery. The mathematical model was later used to investigate various battery management techniques to improve cell capacity and runtime characteristics. Although a mathematical model may provide some useful insights to system designers, they do not have any physical justification and cannot be simulated in a circuit simulator.

2.4.1 Simple battery model

The most commonly used battery model is simply a resistor in series with a voltage source which illustrates an ideal battery [62]. A circuit diagram of the model is shown in Figure 2.10 where E_o is the open circuit voltage, R_o is the equivalent series resistance and V_o is the terminal voltage.

The V_o parameter can be obtained by measuring the open circuit voltage of a cell, whereas R_o can be found using the DC load method. During this ohmic measurement, the cell is discharged for a short duration with known load current and both the open circuit voltage with no load (OCV) and load voltage

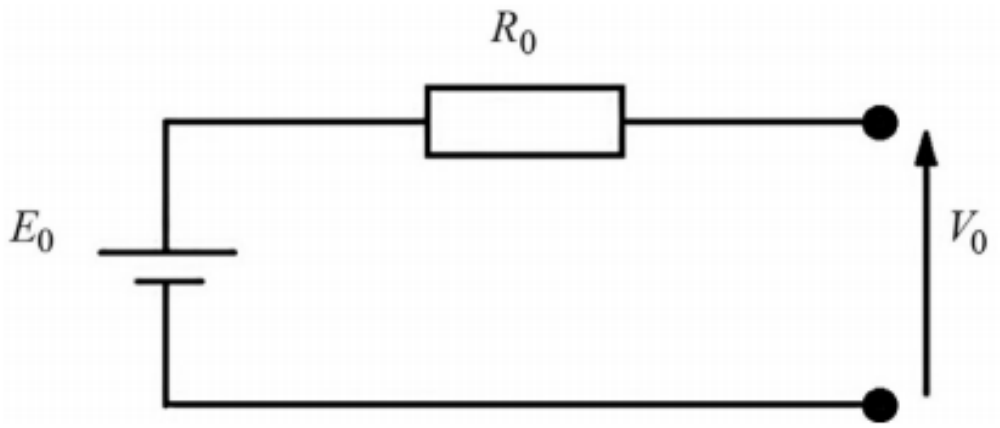

Figure 2.10: Circuit diagram of a simple battery model reproduced from [62]

are measured with a multimeter. The internal resistance is then calculated using equation 2.2. Although this type of measurement is accurate and reliable and works well for large stationary batteries, it only outputs the combined resistance and ignores any capacitance [62].

$$R_o = \frac{OCV - V_{load}}{I_{load}} \tag{2.2}$$

While such a model has been widely used by many researchers, it does not take into consideration the different characteristics of the internal impedance which changes with state of charge, electrolyte concentration and sulphate formation [62]. This limitation makes the model only suitable for circuit simulations where it is assumed that the energy drawn from the battery is unlimited or where the state of charge can be neglected. This type of model is not suitable for the applications of electric vehicles [62].

2.4.2 Modified version of the simple battery model

A modified version of the simple battery model mentioned above was presented by Jean Cun et al. in [63]. The model now takes into consideration the state of charge of the cell. The authors improved the model by introducing a variable internal resistance which changes with the state of charge of the battery. The relationship between the actual resistance during discharge and the constant

initial internal resistance is

$$R = \frac{R_o}{S^k} \tag{2.3}$$

where R_o is the internal resistance calculated from the battery manufacturer's data and k is a coefficient that is unique for every discharge curve. S is the charge status which changes between 0 and 1, where 0 is the battery fully discharged and 1 represents the battery fully charged. It is calculated using [63].

$$S = 1 - \frac{\sum Ah}{C_{10}} \tag{2.4}$$

where C_{10} represents the ten-hour capacity of the cell at the reference temperature. This value is subjected to change with the age of the battery. Many battery manufacturers employed this model for the purpose of battery monitoring.

2.4.3 Thevenin first-order battery model

A literature review of recent papers revealed that a vast number of papers propose first-order Thevenin-style RC models [7, 64–73]. The parameters of this model were identified by inspecting the cell impedance over a range of frequencies at a single state of charge. A circuit diagram of a first-order RC model reproduced from [7] is shown in Figure 2.11.

The model contains an ideal voltage source (V_{OCV}), a series internal resistance (R_o) and an RC network of R_1 and C_1. The capacitance, C_1 characterises the capacitance between the parallel plates of the cell and R_1 is the non-linear contact resistance between the plate and the electrolyte. One of the main disadvantages of such model is that the parameters are all assumed to stay constant, but in fact they all change with the condition of the cell.

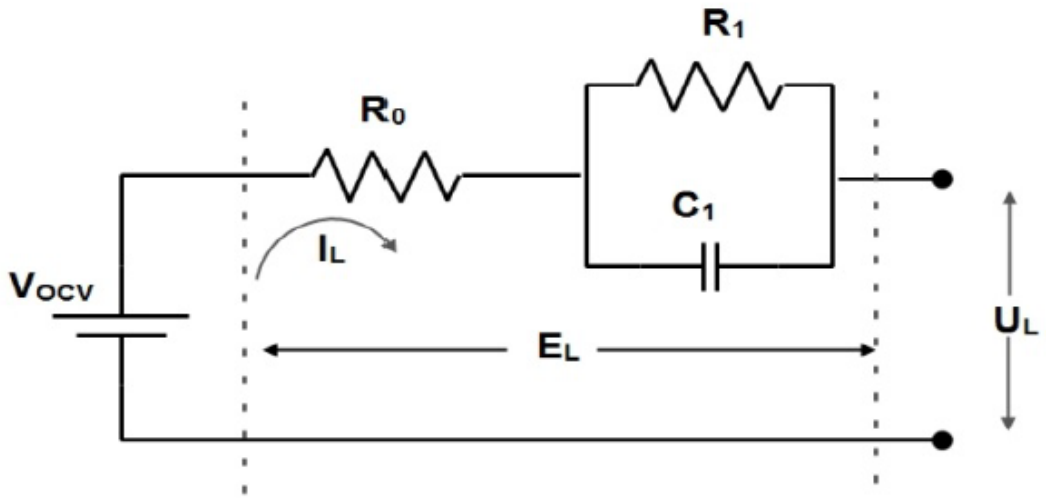

Figure 2.11: Circuit diagram of a first order RC model. [7]

2.4.4 Thevenin second-order battery model

A comparative study on battery models shows that a first-order Thevenin RC model is not accurate enough to predict the transient recovery behaviour of the terminal voltage caused when a battery is subjected to a current pulse [74, 75]. This encouraged authors to adopt a second-order Thevenin RC model with two extra degrees of freedom to predict cell SoC characteristics [8, 9, 76–87]. Figure 2.12 depicts a second-order Thevenin battery model reproduced from [77] where U_{OC} and U_t are open circuit and terminal voltages of the cell. R_o represents the series resistance. The first RC network models the mass transport effects and the second RC network represents the double layer effect [11].

Even though a second-order RC model is better at predicting the transient terminal voltage recovery curve, [88] mentions that the model is only true for high frequencies and produces significant SoC estimation errors as frequency gets lower.

2.4.5 Dynamic battery model

Although there are a few models of rechargeable battery that are based on the electrolyte chemistry, the state of charge and the thermal effects, none of

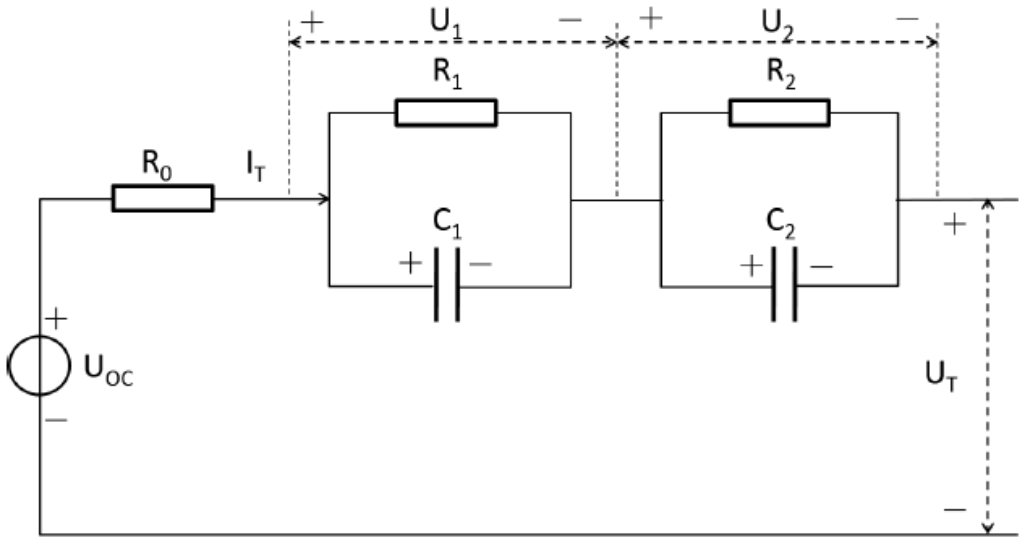

Figure 2.12: A second order Thevenin RC model. [77]

these models included all the significant cell characteristics for applications in electric vehicles and hybrid energy systems.

Wijewardana et.al introduced a dynamic battery model in [89] that takes into consideration both the electrical and the thermal effect of the cell. Figure 2.13 depicts the new proposed model. The model contains a voltage source with a resistance in parallel which models the self-discharge characteristics. This is a function of external cell temperature, state of charge and the number of times the cell has been charged and discharged. There are also two internal resistances representing the electrolytic resistance and the resistance change due to the charging and discharging of the cell. The two RC networks characterise the short and long transient properties of the cell and both the variable voltage sources are temperature dependent.

The authors claimed that their model is almost 98% accurate for a lithium-ion cell but one of the main drawback of the model is the number of parameters involved. It is known that almost any model can be accurately fitted to any measured data given there are sufficient degrees of freedom [89].

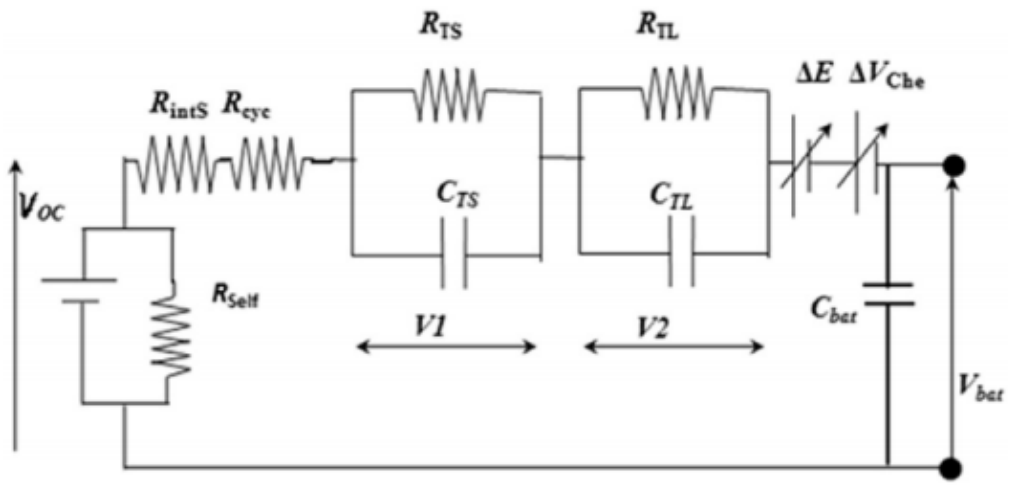

Figure 2.13: Dynamic model of a lithium-ion cell that accommodates both the electrical and thermal effects. [89]

2.4.6 Why all RC type battery models are theoretically inappropriate

All rechargeable batteries when exposed to a step-change in current produce an instantaneous step change in voltage due to the internal resistance of the cell followed by a slow decay curve. This gradual recovery tail is usually attributed to the change in chemical behaviour within the cell due to the sudden exposure to a current pulse. Figure 2.14 portrays the measured terminal voltage of an 800 mAh, 14500 lithium-ion cell when exposed to a current pulse of 100 mA for 60 seconds. Since steady-state, open circuit voltage is the most accurate measure of the state of charge of a cell, a battery model must be able to represent this phenomenon as accurately as possible.

Swingler in [90] presented a mathematical approach to extract exponential components from a transient function using Fourier transform processing. This work is a modification of the approach used by Gardener to solve summed exponential functions. Swingler's proposed algorithm transforms a function $f(x)$ containing n exponential components into a series of delta functions whose amplitude and delay represent the properties of the corresponding exponential that was summed into the function. Although the algorithm looked promising

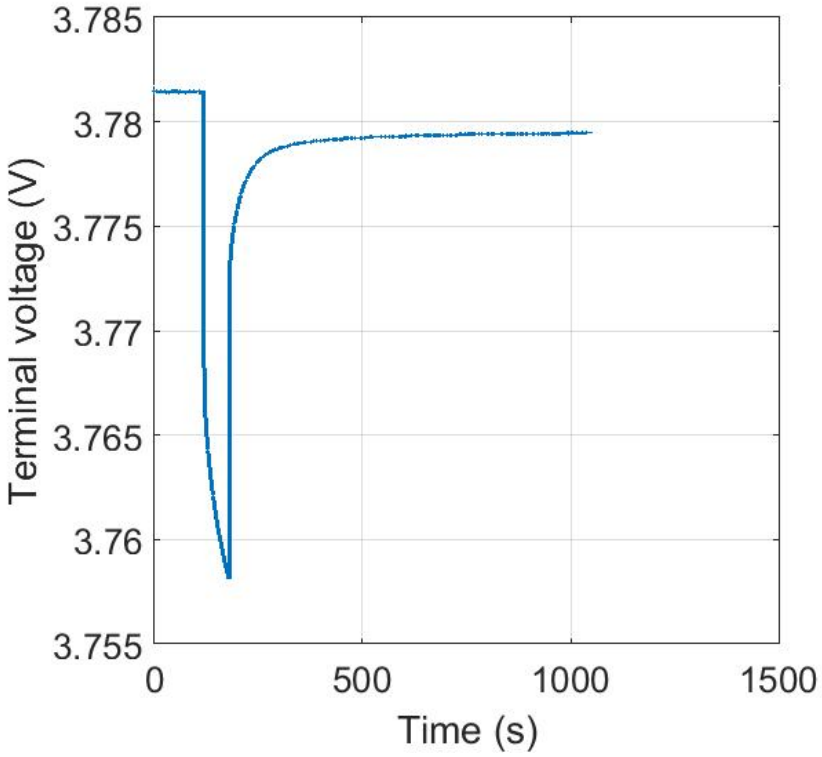

Figure 2.14: The terminal voltage of a 800 mAh, 14500 lithium-ion cell when subjected to a current pulse of 100 mA for a period of 60 seconds.

at first, applying it to a set of non-equispaced data proved to be less simple than promised. A modified version of the algorithm which deals with non-equispaced data was later proposed in [10] which yielded better results.

The modified algorithm was then applied to the measured transient voltage waveform in figure 2.14 which should identify the multiplicity of the reactive elements needed in the battery compact circuit model, as each will give rise to a single delta function. The output from the modified Swingler's algorithm is shown in figure 2.15. The result shows no proof of any exponential components present in the measured recovery data. For comparison, the algorithm was applied to the recovery curve simulated from a second-order battery model. The figure clearly shows two distinct peaks above the 50 dB noise floor. This concludes that RC models are not theoretically appropriate for modelling rechargeable batteries. The result from the Swingler analysis, however, suggests that a constant-phase element might be a better fit for modelling batteries

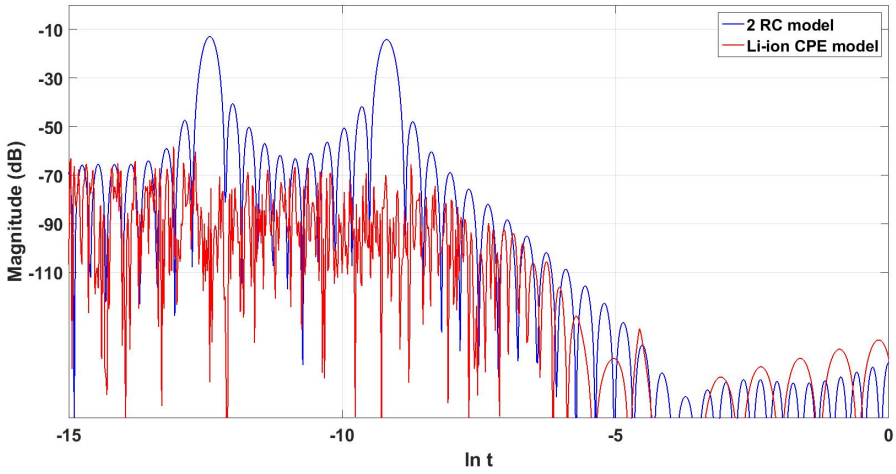

Figure 2.15: Output of the modified Swingler's algorithm applied to the transient voltage waveform curve of figure 2.14 and to a transient curve produced using a second-order RC model for comparison.

because the time-domain function of the constant-phase element is an approximation of an infinite series of exponentials and is not expected to display any peaks on this type of analysis.

2.5 Simple PSpice battery model

Hageman in [91] proposed a compact, electrical circuit model where he used PSpice to characterise rechargeable batteries, for example, nickel-cadmium, lead-acid and alkaline batteries. The core features of all the models were the same: use of a capacitor to represent the capacity of the battery, a discharge-rate normalizer to characterise the loss of capacity at high discharge currents, a circuit which allows discharge of the capacity of the cell, a lookup table for voltage versus the state of charge and a resistor which represents the internal resistance of the cell. Figure 2.16 portrays the first electrical model which covered all cell types.

Although such models are simpler to compute compared to a electrochemical model and requires a minor change to represent a particular cell type, configuring the electrical models still requires some effort. Moreover, these

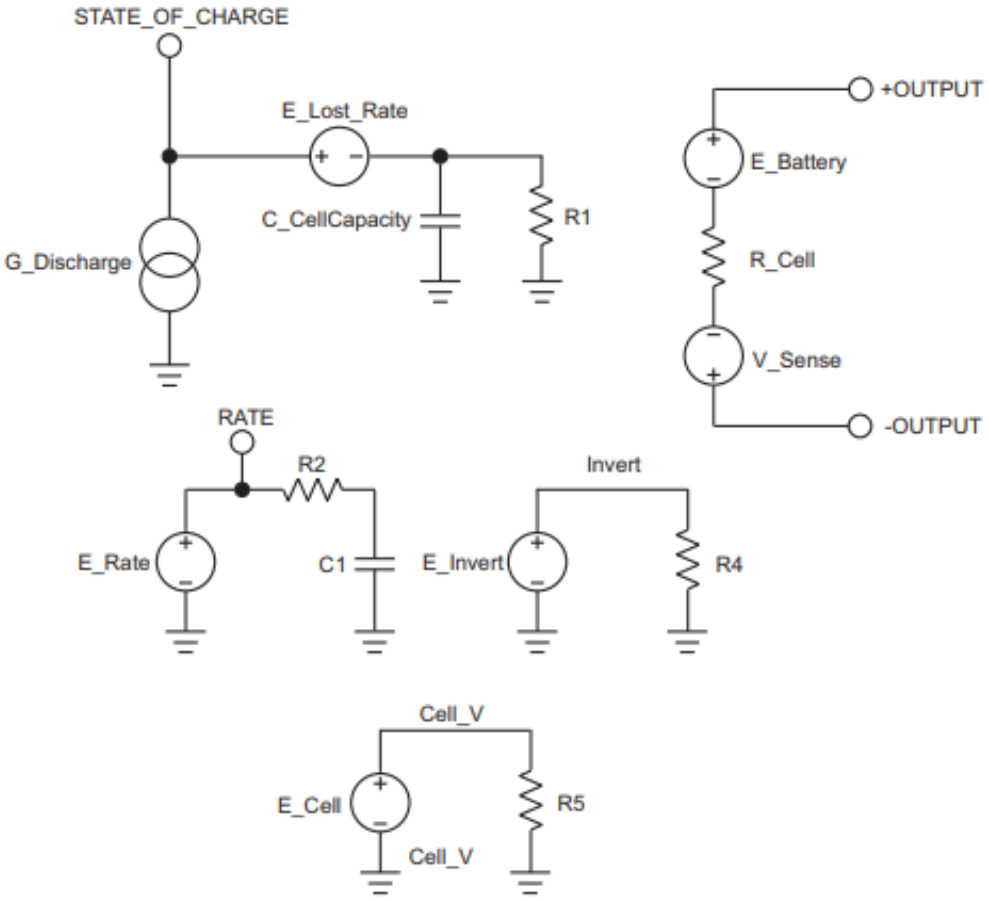

Figure 2.16: Circuit diagrams of the first electrical model covering all cell types [91]

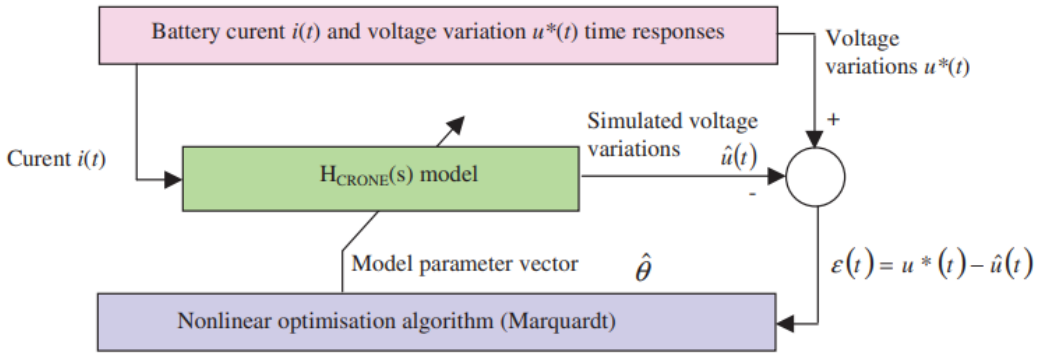

Figure 2.17: The H_{CRONE} with the parameter identification method proposed in [92].

types of models are less accurate than other existing models with an error of about 10%.

2.6 Existing fractional models

2.6.1 Mathematical fractional model for battery

Although for decades, researchers have preferred a non-fractional model, in recent years the fractional type battery model has drawn more attention due to better accuracy and the ability to adjust computational burden. Cugnet et al. in 2006 [92] proposed the concept of modelling rechargeable batteries with fractional system. The paper presented a method for estimating the state of charge of lead-acid battery based on the parameter variations of the model. The fractional model was acquired using a recently developed fractional order identification method. The parametric estimation process of the model is shown in figure 2.17. The authors claimed that the mathematical model can approximate the state of charge of a lead-acid battery with 5% error. It is important to note that the mathematical model was based on the frequency response of the cell from 2 mHz-200 Hz [92]. The main drawbacks of the model are the time required to get an estimation of the state of charge and lack of any physical justification or any compact circuit model.

A similar mathematical model with a more complex algorithm was later presented by authors of [93] in 2010. This time, the model is used to approximate the internal resistance of a cell with fewer parameters. This is directly correlated to the crankability property of a lead-acid battery. In conclusion, this work tends to confirm that batteries are of a fractional nature.

2.6.2 Randles' battery model

Many authors tend to frequently use the Randles' Warburg impedance model for modelling lead-acid cells [94–96]. The model consists of a Warburg element that is a constant phase element with a fixed phase angle of -45 degrees [97]. Such a model is only applicable in situations where the measured complex impedance has a fixed slope of 0.5. Figure 2.18 produced from [94] shows a Randles battery model containing a Warburg element. The transfer function of the model is [92]

$$H(s) = \frac{U(s)}{I(s)} = (Ls + R_l) + \frac{(1/C_s)(R + \sigma/s^n)}{(1/C_s + R + \sigma/s^n)} \tag{2.5}$$

The authors of the paper [95] measured the impedance spectra of a lithium-ion cell over high, mid, and low frequency bands to derive the Randles' fractional model. The point where the impedance curve intersects with the real axis in the high frequency portion defines the series resistance, the low frequency region where the impedance curve is a straight line with a constant gradient is referred to a Warburg element and the mid frequency band where the curve is a depressed semicircle is reminiscent of a resistor in parallel with a constant phase element.

Although at first glance the work seems powerful, a closer look at the impedance calculation revealed that the transfer function equation is incorrect: rather than summing the individual impedance elements, the authors multiplied them. Since the rest of parameter identification algorithm is based on this erroneous transfer function, it can be said that the conclusions are unfounded.

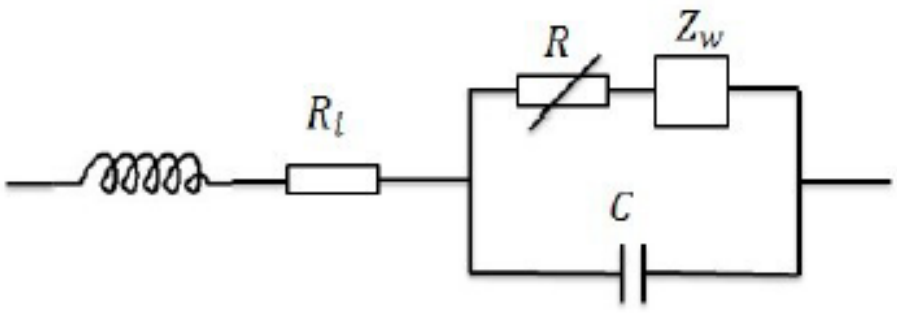

Figure 2.18: Randles Battery model containing a Warburg element. [94]

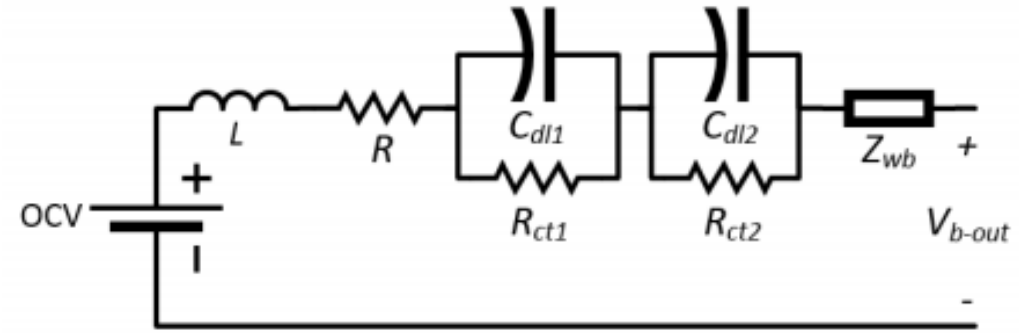

Figure 2.19: Second-order Randles' Battery model reproduced from [96].

Other authors used a second-order Randles' model to characterise a Panasonic 18650PF LiNiCoAlO_2 battery in [96]. A schematic diagram of the model is shown in figure 2.19. The two RC networks denote the charge transfer resistance and electrochemical double layer capacitance. The authors measured the impedance of the cell from 1 Hz to 1 kHz and then used the frequency response data to identify the parameters of the model. The paper claims that models with a Warburg element produce better results compared to traditional RC models, except at low surrounding temperature. The fitting success of this two RC model is attributed to its having a total number of nine parameters. We believe that almost any model with sufficient degrees of freedom can be fitted to data with reasonable accuracy.

2.6.3 Various fractional models for rechargeable cells

Different variations of fractional models have been presented for rechargeable cells in recent years, mainly for the purpose of voltage simulation and state of charge estimation. The authors of paper [98] performed a comparative analysis of the existing fractional type battery models and the study looked at how these models differ from each other in terms of accuracy and computational burden when it comes to fitting data from two NMC cells. The cells were cycled under different conditions and had a different state of health.

The models compared in [98] are shown below in figure 2.20. The paper mentioned that the most commonly used fractional model is the one with a single CPE and it can simulate the voltage characteristics more accurately than any order of RC models. There is also evidence that for better accuracy, many researchers employed different arrangement of fractional models containing two fractional capacitors to predict the state of charge of lithium-ion cells.

Taking identification accuracy, validation accuracy and computational burden into consideration, a single order constant phase element in series with a Warburg element is found more acceptable for modelling NMC cells. The authors of [98] also observed that a more complex fractional model with more degrees of freedom might only increase the computational burden and provide no added benefits in terms of accuracy.

2.7 Simulation of a constant phase element

In most research papers, a constant phase element is expressed mathematically since it relies on a fractional derivative and can be mathematically calculated with an infinite network of RC elements over an infinite range of frequency. However, in practice, infinity is an abstract concept. Therefore, the complex impedance of a constant phase element for a finite frequency range is approximated with a subcircuit of branch elements in a compact simulator given a required phase tolerance [14].

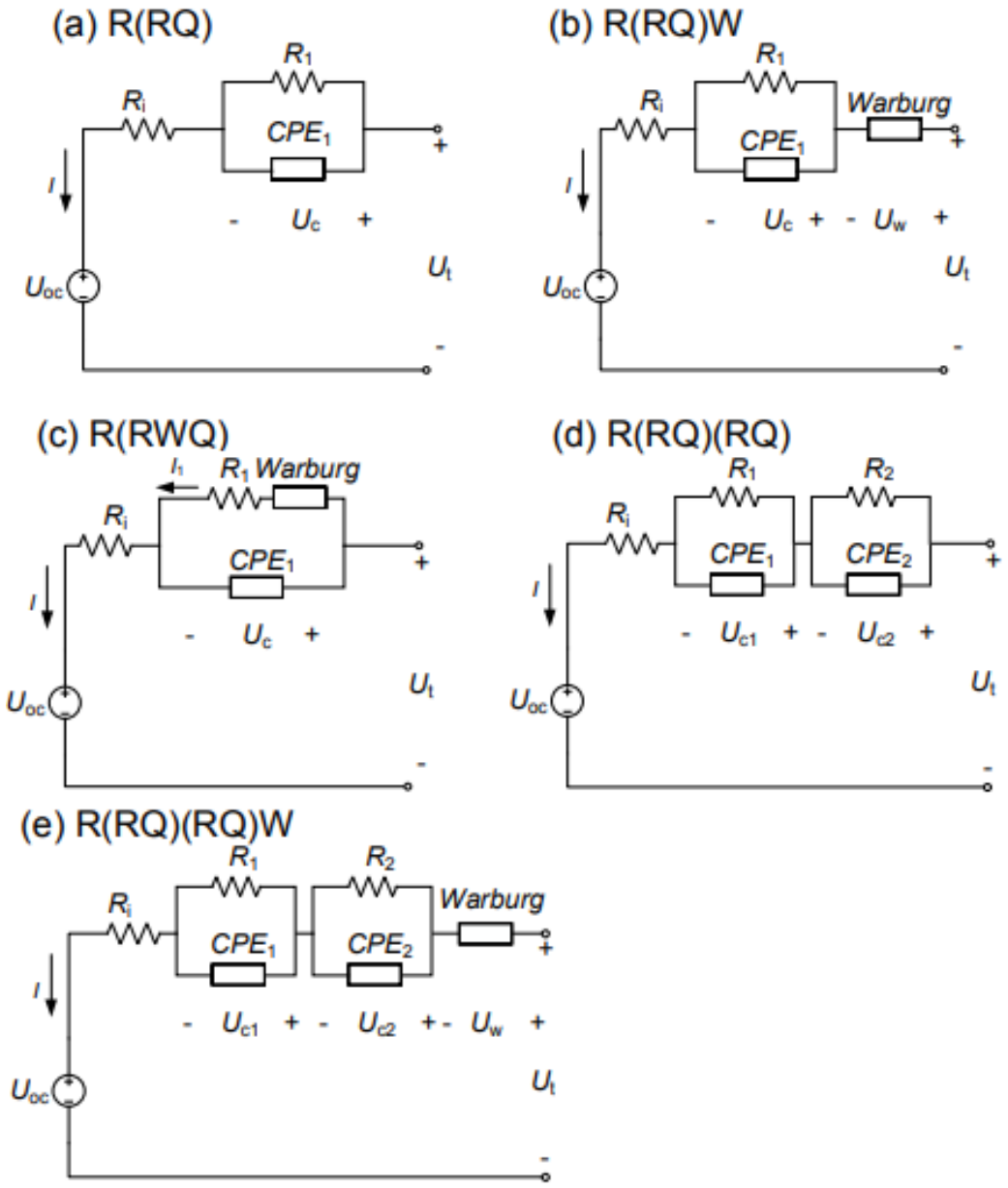

Figure 2.20: Existing fractional order models used for voltage simulation and state estimation [98].

This method is attributed to Morrison [14] whose work presents complex algebraic equations that yield the number of branches required to approximate a constant phase element for a range of frequencies with the resistor and capacitor values in each branch.

A constant phase element can be specified with only two parameters. This is represented by a straight line on a Bode plot. These are a slope parameter, m, and a magnitude parameter found from a measurement of admittance, Y_θ, at some specified frequency, ω_0. The equation to approximate the impedance magnitude of a constant phase element is [14]

$$|Y'_\theta| \approx \frac{(\omega RC)^{1/m}}{R} y_\theta \tag{2.6}$$

where $|Y'_\theta|$ is an approximation of the admittance magnitude of the constant phase element, Y_θ, R and C are the resistance and capacitance values, ω is the angular frequency in radians, m reflects the value of the element's constant phase and y_θ can be calculated by

$$y_\theta = \frac{\pi}{m \ln k} \sec \frac{1}{2}\pi(1 - \frac{2}{m}) \tag{2.7}$$

where k is a spacing factor which defines the geometric spacing of the branches with respect to frequency. The argument of the admittance can be calculated from

$$\angle Y'_\theta \approx \frac{\pi}{2m} - \theta_p \sin[\frac{2\pi \ln \omega RC}{m \ln k} - \frac{1}{2}\pi(1 - \frac{2}{m})] \tag{2.8}$$

and θ_p can be found from the equation below:

$$\theta_p \approx \frac{m \ln k}{\pi} \frac{\cosh \frac{\pi^2}{m \ln k}}{\cosh \frac{2\pi^2}{m \ln k}} \cos \frac{1}{2}\pi(1 - \frac{2}{m}) \tag{2.9}$$

It is worth noting that equations 2.7 and 2.9 contains only 2 main variables in the form of m and k. Equation 2.6 can be used to calculate the admittance magnitude of the constant phase element with a scaling factor obtained from equation 2.7. Equation 2.8 gives the phase of the admittance with a periodic error calculated from equation 2.9.

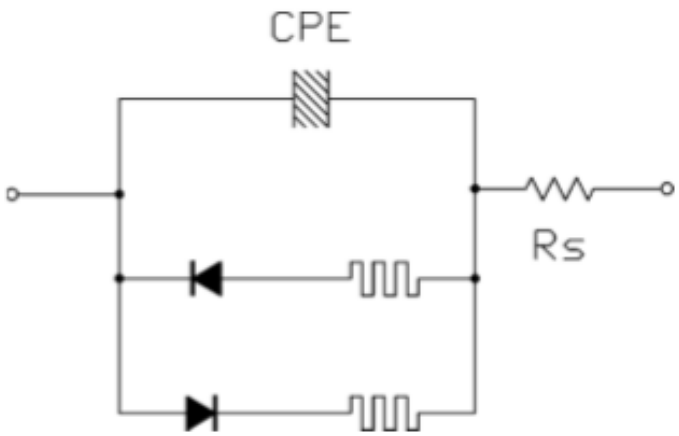

Figure 2.21: Proposed fractional model for electrode-electrolyte interface, containing a constant phase element, a series resistor and two diode-memristor branches [13].

2.8 Previous work adopting Morrison's method

Some authors have adopted Morrison's method to construct a constant phase element in a compact simulator: the following works later laid the foundation of the work conducted in this thesis. Scott and Single in [13] proposed a model of the electrode-electrolyte interface comprising a constant phase element. Figure 2.21 portrays the proposed model. R_s represents the spreading resistance, the CPE models the double layer effect, and the diode-memristor branches track the charge transferred, thus representing the Faradaic contribution.

To compute the constant phase element in a circuit simulator, the authors replaced the constant phase element with one of Morrison's equivalent canonic forms shown in figure 2.22: the figure contains parameters m, k, R and C that can approximate a constant phase element with arbitrary accuracy over a particular frequency range.

From equation 2.8, the authors of [13] derived a simpler relationship to calculate the parameter m from a known phase angle value. The authors described the relationship as:

$$m = \frac{\pi}{2\theta_{CPE}} \tag{2.10}$$

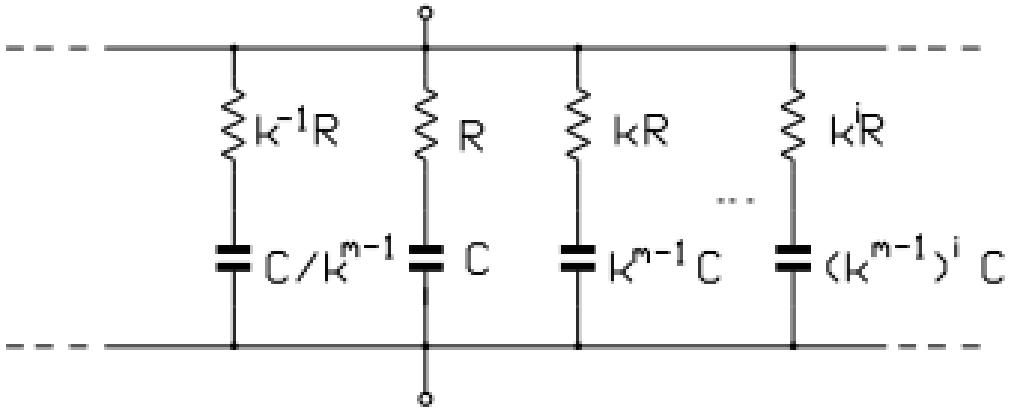

Figure 2.22: Lumped-RC approximation of a constant phase element [13].

where θ_{CPE} was obtained from the measured phase angle of the constant phase element. Instead of relating phase accuracy to simulation accuracy, the authors simply assigned k to a value close to 1 which does not affect the simulation results. With values of m and k identified, and the magnitude of the admittance $|Y_\theta|$ measured at some arbitrary frequency ω_0, R and C values of a branch were found using Morrison's equation 2.6. The number of RC branches was chosen by trial and error for the frequency range over which the model is expected to operate.

Later the same year, Jones and Scott published a paper [99] where a similar type of model was proposed for the electrode-electrolyte interface in phosphate buffered saline. Figure 2.23 shows the proposed model. The reason why this model lacks memristors is that generally, implantable electrodes are never operated in a Faradaic conduction mode and definitely never to the point where diffusion is limited. Using the impedance magnitude and phase of the implantable electrode measured at frequencies between 100 mHz and 10 kHz, the authors later simulated the constant phase element in ngSpice simulator with the equations presented in [13].

Recently, Single and Scott presented an improved version of their single constant phase element model in [16]. The model can now capture the slow transient decaying tails, also referred to as artefacts, produced when platinum electrodes are subjected to a current pulse. This was achieved by splitting the

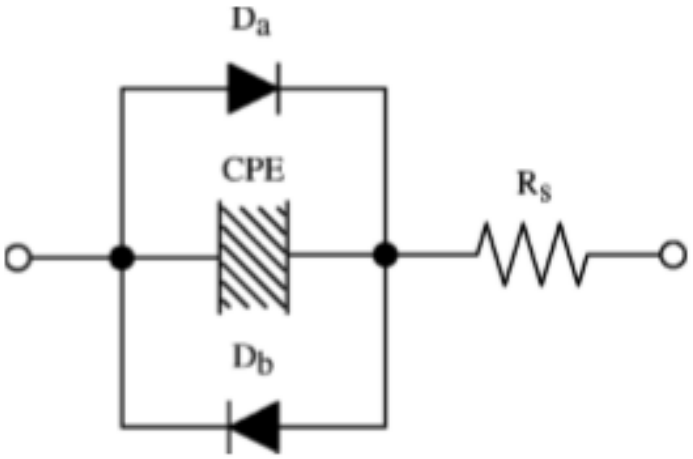

Figure 2.23: Proposed fractional model for electrode-electrolyte interface, containing a constant phase element, a series resistor and two back-back diodes [99].

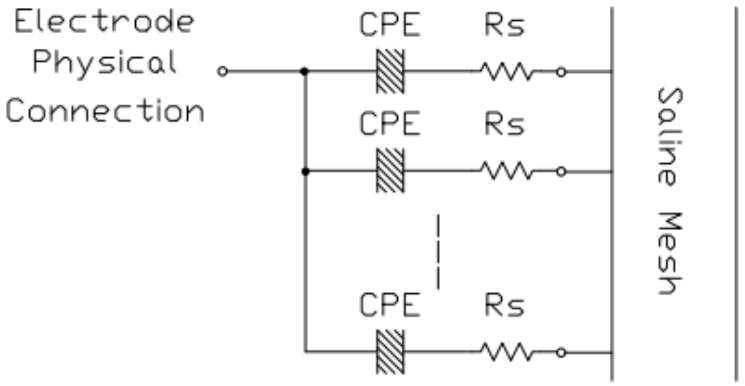

Figure 2.24: Proposed split-electrode model for electrodes of neuromodulation implants [16].

constant phase element into n branches that allows the simulation of uneven distribution of charges along the surface of the electrode. Figure 2.24 depicts the proposed split-electrode model for electrodes of neuromodulation implants. The authors tested the validity of the model with measurements conducted in saline which suggested that artefacts from electrodes are the inherent properties of the electrode-electrolyte system itself. The external influences from external hardware are all negligibly small.

Chapter 3

Tutorial on Swingler's Method and Verifying the Fractional Nature of a Battery

3.1 Summary of Swingler's method for analysis of multicomponent exponentials

This manuscript presents a step-by-step tutorial on how to extract multicomponent exponential components from a transient curve. The proposed method is built upon Swingler's differential approach to the Fourier Transform processing of time-domain functions with multiple summed exponential components. Swingler's technique yields delta functions which are directly proportional to exponential components present in the data. Limitations of this technique is its inability to handle data obtained from compact simulators which may be non-equispaced and not easily interpolatable. This paper provides a series of steps required to extend this complex algorithm to handle time-domain functions which are non-equispaced in nature. The steps mainly involve smart interpolation in both the time-domain and log-time domain and a careful selection of the x-axis range. Unlike Swingler's method, the proposed method does not require data to be artificially windowed. A comparison analysis between the two techniques showed that the method presented in this paper can identify the exponential components of the signal used by Swingler in his paper with higher accuracy. This method was later adopted to identify the presence of any exponential components in the recovery curve of a nickel-metal hydride and lithium-ion cell.

2016 IEEE 12th International Colloquium on Signal Processing & its Applications (CSPA2016), 4 - 6 March 2016, Melaka, Malaysia

Application of Swingler's Method for Analysis of Multicomponent Exponentials with Special Attention to Non-equispaced Data

Rahat Hasan
School of Engineering
University of Waikato, Hamilton, New Zealand
rh163@students.waikato.ac.nz

Jonathan Scott
School of Engineering
University of Waikato, Hamilton, New Zealand

***Abstract*—Swingler enhanced the work of Gardner to provide an elegant deconvolution method by which multiple summed exponential components might be resolved within time-domain data. Nevertheless, the application of the method remains limited owing to subtle complications that discourage many users. We present a tutorial and extend the approach to handle non-equispaced data. Finally the method's limits are identified in the case of closely-spaced exponential components with added input noise.**

I. Introduction

Several authors have employed deconvolution to extract multicomponent exponential components from a transient curve [1]–[5]. The preferred method is attributed to Swingler [2] whose work built upon the original article by Gardner [1]. The method notes that for a time-domain function of the form

$$f(t) = A_1 e^{-\alpha_1 t} + A_2 e^{-\alpha_2 t} \tag{1}$$

where A_1 and A_2 are the magnitudes of the two exponential components and α_1 and α_2 are the reciprocals of the time constants, delta functions exist such that

$$A_1\delta(x-p_1) + A_2\delta(x-p_2) = \mathcal{F}^{-1}\frac{\mathcal{F}\left[\frac{\delta f(e^x)}{\delta x}\right]}{\mathcal{F}\left[-e^x e^{(-e^x)}\right]} \tag{2}$$

where $x = \ln(t)$ and $p = -\ln(\alpha)$. The method generalises to n exponentials straightforwardly. In other words, a multiexponential function can in principle be operated upon to yield a series of delta functions each of whose amplitude and delay indicate the amplitude and decay constant of the corresponding exponential that was summed into the initial function. The algorithm consists of moving to a log-time scale, differentiating, and deconvolving the response signal $-e^x e^{(-e^x)}$ in the "trans-log" domain.

Data obtained from simulators and measurement instruments may be non-equispaced in nature, and in any case the move to log-time is highly nonlinear, with the outcome that real-world data presents to the Fourier transform at the start of the deconvolution process in a form that is not only non-equispaced, but potentially very difficult to interpolate. None of the literature addresses this. In [2], computed data is used and no mention is made of the interpolation issue with the Fourier Transform (FT) that is used. In this manuscript we describe the series of intermediate steps applied to the non-equispaced data prior to deconvolution, and unlike Swingler we find that we do not need to window data artificially.

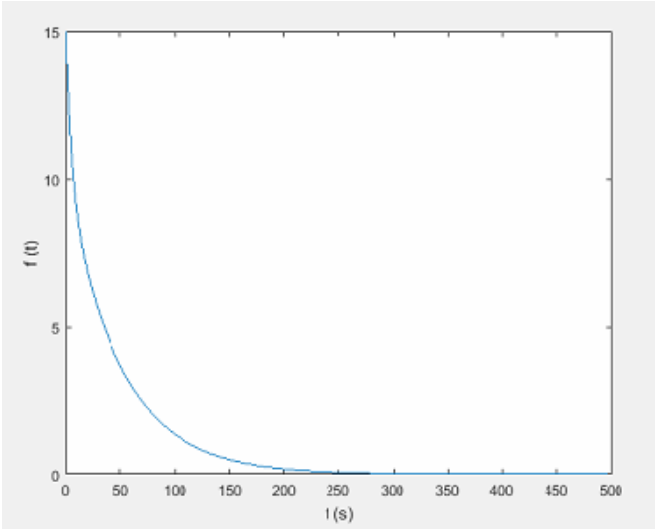

Fig. 1: Transient curve with two exponential functions

II. Step by step procedure

A transient curve with two exponential functions, $f(t) = 5e^{-0.2t} + 10e^{-0.02t}$ is shown in figure 1 by way of example. The first step is to interpolate within the first three data points in order to add more points to the negative axis in the log-time domain. This interpolation is linear in the time domain, since $e^x \approx x$ for small x, giving an exponential. The transformation of the transient curve to the log-time domain is shown in figure 2.

Once the transient curve has been transformed to the log-time domain, the transformed curve is then taken to an equally spaced grid using cubic spline interpolation, since most FFT algorithms only accept equispaced data. We have investigated the possibility of transforming directly from the non-equispaced data in the log-time domain to equispaced data in the trans-log domain using the algorithm from [6]. In this case, where the data is comfortably oversampled, the results are identical. Nevertheless, this approach could offer advantage

978-1-4673-8780-4/16/$31.00 ©2016 IEEE

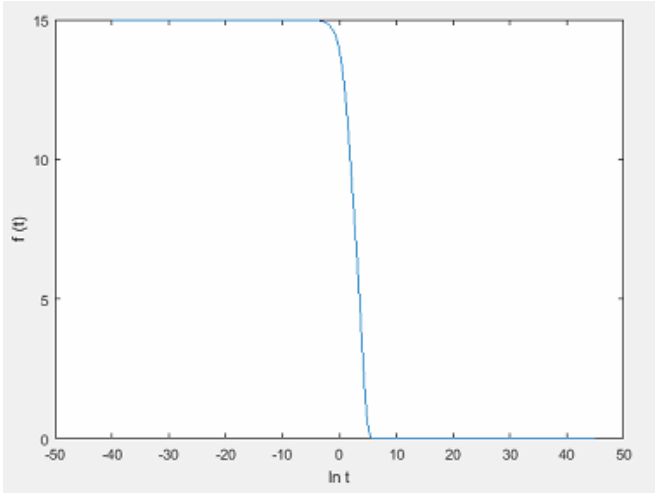

Fig. 2: Transient curve in log-time domain

where the data is sparse. Once on a regular grid in log-time domain, a first-order difference is taken. The resulting curve is shown in figure 3. Looking at this curve in our example, it is possible to see what we know be two blurred peaks, as we chose two functions of comparable magnitude sufficiently far apart. Of course, the peaks will not always be visible in the first-order derivative curve.

The first-order derivative curve is then deconvolved with the response function, $g(x) = -e^{x}e^{(-e^{x})}$. This response function is shown in figure 4. The deconvolution is a point-wise division in the frequency domain. This process is acknowledged to be very sensitive to noise. In our case we can calculate the denominator to any desired precision. To improve the clarity of the outcome it is a well-known technique to add a small constant to the response function in the Fourier domain as required [3]. Figure 5 shows two delta functions with time constants of 6.5 seconds (30 % error) and 59 seconds (18% error) respectively.

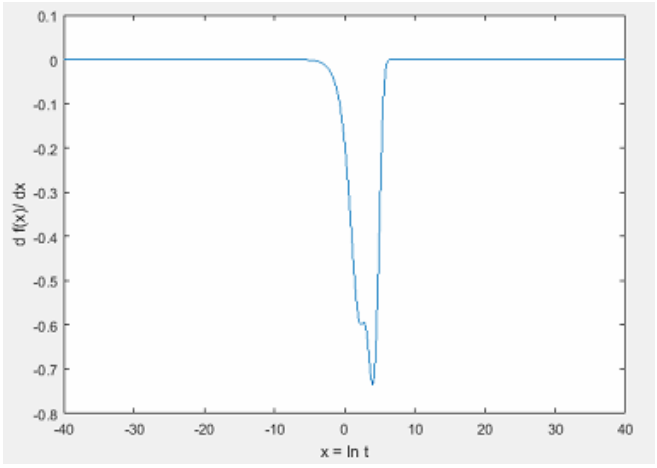

Fig. 3: First-order derivative of the transient curve in log-time domain

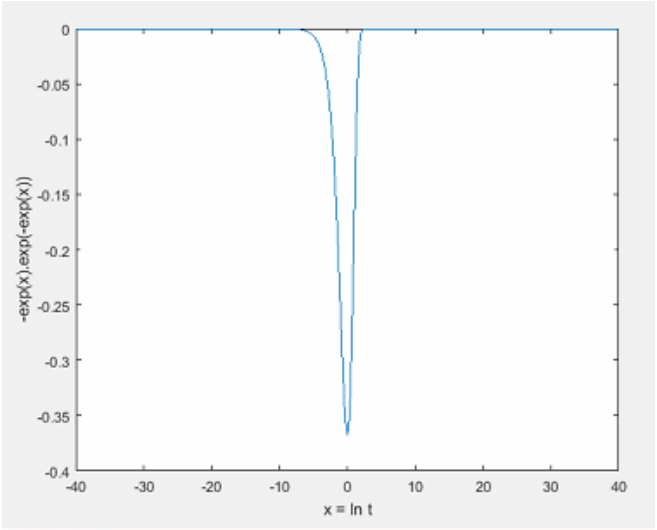

Fig. 4: Plot of the convolving 'response curve'

III. Variation of the noise floor with respect to x-axis range

In this section, we will address the sensitivity of the delta functions with respect to the variation of the x-axis range. The transient and the response functions used in our algorithm will eventually reach zero as x approaches infinity but we are free to choose the x-axis range. The operating range for the x-axis values can be determined empirically. Figure 6 shows the impact of changing that range. For an x-axis range of -30 to 30, the noise floor drops to double precision numerical noise. Further reduction of the range shifts up the noise floor above -270 dB through rectangular windowing.

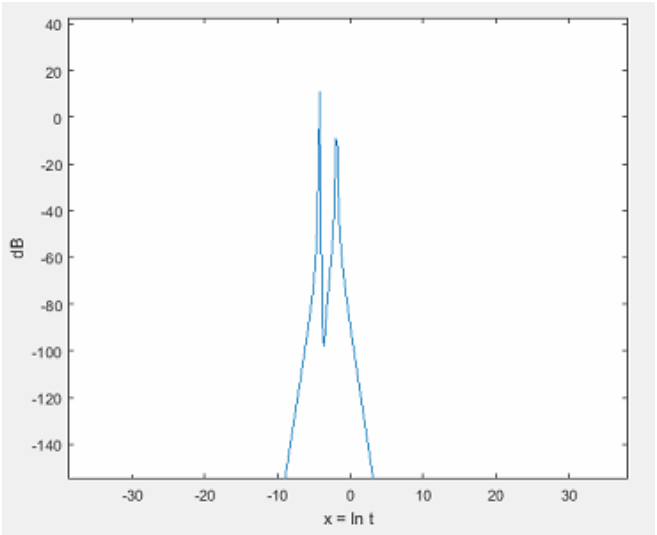

Fig. 5: The resulting curve containing two delta functions

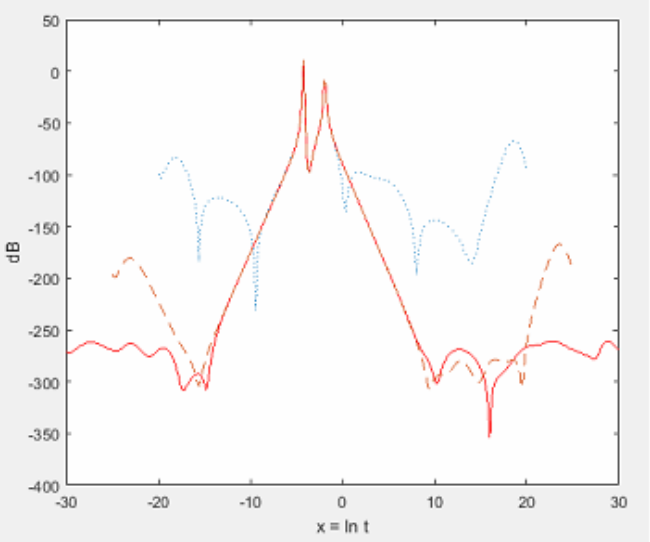

Fig. 6: Variation of the noise floor with respect to x-axis range

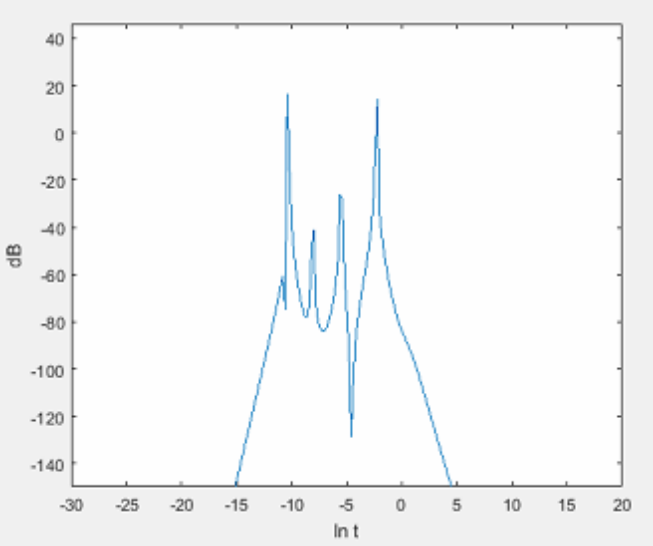

Fig. 7: The resulting curve containing four delta functions

IV. Comparison using Swingler's example

A similar investigation is carried out with the signal used in [2]. The transient function, $f(t) = 12.6e^{-0.1433t} + 2.2e^{-0.0055t} + 0.9e^{-0.00042t} + 13.3e^{-0.000042t}$ has four exponential functions and for the purpose of this article, the signal is generated with non-equispaced data. The function is deconvolved with the known wrapped around response function, $g(x) = -e^x e^{(-e^x)}$ and since the numerical noise in the data is minute, a small noise reduction constant of 10^{-10} is added to improve the clarity of the peaks. The noise reduction constant will increase significantly will the addition of artificial noise to the data. The resulting curve is shown below in figure 7. The time constants of the exponential functions are calculated from the x-axis and compared with the results obtained in [2].

Time constant values for exponential components		
Actual value	Modified algorithm (% error)	Swingler's algorithm (% error)
6.98	9.03 (29%)	11.02 (58%)
181.81	221.41 (22%)	270.42 (49%)
2,380.95	2,980.96 (25%)	4,447.07 (87%)
23,809.52	26,903.19 (13%)	32859.62 (38%)

TABLE I: Comparison of the values obtained from the delta functions using modified and original algorithms.

From table I, observe that our implementation of Swingler's method achieves superior results compared with the original. The amplitudes of the delta functions are less degraded.

V. Discriminating adjacent peaks

We now address the issue of the limitation when discriminating adjacent peaks. To investigate this, we examine a number of non-equispaced transient curves with two, closely-spaced exponential functions.

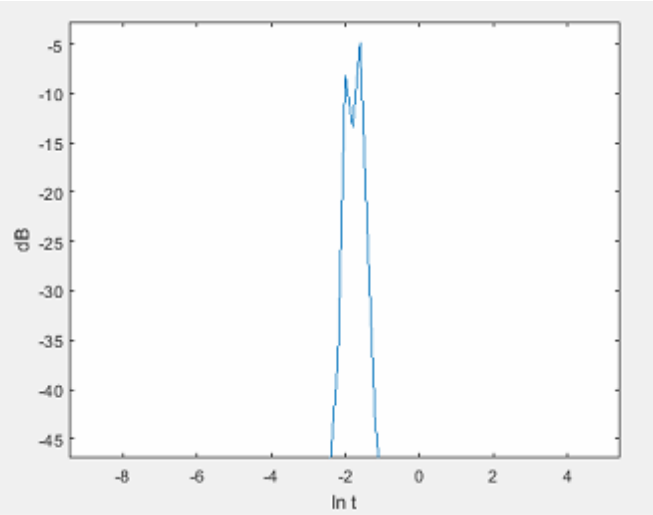

Fig. 8: Two exponentials with time constant ratio of 0.70

Figure 8 shows the output of the algorithm operating on $f(t) = 5.4e^{-0.28t} + 5e^{-0.2t}$ where the ratio of the time constants is 0.7. When the ratio approaches 1 by even a small amount, the adjacent peaks merge together; figure 9 shows the case for a ratio of 0.74. Note that the absolute value of the time constants makes no difference, it is only their ratio that determines proximity.

VI. Noise analysis

Real data contains noise. As an example, -90 dB additive white Gaussian noise (AWGN) is applied to the function used in Section IV. One of the fundamental limitations of this technique is that without the addition of any constant, the

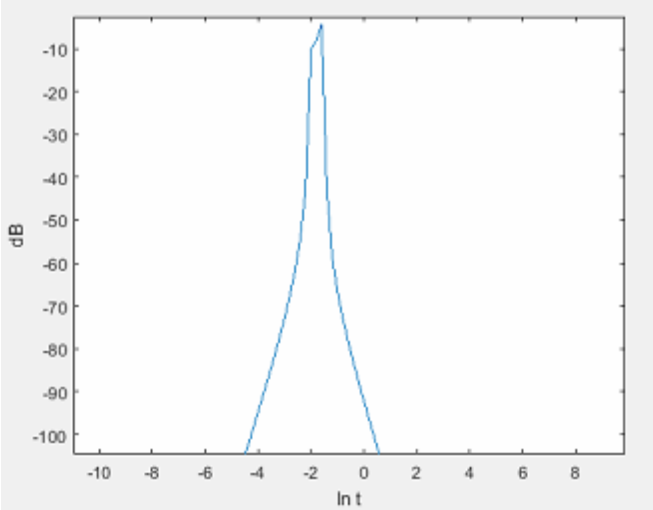

Fig. 9: Two exponentials with time constant ratio of 0.74

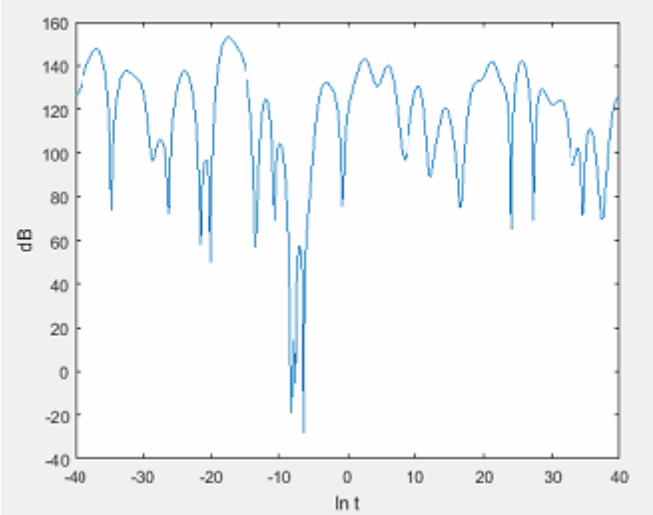

Fig. 10: Presence of noise flooding out the peaks

noise will flood out the peaks of the delta functions as shown in figure 10.

Trial and error quickly shows that a noise reduction parameter of 0.01 optimally cleanses the peaks. Figure 11 shows the result. The peak values remain unaffected compared to the noise-free case (Section IV). Nevertheless, additional scalloping attends each peak. This is to be expected, as the noise reduction parameter effectively reduces the amplitude of the deconvolution division going outwards from the centre region; this is equivalent to adding a window whose effect after the IFFT is to introduce a series of lesser peaks. This is one of the other fundamental limitations of this technique. The results obtained in this case hold for both equispaced and non-equispaced data.

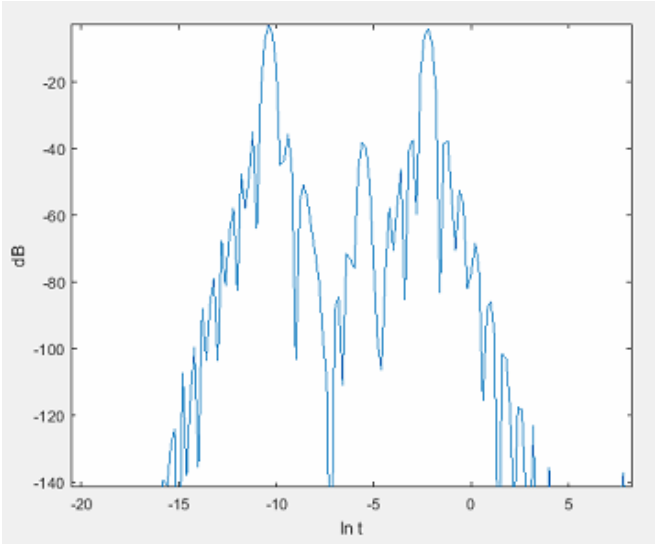

Fig. 11: Addition of a constant making the peaks to stand out from the noise

VII. Conclusion

Through smart interpolation and careful x-axis range selection, we have demonstrated that the method of [2] can straightforwardly produce better approximations of time constant values without the need of windowing, and can handle non-equispaced data. A limitation of this technique is its ability to discriminate delta functions and we quantify this limit. It is also noted that this technique requires a carefully-chosen noise reduction parameter to deal with noisy data.

Acknowledgment

The authors would like to thank Dr Marcus Wilson for helpful discussions.

References

[1] D. G. Gardner, J.C. Gardner and W.W. Meinke, "Method for the Analysis of Multicomponent Exponential Decay Curves", *THE JOURNAL OF CHEMICAL PHYSICS*, Vol. 31, No. 4 , 1959, pp. 978-986.

[2] D. N. Swingler, "A Differential Technique for the Fourier Transform Processing of Multicomponent Exponential Functions", *IEEE Transactions on Biomedical Engineering*, vol. BME-24(4), 1977, pp408–410.

[3] Abdussamad U. Jibia, and Momoh-Jimoh E. Salami, "Analysis of transient multiexponential signals using exponential compensation deconvolution", *Measurement*, vol. 45, 2012, pp. 19-29.

[4] Abdussamad U. Jibia, Momoh-Jimoh E. Salami, Othman O. Khalifa, and A.M. Aibinu, "Analysis of transient multiexponential signals using cepstral deconvolution", *Applied and Computational Harmonic Analysis*, vol. 29, 2010, pp. 88-96.

[5] Abdussamad U. Jibia, and Momoh-Jimoh E. Salami, "Parameter Estimation of Transient Mltiexponential Signals Using SVD-ARMA and Multiparameter Deconvolution Techniques", *International Journal of Computer Theory and Engineering*, vol 4, no. 5, 2012, pp. 751-757.

[6] J. Scott and A. Parker, "Modern Guide to Spectral Analysis with SPICE", *IEEE Circuits and Devices Magazine*, vol. 11, no. 5, pp.10–16, September 1995.

3.2 Evidence suggesting that NiMH cells are fractional in nature

This manuscript presents convincing empirical evidence suggesting that RC-type Thevenin models are inappropriate for modelling NiMH cells. When batteries, such as nickel-metal hydrides are subjected to a step change in current, the terminal voltage displays a slow transient recovery tail. Both first-order and second-order RC models claims to model this behaviour with some degree of success. Application of the proposed Swingler's algorithm from the previous paper to the measured set of data shows that there is no evidence of any distinct exponential components in the measured recovery tail. Absence of any peaks on a Swingler-style analysis hinted that the transient recovery curve can only be approximated with an infinite number of RC networks which is representative of a constant-phase element (CPE). This finding was further explored by measuring the complex impedance of the NiMH cell at frequencies as low as 10 μHz. It is seen that the cell resembles a pure resistor at higher frequencies but depicts the behaviour of a CPE at lower frequencies. This suggested that it may be possible to model a rechargeable battery with a single resistor and a CPE.

Fractional Behaviour of Rechargeable Batteries

Rahat Hasan
School of Science and Engineering
University of Waikato
New Zealand

Jonathan Scott
School of Science and Engineering
University of Waikato
New Zealand

***Abstract*—For decades authors have preferred to model batteries with either Thevenin-style models using RLC, or Randles-style by adding a Warburg element. These are claimed to model accurately. We present convincing empirical evidence suggesting that a fractional-derivative (constant-phase element) model is required. Our data shows that existing state-of-the-art models may be overly complicated, requiring numerical rather than physical considerations to find parameters.**

I. Introduction

When subjected to a step change in current, batteries exhibit a step change in output voltage owing to their internal resistance. Following the step voltage change there additionally follows a gradual decay curve. This is usually attributed to chemical diffusion processes within the cell. Similarly, when the load current returns to zero, the terminal voltage does not immediately return to the steady-state, open-circuit voltage of the cell, but again exhibits a slow recovery.

Figure 1 shows such a recovery curve measured on a 900mAh nickel-metal hydride (NiMH) battery. The battery was cycled carefully to start in the 50-70 percent state of charge (SoC) range. The battery was connected to an E5270B and a constant current of 90mA was drawn for a period of 1 minute. This represents a discharge of only one-sixth of 1 percent of Q, the total capacity of the battery, drawn at the so-called 10C rate. In other words, only a small amount of the battery's capacity was drawn, and at a very modest rate. In spite of this, a significant change in terminal voltage is observed. As steady-state, open-circuit voltage is the most reliable indicator of a cell's state of charge, considerable effort has been put into understanding and modelling this recovery phenomenon.

The authors of [1], [2], [3], [4] modelled this characteristic using RC networks. These works were inspired by Randles original 1947 model [5], but disregard the fractional nature at which his work hints. Figure 2 shows a typical 2^{nd} order RC model where U_{OC} and U_t represent the open circuit and the terminal voltage respectively, and of course R_o represents the Ohmic series resistance. It is claimed that the first RC network of R_c and C_c represents the effects due to mass transport and the second RC network of R_d and C_d represents the double layer effect, after [5]. In the next section we will demonstrate that this entire class of model is inappropriate.

II. Application of Modified Swingler Method

In [6] Swingler proposed a modification of Gardener's method for resolving summed exponential functions. He

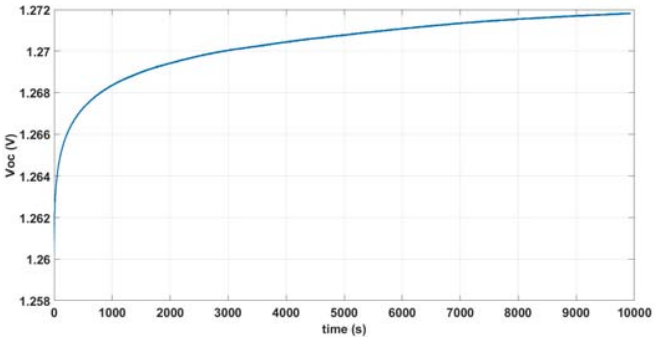

Fig. 1. The recovery curve of a 900mAh NiMH battery immediately after being subjected to a load of 90mA for 60 seconds beginning at a little over 50% SoC.

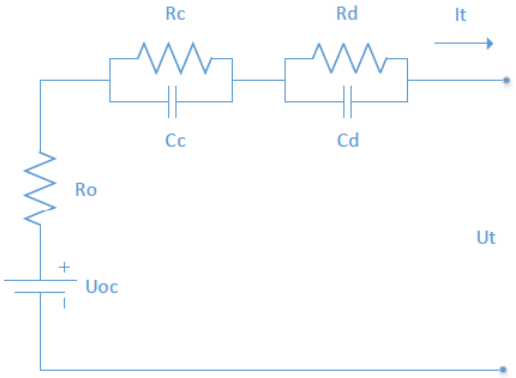

Fig. 2. A typical second-order RC battery equivalent-circuit model, reproduced from [3].

observed that a function $f(x)$ made up by summing a number of exponential decay terms could be processed to yield a series of delta functions whose amplitudes and delays betrayed the amplitudes and decay time constants of the constituent exponential functions. The execution of Swingler's process proved to be less simple than promised, but a modified algorithm was put forward in [7] that gives good results. This technique can be applied to the recovery part of a battery voltage waveform, and ought to identify the multiplicity of reactive elements required in a battery equivalent-circuit model, as each will give rise to a single decay time constant. We applied this algorithm to the recovery

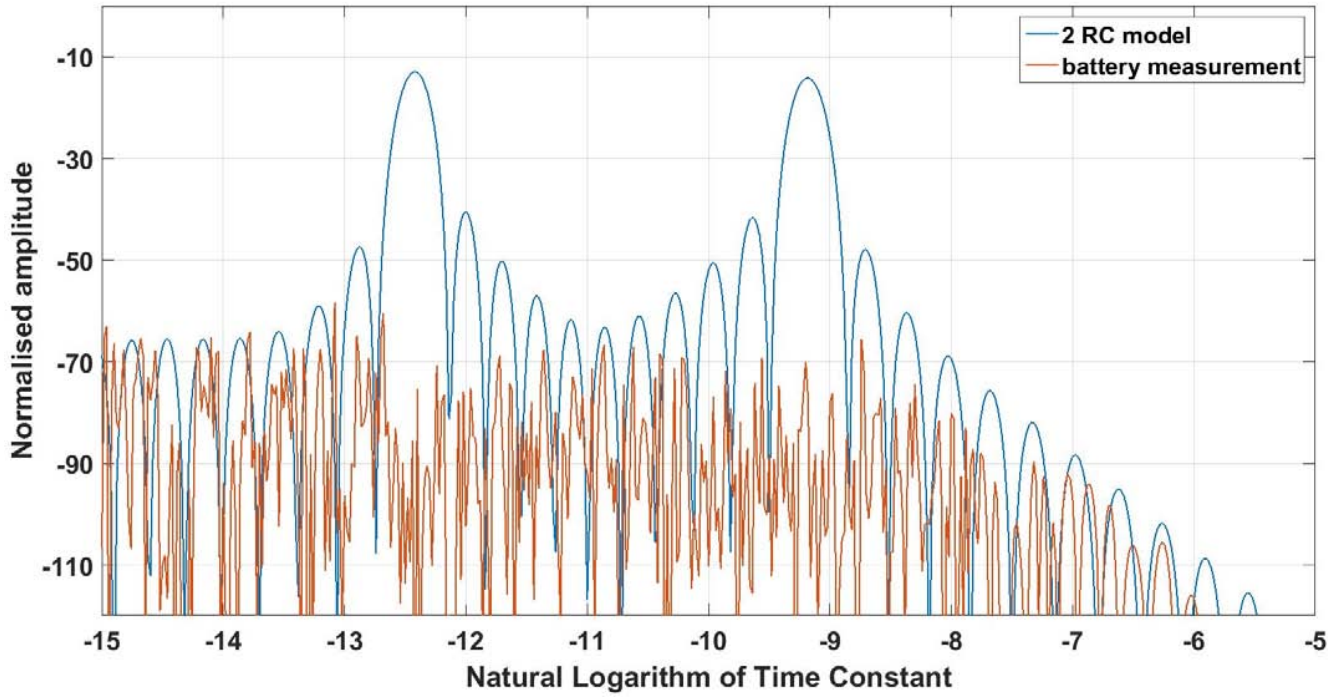

Fig. 3. Output of exponential-function analysis applied to the recovery curve of figure 1 and to a battery recovery curve generated using a two-RC battery model for comparison.

curve shown in figure 1. The result is shown in figure 3. The most important observation is that there is no evidence of any small number of exponential functions. Output of a two-RC model was analysed for comparison, and clearly shows 2 peaks 50dB above the noise floor. This observation suggests that RC models are not appropriate. A Constant-Phase Element (CPE) has a time-domain function that can only be approximated with an infinite series of exponentials, and is not expected to show any peaks on a Swingler-style analysis.

III. Fractional-Order Models

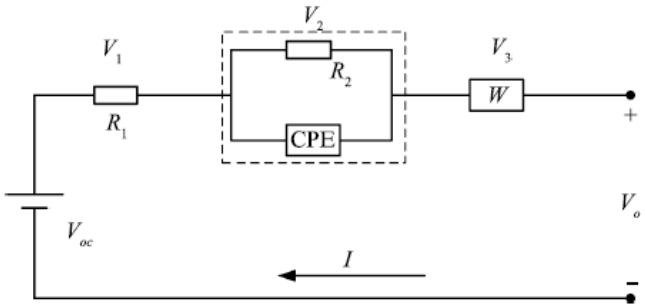

Fig. 4. Fractional equivalent circuit model reproduced from [12].

The idea of modelling batteries with fractional system was first introduced by the authors of [8] in 2006. The authors

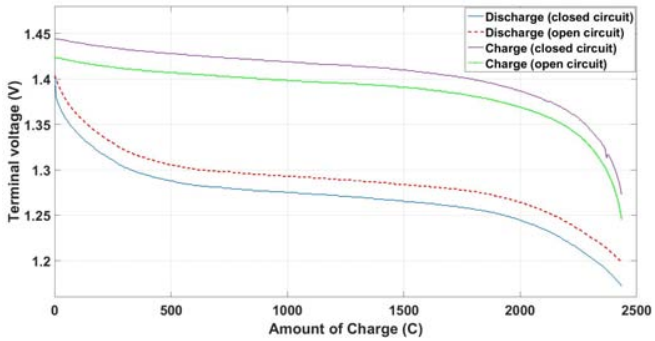

Fig. 5. Cycle test of 900mAh NiMH battery

claimed to be able to estimate the state of charge of lead-acid batteries within 5% error using a mathematical model based on limited frequency band of 2mHz-200Hz. One of the main drawbacks of this model is that it does not have any physical justification or any compact equivalent circuit. It is purely mathematical model with no clear electronic equivalent. A similar mathematical model involving complex algorithm was later proposed in [9] in 2010. This algorithm is specific to the cranking capability of a lead-acid battery. The best that can be said about this work is that it tends to confirm that batteries are fractional in their nature.

Other authors employed Randles battery model with varying degrees of success [10], [11]. In both papers, the authors measured impedance of a lead-acid battery over a certain

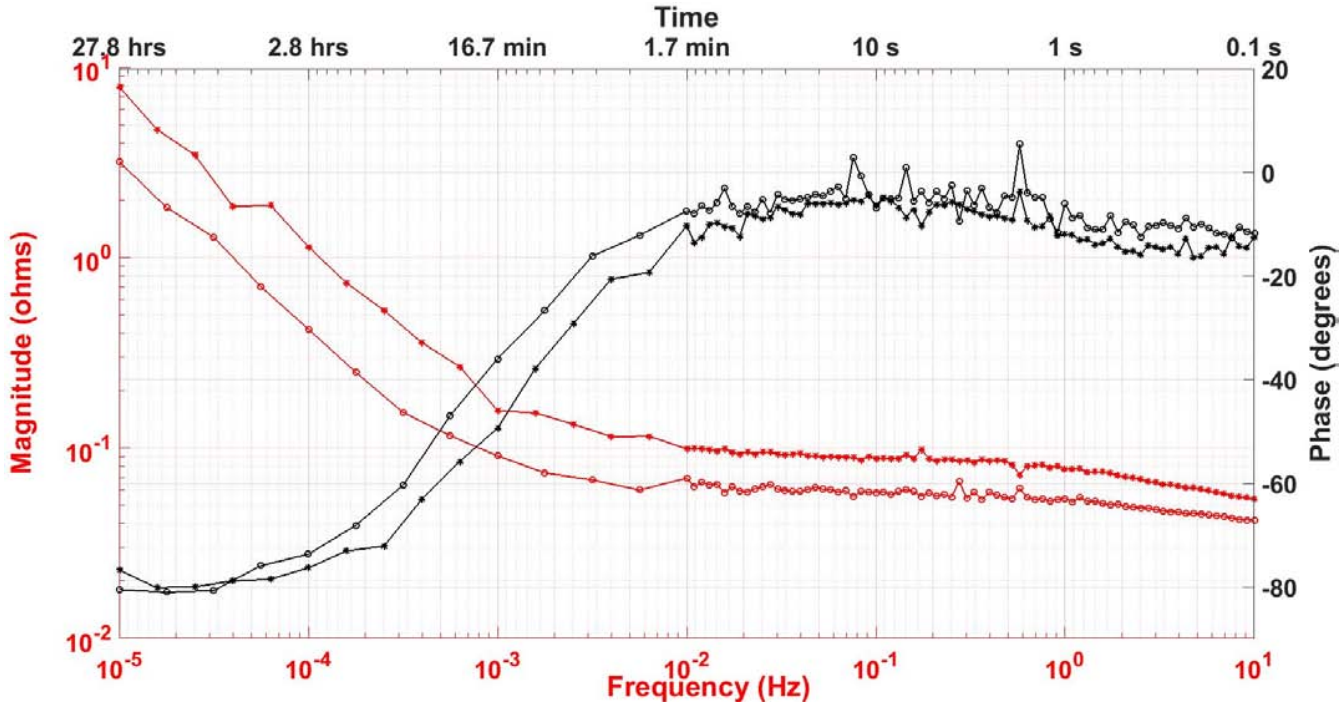

Fig. 6. The bode plot of the magnitude and phase of impedance of two NiMH batteries of 900mAh and 2400mAh capacity.

band of frequencies and used the frequency response to fit the parameters of a first-order Randles model.

As this manuscript was being prepared, Yan Ma et alia in [12] proposed a fractional battery model with a constant phase element (CPE) and a Warburg element as shown in figure 4. V_{oc} represents the open circuit voltage, V_o is the battery terminal voltage, R_1 represents the ohmic series resistance and W denotes the Warburg element. At first this work seems very powerful. In figures 1 and 5 of [12], the authors plot EIS data measured on a 26650 Lithium-ion battery on real/imaginary axes, but nowhere do they state the range of frequencies used in the measurement, nor do the plots show data points or variations with noise. In extracting their model parameters they eventually resort to a numerical fitting process. The model is then tested by having it predict very similar time-voltage data as that to which it was fitted. Finally, they note that the model predicts with "most errors below 20mV" which is claimed to represent only about 1% error in SoC, yet publically-available plots show in the linear region that Li-ion batteries have more like 3mV per percent of SoC.

We contend that any model of the complexity proposed in [12] can be fitted to a set of data and subsequently used to predict similar data. This does *not* suffice to verify the appropriateness of the model, especially if that model is overly complex, perhaps with too many degrees of freedom. We will now show measurement that suggest a simpler fractional-order model is appropriate.

IV. Cycle test

A 900mAh NiMH battery was cycled in order to determine the full capacity of the battery. This is important as we want to be certain that the range of the SoC stays within 50% during impedance measurement. The steps followed to obtain figure 5 are listed below:

- A current pulse of 0.18A (0.2 C) was generated to charge or discharge the battery for a period of 1 minute using Agilent E5270. Agilent E5270B Precision IV Analyzer contains SMUs (Source/Monitor Units) for voltage/current sourcing and voltage/current measurement as low as 0.1 fA.
- The battery was then allowed to rest for 2 minutes for the recovery voltage to settle down after every 0.3% SOC charging and discharging.
- The battery was idled for 12 hours in between charge and discharge.
- Open circuit and under-load terminal voltages of the battery were measured..

V. Impedance measurement

We measured the impedance of two NiMH batteries against frequency from 10μHz to 10Hz using a Solartron 1260A analyser with a fixed dc offset corresponding to 50% SoC. The batteries were rated at 900mAh and 2400mAh. Stimulus levels were chosen to ensure that cells did not deviate more than 10% from 50% SoC for even the lowest stimulus frequencies, where current flowed in one direction for periods approaching 14 hours. Figure 6 depicts the results.

For both cells, the magnitude of impedance is relatively flat at higher frequency, but increases below 10mHz, while phase shifts from about 0 degrees to settle at about -80 degrees. Such a Bode plot is characteristic of a single CPE corresponding to a derivative of order 0.89.

The phase traces in figure 6 show a deviation of 10–15 degrees as frequency increases above 1Hz. We have not conducted any analysis as to what might cause this so far, chiefly as we are interested in modelling SoC, and the response in this frequency range is not really of interest.

The frequency responses of NiMH obtained at higher frequencies are noisy. In order to confirm that the noise were not generated from the measurement system, a resistor of value comparable to the magnitude of battery impedance was measured using Solartron 1260. The results reproduced shown in figure 7 concludes that the noise in the impedance measurement data for batteries were not generated from Solartron 1260.

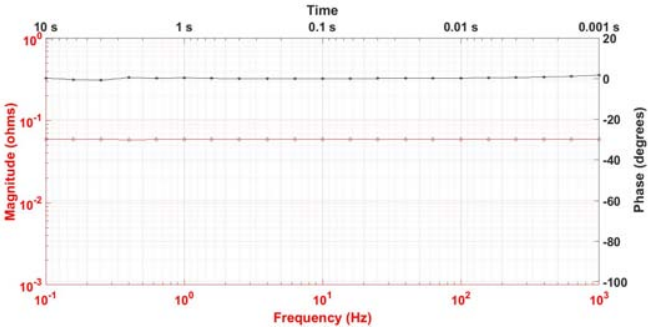

Fig. 7. The bode plot of the magnitude and phase of impedance of a pure resistor in the Solarton measurement setup.

VI. Discussion and Conclusion

We have shown that the impedance characteristic of NiMH batteries corresponds to that of a single CPE in series with a fixed resistor. The authors of [13] and [14] have adopted a similar approach to model the impedance characteristics of electrode-electrolyte interface and implantable electrode respectively with CPE. Since a CPE is defined by two parameters, its magnitude and the order of the derivative function relating current and voltage, this should lead to a battery model with greatly reduced parameter set.

References

[1] J. Chiasson and B. Vairamohan, “Estimating the state of charge of a battery”, *IEEE Transactions on Control Systems Technology*, volume 13, Issue 3, May 2005, pp465–470.

[2] Tiezhou Wu, Lunan Liu, Qing Xiao, Quan Cao, and Xieyang Wang, “Research on SoC Estimation Based on Second-order RC Model”, *Telkomnika*, vol. 10, no. 7, Nov 2012, pp. 1667–1672.

[3] ZeCheng, JikaoLv, YanliLiu, and ZhihaoYan, “Estimation of State of Charge for Lithium-Ion Battery Based on Finite Difference Extended Kalman Filter, *Journal of Applied Mathematics*, 2014, Vol 2014, pp. 1–10.

[4] Wu Guoliang, Lu Rengui, Zhu Chunbo, and C.C.Chan, “State of Charge Estimation for NiMH Battery Based on Electromotive Force Method”, *IEEE Vehicle Power and Propulsion Conference (VPPC)*, September 3–5, 2008, Harbin, China.

[5] Randles, J. E. B., “Kinetics of rapid electrode reactions”, *Discussions of the Faraday Society*, 1:11, 1947. doi:10.1039/df9470100011

[6] D. N. Swingler, “A Differential Technique for the Fourier Transform Processing of Multicomponent Exponential Functions”, *IEEE Transactions on Biomedical Engineering*, vol. BME-24(4), 1977, pp408–410.

[7] Rahat Hasan and Jonathan Scott, ”Application of Swingler’s method for analysis of multicomponent exponentials with special attention to non-equispaced data”, *2016 IEEE 12th International Colloquium on Signal Processing & Its Applications (CSPA)*, 2016, pp. 12-15.

[8] Jocelyn Sabatier, Mohamed Aoun, Alain Oustaloup, Gilles Gregoire, Frank Ragot and Patrick Roy, “Fractional system identification for lead acid battery state of charge estimation”, *Signal Processing - Fractional calculus applications in signals and systems*, Volume 86 Issue 10, October 2006 , pp. 2645 - 2657.

[9] Mikal Cugnet, Jocelyn Sabatier, Stphane Laruelle, Sylvie Grugeon, Bernard Sahut, Alain Oustaloup, and Jean-Marie Tarascon, “On Lead-Acid-Battery Resistance and Cranking-Capability Estimation”, *IEEE TRANSACTIONS ON INDUSTRIAL ELECTRONICS*, VOL. 57, NO. 3, MARCH 2010, pp. 909-917.

[10] Luiz Carlos Stevanatto, Valner Joo Brusamarello, and Stanislav Tairov, “Parameter Identication and Analysis of Uncertainties in Measurements of LeadAcid Batteries”,*IEEE TRANSACTIONS ON INSTRUMENTATION AND MEASUREMENT*, VOL. 63, NO. 4, April 2014, pp. 761-768.

[11] Stanislav Tairov and Luiz Carlos Stevanatto, “Impedance Measurements for Battery State of Health Monitoring”, *2nd International Conference on Control, Instrumentation and Automation (ICCIA)*, 2011, pp. 79-83.

[12] Yan Ma, Xiuwen Zhou, and Hong Chen, “Fractional Modeling and SOC Estimation of Lithium-ion Battery”, *IEEE/CAA Journal of Automatica Sinica*, Vol 3, No. 3, July 2016, pp. 281-287.

[13] Mark H. Jones and Jonathan Scott, “Scaling of Electrode-Electrolyte Interface Model Parameters in Phosphate Buffered Saline”, *IEEE Transactions on Biomedical Circuits and Systems*, November 2013, pp. 1-8.

[14] J. Scott and P. Single, “Compact nonlinear model of an implantable electrode array for spinal cord stimulation (SCS)”, *IEEE Transactions on Biomedical Circuits and Systems*, vol. 8, no. 3, pp. 382-390, Jun 2014.

Chapter 4

Corrections of Existing Battery Models

4.1 Fractional circuit model proposed by Ma et al.

A thorough literature review revealed that there are hundreds of papers in the IEEE stable alone with the phase "battery model" in the title. This paper questions the model presented by Ma et al. The model in question contains a Warburg and a R-CPE network and claims to approximate the state of charge of a lithium-ion cell with a maximum of 0.5% error. A closer look at the model revealed that the impedance transfer function equation of the model is incorrect. Since the authors of the paper based all the approximation on this erroneous equation, it was assumed that all their claims were invalid. It was also noticed that the authors used too many degrees of freedom to obtain a good fit and made no mention of the sensitivity of the fit to individual parameters. Any model with an excessive number of parameters would fit almost any function with reasonable accuracy.

Letter to the Editor Re "Fractional Modeling and SOC Estimation of Lithium-ion Battery"

Rahat Hasan and Jonathan Scott, *Senior Member, IEEE*

A recent paper by Ma et al., claims to estimate the state of charge of Lithium-ion batteries with a fractional-order impedance model including a Warburg and a constant phase element (CPE) with a maximum error of 0.5% [1]. The proposed equivalent circuit model from [1] is reproduced in figure 1.

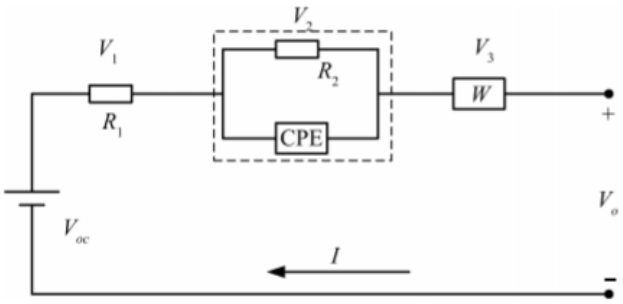

Fig. 1: Fractional equivalent circuit model.

The authors obtain the Laplace-domain impedance of the elements in their model and present this as their equation (12), reproduced here:

$$H(s) = \frac{V(s)}{I(s)} = \frac{1}{Ws^{\alpha}} \times R_1 \times \frac{R_2(\frac{1}{C_2 s^{\beta}})}{R_2 + (\frac{1}{C_2 s^{\beta}})} \qquad (1)$$

This equation is described as a "transfer function". This is confusing and can mislead readers because it is an impedance (one-port) rather than a transfer (two-port) function. The authors also use $V = V_o - V_{oc}$ instead of $V = V_{oc} - V_o$, meaning that their equation actually seeks the negative of the impedance, given the direction they have chosen for the conventional current $I(s)$.

More importantly, the equation is simply incorrect. The individual impedance elements are multiplied instead of being summed. The correct equation has addition rather than multiplication signs, so:

$$\frac{V(s)}{I(s)} = \frac{1}{Ws^{\alpha}} + R_1 + \frac{R_2(\frac{1}{C_2 s^{\beta}})}{R_2 + (\frac{1}{C_2 s^{\beta}})} \qquad (2)$$

In the paper this equation is then carried through to subsequent results. Since the remainder of the paper is based on the initial equation, we must assume that the conclusions are unfounded.

Nevertheless, quite reasonable agreement is obtained when the (erroneous) model is fitted to the data. This might be a result of some numerical co-incidence. Rather, we attribute this outcome to the model having too many degrees of freedom. Almost any reasonable model can be fitted to data within a range given that it has sufficient degrees of freedom. Readers of [1] will note that the model is required only to reproduce data of similar form to that to which the model was originally fitted.

We refer readers to [2] wherein it is shown that a simpler model, with fewer degrees of freedom by virtue of using a single CPE, appears capable of reproducing battery impedance characteristics.

The authors are with the School of Engineering, Faculty of Science and Engineering, University of Waikato, New Zealand

References

[1] Yan Ma, Xiuwen Zhou, Bingsi Li, and Hong Chen, "Fractional Modeling and SOC Estimation of Lithium-ion Battery", *IEEE/CAA JOURNAL OF AUTOMATICA SINICA*, Vol.3, No. 3, July 2016, pp. 281–287.

[2] Hasan, R., and Scott, J. B., "Fractional behaviour of rechargeable batteries", *Proceedings of the 2016 Electronics New Zealand Conference*, November 17–18, 2016, Wellington, New Zealand (pp. 111–114).

4.2 Fractional model proposed by Wang et al.

The following manuscript presents correction to the Wang et al paper which proposes a similar model to the Ma et al paper and predicts the state of charge of a lithium cell. The model contains a Warburg element, a CPE and an inductor. In total, there are 8 different parameters. It can be easily speculated that the authors of the paper in question were using unjustified degrees of freedom to get a better fit of their impedance spectra. For example, the authors varied the angle of their Warburg element between 0 and 1 until they achieved an average mean absolute percentage error of 1.04%. This is simply incorrect because by theory the angle of a Warburg element is fixed to 45 degrees. Any model can be fitted to data with reasonable accuracy given sufficient degrees of freedom.

Comments on "State of Charge-Dependent Polynomial Equivalent Circuit Modeling for Electrochemical Impedance Spectroscopy of Lithium-Ion Batteries"

Rahat Hasan and Jonathan Scott, *Senior Member, IEEE*

A recent paper by Wang et al proposes a state of charge-dependent polynomial equivalent circuit model for lithium batteries. The model consists of an inductor, a Warburg element, a constant phase element (CPE) and two resistors [1]. Figure 1 shows the equivalent circuit model reproduced from [1].

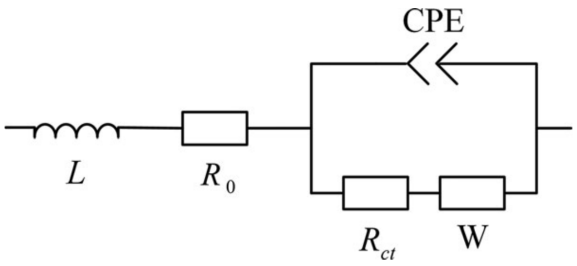

Fig. 1: Equivalent circuit model.

The authors described the complex impedance of a CPE as:

$$Z_{CPE} = \frac{1}{(j\omega)^n Q} \tag{1}$$

The term Q is referred to as a "time constant" by the authors. This can mislead readers. Q has units of F/$s^{1-\alpha}$ where F denotes Farad and s denotes second.

The authors then quote the impedance equation of a Warburg element as:

$$Z_W = R_W \frac{tanh(j\omega\tau)^\phi}{(j\omega\tau)^\phi} \tag{2}$$

where τ is the diffusion time constant, ϕ varies between 0 and 1, and R_W is the Warburg resistance. This equation is wrong; the angle in a Warburg element is fixed to 45 degrees, corresponding to $\phi = 0.5$. The authors cited [2] as a reference, but this paper contains no such equation. The correct equation is of the form [3]:

$$Z_W = R_W \frac{tanh\sqrt{(j\omega\tau)}}{\sqrt{(j\omega\tau)}} \tag{3}$$

In [1] the authors included both CPE and Warburg equations. The angle of the Warburg element, ϕ, was used as an independent variable to fit the measured data. Thus an extra, unjustified degree of freedom has been created. The authors managed to fit the model to their impedance spectra with an average mean absolute percentage error of 1.04%. We attribute the fitting success of the model to its having a total of 8 different parameters. Almost any model can be fitted to data with reasonable accuracy given sufficient degrees of freedom. Other researchers have obtained apparently 'good fit' with quite different models, with a similar, excessive, number of parameters [4]. We refer readers to [5] where it is shown that a single CPE and resistor model is capable of reproducing the impedance characteristics of a lithium battery.

The authors are with the School of Engineering, Faculty of Science and Engineering, University of Waikato, New Zealand

REFERENCES

[1] Qian-Kun Wang, Yi-Jun He, Jia-Ni Shen, Xiao-Song Hu, Zi-Feng Ma, "State of Charge-Dependent Polynomial Equivalent Circuit Modeling for Electrochemical Impedance Spectroscopy of Lithium-Ion Batteries", *IEEE Transactions on Power Electronics*, Volume: 33 , Issue: 10, 2018, pp. 8449 - 8460.

[2] M. Doyle, J. P. Meyers, and J. Newman, "Computer simulations of the impedance response of lithium rechargeable batteries, *J. Electrochem. Soc.*, vol. 147, no. 1, pp. 99110, 2000.

[3] Subrata Sarker, A. J. Saleh Ahammad, Hyun Woo Seo, and Dong Min Kim, "Electrochemical Impedance Spectra of Dye-Sensitized Solar Cells: Fundamentals and Spreadsheet Calculation", *International Journal of Photoenergy*, Volume 2014, Article ID 851705, pages 17.

[4] Yan Ma, Xiuwen Zhou, Bingsi Li, and Hong Chen, "Fractional Modeling and SOC Estimation of Lithium-ion Battery", *IEEE/CAA JOURNAL OF AUTOMATICA SINICA*, Vol.3, No. 3, July 2016, pp. 281–287.

[5] Hasan, R., and Scott, J. B., "Fractional behaviour of rechargeable batteries", *Proceedings of the 2016 Electronics New Zealand Conference*, November 17–18, 2016, Wellington, New Zealand (pp. 111–114).

Chapter 5

Improving On-Load and Off-Load Impedance Measurement of Batteries

5.1 Off-Load Impedance Measurement of Batteries

It is important to measure the impedance of a cell as accurately as possible because the impedance data gives insight to the internal state of a cell such as chemical properties and mechanical design. From the impedance data, one can then approximate the transient runtime and charge-voltage characteristics of a rechargeable battery. This manuscript explores current instruments used for off-load battery impedance measurement and provides an improvement on the impedance measurement technique.

From previous experience, it was known to us that rechargeable cells depict important characteristics at extremely low frequencies, around 10 μHz since in most applications, batteries are cycled once a day or even longer. There exists only a handful of instruments which can conduct such measurements. Several impedance analysers measure impedance to 1 mHz or less, at least one reaches 10 μHz, Solartron 1260A impedance analyser. This manuscript gives empirical evidence that this instrument is prone to unreliable measurements at low frequencies, especially for wet chemistries. The accuracy of this instrument was tested by first comparing the impedance data obtained from Solartron 1260A of a single NiMH cell and its back-back pair. A back-back pair is simply two cells connected in anti-parallel combination so as to cancel out their dc voltage offset. The results obtained were unsatisfactory.

Confused by the lack of agreement, a single NiMH cell was repeatedly measured with two different hardware setup: a Keysight 33220A Function/Arbitrary Waveform Generator and two 34401A DMMs, Agilent E5270A Precision IV Analyzer with E5281A source/monitor units (SMUs). Refer to appendix B for details of the equipments. The method used to obtain the impedance data from the SMUs is superior because it can produce a signal with arbitrarily low frequency and the post-processing of the data is immune to offset drifts, imperfect waveshape, and distortions by virtue of the windowing and

filtering. Agreement between the two measurements were excellent and were very different from the data previously obtained from Solartron 1260A. It was speculated that there are two possible reasons for this low performance on Solartron's behalf: drift in voltage waveform and signal distortion.

Later, the impedance of a lithium-ion cell was measured with confidence using the Agilent E5270A Precision IV Analyzer. The measured data was first fitted to a mathematical model produced in Matlab and then to a 10-way split R-CPE model simulated in Spice. Although the mathematical model and the measured data exhibited a good fit, the split model fitted the region of the corner frequency better. This showed any rechargeable cell can be easily modelled with only four parameters.

IEEE Access
Multidisciplinary ⋮ Rapid Review ⋮ Open Access Journal

Received July 14, 2019, accepted July 28, 2019, date of publication July 30, 2019, date of current version August 16, 2019.

Digital Object Identifier 10.1109/ACCESS.2019.2932094

New Results for Battery Impedance at Very Low Frequencies

JONATHAN SCOTT, (Senior Member, IEEE), AND RAHAT HASAN, (Student Member, IEEE)
School of Engineering, The University of Waikato, Hamilton, New Zealand

Corresponding author: Rahat Hasan (rh163@students.waikato.ac.nz)

This work was supported in part by the Intelligent Tek Limited, and in part by the WaikatoLink Limited.

ABSTRACT In search of an equivalent circuit model for rechargeable batteries, many authors start with a measurement of battery impedance, spanning what is presumed to be the frequency range of interest. Various networks have been suggested in the literature to account for the measured impedance characteristic. Most incorporate two or more resistors, at least one capacitor, some include at least one Warburg element, and more recently ''constant phase elements'' (CPE), otherwise identified as fractional-derivative capacitors. Networks that are more successful at reproducing the measured impedance have from five up to tens of degrees of freedom. The frequency range upon which most models are based extends only to 1mHz. This is surprising since many batteries see a daily or longer usage cycle, corresponding to a frequency of $\approx 11.6\ \mu$Hz or lower. We show in this manuscript that the most-cited impedance measurement instrument, and one of the few that can operate below 1mHz, can be unreliable at and below this boundary. We present a novel impedance measurement algorithm robust against the issues present while measuring the impedance of electrochemical systems to as low as 1 μHz. Next, we present reliable impedance data extending to a lower frequency limit of 10 μHz. A remarkable characteristic appears at the lower frequencies, suggesting a surprisingly simple and elegant equivalent circuit consisting of a single fractional capacitor. A new model is proposed, which requires only four parameters to predict the measured impedance as a function of frequency.

INDEX TERMS Equivalent circuit model, frequency domain analysis, impedance measurement, rechargeable batteries.

I. INTRODUCTION

A great many manuscripts appear in the literature describing rechargeable battery equivalent-circuit models of widely-varying complexity. Some 100 papers have been published in IEEE journals in the last 6 years alone with the words ''battery model'' and ''equivalent circuit'' in the title, with a commensurately larger number of conference manuscripts appearing. Researchers sometimes use time-domain I/V data to which to fit their model, but most carry out an Electro-Impedance Spectroscopy (EIS) measurement, yielding the complex impedance as a function of frequency. The challenge is then to select a circuit topology that is as simple as possible, yet fits the impedance data reasonably well.

A circuit battery model is considered key to prediction of behaviour, including state-of-charge (SoC) and state-of-health (SoH). [1], [2] Most commonly-appearing models are Thévenin-like RC models based around a voltage source [1], [3]–[6] In particular [6] sets the scene well and provides a very comprehensive equivalent circuit, but one requiring a lot of parameters. In [7] an arbitrary number of RC networks are considered, while [8] provides tables of sensitivities of model performance to various parameters, exemplifying the tendency towards ever-increasing complexity. In contrast, [9] trades complexity for speed, potentially using only 3 resistors and 2 capacitors in the model of series impedance.

More recently, researchers have returned to the idea that batteries have fractional characteristics, first noted by Randles in 1947 [10]. The authors have adapted Swingler's method as described in [11] to confirm that rechargeable batteries are fractional in nature and thus not readily accounted for by any finite, compact, equivalent-circuit model [12]. Various manuscripts present models that include fractional characteristics. For example, [13] and [14] approach the problem mathematically rather than through an equivalent circuit, while [15] presents an equivalent-circuit model incorporating both a fractional capacitor, and a Warburg element

The associate editor coordinating the review of this manuscript and approving it for publication was Xiaosong Hu.

(a fractional capacitor of fixed order equal to 0.5, as employed by Randles).

References [13], [14], [16]–[21] all discuss fitting models to batteries using impedance data starting at frequencies of 1mHz, 2mHz, and higher. Many references are not specific about their frequency range, and present only Nyquist, not Bode plots. This is surprising, since many batteries are in appliances charged daily, corresponding to a frequency of $\approx$11.6μHz. Reference [22], now over 20 years old, appears to be alone in arguing that data down to 1μHz may be useful, but even this manuscript presents data down to only 6.8μHz, and there is no discussion of how this data was obtained. In many manuscripts the instrument used to obtain impedance measurement is not stated. We are left to speculate about the reasons for this choice of frequencies.

It may be as simple a reason as convenience. Various manufacturers make instruments that can measure complex impedance to low frequencies, such as the Solartron 1260A Impedance/Gain-Phase Analyzer [23], Chemical Impedance Analyzer IM3590 [24] and MFIA 500 kHz Impedance Analyzer [25]. Most of the available instruments do not go below 1mHz. The instrument in [23], Solartron 1260A, boasts the lowest available frequency of operation of any commercial instrument we could find, 10μHz. This instrument is specifically mentioned in several manuscripts, e.g. [21], [26], [27], and appears to be a popular choice for battery measurements, at which it is specifically targeted by its makers.

II. BATTERY IMPEDANCE MEASUREMENT

Using Solartron 1260A we measured first a single 55123 1850mAh NiMH battery. The cell was set to about 60% state-of-charge (SoC) and allowed to stabilise. The cell was maintained at an ambient temperature of 25 Celcius using a Contherm Polar 1000. We then measured a back-to-back pair, connected in anti-parallel so as to cancel out their dc voltages. The results appear in figure 1.

Confused by the lack of agreement between the two traces, we repeated a measurement of the impedance of the single original cell at 1mHz a number of times using Solartron 1260A. In eight sequential measurements we obtained values varying randomly between 0.59Ω and 0.72Ω. It is obvious that factors beyond the user's control affect the measured impedance. We then measured a 100μF capacitor from 1Hz to 10μHz and obtained the correct result with the stated accuracy for the machine. In other words, a standard electronic component would be measured correctly, but a battery gave results that were not repeatable. Attempts to measure the impedance of human-implantable electrodes using the same instrument, a case where the correct answer is known [28], [29], were similarly unsuccessful [30].

In order to discover whether it was the "wet" device, our use of the instrument, or a shortcoming of the instrument itself, we devise a more rigorous measurement method. The intention is to measure impedance using a programmable current source that is reprogrammed moment by moment to produce a sine-varying current, and frequency by frequency

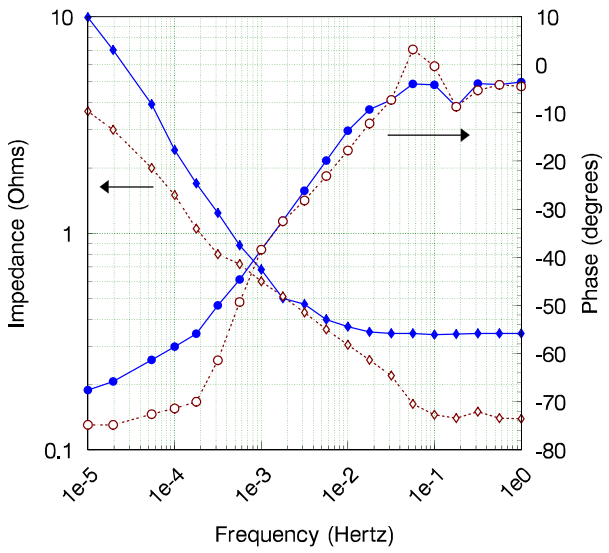

FIGURE 1. Impedance magnitude (diamonds) and phase (dots) of a single 55123 NiMH battery (solid lines) and half the impedance of a back-to-back pair (dashed lines) measured using the impedance analyser of [23].

to adjust the stimulus level. This will ensure that zero net charge is transferred in each cycle of the stimulus. The stimulus level needs to be adjusted, since "small signal" in the case of a battery is the size of the charge inserted in positive half cycles of the stimulus and removed in the negative half cycles. Assume the signal has an amplitude of I_0 and frequency f. The time domain equation of the signal is

$$I = I_0 sin(2\pi ft) \tag{1}$$

The integral of current will yield the amount of charge transferred to and from the cell. The area under the positive half cycle is the amount of charge moved into the cell, Q_{in} and the negative half of the cycle represents the amount of charge moved out of the cell, Q_{out}:

$$Q_{in} = \int_0^{T/2} Idt = \int_0^{T/2} I_0 sin(2\pi ft)dt \tag{2}$$

and

$$Q_{out} = \int_{T/2}^{T} Idt = \int_{T/2}^{T} I_0 sin(2\pi ft)dt \tag{3}$$

Integration of (2) and (3) produces

$$Q_{in} = -\frac{I_0}{2\pi f}[cos(2\pi ft)]_0^{T/2} = -\frac{I_0}{2\pi f}[cos(\pi fT) - 1] \tag{4}$$

and similarly

$$Q_{out} = -\frac{I_0}{2\pi f}[cos(2\pi fT) - cos(\pi fT)] \tag{5}$$

but $fT = 1$ leading to the simple results

$$Q_{in} = \frac{I_0}{\pi f} \tag{6}$$

and

$$Q_{out} = -\frac{I_0}{\pi f} \tag{7}$$

The negative sign denotes the direction of the charge flow with respect to the source. Of course the charge flow over one complete cycle, $\Delta Q = 0$. In situations where ΔQ does not equal zero, there may be unexpected waveform distortion. Observe that the peak amplitude of the charge delivered is dependent on the frequency of the signal. As the frequency of the signal gets smaller and smaller, the current stimulus must be dropped dramatically to prevent the charge excursion flattening or overcharging the DUT (Device Under Test). In our experience, it is prudent to limit charge flow at ± 10 % of the available charge or less in order to stay away from the sharp non-linearities that arise at either end of the charge/discharge characteristic. Much less is better. For low frequencies, low current stimuli must be used, often so low that noise is a major consideration in the measurement. It is worth noting that no instrument we have investigated permits alteration of the stimulus level during an automated sweep. Furthermore, no authors citing measurements discuss the frequency-dependence of what constitutes a ''small-signal'' measurement.

A range of instruments are able to achieve such a measurement, for example Hameg HM8143 two-quadrant power supplies, Tektronix (Keithley) 2400-series Source-Measurement Units (SMUs), Keysight Precision I/V Analyzers, and Chroma 17000-series Programmable Battery Charge/Discharge Test Systems. The procedure is as follows.

1) Use current drive for the test stimulus signal if possible. This makes it easy to ensure that equal charge is delivered in the positive and negative half sine waves.
2) Before each test frequency, the SoC of the DUT is preset, and the cell rested by fixing the drive voltage corresponding to the required SoC and allowing the cell current to fall to a low value.
3) Fix the amplitude of the stimulus at each new frequency in accordance with equations (6) and (7) and below the maximum safe current level of the DUT.
4) Generate the sinusoidal current waveform at each required frequency.
5) Carry out the measurement over several cycles. Multiple cycles makes Fourier post-processing easier, and can reveal inconsistencies in the time-domain data as the measurement progresses.
6) Store the current and voltage values in a data file for possible diagnostic analysis, as suggested in the last point.
7) Apply a suitable window to the data to account for any signal drift, and extract the magnitude and phase of current and voltage using a Discrete Fourier Transform (DFT) calculated at the stimulus frequency. A suitable DFT algorithm [31] can be computed progressively, and can simultaneously allow for irregular spacing in time of the samples. We use a Hann window.

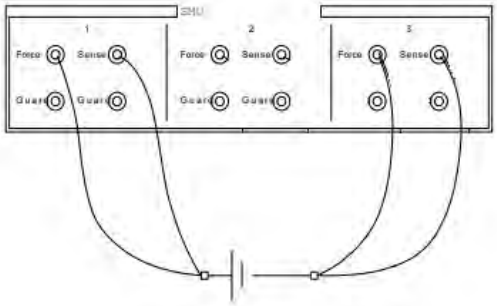

FIGURE 2. Connection to E5270 instrument to measure impedance.

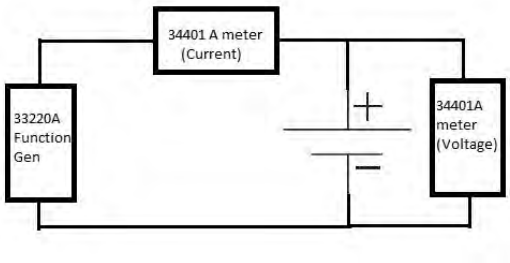

FIGURE 3. The set-up used to measure impedance of NiMH cell using Keysight 33220A Function / Arbitrary Waveform Generator and two 34401A digital multimeters.

8) Calculate the complex impedance by taking the quotient of the voltage and current at the stimulus frequency.

This method is superior because it can produce a signal with arbitrarily low frequency and the post-processing of the IV data is immune to offset drifts, imperfect waveshape, and distortions by virtue of the windowing and filtering.

We repeated the impedance measurement of the same single NiMH cell with our proposed method. Initially, one of us (Hasan) used an Agilent E5270A Precision IV Analyzer with E5281A source/monitor units (SMUs) to achieve this. The connection is shown in Figure 2. The SMU was programmed with a python script. The software communicates with the instrument using the SCPI programming language. For valid comparison between methods, we used the same rested SoC level as before. Throughout the measurement, we kept the external temperature of the cell constant as before. At each frequency, we continued the signal for 6 cycles. All current and corresponding voltage points were saved. Since we had no theoretical expectation with which to compare this result, we decided to confirm it by implementing the same algorithm with code written by a different person (Scott) in a different language (C) on different hardware (Hameg 2-quadrant supply, Agilent DMM). The set-up is shown in Figure 3. The outcomes of these measurements are presented in Figure 4. Our two measurements agreed.

We next used our proposed method to measure the impedance of an 800mAh, 14500 lithium battery. We maintained the external temperature of the cell at 25 degrees Celsius. The measurements were done at 62%

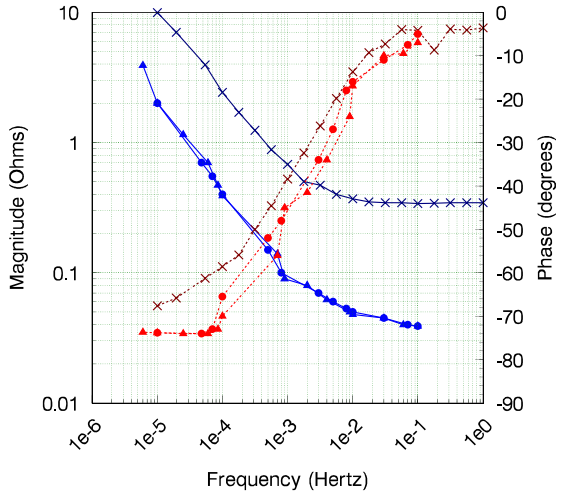

FIGURE 4. Magnitude (left vertical axis, blue traces) and phase (right axis) of the NiMH cell using an SMU (lines with triangle symbols) and a function generator and DMMs (lines with dots) compared with data measured using the commercial impedance analyser (lines with multiplication symbols).

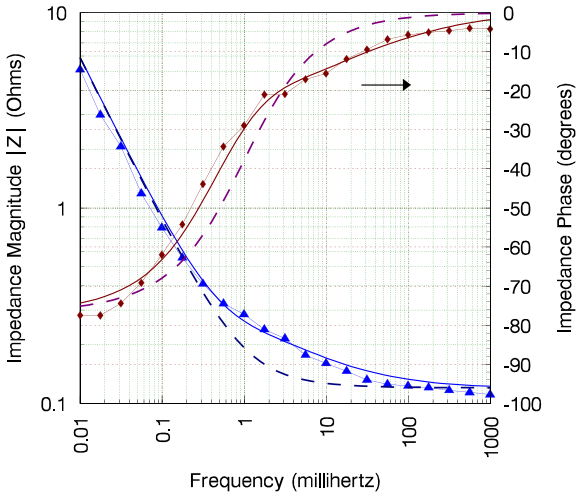

FIGURE 5. Impedance magnitude (left vertical axis, blue traces) and phase (right axis, grey traces) of a 14500 Lithium-ion battery for frequencies starting at 10μHz. Measured data (lines with symbols) compared with the simple R-CPE mathematical model of figure 9 (dashed lines) simulated in Matlab and the split-CPE model of figure 10 (solid lines) simulated in Spice.

State-of-Charge (SoC), although the results do not vary greatly with SoC in the near-linear, middle region. We chose the stimulus level so that the cell SoC does not fluctuate by more than 10% even at 10μHz, where the period of a sinewave is about 27 hours, somewhat more than 1 day, and the test signal can easily overcharge or discharge the battery if chosen too large. The measured values of the magnitude and phase of the impedance of this cell appear in figure 5 (lines with symbols).

III. POSSIBLE REASONS FOR LOW PERFORMANCE

In this section some circumstances that may disturb operation of the Solartron impedance analyser are identified.

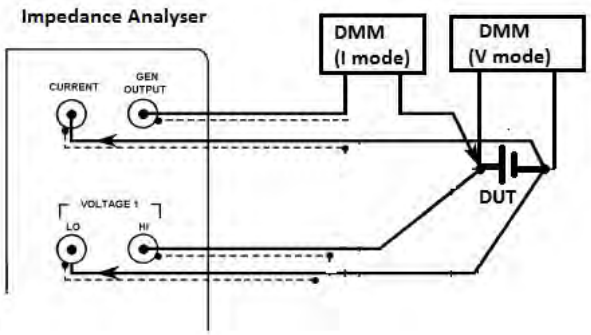

FIGURE 6. Connections to measure the current and voltage during measurement by the impedance analyser.

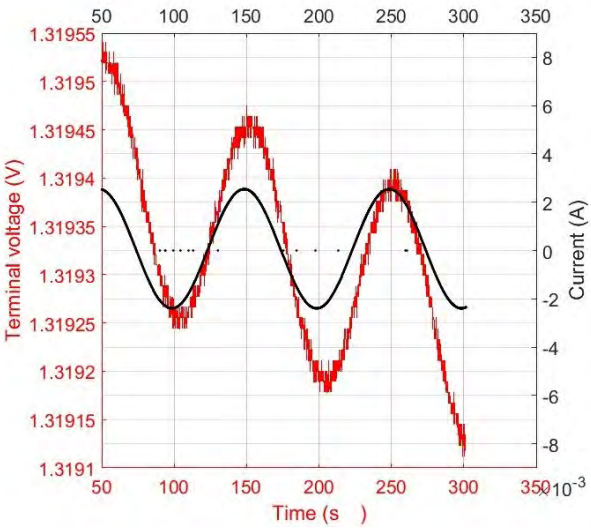

FIGURE 7. Current and voltage measured across the single NiMH cell at 10 mHz.

A. DRIFT IN VOLTAGE WAVEFORM

Curious to understand what causes the impedance analyser to produce erroneous impedance readings when measuring a single cell, we inspected the current and voltage waveforms sourced by the built-in generator. We achieved this by using two Agilent 34401A digital multimeters (DMMs). Figure 6 shows the set-up used to observe the current and voltage responses of the battery. We used identical stimulus level as before. Figure 7 portrays the captured current and voltage waveforms at 10 mHz. Note that the voltage signal is only a few hundred microvolts peak-to-peak, even at 10mHz.

It is clear that there is a downward drift in the voltage waveform measured across the cell, although the current waveform stays sinusoidal. The DC offset of the input signal and the terminal voltage of the battery apparently drifted apart, despite the control of cell temperature.

It may be that the impedance analyser calculates impedance via discrete Fourier Transform. The algorithm of a Fourier Transform assumes that the two endpoints of signals are continuous and there is no discontinuity. Where the endpoints of a signal do not meet, results may be corrupted. This might explain the inaccuracy in impedance measurement. It should also be noted that the analyser carries

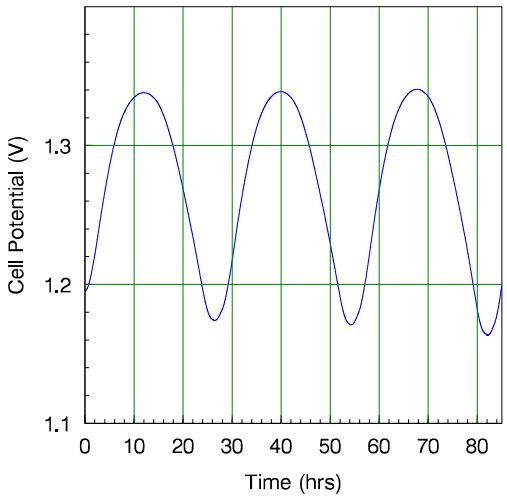

FIGURE 8. Distorted voltage signal observed across a single NiMH cell during measurement at 10 μHz.

out its measurement in one stimulus cycle. This is desirable because of the exceptionally long periods involved. Having only one stimulus cycle makes processes such as windowing data difficult.

B. SIGNAL DISTORTION

Batteries may be close to linear in the mid-range of state-of-charge, typically 40–80%, but are apt to be quite non-linear in the last few percent of their range at both the flat and fully-charged ends of the characteristic. In the case of the NiMH chemistry, trickle-charging is permitted, as there is a mechanism that safely dissipates excess charge delivered as the cell approaches full charge. This mechanism starts to kick in before the last few percent capacity is filled, especially at higher currents. This mechanism can cause the voltage waveform to lose its sinusoidal shape. Figure 8 shows an example voltage signal. This distortion seems to affect our impedance analysers. This reinforces the need to regulate the stimulus magnitude as outlined in section II, as well as to stay away from the ends of the charge curve.

IV. IMPLICATION OF THE IMPEDANCE DATA

A constant phase element/fractional capacitor is an element that obeys the characteristic equation

$$I = C_F \frac{d^\alpha V}{dt^\alpha} \tag{8}$$

which in the Laplace domain is represented by an impedance

$$Z_{C_F} = \frac{-J}{(\omega C_F)^\alpha} \tag{9}$$

giving a straight line on a Bode plot whose slope is not 1 but α, and whose phase is a constant value of $\theta = \pi/2\alpha$, hence the alternate name "constant phase element". In the data of figure 5 for example, at lower frequencies where the impedance of the CPE dominates the series pair, the phase settles to a value of $\approx$76 degrees, and the slope of the magnitude trace shows a straight line, but one with slope less than 20dB/decade. The suggested "R-CPE" equivalent circuit is

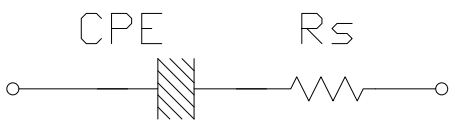

FIGURE 9. Circuit suggested by the asymptotes of the impedance plots.

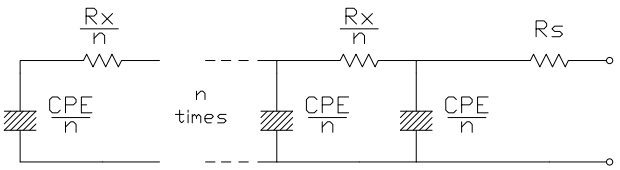

FIGURE 10. Equivalent circuit model with n-way split CPE and series resistance.

shown in figure 9. The pure, Ohmic, series resistance of the battery is $R_S = 0.12\Omega$.

This equivalent circuit was simulated in SPICE using the method outlined in [28] with corrections from [32]. The model parameters are $m = \pi/2\theta_{CPE} = 1.161$ and $Y_\theta = 0.842$ for $\omega_0 = 55.7 \times 10^{-6}$. An accuracy parameter of $k = 1.3$ is found to be more than adequate by trial and error. The simulated impedance from the circuit of figure 9 is shown plotted with the measured data as dashed lines in figure 5. Agreement is good except for the region of the corner frequency.

Recent work described in [33] has shown that allowing for the distributed nature of electrodes by splitting the CPE improves fit in transitional regions. This suggests the equivalent circuit of 10, adding one parameter, R_X. The CPE of the simple model is arbitrarily divided into n smaller CPEs, each of which has the same phase but n times lower an admittance, $Y_{\theta_{split}} = Y_\theta/n$. It remains to discover the value of the $n-1$ resistors R_X present in the split model. The value of R_X has been numerically optimized to obtain the best fit. In this case, we chose a value $R_X = 29\text{m}\Omega$. A 10-way split, that is $n = 10$, was chosen, again by trial and error observing that larger values conferred little advantage. Repeating the simulation of battery impedance with the split-CPE model shows that the new model is more appropriate in the frequency domain. The simulated impedance from the circuit of figure 10 is shown plotted with the measured data as the solid lines in figure 5. Now the fit is excellent.

V. CONCLUSION

We presented impedance measurements on two different batteries extending to very low frequencies. The measurement required the development of a novel algorithm to provide robust, repeatable data. This exposed an exciting characteristic, namely that the impedance data forms a straight line, characteristic of a fractional capacitor, at such very low frequencies. This characteristic has not been observed before.

Based on this impedance characteristic we suggest a new equivalent circuit consisting of a single fractional capacitor or CPE in series with a single resistor. This circuit reproduces the impedance, magnitude and phase, with reasonable

accuracy, using only three parameters. A split-CPE model can reproduce the impedance with greater accuracy. This increases the number of parameters to four.

REFERENCES

[1] G. Nobile, M. Cacciato, G. Scarcella, and G. Scelba, "Performance assessment of equivalent-circuit models for electrochemical energy storage systems," in *Proc. 43rd Annu. Conf. IEEE Ind. Electron. Soc. (IECON)*, Oct./Nov. 2017, pp. 2799–2806.
[2] C. Zhang, K. Li, S. Mcloone, and Z. Yang, "Battery modelling methods for electric vehicles—A review," in *Proc. Eur. Control Conf. (ECC)*, Strasbourg, France, Jun. 2014, pp. 2673–2678.
[3] J. Chiasson and B. Vairamohan, "Estimating the state of charge of a battery," *IEEE Trans. Control Syst. Technol.*, vol. 13, no. 3, pp. 465–470, May 2005.
[4] T. Wu, L. Liu, Q. Xiao, Q. Cao, and X. Wang, "Research on SoC estimation based on second-order RC model," *Telkomnika*, vol. 10, no. 7, pp. 1667–1672, Nov. 2012.
[5] Z. Cheng, J. Lv, Y. Liu, and Z. Yan, "Estimaon of state of charge for lithium-ion battery based on finite difference extended Kalman filter," *J. Appl. Math.*, vol. 2014, Mar. 2014, Art. no. 348537.
[6] M. Chen and G. A. Rincón-Mora, "Accurate electrical battery model capable of predicting runtime and I-V performance," *IEEE Trans. Energy Convers.*, vol. 21, no. 2, pp. 504–511, Jun. 2006.
[7] G. Liu, L. Lu, H. Fu, J. Hua, J. Li, M. Ouyang, Y. Wang, S. Xue, and P. Chen, "A comparative study of equivalent circuit models and enhanced equivalent circuit models of lithium-ion batteries with different model structures," in *Proc. IEEE Conf. Expo Transp. Electrific. Asia–Pacific (ITEC Asia–Pacific)*, Aug./Sep. 2014, pp. 1–6.
[8] A. Seaman, T.-S. Dao, and J. McPhee, "A survey of mathematics-based equivalent-circuit and electrochemical battery models for hybrid and electric vehicle simulation," *J. Power Sour.*, vol. 256, pp. 410–423, Jun. 2014.
[9] A. Fotouhi, D. J. Auger, K. Propp, and S. Longo, "Accuracy versus simplicity in online battery model identification," *IEEE Trans. Syst., Man, Cybern., Syst.*, vol. 48, no. 2, pp. 195–206, Feb. 2018.
[10] J. E. B. Randles, "Kinetics of rapid electrode reactions," *Discussions Faraday Soc.*, vol. 1, pp. 11–19, Mar. 1947.
[11] R. Hasan and J. Scott, "Application of Swingler's method for analysis of multicomponent exponentials with special attention to non-equispaced data," in *Proc. IEEE 12th Int. Colloq. Signal Process. Appl. (CSPA)*, Kuala Lumpur, Malaysia, Mar. 2016, pp. 12–15.
[12] R. Hasan and J. B. Scott, "Fractional behaviour of rechargeable batteries," in *Proc. Electron. New Zealand Conf. (ENZCon)*, Nov. 2016, pp. 111–114. [Online]. Available: https://ecs.victoria.ac.nz/foswiki/pub/Events/ENZCon2016/WebHome/ENZCon2016Proceedings.pdf
[13] M. Cugnet, J. Sabatier, S. Laruelle, S. Grugeon, B. Sahut, A. Oustaloup, and J.-M. Tarascon, "On lead-acid-battery resistance and cranking-capability estimation," *IEEE Trans. Ind. Electron.*, vol. 57, no. 3, pp. 909–917, Mar. 2010.
[14] J. Sabatier, M. Merveillaut, J. M. Francisco, F. Guillemard, and D. Porcelatto, "Fractional models for lithium-ion batteries," in *Proc. Eur. Control Conf. (ECC)*, Zurich, Switzerland, Jul. 2013, pp. 3458–3463.
[15] Y. Ma, X. Zhou, B. Li, and H. Chen, "Fractional modeling and SOC estimation of lithium-ion battery," *IEEE/CAA J. Automatica Sinica*, vol. 3, no. 3, pp. 281–287, Jul. 2016.
[16] B. Saha, K. Goebel, S. Poll, and J. Christophersen, "Prognostics methods for battery health monitoring using a Bayesian framework," *IEEE Trans. Instrum. Meas.*, vol. 58, no. 2, pp. 291–296, Feb. 2009.
[17] D. V. Do, C. Forgez, K. El Kadri Benkara, and G. Friedrich, "Impedance observer for a Li-ion battery using Kalman filter," *IEEE Trans. Veh. Technol.*, vol. 58, no. 8, pp. 3930–3937, Oct. 2009.
[18] H. Chaoui, N. Golbon, I. Hmouz, R. Souissi, and S. Tahar, "Lyapunov-based adaptive state of charge and state of health estimation for lithium-ion batteries," *IEEE Trans. Ind. Electron.*, vol. 62, no. 3, pp. 1610–1618, Mar. 2015.
[19] A. Guha and A. Patra, "Online estimation of the electrochemical impedance spectrum and remaining useful life of lithium-ion batteries," *IEEE Trans. Instrum. Meas.*, vol. 67, no. 8, pp. 1836–1849, Aug. 2018.
[20] A. Carullo, F. Ferraris, M. Parvis, A. Vallan, E. Angelini, and P. Spinelli, "Low-cost electrochemical impedance spectroscopy system for corrosion monitoring of metallic antiquities and works of art," *IEEE Trans. Instrum. Meas.*, vol. 49, no. 2, pp. 371–375, Apr. 2000.
[21] Y.-D. Lee, S.-Y. Park, and S.-B. Han, "Online embedded impedance measurement using high-power battery charger," *IEEE Trans. Ind. Appl.*, vol. 51, no. 1, pp. 498–508, Jan./Feb. 2015.
[22] P. Mauracher and E. Karden, "Dynamic modelling of lead/acid batteries using impedance spectroscopy for parameter identification," *J. Power Sources*, vol. 67, nos. 1–2, pp. 69–84, 1997.
[23] Ametek Scientific Instruments. *Solartron 1260A Impedance/Gain-Phase Analyzer*. Accessed: Jul. 2018. [Online]. Available: https://www.ameteksi.com/products/frequency-response-analyzers/1260a-impedance-analyzer
[24] Hioki E.E. Corporation. (Oct. 2018). *Chemical Impedance Analyzer IM3590, Battery Impedance Meter BT4560*. [Online]. Available: https://www.hioki.com/en/products/detail/?product_key=5749 and https://www.hioki.com/en/products/detail/?product_key=5664
[25] Zurich Instruments. (Oct. 2018). *MFIA 500 kHz Impedance Analyzer*. [Online]. Available: https://www.zhinst.com/products/impedance
[26] Q.-K. Wang, Y.-J. He, J.-N. Shen, X.-S. Hu, and Z.-F. Ma, "State of charge-dependent polynomial equivalent circuit modeling for electrochemical impedance spectroscopy of Lithium-ion batteries," *IEEE Trans. Power Electron.*, vol. 33, no. 10, pp. 8449–8460, Oct. 2018.
[27] G.-A. J. Francisco, R.-G. Juan, G.-C. Manuel, and R.-H. JoséRoberto, "Fractional RC and LC electrical circuits," *Ingeniería, Investigación y Tecnología*, vol. 15, pp. 311–319, Apr./Jun. 2014.
[28] J. Scott and P. Single, "Compact nonlinear model of an implantable electrode array for spinal cord stimulation (SCS)," *IEEE Trans. Biomed. Circuits Syst.*, vol. 8, no. 3, pp. 382–390, Jun. 2014.
[29] M. H. Jones and J. Scott, "Scaling of electrode-electrolyte interface model parameters in phosphate buffered saline," *IEEE Trans. Biomed. Circuits Syst.*, vol. 9, no. 3, pp. 441–448, Jun. 2015.
[30] D. MacCallum, "Automatic measurement of implantable electrode characteristics using a single impedance analyser," M.S. thesis, School Eng., Univ. Waikato, Hamilton, New Zealand, 2017.
[31] J. Scott and A. Parker, "Modern guide to spectral analysis with SPICE," *IEEE Circuits Devices Mag.*, vol. 11, no. 5, pp. 10–16, Sep. 1995.
[32] S. Seshadri and J. Scott, "Correction to 'compact nonlinear model of an implantable electrode array for spinal cord stimulation' [Jun 14 382-390]," *IEEE Trans. Biomed. Circuits Syst.*, vol. 12, no. 4, pp. 963–964, Aug. 2018.
[33] P. Single and J. Scott, "Cause of pulse artefacts inherent to the electrodes of neuromodulation implants," *IEEE Trans. Neural Syst. Rehabil. Eng.*, vol. 26, no. 10, pp. 2078–2083, Oct. 2018.

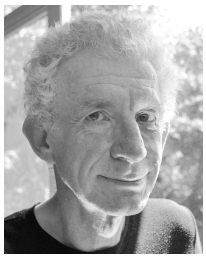

JONATHAN SCOTT (M'80–SM'99) was a Chief Engineer with the RF Technology, Sydney, from 1997 to 1998. From 1998 to 2006, he was with the Hewlett-Packard and Agilent Technologies Microwave Technology Center, Santa Rosa, California, where he was responsible for advanced measurement systems operating from dc to millimeter-wave. He was with the Department of Electrical Engineering, University of Sydney, prior to 1997. He is currently the Foundation Professor of electronic engineering with The University of Waikato, New Zealand. Prof. Scott holds five degrees, has authored over 150 refereed publications, several book chapters and a textbook, and he holds a dozen patents, several covering active products. His research interests include characterization and modeling of implantable electrodes, semiconductor device, battery, and acoustic systems. Professor Scott's educational interest includes Threshold Concepts and their application, particularly across engineering disciplines.

RAHAT HASAN received the B.Eng. degree (Hons.) in electrical and electronic engineering from London South Bank University, U.K. He is currently pursuing the Ph.D. degree with The University of Waikato, New Zealand. From 2011 to 2012, he was with Visteon Engineering Services Ltd, U.K., as a Software Validation Engineer. He is also the CEO and the Co-Founder of Smart Farmer Ltd. and Intelligent Tek Ltd. both of which are working on Agritech Projects.

5.2 On-Load Impedance Measurement of Batteries

The previous paper discussed how to accurately measure the impedance of a cell but at a single state of charge (SoC). This method can become really slow and tedious, especially when dealing with very low frequencies, 10 μHz and below. There also exist no instruments which can vary the SoC of a cell and simultaneously sweep the impedance from 10 μHz - 1 μHz. In this manuscript, a faster way to measure the impedance of a cell under load while varying the SoC is proposed. Such measurement will allow valuable insights on how the impedance of a cell changes over a range of SoC.

To test the validity of the proposed measurement, first the traditional method of measuring cell impedance at a single SoC was employed. The impedance of a 800 mAh lithium ion cell was measured at two random frequencies, 10 mHz and 1 mHz at a single SoC. This was repeated in steps of 0.4% charge until the cell was full discharged. The impedance phase data obtained was quantized and is attributed to the property of the cell. Although it is known that the impedance phase data is more prone to noise than impedance magnitude data.

The impedance of the same cell was next measured with the new proposed method while simultaneously altering the SoC . The superiority of the proposed method is that such measurement can be performed by any power supplies which can sink and source current such as Hameg HM8143 two-quadrant power supplies, Tektronix (Keithley) 2400-series Source-Mearurement Units (SMUs), Keysight Precision I/V Analyzers, and Chroma 17000-series Programmable Battery Charge/Discharge Test Systems. One can also use the same method to conduct impedance measurement at frequencies below 1 mHz and at the same time vary the SoC.

Data obtained from the two method was then compared. The percentage difference between the impedance obtained using the two method is within

10% at 1 mHz. The only drawback of this method is its limitation of measuring impedance at extremely low frequencies where noise is introduced in the measured data due to low stimuli level.

Impedance Measurement of Batteries under load

Rahat Hasan
School of Engineering
University of Waikato, Hamilton, New Zealand

Professor Jonathan Scott
School of Engineering
University of Waikato, Hamilton, New Zealand

***Abstract*—The impedance of a lithium battery at a single state-of-charge (SoC) is obtained from the current and voltage response of the cell. Making this measurement is important in order to understand cell characteristics. There exist some impedance analysers which can make suitable measurements at a single SoC. Measuring this impedance at multiple SoC is slow and tedious especially at lower frequencies. We present a new method which computes the impedance over a range of SoC while simultaneously varying the SoC. The proposed method produces reliable data even when the device under test is behaving non-linearly. The data obtained from this measurement is validated by comparing impedance data obtained at different SoC from a cell under no load.**

***Index Terms*—batteries, impedance measurement, frequency domain analysis, state-of-charge**

I. Introduction

In recent years, there is an increasing interest in measuring the impedance of batteries over a range of frequencies [1]–[4]. Most commonly the impedance is measured using the I-V method which observes the current and response voltage signals. The impedance is then obtained by dividing the complex voltage by the complex current.

There exist instruments which make this measurement [5], [6]. A more robust method of measuring impedance was proposed which yields accurate data at extremely low frequencies when measuring non-linear components via adjusting the stimuli level at each frequency [7]. All of these methods assume that the battery is disconnected from the load.

Most authors propose battery models [8]–[14] mainly for the purpose of estimating the state-of-charge and state-of-health. All these models were produced from frequency response data obtained at a single SoC. A typical impedance plot of a single 800mAh Li-ion cell is shown in figure 1. The steps used to produce figure 1 is adopted from paper [7]. It is seen from this simple curve that a battery resembles a pure resistor at higher frequencies but depicts the behaviour of a capacitor (possibly fractional) at lower frequencies.

The impedance of a battery is subject to change depending on external factors such as temparature and SoC. Paper [15] inspects how the impedance of a LiFePo4 battery varies with temperature at different state of charge. On the other hand, authors of paper [16] speculate how the impedance changes with the SoC. They estimated this parametric change from a fractional-order derivatives using recursive least square technique.

In this paper, we propose a method which can measure the impedance of a cell under load while varying the SoC. Section II investigates the current method of measuring impedance at a single SoC. Section III gives a tutorial of an alternative method which measures impedance while the SoC of a cell is varied. Section IV proposes our conclusion.

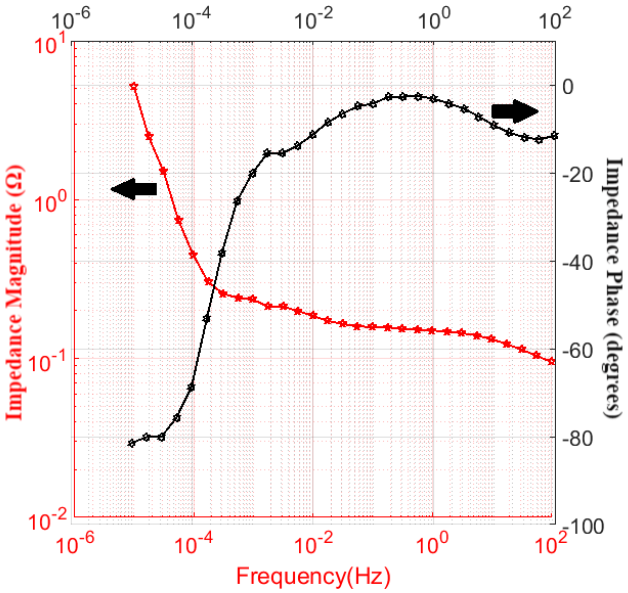

Fig. 1. Impedance curve of a 800mAh Li-ion cell.

II. Traditional method

Traditionally, the impedance of a cell is measured under no load at a single SoC. To measure impedance at different SoC, first a certain amount of charge is drawn out of the cell over a period of time. A small current stimuli is then applied and the response voltage across the cell is measured under no load. The impedance of the cell is then calculated and stored. This procedure is continued until the cell is fully discharged.

We reproduced this method on a 800mAh Li-ion cell. The external temperature of the battery is maintained at 25 degrees Celsius throughout the measurement using a Contherm Polar 1000. We used an Agilent E5270 with E5281A source/monitor to make this measurement. The source monitor unit (SMU) was programmed in python. The connection is shown in figure 2. The steps followed are as below:

1) Use a current source to charge the cell to its full capacity.
2) Rest for 30 minutes to ensure that the chemistry inside the cell is stable.

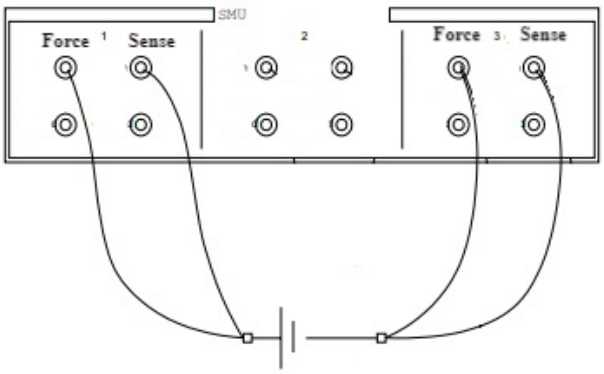

Fig. 2. The setup used to measure impedance of Li-ion cell at different SoC.

3) Draw 0.1A for 120 seconds. This is equivalent to drawing 12 Coulombs or 0.4% of charge.
4) Rest for 30 seconds.
5) Reproduce the impedance measurement steps at 10mHz and 1mHz from paper [7].
6) Store the measured impedance in a data file.
7) Repeat steps 3-6 until the cell is fully discharged.

Figure 3 presents the result. We speculate the quantization of the phase data at 10mHz is a property of the cell. Although we know that impedance phase data is more prone to noise than impedance magnitude data.

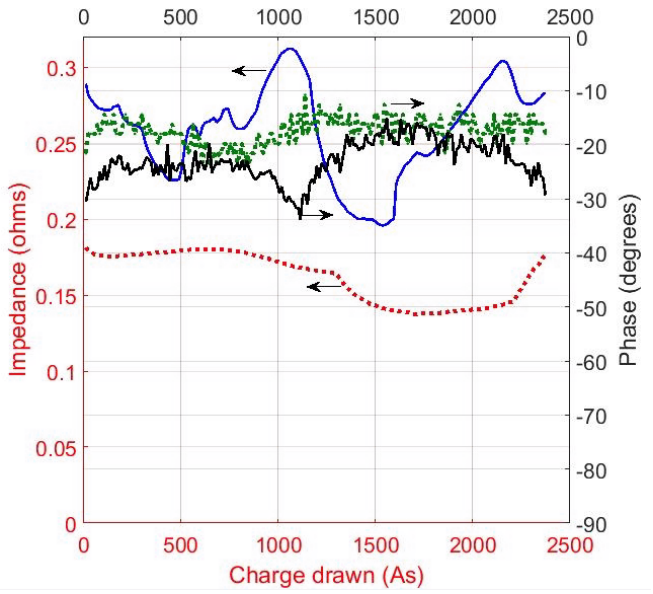

Fig. 3. Impedance magnitude and phase measured using traditional method under no load at different SoC for a Li-ion cell at 10mHz (dotted lines) and 1mHz (solid lines).

III. Proposed Method

In this section, we discuss a method which measures the impedance of a battery while simultaneously varying the SoC. We used a programmable current source to produce a sinusoidal current with a DC offset. Such measurement can be performed by a range of power supplies which can sink and source current such as Hameg HM8143 two-quadrant power supplies, Tektronix (Keithley) 2400-series Source-Mearurement Units (SMUs), Keysight Precision I/V Analyzers, and Chroma 17000-series Programmable Battery Charge/Discharge Test Systems. We will show that this alternative method is superior because it conducts an impedance measurement at frequencies below 1mHz while simultaneously altering the SoC.

A. Selecting the parameters of the current stimuli

To measure the impedance of a cell over a range of SoC, a small sine-varying current signal with a DC offset is applied. The response voltage across the cell is measured simultaneously. The time domain equation of the current signal is

$$I = I_0 sin(2\pi ft) - I_{os} \tag{1}$$

Where I_0 is the amplitude of the signal, f is the desired frequency and I_{os} is the negative offset of the signal. The integral of the positive and negative half of the cycle will yield the amount of charge transferred to and from the cell respectively. For the purpose of the calculation, we denote the charge transferred to the cell as Q_{in} and charge moved out the cell as Q_{out}.

$$Q_{in} = \int_0^{T/2} Idt = \int_0^{T/2} I_0 sin(2\pi ft) - I_{os} dt \tag{2}$$

and

$$Q_{out} = \int_{T/2}^{T} Idt = \int_{T/2}^{T} I_0 sin(2\pi ft) - I_{os} dt \tag{3}$$

Integration of equations 2 and 3 gives

$$Q_{in} = -\frac{I_0}{2\pi f}[cos(\pi fT) - 1] - \frac{I_{os}T}{2} \tag{4}$$

and similarly

$$Q_{out} = -\frac{I_0}{2\pi f}[cos(2\pi fT) - cos(\pi fT)] - \frac{I_{os}T}{2} \tag{5}$$

substituting $fT = 1$ leads to

$$Q_{in} = \frac{I_0}{\pi f} - \frac{I_{os}}{2f} \tag{6}$$

and

$$Q_{out} = -\frac{I_0}{\pi f} - \frac{I_{os}}{2f} \tag{7}$$

In both equations 6 and 7, the term $\frac{I_{os}}{2f}$ determines the discharging rate of the cell and $\frac{I_0}{\pi f}$ decides the nature of the sinusoidal signal. Since both terms are dependant on the frequency of the signal, the offset and amplitude of the current signal are selected accordingly for each frequency. In all our measurement, we limited the charge flow in the cell at $\pm$ 10 $\%$ of the total cell charge.

B. Proposed method

The steps for the measurement procedures are listed as follows:

1) Use a current source to charge the cell to its full capacity.
2) Rest for 30 minutes to ensure that the chemistry inside the cell is stable.
3) Use current drive to generate the stimulus signal.
4) Fix the amplitude and the offset of the signal at desired frequency according to subsection III-A.
5) Execute the measurement over at least 100 cycles until the cell is fully discharged. Using equations 6 and 7, select appropriate current stimuli level at each frequency to maintain the SoC within 10% in either direction.
6) Slice the data into n number of cycles and save the input current and measured response voltage data in a text file for further analysis.
7) Apply hann window to each data slice to compensate for truncation.
8) Obtain the complex magnitude and phase of the current and voltage signal using Fourier Transform at the signal frequency.
9) Divide the complex voltage by the complex current to calculate the impedance of the cell.

C. Measuring impedance over a range of SoC of a single Li-ion battery

We next measured the impedance of a 800mAh Li-ion cell over a range of SoC using our proposed method. We programmed the SMUs of Agilent E5270A with python to produce the stimuli at 10mHz and 1mHz. The connection used in our proposed method is still the same as the traditional one. Appropriate amplitude and offset of the stimuli were chosen which will cycle the cell 200 times before it gets fully discharged. Throughout the entire measurement, the external temperature of the battery is kept constant as before. Figure 4 depicts the first 30 cycles of the current and response voltage waveform measured at 10mHz. Readers may notice the need for windowing the response voltage data prior Fourier Transform since the end points of a cycle are not the same.

Figure 5 shows the new impedance magnitude and phase measured at different SoC using our method. The magnitude and the phase change significantly at different SoC as the frequency gets smaller. This is expected since batteries only exhibit interesting behaviour at extremely low frequencies. At 1mHz, the percentage difference between the impedance obtained using our method and the traditional method seen previously in figure 2 is within 10%. We attributed the discrepancies in the noisy phase data obtained using traditional method to instrument noise and uncertainties.

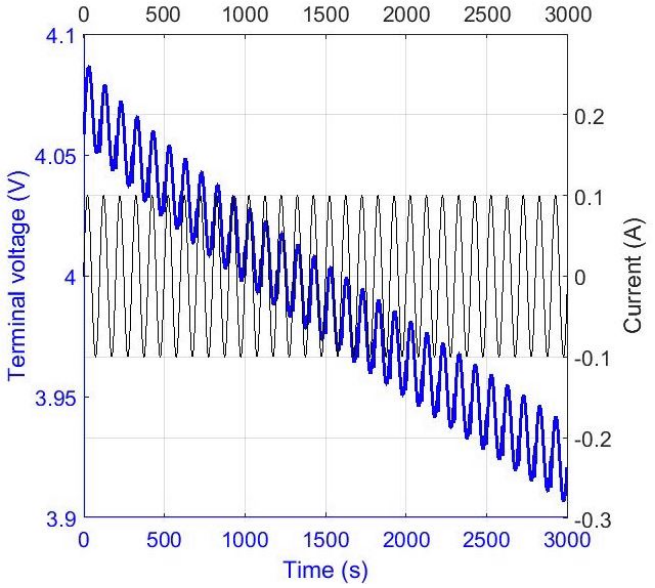

Fig. 4. Time-domain current and response voltage values obtained at 10mHz stimulus frequency.

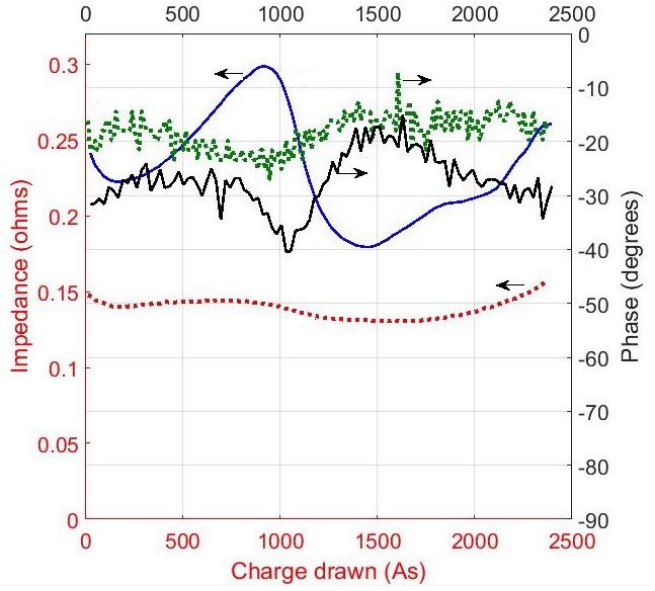

Fig. 5. Impedance magnitude and phase measured under load in comparison to figure 3 using our proposed method at different SoC for a Li-ion cell at 10mHz (dotted lines) and 1mHz (solid lines).

IV. Conclusion

In this paper, we have shown there are other ways to measure the impedance of a battery over a range of SoC. Our method is superior to the existing one because it can measure impedance for a given cell while smoothly varying the SoC. Unlike the traditional method, this new technique measures the impedance of a cell under load. Data was shown to be valid by comparison with data obtained using the traditional method. The percentage difference between the impedance obtained using the two method is within 10% at 1mHz. The only drawback of this method is its limitation of measuring impedance at extremely low frequencies where noise is introduced in the measured data due to low stimuli level.

REFERENCES

[1] Jaber A. Abu Qahouq, "Online battery impedance spectrum measurement method", *2016 IEEE Applied Power Electronics Conference and Exposition (APEC)*, 2016, pages: 3611 - 3615.

[2] Md. Kamal Hossain, S.M. Rakiul Islam, "Battery Impedance Measurement Using Electrochemical Impedance Spectroscopy Board", *2017 2nd International Conference on Electrical and Electronic Engineering (ICEEE)*, 2017, pages: 1 - 4.

[3] David A. Howey, Paul D. Mitcheson, Vladimir Yufit, Gregory J. Offer, Nigel P. Brandon, "Online Measurement of Battery Impedance Using Motor Controller Excitation", *IEEE Transactions on Vehicular Technology*, 2014, Volume: 63 , Issue: 6, pages: 2557 - 2566.

[4] Yuan Cao, Jaber A. Abu Qahouq, "Evaluation of paralleled battery system with SOC balancing and battery impedance magnitude measurement", *2018 IEEE Applied Power Electronics Conference and Exposition (APEC)*, 2018, pages: 437 - 441.

[5] *Solartron 1260A Impedance/Gain-Phase Analyzer*, Ametek Scientific Instruments. Accessed July, 2018. [Online]. Available: https://www.ameteksi.com/products/frequency-response-analyzers/1260a-impedance-analyzer.

[6] *MFIA User Manual*, Zurich Instruments AG. Accessed October, 2018. [Online]. Available: https://www.zhinst.com/sites/default/files/ziMFIA_UserManual_53400.pdf.

[7] Hasan, R., and Scott, J. B., "Measurement of Battery Impedance Extending to Extremely Low Frequencies", *IEEE Transactions on Industrial Electronics*, submitted.

[8] Jocelyn Sabatier, Mohamed Aoun, Alain Oustaloup, Gilles Gregoire, Frank Ragot and Patrick Roy, "Fractional system identification for lead acid battery state of charge estimation", *Signal Processing Fractional calculus applications in signals and systems*, Vol. 86, Issue 10, October 2006, pp.2645–2657.

[9] Yan Ma, Xiuwen Zhou, and Hong Chen,"Fractional Modeling and SOC Estimation of Lithium-ion Battery", *IEEE/CAA Journal of Automatica Sinica*, Vol 3, No. 3, July 2016, pp. 281-287.

[10] Jocelyn Sabatier, Mathieu Merveillaut, Junior Mbala Francisco, Franck Guillemard, Denis Porcelatto, "Fractional models for lithium-ion batteries", *2013 European Control Conference (ECC)*, Zrich, Switzerland, July 2013, pp. 3458-3463.

[11] Luiz Carlos Stevanatto, Valner Joo Brusamarello, and Stanislav Tairov, "Parameter Identication and Analysis of Uncertainties in Measurements of Lead Acid Batteries", *IEEE TRANSACTIONS ON INSTRUMENTATION AND MEASUREMENT*, VOL. 63, NO. 4, APRIL 2014, pp. 761-768.

[12] J. Chiasson and B. Vairamohan, "Estimating the state of charge of a battery", *IEEE Transactions on Control Systems Technology*, volume 13, Issue 3, May 2005, pp: 465–470.

[13] Tiezhou Wu, Lunan Liu, Qing Xiao, Quan Cao, and Xieyang Wang, "Research on SoC Estimation Based on Second-order RC Model", *Telkomnika*, vol. 10, no. 7, Nov 2012, pp. 1667–1672.

[14] ZeCheng, JikaoLv, YanliLiu, and ZhihaoYan, "Estimation of State of Charge for Lithium-Ion Battery Based on Finite Difference Extended Kalman Filter, *Journal of Applied Mathematics*, 2014, Vol 2014, pp. 1–10.

[15] Luc H. J. Raijmakers, Dmitri L. Danilov, Joop P. M. van Lammeren, Thieu J. G. Lammers, Henk Jan Bergveld, Peter H. L. Notten, "Non-Zero Intercept Frequency: An Accurate Method to Determine the Integral Temperature of Li-Ion Batteries", *IEEE Transactions on Industrial Electronics*, 2016, Volume: 63, Issue: 5, pages: 3168 - 3178.

[16] Arijit Guha, and Amit Patra, "Online Estimation of the Electrochemical Impedance Spectrum and Remaining Useful Life of Lithium-Ion Batteries", *IEEE TRANSACTIONS ON INSTRUMENTATION AND MEASUREMENT*, VOL. 67, NO. 8, AUGUST 2018, pp. 1836-1849.

Chapter 6

Mathematical Model

6.1 Mathematical model for rechargeable batteries

This manuscript first shows that RC type models are inappropriate for modelling lithium ion cells and then proposes a mathematical model. The mathematical model was then used to approximate the charge-voltage characteristics of a 800 mAh lithium ion cell.

In one of the previous papers, a modified Swingler's algorithm was applied to the transient recovery curve of a NiMH cell to extract exponential components. A similar approach was adopted in this paper to investigate if Li-ion cells are any different. However, the output result from the algorithm was very similar to the one from NiMH. This concluded that first and second-order RC networks are also theoretically inappropriate for Li-ion cells and a CPE model is more favourable for characterising cell behaviour.

The impedance of the 800mAh Li-ion cell was next measured with a programmable current source. From the measured data, it was deduced that the equivalent impedance equation of the cell in the frequency domain is the summation of a complex impedance of a resistor and a CPE. Re-arranging this equation produced a time domain equation where there is a direct relationship between charge and voltage. The equation contains only 3 parameters which can all be easily calculated from the impedance-frequency curve.

The mathematical model was then fitted to the measured charge-voltage curve. The model predicted the terminal voltage of the cell with an accuracy of 0.5% between 20-80% SoC region. This is extraordinary for practical applications since most battery manufacturers recommends to stay within the linear region of the charge-voltage curve to extend the lifetime of the cell.

Measurement for fractional characteristic of Lithium batteries

Rahat Hasan
School of Engineering
University of Waikato, Hamilton, New Zealand

Professor Jonathan Scott
School of Engineering
University of Waikato, Hamilton, New Zealand

***Abstract*—It is shown that RC circuits are inappropriate for modelling the transient runtime characteristics of battery voltage. In contrast, impedance-frequency measurements suggest that a fractional capacitor or "constant phase element" (CPE) can represent battery impedance over a wide frequency range. In this paper, we present evidence that shows RC models of rechargeable batteries to be theoretically inappropriate. We then propose a fractional mathematical model which uses 3 parameters to predict charge-voltage characteristics or steady-state Q-V function of a Li-ion cell.**

I. Introduction

In recent years, various models have been proposed which attempts to estimate the state-of-charge (SoC) and state-of-health (SoH). [1]–[3] A number of authors model these characteristic using Thevenin-style second-order RC battery model consisting of two RC networks with a series resistor. [4]–[6]. Employing capacitors, such circuits must predict transients that are exponential decays, or the sum of a small number of exponentials. We will next show that these models are inherently incorrect.

Figure 1 shows the voltage-time characteristic measured on a small rechargeable battery subjected to a rectangular current pulse. The battery is a 800mAH 14500 Lithium-ion single cell. The measurements were made with an Agilent E5270 Precision IV Analyzer and an Agilent 34401A DMM. Figure 2 depicts the connection. All measurements were made with the battery held at a constant environmental temperature of 25 Celsius using a Contherm Polar 1000.

It turns out that the recovery curve is not an exponential decay at all. A neat method is presented in [7] that analyses a decay curve to identify the magnitudes and time constants of exponential functions that may have been summed to produce the composite decay curve. In other words, it permits the identification of exponential components within a multi-exponential function. Applying this to the recovery portion of the battery characteristic presented in figure 1 yields the result in figure 3. If the recovery transient was to be exponential, or the sum of a small number of exponentials, figure 3 would evidence this by showing distinct peaks in the analysis of the measured data, just as it does for the data generated from a 2-RC model, also shown in the figure. Instead the result is essentially noise.

In this manuscript, we present a mathematical model based on impedance-frequency plot and predict the charge-voltage characteristic of 800mAH 14500 Lithium-ion single cell. Section II derives a mathematical equation from the measured impedance of the cell. Section III describes the fitting of the mathematical model to the charge-voltage characteristic of the cell. Section IV provides valuable discussion and section V presents our conclusion.

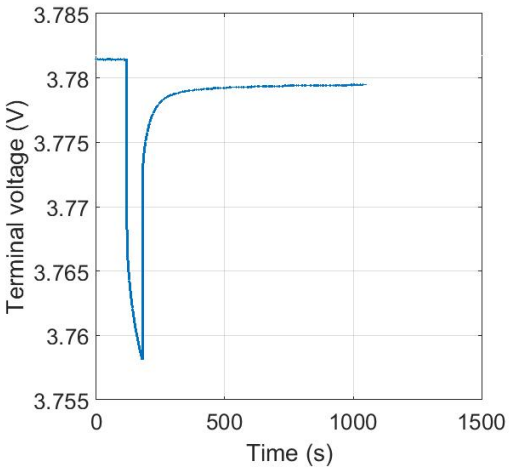

Fig. 1. The voltage characteristic measured across an 800mAh, 14500 lithium battery when subjected to a current pulse of 100mA for 60 seconds.

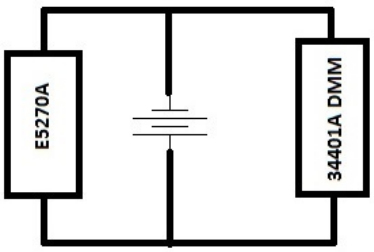

Fig. 2. The set-up required to measure the transient response of a cLi-ion cell.

II. Mathematical model derivation

We previously measured the impedance of a 800mAH 14500 Lithium-ion cell. [8] Some authors conducted similar

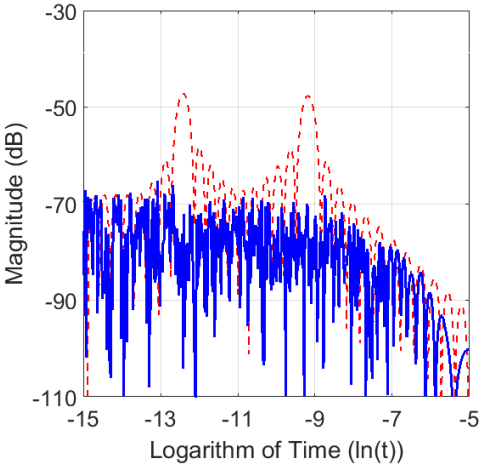

Fig. 3. Plot of the analysis output for the measured recovery curve presented in figure 1 (noisy trace) along with the same analysis applied to a similar magnitude recovery transient simulated using a second-order RC battery model (scalloped, dashed trace).

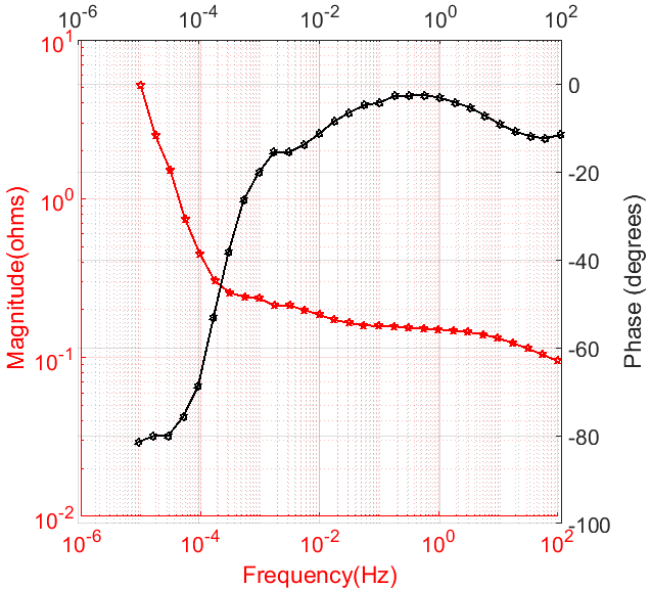

Fig. 4. Impedance and phase measurement of a single 800mAh Li-ion cell reproduced from [8].

measurement which only extends to 100Hz. [9], [10] However, a Li-ion cell only reveals fractional behaviour at frequencies as low as 100μHz. This is shown in figure 4. From this simple curve we can deduce that a Li-ion cell can be represented with a single resistor and a Constant Phase Element (CPE). Therefore, the equivalent impedance equation in frequency domain is

$$Z = R + \frac{1}{C_F s^{\alpha}} \tag{1}$$

Where R is the series resistance, C_F is the capacitance of the CPE and α is a slope parameter which varies between 0 and 1. The terminal voltage of the cell can then be expressed as follows

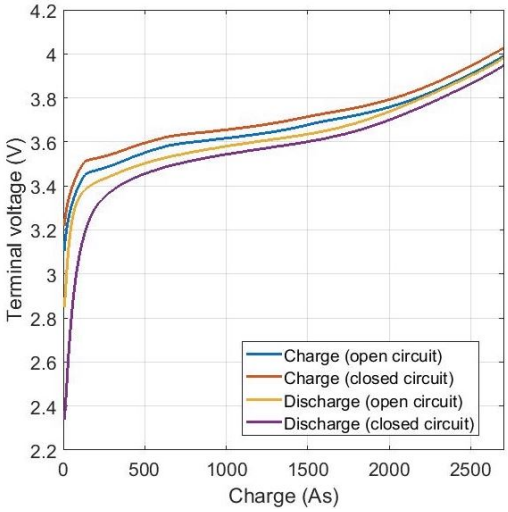

Fig. 5. Q-V characteristic of 800mAh Li-ion cell.

$$\frac{V}{s} = \frac{I}{s}(R + \frac{1}{C_F s^{\alpha}}) \tag{2}$$

Applying Inverse Laplace Transform to equation 2 yields

$$V = IR + \frac{It^{\alpha}}{C_F \Gamma(\alpha + 1)}) \tag{3}$$

Since the second term (voltage across the CPE) only contributes to the Q-V function, it can be written as

$$V(Q) = \frac{It^{\alpha}}{C_F \Gamma(\alpha + 1)}) \tag{4}$$

Substituting $t = Q/I$ in equation 4 leads to

$$V(Q) = \frac{I^{(1-\alpha)} \times Q^{\alpha}}{C_F \Gamma(\alpha + 1)} \tag{5}$$

Where I is the charging/discharging current and Q is the amount of charge drawn. In the next section, we derive the values for the 3 parameters in equation 5 and fit the model to the measured Q-V characteristic.

III. Model Fitting

A. Measuring the Q-V characteristic

The problem with measuring a battery charge voltage characteristic is that this is a dynamic measurement. When charging a cell,the terminal voltage will be higher than would be the steady-state voltage perceived if the battery were completely at rest. A common response to this is to measure the voltage of the cell under constant-current charging and then to discharge at the same constant current, relying on the impedance characteristic to be linear and symmetrical. The steady-state characteristic is then approximated by averaging

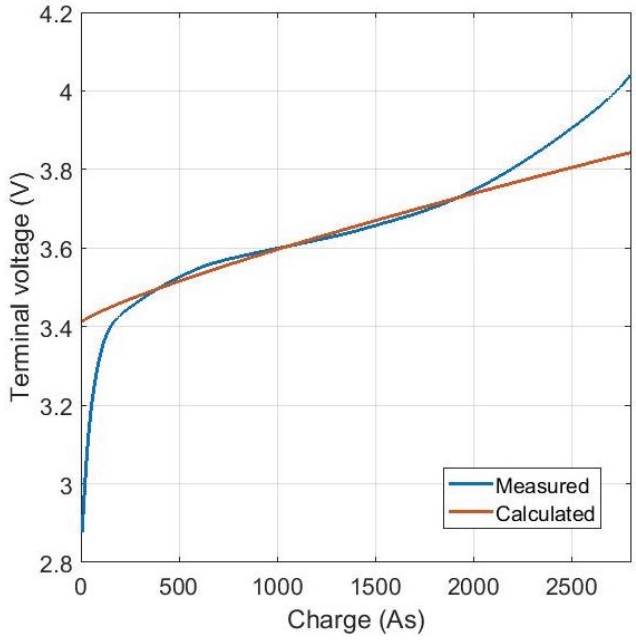

Fig. 6. The estimated steady-state cell voltage obtained by averaging the traces from figure 5 is plotted against the voltage predicted by the mathematical model.

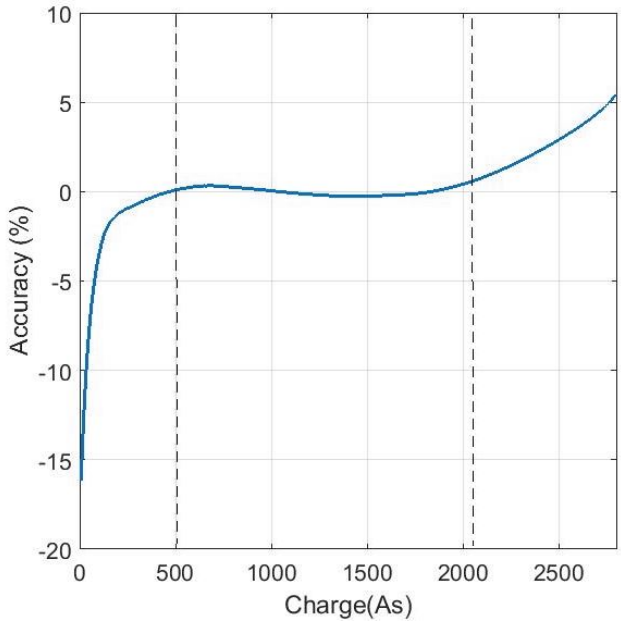

Fig. 7. Percentage error between the measured and calculated data portrayed in figure 6. The dashed lines shows the region where the error is within 0.5%.

the two data sets point by point to yield the average characteristic. A very similar, but more informative, variant is used here. The battery was charged at 100mA for 60 seconds using the E5270. Then the voltage was measured, the current set to zero for 60 seconds, and the voltage measured again. Reference to the measured data trace in figure 1 will indicate that 60 seconds should allow the battery to settle only some of the way towards its asymptotic value, owing to the exceptionally slow decay of the fractional tail. This cycle was repeated until the battery reached full charge. At the end of a sweep the battery was rested for 12 hours to allow complete equalisation. Next the current was set for discharge, and the same minute-off, minute on scenario used to discharge the battery. Figure 5 shows four traces, being the charge and discharge characteristics during current flow (”closed circuit”) and after the 60-second rest (”open circuit”). The steady-state characteristic is calculated by averaging the traces point by point. This is shown in figure 6.

B. Fitting the mathematical model

We next calculated the three parameters of equation 5. As previously stated in III-A, the charging/discharging current, I is 100mA. Using figure 4 the slope parameter, α is calculated from the CPE phase settled to 80 degrees at 20μHz yielding

$$\alpha = \frac{80}{90} = 0.889 \tag{6}$$

The CPE capacitance is obtained from the measured impedance of the cell which was taken as 0.75Ω at 55.7μHz giving

$$C_F = \frac{1}{Z(2\pi f)^\alpha} = 1587.6 S.s^\alpha \tag{7}$$

The mathematical model was then fitted to predict the relationship between terminal voltage and SoC. The calculated terminal voltage trace shown in figure 6 was obtained using Matlab with appropriate initial condition. To understand the validity of the model, we calculated the accuracy of the fitted data. Figure 7 portrays this.

IV. Discussion

Most battery manufacturers recommend to stay within the linear region of the Q-V curve in order to extend the lifetime of a cell. However, in a Prius hybrid, the SoC is maintained between 40% and 80% to make the battery last longer. Existing mathematical model can predict this to an accuracy of 5% using a complex algorithm containing 6 parameters. [11], [12] Some authors adopt a different model which achieves a better accuracy (0.5%) with the same number of parameters. [13], [14]

Our mathematical model predicts the 20%–80% SoC region of the charge-voltage characteristic with a similar accuracy but uses only 3 parameters. There exists a possibility to extend this model to the non-linear region of the Q-V function by incorporating with a non-linear function.

V. Conclusion

We presented a revolutionary mathematical model consisting of only 3 parameters. All parameters can be easily identified from a simple impedance-frequency curve of the cell under test. The model predicts the linear of the Q-V characteristic which an extraordinary accuracy of 0.5%. It

is possible to stretch the model to the non-linear region by including a polynomial based function.

REFERENCES

[1] ZeCheng, JikaoLv, YanliLiu, and ZhihaoYan, "Estimation of State of Charge for Lithium-Ion Battery Based on Finite Difference Extended Kalman Filter, *Journal of Applied Mathematics*, 2014, Vol 2014, pp. 1–10.

[2] J. Chiasson and B. Vairamohan, "Estimating the state of charge of a battery", *IEEE Transactions on Control Systems Technology*, volume 13, Issue 3, May 2005, pp. 465–470.

[3] N. Lotfi, J. Li, R. G. Landers and J. Park, "Li-ion Battery State of Health Estimation based on an improved Single Particle model", *2017 American Control Conference (ACC)*, May 2017, pp. 86–91.

[4] Qun-Zhi Zhang, Xin-Yue Wang and Hui-Mei Yuan, "Estimation for SOC of Li-ion battery based on two-order RC temperature model", *2018 13th IEEE Conference on Industrial Electronics and Applications (ICIEA)*, June 2018, pp. 2601–2606.

[5] Tiezhou Wu, Lunan Liu, Qing Xiao, Quan Cao, and Xieyang Wang, "Research on SoC Estimation Based on Second-order RC Model", *Telkomnika*, vol. 10, no. 7, Nov 2012, pp. 1667–1672.

[6] Maryam Yazdanpour, Peyman Taheri, Abraham Mansouri and Ben Schweitzer, "A circuit-based approach for electro-thermal modeling of lithium-ion batteries", *2016 32nd Thermal Measurement, Modeling & Management Symposium (SEMI-THERM)*, March 2016, pp. 113–127.

[7] Hasan, R., and Scott, J. B., "Application of Swingler's Method for Analysis of Multicomponent Exponentials with Special Attention to Non-equispaced Data", *12th IEEE International Colloquium on Signal Processing & Its Applications (CSPA)*, 4–6 March 2016, Malaysia, pp.12–15.

[8] Hasan, R., and Scott, J. B., "Impedance Measurement of Batteries under load", *2019 IEEE International Instrument & Measurement Technology Conference*, 20–23 May 2019, New Zealand, submitted.

[9] Roberto E. Serrano-Finetti, "Output Impedance Measurement in Low-Power Sources and Conditioners", *IEEE Transactions on Instrumentation and Measurement*, Vol. 58, No. 1, January 2009, pp 180–186.

[10] Roberto E Serrano-Finetti and Ramon Pallas-Areny, "Output Impedance Measurement in Power Sources and Conditioners", *IEEE Instrumentation & Measurement Technology Conference (IMTC)*, 1–3 May, 2007, pp1–5.

[11] Jocelyn Sabatier, Mohamed Aoun, Alain Oustaloup, Gilles Gregoire, Frank Ragot and Patrick Roy, "Fractional system identification for lead acid battery state of charge estimation", *Signal Processing Fractional calculus applications in signals and systems*, Vol. 86, Issue 10, October 2006, pp.2645–2657.

[12] Jocelyn Sabatier, Mathieu Merveillaut, Junior Mbala Francisco, Franck Guillemard, Denis Porcelatto, "Fractional models for lithium-ion batteries", *2013 European Control Conference (ECC)*, Zrich, Switzerland, July 2013, pp. 3458-3463.

[13] Yan Ma, Xiuwen Zhou, and Hong Chen,"Fractional Modeling and SOC Estimation of Lithium-ion Battery", *IEEE/CAA Journal of Automatica Sinica*, Vol 3, No. 3, July 2016, pp. 281-287.

[14] Rahat Hasan and Jonathan Scott, "Comments on 'Fractional Modeling and SOC Estimation of Lithium-ion Battery' ", IEEE/CAA Journal of Automatica Sinica, Vol. 4, no. 1, 2018.

Chapter 7

Passive Fractional Equivalent-circuit Battery Model

7.1 Fractional circuit model for rechargeable batteries

Although the mathematical model proposed previously successfully predicted the charge-voltage characteristics of a cell, it does not have any physical justification and cannot be reproduced in a compact simulator. The whole idea of a compact, equivalent circuit model is to relate voltage and current as a function of time, and simultaneously calculate stored energy and charge. The aim of this manuscript is to show that a linear model comprised of a resistor in series with a CPE is sufficient to predict the impedance, charge-voltage and runtime characteristics of a rechargeable cell and does not require a voltage or current source. This makes the model suitable to calculate the efficiency of energy stored in a cell that has not been proposed before.

The inspiration for this work originated from Randles' fractional element based model presented in 1947 that was used to investigate rapid electrode reactions in an electrode system. Unlike most models found during the literature review, Randles' model does not contain any voltage or current source. Closer examination of the model revealed that the capacitance parallel to the series RC is minute in the absence of electrochemical phenomena and can be ignored at low frequencies. A similar type of model can be proposed for rechargeable cells. Impedance measurement of both nickel-metal hydride and lithium-ion cells expose the character of a CPE at low frequencies whose angle varies with cell chemistry and a resistive behaviour as the frequency gets higher.

The model was then constructed in SPICE to see if it fit the measured data from the impedance, transient recovery, and charge-voltage domains. The CPE was split n-way to account for the distributed nature of the structure within the battery. The new split-CPE model was simulated in SPICE where the CPE component is approximated with a network of RC elements. The theory leading to the approximation is attributed to Morrison [14] .

Fitting the simulation of battery impedance with split-CPE model to the

measured impedance data shows that the new model achieves considerably better approximation with no more complexity than a first-order RC model. The model can also predict the measured transient tail of a single 800mAh, 14500 lithium battery with only 3% error. With suitably-selected initial conditions, the model also fits the measured charge-voltage characteristic of the cell with extraordinary accuracy. The model predicted the linear region of the charge-voltage curve with a percentage error which is less than 1%.

The model was then adopted to predict the transient runtime and charge-voltage characteristic of a nickel-metal hydride cell with a nominal capacity of 1850mAh. The fit was sufficient for practical applications. It is speculated that such a model is not restricted to only lithium-ion and nickel-metal hydride cell but is applicable to all cell types.

IEEE Access
Multidisciplinary ⋮ Rapid Review ⋮ Open Access Journal

Received April 3, 2020, accepted May 1, 2020. Date of publication xxxx 00, 0000, date of current version xxxx 00, 0000.

Digital Object Identifier 10.1109/ACCESS.2020.2992771

Extending Randles's Battery Model to Predict Impedance, Charge–Voltage, and Runtime Characteristics

RAHAT HASAN, (Student Member, IEEE), AND JONATHAN SCOTT, (Senior Member, IEEE)
School of Engineering, The University of Waikato, Hamilton 3216, New Zealand

Corresponding author: Rahat Hasan (rh163@students.waikato.ac.nz)

This work was supported in part by RH Innovation Ltd., and in part by Waikatolink Ltd.

ABSTRACT The impedance of a battery can be modelled with an elegant fractional-capacitor or ''constant phase element'' (CPE) equivalent circuit and a series resistor. In this manuscript, we present new evidence that suggests that a linear model similar to Randles' comprised solely of this impedance network is able to predict both the charge-voltage relationship epitomised by the familiar hysteresis curve of voltage as a function of charge as a battery charges and discharges through its linear region, and the recovery or ''equilibration'' transient that results from a step change in load current. The proposed model is unique in that it does not contain a source, either voltage or current, nor any purely reactive elements. There are important potential advantages of a passive battery model.

INDEX TERMS Rechargeable battery, lithium-ion battery, state of charge, fractional modelling.

I. INTRODUCTION

The literature reveals hundreds of papers in recent decades with the phrase ''battery model'' in the title, while thousands can be found on the subject in general in the IEEE stable alone. A battery model is considered key to prediction of behaviour, including state-of-charge (SoC) [1]–[5]. Readers not already familiar with the state of the art are directed to [1] which provides a broad literature review and an excellent summary of the various approaches including open-loop sensing based on open-circuit voltage (OCV) or Coulomb counting (CC) methods, and closed-loop state estimation using either a ''black box'' or equivalent-circuit. Further, some detail in the case of equivalent-circuit approaches were presented in [6]. In the preferred case of an equivalent-circuit model, the circuit is invariably a voltage source with a network of elements fitted to the apparent impedance of the cell [2], [6]. We might describe these as ''Thévenin-like RC'' models. Figure 1 depicts the popular first- and second-order examples of this type. More applications of a second-order ''Thévenin-like RC model appeared in [7], [8] which is preferred by researchers than its predecessor when characterising cell SoC due to the extra degree of freedom.

The associate editor coordinating the review of this manuscript and approving it for publication was Mark Kok Yew Ng.

We have shown elsewhere that such models are theoretically unsuitable for modelling the runtime characteristics of a cell [9], [10].

More models in the last few years have returned to the use of fractional-derivative elements, mostly fractional capacitors, also known as Constant-Phase Elements or CPEs. A fractional element was reported by Randles in 1947 [11] in a equivalent-circuit model. The paper investigated rapid electrode reactions with a electrode system shown in figure I. In Randles' model, Cl represents capacitance in the absence of electrochemical phenomena, and is small enough that it only comes into play at higher frequencies. It is what might be called ''parasitic capacitance'' in the electronic world. Cr, on the other hand, is a capacitive element with the angle fixed to 45 degrees. This non-ideal element was later introduced in [12] as a Warburg element. The basic form of Randles model for low frequencies is of a resistor in series with a Warburg element.

More recently, fractional derivatives were used in [13] and [14], but in a mathematical approach rather than through an equivalent circuit. Equivalent-circuit models incorporating fractional capacitors and Warburg elements have also appeared with varied success in [15]–[18].

This manuscript rests on certain key observations made in [19]. The impedance of a battery must be examined (and

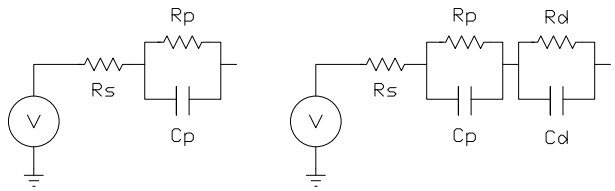

FIGURE 1. Thévenin-style first- and second-order RC battery models.

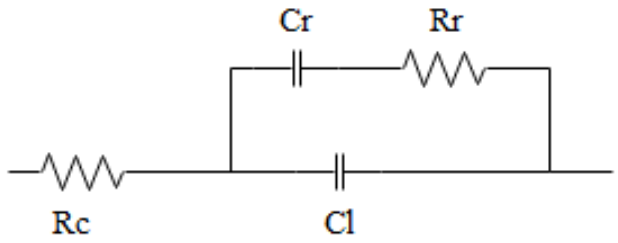

FIGURE 2. Randles' equivalent-circuit model for rapid electrode reactions reproduced from [11].

modelled) across the whole frequency range of signals to which it is subjected; for a typical battery application with daily or less frequent recharging, this will run from a period of at least a day and quite possibly longer, to less than 1 second. This corresponds to a frequency span commencing no higher than 10μHz. Few authors venture below 1mHz for practical reasons, and some instrument setups give inaccurate impedance results in the case of fractional systems at low frequencies.

Drawing on the impedance results, a ''R-CPE'' model was presented in [19] for a Lithium-ion battery which follows Randles' model for lower frequencies, following the exception of a CPE angle which is now approximately 76 degrees. Although the model does a reasonable job of predicting the battery impedance, it is not perfect, and no attempt was made to investigate recovery transients and voltage hysteresis. Recent work described in [20] has shown that critical decay tails observed on neural implant electrodes are only correctly reproduced in simulation when the physically distributed nature of the electrodes is accounted for by ''splitting'' the CPE that represents the interface in the equivalent-circuit model. The splitting accounts for the distributed nature of the structure; the battery has energy stored in chemical species whose distance from the conducting plates varies. The split-CPE model is shown in figure 3, reproduced from [19]. The whole idea of an equivalent-circuit model is that you can relate voltage and current as functions of time, and simultaneously know about stored charge and energy. The new model perfectly fits the measured data in frequency domain as can be seen in figure 4. This manuscript now addresses the question of whether the split-CPE impedance model of [19] can predict working current, voltage, charge and energy.

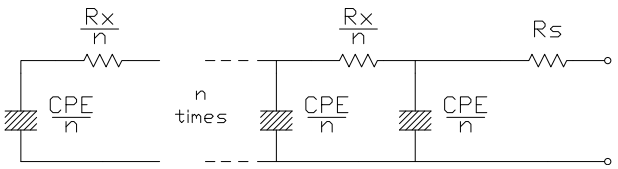

FIGURE 3. Equivalent circuit model with n-way split CPE and series resistance. The model requires four parameters, the order α and value C_F of the CPE, the series Resistance R_S and the splitting Resistance R_X, provided n is "sufficiently large".

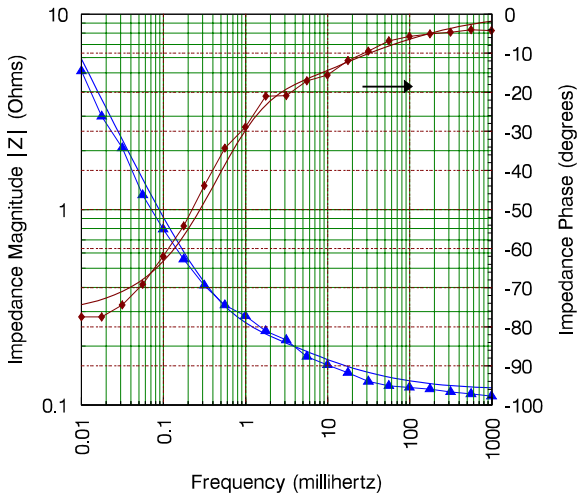

FIGURE 4. Impedance magnitude (left vertical axis, blue traces) and phase (right axis) of a 14500 Lithium-ion battery for frequencies corresponding to periods from 1 second to 1 day. Measured data (symbols) are compared with simulations using the split R-CPE model from [19]. The split-CPE equivalent circuit is reproduced in figure 3.

II. INTRODUCTION TO FRACTIONAL CALCULUS

Many scientific and engineering communities remain unaware of fractional calculus. The most common reason for that is the lack of practical application; fractional calculus is often considered as a conceptual area that is of interest only to mathematicians. However, applications of fractional calculus have emerged in the areas of physics, biology and engineering [21]–[23]. Fractional calculus can provide simpler and more faithful models of physical systems that depend upon diffusion or that possess fractal properties. Such a model tends to provide ''more entropy compared to its integer order counterpart with same number of parameters'' [24], which is to say that it requires fewer parameters.

Fractional calculus was first defined by Liouville, Riemann and Grunwald in 1834, 1847 and 1867, respectively [25]. The Riemann-Liouville fractional-order derivative, preferred in engineering for causality reasons, is of the form:

$$\frac{d^{\alpha}v(t)}{dt^{\alpha}} = \frac{1}{\Gamma(1-\alpha)}\frac{d}{dt}\int_0^t (t-\tau)^{-\alpha}v(\tau)d\tau \qquad (1)$$

where Γ is the well-known Gamma function and $0 < \alpha < 1$ is an arbitrary real value called the order. In the same way that the Gamma function provides a real interpolation between the values of the integer factorial function, this definition

provides a continuous transformation that happens to yield the same result as conventional, integer-order differentiation for integer arguments. This work lay unused for a long time.

The lack of ''any acceptable geometric and physical interpretation'' of fractional-order calculus has been lamented before [27]. There have been attempts to provide geometrical and physical interpretations of fractional operators, see for example [26], [27]. In [26] the author claims to develop 'an understandable geometric interpretation' using a Cantor's fractal set. This may explain the discrete nature of the impulse response function of a fractional integral. Later, a fascinating physical interpretation of Riemann-Liouville and Caputo fractional-order derivatives in relation to the cosmic time and the individual time was proposed in [27]. We contend that this 'understanding' is not helpful in circuit terms. It may help a mathematician grasp the idea, but it gives no circuit insight. We thus need to rely upon a simple formulation that fortunately results for a fractional capacitor in the Laplace domain.

Considering a fractional capacitor to be an element whose branch current is a fractional derivative of the branch potential expressed as a function of time, applying the Laplace transform to (1) with zero initial conditions produces a fractional-order function which portrays the current-voltage relationship of fractional capacitors:

$$I(s) = Cs^{\alpha}V(s) \tag{2}$$

Re-arranging the above equation gives the impedance of a fractional capacitor (CPE) in a form more familiar to circuit theorists:

$$Z(s) = \frac{V(s)}{I(s)} = \frac{1}{C_F s^{\alpha}} \tag{3}$$

where C is the ''capacitance'' of the fractional capacitor and α ranges between 0 and 1. The expression in (3) is perhaps the most compact and easily grasped representation of a CPE; it resembles a capacitor, but the slope of the impedance magnitude in a Bode plot will not quite be right; it will be $-\alpha$ instead of -1. Referring back to figure 4, it is straightforward to observe that at the very lowest frequencies a capacitor-like impedance characteristic appears. One then observes that the slope of the straight part is more like -0.85 than -1, implying that the ''capacitor'' is fractional.

III. CONSTRUCTING A CPE IN SPICE

As CPE rely on a fractional derivative, they are not routinely available as branch elements in compact simulators. Nevertheless, it is possible to generate a compact SPICE subcircuit that approximates the impedance of a CPE with arbitrary accuracy. The theory leading to the approximation is attributed to Morrison [28]. The data from the battery impedance in figure 4 permits the magnitude and angle of the CPE to be determined and a SPICE subcircuit generated as described in [29], with corrections from [30]. Two parameters are required to specify a CPE, corresponding to C_F and α from equation 3. For the Morrison formulation, these are a slope parameter, m, and a magnitude parameter found from a measurement of CPE admittance, Y_θ, at some arbitrary frequency, ω_0. Here the slope parameter m is found by observing that the CPE phase settles to 77.5 degrees or 1.35 radians around 10–20μHz, giving

$$m = \frac{\pi}{2\theta_{CPE}} = 1.161 \tag{4}$$

The CPE impedance is found from the measured impedance of the cell in the straight-line region at the low-frequency extreme. This gives values of 1.188Ω at 55.7μHz, yielding

$$Y_\theta = 0.842 \tag{5}$$

for $\omega_0 = 55.7 \times 10^{-6}$. An accuracy parameter of $k = 1.3$ is found to be more than adequate by trial and error.

IV. PREDICTING TRANSIENT RECOVERY

In this section, we will show that our proposed impedance network predicts more precisely the transient recovery of a battery. The measured tail of a single 800mAh, 14500 lithium battery is compared with various simulated tails. The test sequence consists of subjecting the cell to an isolated current pulse of 60 seconds, and the overall response is reproduced in the inset within the figure. The measurements were made with an Agilent E5270 Precision IV Analyzer and an Agilent 34401A DMM. All measurements were made with the battery held at a constant environmental temperature of 25 Celsius using a Contherm Polar 1000. Figure 5 shows the measured recovery transient of the same battery whose impedance appears in figure 4.

If we assume that for sufficiently low frequencies, the battery impedance is dominated by a CPE we can write

$$I(t) = C_F \frac{d^{\alpha}V(t)}{dt^{\alpha}} \tag{6}$$

or in the Laplace domain

$$Z_{batt} \approx Z_{CPE} = \frac{1}{C_F s^{\alpha}} = \frac{1}{C_F} s^{-\alpha} \tag{7}$$

The battery voltage recovery tail resulting from a square current pulse of period T and amplitude I_0 can be estimated by considering the current pulse to be the sum of two equal-sized step functions u, so that

$$I(t) = I_0 u(t) - I_0 u(t - T) \tag{8}$$

whose Laplace transform is

$$I(s) = \frac{I_0}{s} - \frac{I_0}{s} e^{-Ts} \tag{9}$$

thence

$$V(s) = \frac{I_0}{C_F} s^{-(1+\alpha)} - \frac{I_0}{C_F} s^{-(1+\alpha)} e^{-Ts} \tag{10}$$

Noting that the inverse Laplace transform

$$\mathcal{L}^{-1}(s^{-k}) = \frac{t^{k-1}}{\Gamma(k)} \tag{11}$$

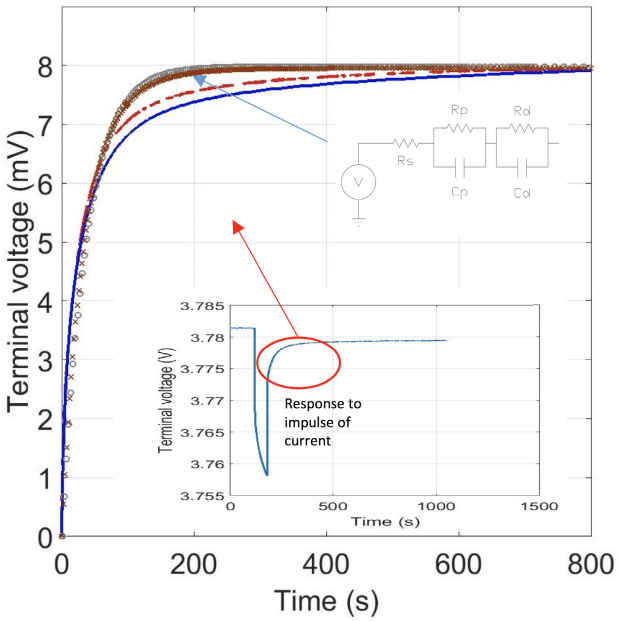

FIGURE 5. The response tails of a split-CPE model (solid line), one RC (∘) and two RC (×) network models shown with measured data (dashed red line). Inset shows the full voltage response of the battery to a 60-second, 100mA pulse of load current and indicates the region where the "tail" appears.

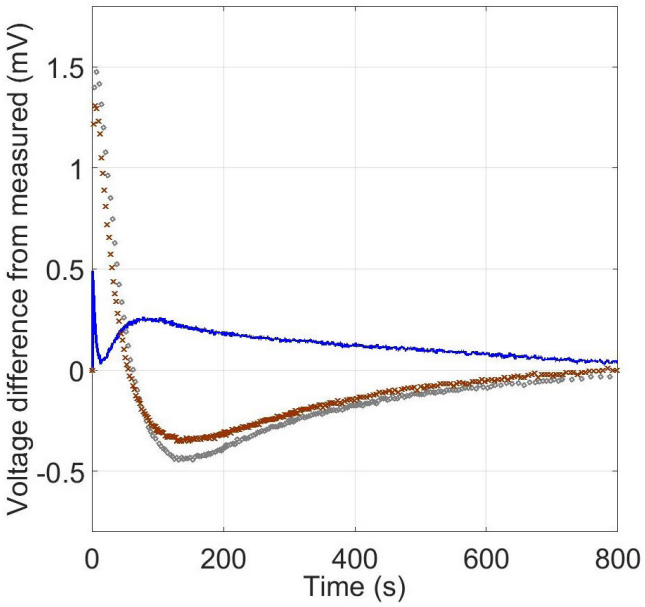

FIGURE 6. Voltage difference between measured data and single-RC (∘), two-RC (×), and split-CPE (solid blue line) predictions presented in figure 5.

putting $k = 1 + \alpha$, some algebra leads to an expression for the pulse voltage tail

$$v_{\mathrm{Eq}}(t) = \frac{I_0}{C_F \Gamma(1+\alpha)} \left[t^{\alpha} - (t+T)^{\alpha} \right] \tag{12}$$

It is worth emphasizing that the voltage tail that follows a current pulse stimulus applied to a CPE, as given by (12), decays unusually slowly. It is remarkably different from a first or second-order conventional, exponential decay curve.

Returning to the recovery tail in figure 5, note that the first- and second-order Thévenin-style RC circuit models cannot fit the measured data, even when allowed to optimise freely, but the solid blue line predicted from the fitted split-CPE model comes much closer and has the correct curvature. The value of the splitting parameter R_X has been numerically optimised to obtain the best fit. In this case, we chose a value $R_X = 29\mathrm{m}\Omega$. A 10-way split, that is $n = 10$, was chosen, again by trial and error observing that larger values conferred little advantage. Figure 6 plots the difference between each of the three predictions and the measured data. The new split-CPE model can predict the measured data with less than 3% error whereas, the percentage error of a single-RC and two-RC models is around 7% and 5.6% respectively. It is clear that the split-CPE model achieves considerably better an approximation with no more complexity than a first-order RC model.

V. CHARGE/VOLTAGE CHARACTERISTIC

The problem with measuring a battery charge-voltage characteristic is that this is a dynamic measurement. When charging a cell, the terminal voltage will be higher than would be the steady-state voltage perceived if the battery were completely at rest. A common response to this is to measure the voltage of the cell under constant-current charging and then to discharge at the same constant current, relying on the impedance characteristic to be linear and symmetrical. The steady-state characteristic is then approximated by averaging the two data sets point by point to yield the average characteristic. A very similar, but more informative, variant is used here. The battery was charged at 100mA for 60 seconds using the E5270. Then the voltage was measured, the current set to zero for 60 seconds, and the voltage measured again. Reference to the measured data trace in figure 5 will indicate that 60 seconds should allow the battery to settle only some of the way towards its asymptotic value, owing to the exceptionally slow decay of the fractional tail. This cycle was repeated until the battery reached full charge. At the end of a sweep the battery was rested for 12 hours to allow equalisation. Next the current was set for discharge, and the same minute-off, minute-on scenario used to discharge the battery. Figure 7 shows four traces, being the charge and discharge characteristics during current flow ("closed circuit") and after the 60-second rest ("open circuit"). The steady-state characteristic is calculated by averaging the traces point by point. This is shown in figure 8.

Battery models are most usually sought to relate terminal voltage to SoC. The reader should note that the split-CPE model has been fitted to data obtained only from impedance and short-term dynamic response of the subject cell. The question arises as to how it will predict the charge-voltage characteristic of the cell. The simulated voltage trace in figure 8 was produced using SPICE with suitably-selected

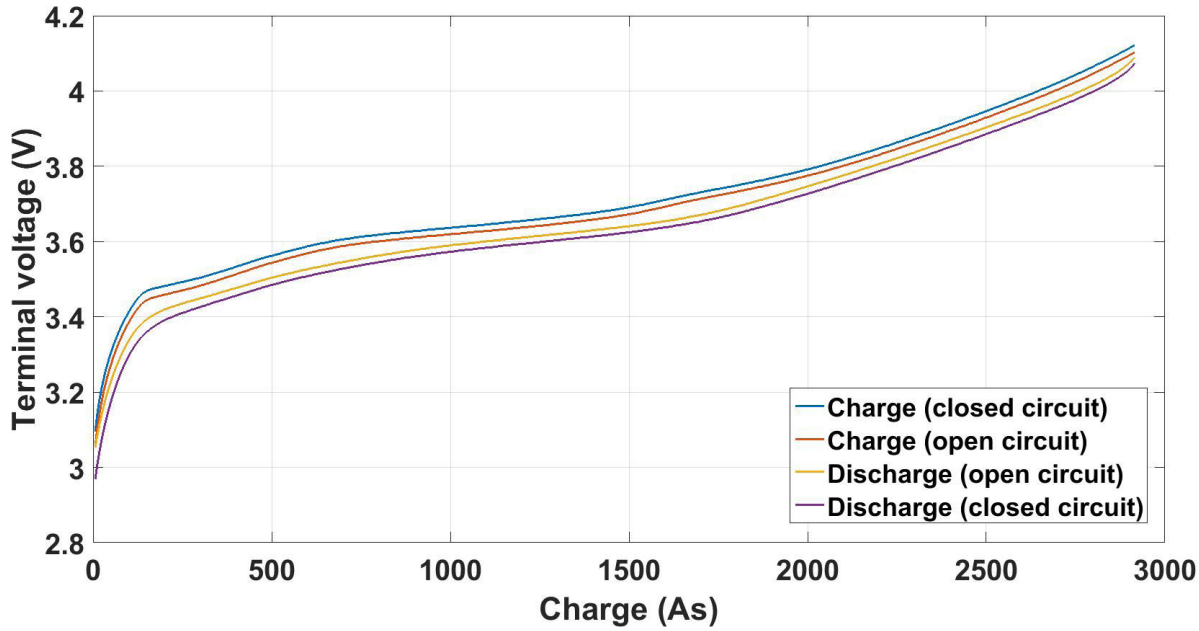

FIGURE 7. Voltage-charge characteristic of the 14500 Lithium-ion battery. Open-circuit trace voltages are measured after a 60-second rest, closed-circuit ones with current flowing.

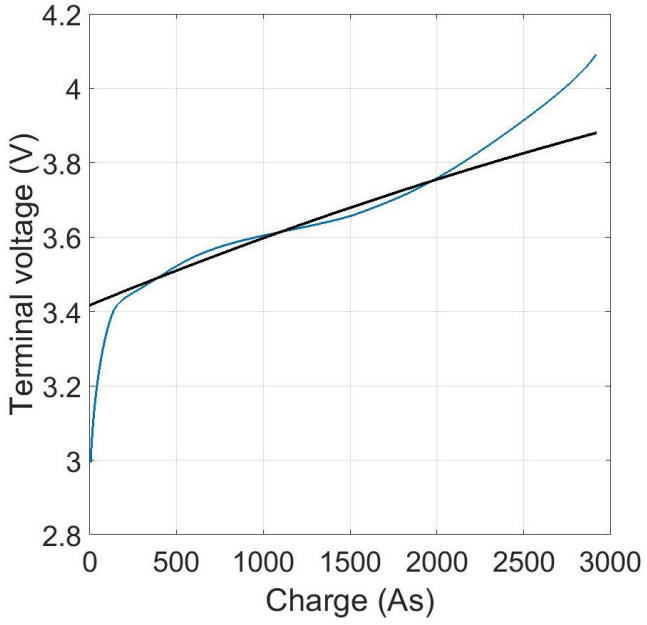

FIGURE 8. The estimated steady-state cell voltage obtained by averaging the traces from figure 7 (curved trace) is plotted against the voltage predicted by the split-CPE model (straight line).

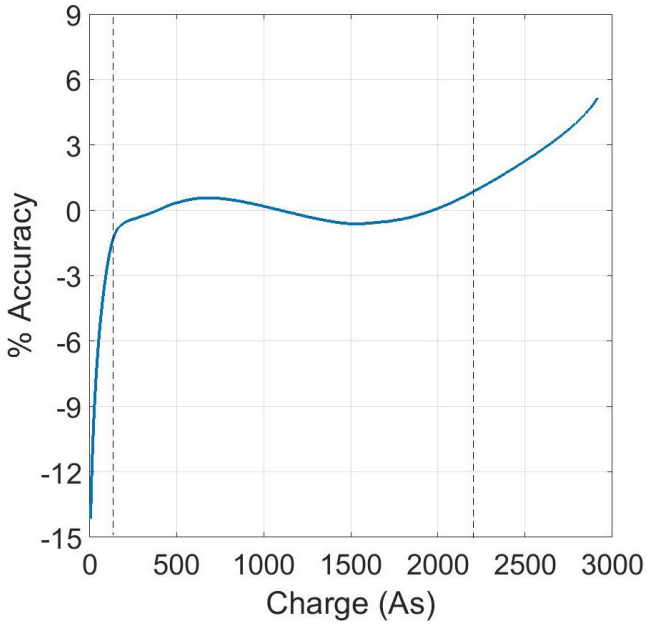

FIGURE 9. Plot of the percentage error between the measured and predicted traces shown in figure 8. The dotted lines mark the region within which error is less than 1%.

initial conditions. The fit is extraordinary as shown in figure 9, considering that the model was fitted without reference to the data of figure 7 except to obtain the dc offset.

VI. OTHER CHEMISTRIES

The model is not restricted to Lithium chemistry. In this section the split-CPE model is fitted to a Nickel-Metal Hydride cell type 55123 with 1850mAh nominal capacity. The present linear model is of limited use in the case of chemistries that permit float-current charging. This is because the model does not (yet) consider the ''charge-dumping'' process that effectively wastes energy as the energy-storing reactants deplete approaching the full-charge condition. We hope to extend the model to include the nonlinear ''end effects''

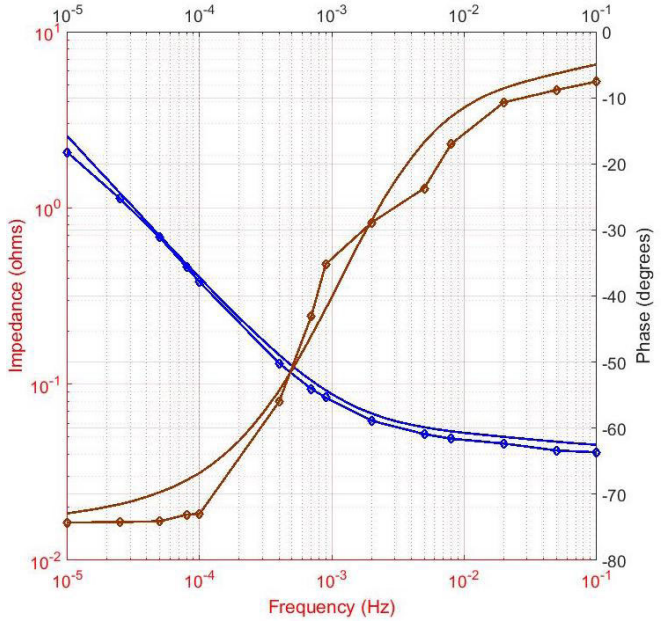

FIGURE 10. Measured (symbols) and simulated magnitude and phase of cell impedance for a single 55123 NiMH cell. Phase is the sigmoid curve, magnitude the hockey-stick curve.

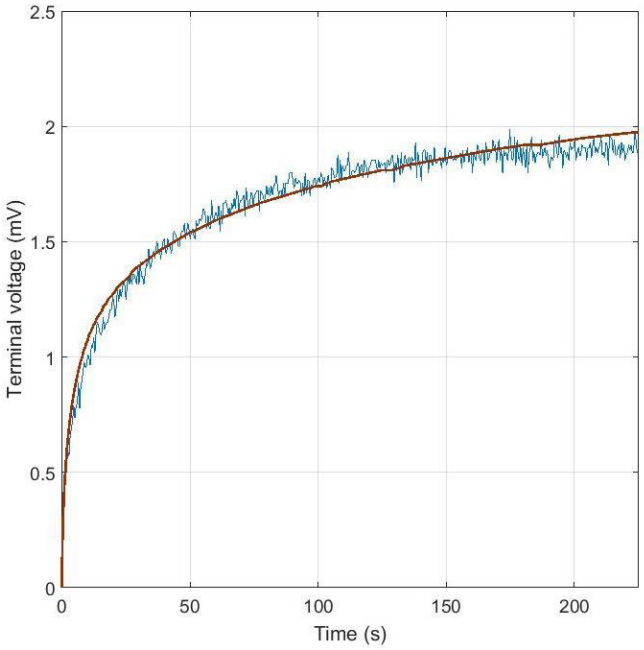

FIGURE 11. Measured (noisy trace) and simulated normalised recovery curve of the single 55123 NiMH cell following a 100mA current pulse of 90 seconds duration. The minimum terminal voltage is subtracted to leave only the change in terminal voltage after cessation of the pulse, i.e., the plot shows only the slow recovery.

that shape the flat and full-charge ends of the characteristics. In the meantime, we seek to demonstrate that the idea of a passive model is not limited to the Lithium system.

The input data is as usual

1) a measurement of battery impedance versus frequency from which R_S and CPE parameters are obtained (figure 10);
2) the pulse response voltage recovery curve (figure 11); and
3) the characteristic of terminal voltage against charge measured in some particular fashion (figure 12).

The model is optimised to match the measured data, starting with values obtained from the impedance-frequency data. Simulated data obtained with SPICE using the method outlined in [29] with corrections from [30] and the fitted model parameters appear in figures 10, 11 and 12. The fit is sufficient for practical applications.

VII. DISCUSSION

A. BATTERY OPERATING RANGE

Battery manufacturers choose charge and discharge voltage points that are as far apart as possible in order to have the largest possible specified capacity. Thereafter the recommendation is to stay within a range such as 20–90% SoC for maximum life. For example, a Prius hybrid tries to keep its battery between 40% and 80% SoC to give long battery life [31]. The model proposed here is entirely linear; it makes no attempt to model the nonlinear subtleties of the voltage characteristic of figure 8. Nevertheless, reference to figure 9 shows that even without taking the nonlinearity of the voltage-charge characteristic into account, the model is accurate to a few

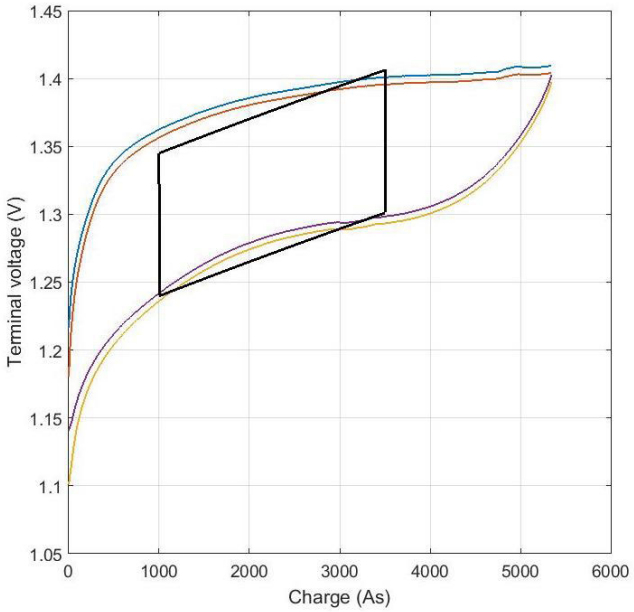

FIGURE 12. Measured (curves) and simulated (box) characteristic of a single 55123 NiMH cell charged and discharged in 60-second bursts spaced 120 seconds apart. Inner and outer curve pairs are the voltage at the ends of the 60-second periods of loading and the 120 seconds of rest at zero current, respectively.

percent from about 10% SoC to 90% SoC. The fuel gauge of a petrol car provides a measure that is only accurate to about 5%, and while portable devices read out battery status to 1% most users notice that they are not that accurate and prone to

sudden large corrections. The authors submit that the linear model may already be sufficient for many practical uses.

B. NONLINEAR EXTENSION

Nevertheless, extension to predicting the subtle nonlinear curves visible in an actual battery characteristic such as figure 7 is expected to be possible. The approach favoured by the authors involves modelling the reduction of chemical species at the electrode interface by way of charge-dependent capacitances in the CPE subcircuit through the magnitude parameter of the CPE, Y_θ [29]. This approach is easy to incorporate in nodal simulators, and has a strong physical basis in the modelling of species concentrations at an electrode interface through the general form of the Butler-Volmer equation [32]. This extension is considered to be beyond the scope of this manuscript, but is the logical next step.

C. EFFICIENCY

The model contains no sources, and can thus neither add nor subtract energy in an arbitrary fashion—just as in the case of a rechargeable battery. We expect the lossy CPEs will model the energy difference between that supplied in charging and that obtained in discharge. Thus a collateral benefit of this compact model is expected to be the ability to straightforwardly calculate the efficiency of energy storage for any scenario, i.e., it will predict how much of the energy invested in charging is returned in the discharge phase for an arbitrary dynamic load. An investigation of the model's accuracy in predicting the efficiency of energy return is considered out of the scope of this manuscript, but is being addressed separately.

VIII. CONCLUSION

This manuscript extends Randles' model to low frequencies to characterise behaviour of a Lithium-ion cell. The modified model is now simple and contains only a series resistor and a CPE with an angle that varies with cell chemistry. It also does not require any voltage or current sources. Although, the work reported here is carried out with single Lithium-ion and NiMH cells but it is applicable to all cell types. It is clear that such a model is superior to existing, complex models that do not seem to add anything for their extra parameters.

To further investigate the model's ability to predict recovery or hysteresis which most authors do not check, the CPE in the model is arbitrarily divided into smaller CPEs to account for the distributed nature of the electrodes. Now with only 4 parameters, it can accurately estimate the battery's runtime transient characteristics and the variation of voltage with state-of-charge in the ''linear'' range within a few percents. The new split-CPE model also fits the impedance-frequency data better.

Such a model is expected to exhibit very powerful properties. The possibility exists to extend the model in the future into the end regions where the voltage becomes a strongly non-linear function of available charge. The absence of a voltage or current source means that the model can be used to calculate the efficiency of energy stored in a cell that has not been proposed previously.

REFERENCES

[1] J. Yang, B. Xia, Y. Shang, W. Huang, and C. C. Mi, ''Adaptive State-of-Charge estimation based on a split battery model for electric vehicle applications,'' *IEEE Trans. Veh. Technol.*, vol. 66, no. 12, pp. 10889–10898, Dec. 2017.

[2] G. Nobile, M. Cacciato, G. Scarcella, and G. Scelba, ''Performance assessment of equivalent-circuit models for electrochemical energy storage systems,'' in *Proc. 43rd Annu. Conf. IEEE Ind. Electron. Soc.*, Oct. 2017. pp2799–2806

[3] D. Vinh Do, C. Forgez, K. El Kadri Benkara, and G. Friedrich, ''Impedance observer for a li-ion battery using Kalman filter,'' *IEEE Trans. Veh. Technol.*, vol. 58, no. 8, pp. 3930–3937, Oct. 2009.

[4] H. Chaoui, N. Golbon, I. Hmouz, R. Souissi, and S. Tahar, ''Lyapunov-based adaptive state of charge and state of health estimation for lithium-ion batteries,'' *IEEE Trans. Ind. Electron.*, vol. 62, no. 3, pp. 1610–1618, Mar. 2015.

[5] A. Guha and A. Patra, ''Online estimation of the electrochemical impedance spectrum and remaining useful life of lithium-ion batteries,'' *IEEE Trans. Instrum. Meas.*, vol. 67, no. 8, pp. 1836–1849, Aug. 2018.

[6] C. Zhang, K. Li, S. Mcloone, and Z. Yang, ''Battery modelling methods for electric vehicles—A review,'' in *Proc. Eur. Control Conf. (ECC)*, Strasbourg, France, Jun. 2014, pp. 2673–2678.

[7] K. Liu, X. Hu, Z. Yang, Y. Xie, and S. Feng, ''Lithium-ion battery charging management considering economic costs of electrical energy loss and battery degradation,'' *Energy Convers. Manage.*, vol. 195, pp. 167–179, Sep. 2019.

[8] K. Liu, C. Zou, K. Li, and T. Wik, ''Charging pattern optimization for lithium-ion batteries with an electrothermal-aging model,'' *IEEE Trans. Ind. Informat.*, vol. 14, no. 12, pp. 5463–5474, Dec. 2018.

[9] R. Hasan and J. Scott, ''Measurement for fractional characteristic of lithium batteries,'' in *Proc. IEEE Int. Instrum. Meas. Technol. Conf. (IMTC)*, Auckland, New Zealand, May 2019, pp. 1–5.

[10] R. Hasan and J. Scott, ''Application of Swingler's method for analysis of multicomponent exponentials with special attention to non-equispaced data,'' in *Proc. IEEE 12th Int. Colloq. Signal Process. Appl. (CSPA)*, Kuala Lumpur, Malaysia, Mar. 2016, pp. 12–15.

[11] J. E. B. Randles, ''Kinetics of rapid electrode reactions,'' *Discuss. Faraday Soc.*, vol. 1, p. 11, Oct. 1947.

[12] S. Grimnes and O. Martinsen, *Bioimpedance and Bioelectricity Basics*. New York, NY, USA: Academic, 2008.

[13] M. Cugnet, J. Sabatier, S. Laruelle, S. Grugeon, B. Sahut, A. Oustaloup, and J.-M. Tarascon, ''On Lead-Acid-Battery resistance and cranking-capability estimation,'' *IEEE Trans. Ind. Electron.*, vol. 57, no. 3, pp. 909–917, Mar. 2010.

[14] J. Sabatier, M. Merveillaut, J. M. Francisco, F. Guillemard, and D. Porcelatto, ''Fractional models for lithium-ion batteries,'' in *Proc. Eur. Control Conf. (ECC)*, Zurich, Switzerland, Jul. 2013, pp. 3458–3463.

[15] Y. Ma, X. Zhou, B. Li, and H. Chen, ''Fractional modeling and SOC estimation of lithium-ion battery,'' *IEEE/CAA J. Automatica Sinica*, vol. 3, no. 3, pp. 281–287, Jul. 2016.

[16] R. Hasan and J. Scott, ''Letter to the editor re 'Fractional modeling and SOC estimation of lithium-ion battery,'' *IEEE/CAA J. Automatica Sinica*, vol. 5, no. 2, p. 644, Mar. 2018.

[17] Q.-K. Wang, Y.-J. He, J.-N. Shen, X.-S. Hu, and Z.-F. Ma, ''State of charge-dependent polynomial equivalent circuit modeling for electrochemical impedance spectroscopy of lithium-ion batteries,'' *IEEE Trans. Power Electron.*, vol. 33, no. 10, pp. 8449–8460, Oct. 2018.

[18] R. Hasan and J. Scott, ''Comments on 'state of charge-dependent polynomial equivalent circuit modeling for electrochemical impedance spectroscopy of lithium-ion batteries,''' *IEEE Trans. Power Electron.*, vol. 35, no. 4, p. 4448, Apr. 2019.

[19] J. B. Scott and R. Hasan, ''New results for battery impedance at very low frequencies,'' *IEEE Access*, vol. 7, pp106925–106930, 2019, doi: 10.1109/ACCESS.2019.2932094.

[20] P. Single, J. Scott, and ''Cause of pulse Artefacts inherent to the electrodes of neuromodulation implants,'' *IEEE Trans. Neural Syst. Rehabil. Eng.*, vol. 26, no. 10, pp. 2078–2083, Oct. 2018.

[21] R. J. Hilfer, *Applications of Fractional Calculus in Physics*. Singapore: World Scientific, 2000.

[22] R. L. Magin, "Fractional calculus models of complex dynamics in biological tissues," *Comput. Math. Appl.*, vol. 59, no. 5, pp. 1586–1593, Mar. 2010.
[23] C. M. Ionescu, J. A. T. Machado, and R. De Keyser, "Modeling of the lung impedance using a fractional-order ladder network with constant phase elements," *IEEE Trans. Biomed. Circuits Syst.*, vol. 5, no. 1, pp. 83–89, Feb. 2011.
[24] A. Adhikary, P. Sen, S. Sen, and K. Biswas, "Design and performance study of dynamic fractors in any of the four quadrants," *Circuits, Syst., Signal Process.*, vol. 35, no. 6, pp. 1909–1932, Jun. 2016.
[25] I. Podlubny, *Fractional Differential Equations*. New York, NY, USA: Academic, 1999.
[26] M. Moshrefi-Torbati and J. K. Hammond, "Physical and geometrical interpretation of fractional operators," *J. Franklin Inst.*, vol. 335, no. 6, pp. 1077–1086, Aug. 1998.
[27] I. Podlubny, "Geometric and physical interpretation of fractional integration and fractional differentiation," *Fract. Calc. Appl. Anal.*, vol. 5, no. 4, pp. 367–386, 2002.
[28] R. Morrison, "RC constant-argument driving-point admittances," *IRE Trans. Circuit Theory*, vol. 6, no. 3, pp. 310–317, Sep. 1959.
[29] J. Scott and P. Single, "Compact nonlinear model of an implantable electrode array for spinal cord stimulation (SCS)," *IEEE Trans. Biomed. Circuits Syst.*, vol. 8, no. 3, pp. 382–390, Jun. 2014.
[30] S. Seshadri and J. Scott, "Correction to 'compact nonlinear model of an implantable electrode array for spinal cord stimulation' [Jun 14 382-390]," *IEEE Trans. Biomed. Circuits Syst.*, vol. 12, no. 4, pp. 963–964, Aug. 2018.
[31] P. Leijen, D. A. Steyn-Ross, and N. Kularatna, "Use of effective capacitance variation as a measure of State-of-Health in a series-connected automotive battery pack," *IEEE Trans. Veh. Technol.*, vol. 67, no. 3, pp. 1961–1968, Mar. 2018.
[32] D. R. Merrill, M. Bikson, and J. G. R. Jefferys, "Electrical stimulation of excitable tissue: Design of efficacious and safe protocols," *J. Neurosci. Methods*, vol. 141, no. 2, pp. 171–198, Feb. 2005.

RAHAT HASAN (Student Member, IEEE) received the B.Eng. degree (Hons.) in electrical and electronics engineering from London South Bank University, U.K. He is currently pursuing the Ph.D. degree with The University of Waikato, New Zealand. From 2011 to 2012, he worked at Visteon Engineering Services Ltd., U.K., as a Software Validation Engineer. He is the CEO and Co-Founder of RH Innovation Ltd., where he is working on agritech projects.

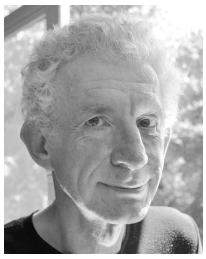

JONATHAN SCOTT (Senior Member, IEEE) received five degrees. From 1998 to 2006, he was with the Hewlett-Packard and Agilent Technologies Microwave Technology Center, Santa Rosa, CA, USA, where he was responsible for advanced measurement systems operating from dc to millimeter-wave. From 1997 to 1998, he was a Chief Engineer at RF Technology, Sydney. He was with the Department of Electrical Engineering, The University of Sydney, prior to 1997. He is the Foundation Professor of electronics engineering with The University of Waikato, New Zealand. He has authored over 150 refereed publications, several book chapters, and a textbook, and he holds a dozen patents, several covering active products. His research interests are in the characterization and modeling of implantable electrodes, semiconductor devices, batteries, and acoustic systems. His educational interests include threshold concepts and their applications, particularly across engineering disciplines.

Chapter 8

Conclusion

Obtaining accurate battery models is still an unsolved problem that hinders the correct estimation of state of charge and state of health of rechargeable cells. This explains why there are hundreds of published battery modelling papers in the IEEE stable alone. In search of a compact circuit model, many researchers begin by measuring the impedance of the cell spanning the frequency range of interest. Most of these models are Thevenin-style containing one or two RC networks. The results in chapter 3 show that the recovery curve of the cell terminal voltage obtained when subjected to a step-change in current is not exponential at all. Thus all first and second-order Thevenin RC models are inappropriate for modelling the transient runtime characteristics of batteries.

Some authors prefer a fractional approach when modelling rechargeable cells. Almost all these equivalent circuit fractional models are based on frequency response measurement which extend to only 1 mHz and require up to tens of parameters to successfully estimate the measured impedance. Chapter 4 contains two examples where the authors used unjustified parameters to obtain a good fit [95] and made no mention of the sensitivity of the fit to the parameters in the model.

The most likely reason why many authors limit the frequency range to 1 mHz is because of the lack of instruments that can reliably measure impedance at low frequencies. Although in most manuscripts the instrument used to

measure impedance is not stated, there exists an impedance analyser, Solartron 1260 [29] that claims to measure impedance at frequencies as low as 10 μHz.

Chapter 5 shows that Solartron 1260 is prone to incorrect measurements in the case of the non-linear behaviour of the device under test. The possible reasons for its low performance are its incapability to account for drift in the voltage waveform and distortion of the signal at low frequencies. Two robust methods of measuring impedance at low frequencies were proposed in that chapter. Both methods require a novel algorithm to yield robust, reliable data.

The main contribution of this work to the battery modelling community is that it shows the importance of venturing in the frequency domain at frequencies derived from expected time scales of operation and well beyond those where a system is expected to operate. For a typical battery application, recharging happens daily or perhaps longer which corresponds to a frequency of approximately 11.6 μHz or lower. At these frequencies, the impedance of a cell is reminiscent of a CPE whose angle varies with cell chemistry. This characteristic of the battery was not previously taken into account.

In chapter 6, a mathematical model was derived from the equivalent impedance equation in the frequency domain. In the equation, the term representing the series resistance of a cell was neglected because only the voltage across the CPE contributed to the charge-voltage function of a cell. The proposed mathematical model predicts the linear region of the charge-voltage characteristic of a cell with an accuracy of 0.5% with only 3 parameters.

Chapter 7 presents a new, compact, equivalent circuit model for rechargeable cells that does not contain a voltage or current source. The new fractional model was tested against measured impedance, charge-voltage and transient recovery data from lithium-ion and nickel-metal hydride cells. Few models exist that can operate in all these three domains with reasonable accuracy. To simulate the transient recovery tail, the CPE in the proposed model is arbitrarily split into n-way to account for the distributed nature of the electrodes

within the cell. With only 4 parameters, the model can now estimate the transient runtime curve with less than 3% error.

Since most battery manufacturers recommend to stay within a range of 20-80% to maximise battery life, the model was tested against the linear region from about 10-90% in the charge-voltage curve. The estimation has improved significantly where the error is now within a few percent. This accuracy is adequate for most practical use because the current fuel gauge of a car is only accurate to about 5% [18]. The model also fits the impedance-frequency data better than any Thevenin-style RC model.

It was then realised that the proposed model can also be used to indicate the state of health of a cell under load. A patent was filed by WaikatoLink Limited for battery performance and quality assessment method and apparatus that uses the parameters of a sequence of CPEs in the split-CPE model to estimate the state of health performance and identify any trends in the state of health of the battery.

8.1 Potential for the Future

The findings portrayed in this study paved the way to other masters and PhD level research work.

8.1.1 Nonlinear Extension

Since the proposed model is only limited to the linear region of the charge-voltage curve, the next logical step is to extend it to the non-linear region. The approach is similar to that of [13] where memristor is used to model the reduction of species concentration as the net charge transferred increases. This behaviour can be best described with the general form of the Butler-Volmer equation, also known as the current-overpotential equation [100].

8.1.2 Efficiency

The uniqueness of the model proposed in this thesis is that it does not contain any voltage or current source. This means that energy cannot be added or subtracted arbitrarily and the model can predict the energy difference between the charging and discharging period of a battery from the lossy CPE. Such information can then be used to calculate the efficiency of energy storage in a cell that has not been proposed in the past. Professor Jonathan Scott at The University of Waikato is currently seeking a PhD candidate to develop a software module that can calculate the remaining available energy from current and voltage data [101].

8.1.3 State of Health Prediction

It is postulated that the CPE in the model can be used to characterise the state of health (SoH) of a battery. As a battery gets older, the capacity of the battery decreases. We expect the capacitance and the order of fractionality of the CPE to mirror this loss in capacity. This information can be employed to predict how much life is left in a battery. Vance Farrow, a ME candidate at The University of Waikato, is currently exploring this line of investigation [102].

8.1.4 In-situ Impedance Measurement of Rechargeable Batteries

It takes a long time to measure the impedance of a system at low frequencies. For example, a sweep from 1 Hz-10 μHz takes roughly 6 days to complete. This makes the impedance measurement slow and prone to errors. Christopher Dunn is expected to commence his PhD after this thesis is submitted. [103].

8.1.5 Temperature Model

Since external temperature affects both the complex impedance and battery capacity, results from one of our recent measurements show that the capacity of

the cell varies with temperature as well as the age of the cell. Such observation may be very useful in the future.

Appendix A

Co-Authorship Forms

THE UNIVERSITY OF WAIKATO
Te Whare Wānanga o Waikato

Postgraduate Studies Office
Student and Academic Services Division
Wahanga Ratonga Matauranga Akonga
The University of Waikato
Private Bag 3105
Hamilton 3240, New Zealand
Phone +64 7 838 4439
Website: http://www.waikato.ac.nz/sasd/postgraduate/

Co-Authorship Form

This form is to accompany the submission of any PhD that contains research reported in published or unpublished co-authored work. **Please include one copy of this form for each co-authored work**. Completed forms should be included in your appendices for all the copies of your thesis submitted for examination and library deposit (including digital deposit).

Please indicate the chapter/section/pages of this thesis that are extracted from a co-authored work and give the title and publication details or details of submission of the co-authored work.

Chapter 3, Tutorial on Swingler's Method and Verifying the Fractional Nature of a Battery, pp45-48.

"Application of Swingler's Method for Analysis of Multicomponent Exponentials with Special Attention to Non-equispaced Data", IEEE 12th International Colloquium on Signal Processing & its Applications, 4-6 March, 2016, Malaysia.

Nature of contribution by PhD candidate	Methodology; Writing - Review & Editing; Software; Validation; Formal analysis; Investigation; Writing - Original Draft; Visualization.
Extent of contribution by PhD candidate (%)	60%

CO-AUTHORS

Name	Nature of Contribution
Jonathan Scott	Writing - Original Draft; Writing - Review & Editing; Methodology; Software; Conceptualization; Validation; Formal analysis; Resources; Visualization; Supervision; Project administration.

Certification by Co-Authors

The undersigned hereby certify that:

- the above statement correctly reflects the nature and extent of the PhD candidate's contribution to this work, and the nature of the contribution of each of the co-authors; and

Name	Signature	Date
Jonathan Scott		16 Nov 2020

THE UNIVERSITY OF WAIKATO
Te Whare Wānanga o Waikato

Postgraduate Studies Office
Student and Academic Services Division
Wahanga Ratonga Matauranga Akonga
The University of Waikato
Private Bag 3105
Hamilton 3240, New Zealand
Phone +64 7 838 4439
Website: http://www.waikato.ac.nz/sasd/postgraduate/

Co-Authorship Form

This form is to accompany the submission of any PhD that contains research reported in published or unpublished co-authored work. **Please include one copy of this form for each co-authored work**. Completed forms should be included in your appendices for all the copies of your thesis submitted for examination and library deposit (including digital deposit).

Please indicate the chapter/section/pages of this thesis that are extracted from a co-authored work and give the title and publication details or details of submission of the co-authored work.

Chapter 3, Tutorial on Swingler's Method and Verifying the Fractional Nature of a Battery, pp50-53.

"Fractional behaviour of rechargeable batteries", in Proceedings of the 2016 Electronics New Zealand Conference, 17-18 November, 2016, New Zealand.

Nature of contribution by PhD candidate	Methodology; Writing - Review & Editing; Software; Validation; Formal analysis; Investigation; Writing - Original Draft; Visualization.
Extent of contribution by PhD candidate (%)	70%

CO-AUTHORS

Name	Nature of Contribution
Jonathan Scott	Writing - Review & Editing; Conceptualisation; Supervision

Certification by Co-Authors

The undersigned hereby certify that:

- the above statement correctly reflects the nature and extent of the PhD candidate's contribution to this work, and the nature of the contribution of each of the co-authors; and

Name	Signature	Date
Jonathan Scott		16 Nov 2020

THE UNIVERSITY OF WAIKATO
Te Whare Wānanga o Waikato

Co-Authorship Form

Postgraduate Studies Office
Student and Academic Services Division
Wahanga Ratonga Matauranga Akonga
The University of Waikato
Private Bag 3105
Hamilton 3240, New Zealand
Phone +64 7 838 4439
Website: http://www.waikato.ac.nz/sasd/postgraduate/

This form is to accompany the submission of any PhD that contains research reported in published or unpublished co-authored work. **Please include one copy of this form for each co-authored work**. Completed forms should be included in your appendices for all the copies of your thesis submitted for examination and library deposit (including digital deposit).

Please indicate the chapter/section/pages of this thesis that are extracted from a co-authored work and give the title and publication details or details of submission of the co-authored work.

Chapter 4, Corrections of Existing Battery Models, pp56-56.

"Letter to the Editor Re 'Fractional Modeling and SOC Estimation of Lithium-ion Battery", IEEE Caa Journal of Automatica Sinica, 2018, 5(2), 644–644.

Nature of contribution by PhD candidate	Writing - Review & Editing; Validation; Formal analysis; Investigation; Writing - Original Draft; Visualization.
Extent of contribution by PhD candidate (%)	90%

CO-AUTHORS

Name	Nature of Contribution
Jonathan Scott	Writing - Review & Editing;

Certification by Co-Authors

The undersigned hereby certify that:

- the above statement correctly reflects the nature and extent of the PhD candidate's contribution to this work, and the nature of the contribution of each of the co-authors; and

Name	Signature	Date
Jonathan Scott		16 Nov 2020

THE UNIVERSITY OF WAIKATO
Te Whare Wānanga o Waikato

Postgraduate Studies Office
Student and Academic Services Division
Wahanga Ratonga Matauranga Akonga
The University of Waikato
Private Bag 3105
Hamilton 3240, New Zealand
Phone +64 7 838 4439
Website: http://www.waikato.ac.nz/sasd/postgraduate/

Co-Authorship Form

This form is to accompany the submission of any PhD that contains research reported in published or unpublished co-authored work. **Please include one copy of this form for each co-authored work**. Completed forms should be included in your appendices for all the copies of your thesis submitted for examination and library deposit (including digital deposit).

Please indicate the chapter/section/pages of this thesis that are extracted from a co-authored work and give the title and publication details or details of submission of the co-authored work.

Chapter 4, Corrections of Existing Battery Models, pp58-58.

"Comments on "State of Charge-Dependent Polynomial Equivalent Circuit Modeling for Electrochemical Impedance Spectroscopy of Lithium-Ion Batteries"", IEEE Transactions on Power Electronics, 2019, 1–1.

Nature of contribution by PhD candidate	Writing - Review & Editing; Validation; Formal analysis; Investigation; Writing - Original Draft; Visualization.
Extent of contribution by PhD candidate (%)	90%

CO-AUTHORS

Name	Nature of Contribution
Jonathan Scott	Writing - Review & Editing; Supervision

Certification by Co-Authors

The undersigned hereby certify that:

- the above statement correctly reflects the nature and extent of the PhD candidate's contribution to this work, and the nature of the contribution of each of the co-authors; and

Name	Signature	Date
Jonathan Scott		16 Nov 2020

THE UNIVERSITY OF WAIKATO
Te Whare Wānanga o Waikato

Postgraduate Studies Office
Student and Academic Services Division
Wahanga Ratonga Matauranga Akonga
The University of Waikato
Private Bag 3105
Hamilton 3240, New Zealand
Phone +64 7 838 4439
Website: http://www.waikato.ac.nz/sasd/postgraduate/

Co-Authorship Form

This form is to accompany the submission of any PhD that contains research reported in published or unpublished co-authored work. **Please include one copy of this form for each co-authored work**. Completed forms should be included in your appendices for all the copies of your thesis submitted for examination and library deposit (including digital deposit).

Please indicate the chapter/section/pages of this thesis that are extracted from a co-authored work and give the title and publication details or details of submission of the co-authored work.

Chapter 5, Improving On-Load and Off-Load Impedance Measurement of Batteries, pp62-67.

"New results for battery impedance at very low frequencies", IEEE Access, 2019, 7, 106924–106929.

Nature of contribution by PhD candidate	Methodology; Software; Writing - Review & Editing; Validation; Formal analysis; Investigation; Writing - Original Draft; Visualization.
Extent of contribution by PhD candidate (%)	50%

CO-AUTHORS

Name	Nature of Contribution
Jonathan Scott	Conceptualization; Writing - Original Draft; Visualization; Supervision; Methodology; Writing - Review & Editing.

Certification by Co-Authors

The undersigned hereby certify that:

- the above statement correctly reflects the nature and extent of the PhD candidate's contribution to this work, and the nature of the contribution of each of the co-authors; and

Name	Signature	Date
Jonathan Scott		16 Nov 2020

THE UNIVERSITY OF WAIKATO
Te Whare Wānanga o Waikato

Postgraduate Studies Office
Student and Academic Services Division
Wahanga Ratonga Matauranga Akonga
The University of Waikato
Private Bag 3105
Hamilton 3240, New Zealand
Phone +64 7 838 4439
Website: http://www.waikato.ac.nz/sasd/postgraduate/

Co-Authorship Form

This form is to accompany the submission of any PhD that contains research reported in published or unpublished co-authored work. **Please include one copy of this form for each co-authored work**. Completed forms should be included in your appendices for all the copies of your thesis submitted for examination and library deposit (including digital deposit).

Please indicate the chapter/section/pages of this thesis that are extracted from a co-authored work and give the title and publication details or details of submission of the co-authored work.

Chapter 5, Improving On-Load and Off-Load Impedance Measurement of Batteries, pp70-73.

"Impedance measurement of batteries under load", 2019 IEEE International Instrumentation and Measurement Technology Conference, 2019, New Zealand.

Nature of contribution by PhD candidate	Conceptualization; Methodology; Software; Writing - Review & Editing; Validation; Formal analysis; Investigation; Writing - Original Draft; Visualization.
Extent of contribution by PhD candidate (%)	90%

CO-AUTHORS

Name	Nature of Contribution
Jonathan Scott	Writing - Review & Editing; Validation

Certification by Co-Authors

The undersigned hereby certify that:

- the above statement correctly reflects the nature and extent of the PhD candidate's contribution to this work, and the nature of the contribution of each of the co-authors; and

Name	Signature	Date
Jonathan Scott		16 Nov 2020

THE UNIVERSITY OF WAIKATO
Te Whare Wānanga o Waikato

Postgraduate Studies Office
Student and Academic Services Division
Wahanga Ratonga Matauranga Akonga
The University of Waikato
Private Bag 3105
Hamilton 3240, New Zealand
Phone +64 7 838 4439
Website: http://www.waikato.ac.nz/sasd/postgraduate/

Co-Authorship Form

This form is to accompany the submission of any PhD that contains research reported in published or unpublished co-authored work. **Please include one copy of this form for each co-authored work**. Completed forms should be included in your appendices for all the copies of your thesis submitted for examination and library deposit (including digital deposit).

Please indicate the chapter/section/pages of this thesis that are extracted from a co-authored work and give the title and publication details or details of submission of the co-authored work.

Chapter 6, Mathematical Model, pp76-79.

"Measurement for fractional characteristic of lithium batteries", 2019 IEEE International Instrumentation and Measurement Technology Conference, 2019, New Zealand.

Nature of contribution by PhD candidate	Conceptualization; Methodology; Software; Writing - Review & Editing; Validation; Formal analysis; Investigation; Writing - Original Draft; Visualization.
Extent of contribution by PhD candidate (%)	95%

CO-AUTHORS

Name	Nature of Contribution
Jonathan Scott	Writing - Review & Editing

Certification by Co-Authors

The undersigned hereby certify that:

- the above statement correctly reflects the nature and extent of the PhD candidate's contribution to this work, and the nature of the contribution of each of the co-authors; and

Name	Signature	Date
Jonathan Scott		16 Nov 2020

THE UNIVERSITY OF WAIKATO
Te Whare Wānanga o Waikato

Postgraduate Studies Office
Student and Academic Services Division
Wahanga Ratonga Matauranga Akonga
The University of Waikato
Private Bag 3105
Hamilton 3240, New Zealand
Phone +64 7 838 4439
Website: http://www.waikato.ac.nz/sasd/postgraduate/

Co-Authorship Form

This form is to accompany the submission of any PhD that contains research reported in published or unpublished co-authored work. **Please include one copy of this form for each co-authored work**. Completed forms should be included in your appendices for all the copies of your thesis submitted for examination and library deposit (including digital deposit).

Please indicate the chapter/section/pages of this thesis that are extracted from a co-authored work and give the title and publication details or details of submission of the co-authored work.

Chapter 7, Passive Fractional Equivalent-circuit Battery Model, pp83-90.

"Extending randles's battery model to predict impedance, charge-voltage, and runtime characteristics", IEEE Access, 1–1. https://doi.org/10.1109/access.2020.2992771.

Nature of contribution by PhD candidate	Conceptualization; Methodology; Software; Writing - Review & Editing; Validation; Formal analysis; Investigation; Writing - Original Draft; Visualization.
Extent of contribution by PhD candidate (%)	65%

CO-AUTHORS

Name	Nature of Contribution
Jonathan Scott	Conceptualization; Methodology; Writing - Review & Editing; Validation;

Certification by Co-Authors

The undersigned hereby certify that:

- the above statement correctly reflects the nature and extent of the PhD candidate's contribution to this work, and the nature of the contribution of each of the co-authors; and

Name	Signature	Date
Jonathan Scott		16 Nov 2020

Appendix B

Patent on battery performance assessment method and apparatus

UNITED STATES PATENT AND TRADEMARK OFFICE

UNITED STATES DEPARTMENT OF COMMERCE
United States Patent and Trademark Office
Address: COMMISSIONER FOR PATENTS
P.O. Box 1450
Alexandria, Virginia 22313-1450
www.uspto.gov

APPLICATION NUMBER	FILING or 371(c) DATE	GRP ART UNIT	FIL FEE REC'D	ATTY.DOCKET.NO	TOT CLAIMS	IND CLAIMS
15/930,989	05/13/2020		915	815003-000041	21	1

CONFIRMATION NO. 7694

78198
Studebaker & Brackett PC
8255 Greensboro Drive
Suite 300
Tysons, VA 22102

FILING RECEIPT

OC000000117132959

Date Mailed: 05/21/2020

Receipt is acknowledged of this non-provisional utility patent application. The application will be taken up for examination in due course. Applicant will be notified as to the results of the examination. Any correspondence concerning the application must include the following identification information: the U.S. APPLICATION NUMBER, FILING DATE, NAME OF FIRST INVENTOR, and TITLE OF INVENTION. Fees transmitted by check or draft are subject to collection.

Please verify the accuracy of the data presented on this receipt. If an error is noted on this Filing Receipt, please submit a written request for a corrected Filing Receipt, including a properly marked-up ADS showing the changes with strike-through for deletions and underlining for additions. If you received a "Notice to File Missing Parts" or other Notice requiring a response for this application, please submit any request for correction to this Filing Receipt with your reply to the Notice. When the USPTO processes the reply to the Notice, the USPTO will generate another Filing Receipt incorporating the requested corrections provided that the request is grantable.

Inventor(s)

Jonathan Brereton SCOTT, Hillcrest, NEW ZEALAND;
Peter Scott Vallack SINGLE, Lane Cove, AUSTRALIA;
Rahat HASAN, Hamilton, NEW ZEALAND;

Applicant(s)

Waikatolink Limited, Hamilton, NEW ZEALAND;

Assignment For Published Patent Application

Waikatolink Limited, Hamilton, NEW ZEALAND

Power of Attorney: None

Domestic Applications for which benefit is claimed - None.
A proper domestic benefit claim must be provided in an Application Data Sheet in order to constitute a claim for domestic benefit. See 37 CFR 1.76 and 1.78.

Foreign Applications (You may be eligible to benefit from the **Patent Prosecution Highway** program at the USPTO. Please see http://www.uspto.gov for more information.)
NEW ZEALAND 753706 05/20/2019 Access Code Provided

Permission to Access Application via Priority Document Exchange: Yes

Permission to Access Search Results: Yes

Applicant may provide or rescind an authorization for access using Form PTO/SB/39 or Form PTO/SB/69 as appropriate.

Request to Retrieve - This application either claims priority to one or more applications filed in an intellectual property Office that participates in the Priority Document Exchange (PDX) program or contains a proper **Request to Retrieve Electronic Priority Application(s)** (PTO/SB/38 or its equivalent). Consequently, the USPTO will attempt to electronically retrieve these priority documents.

If Required, Foreign Filing License Granted: 05/20/2020

The country code and number of your priority application, to be used for filing abroad under the Paris Convention, is **US 15/930,989**

Projected Publication Date: 11/26/2020

Non-Publication Request: No

Early Publication Request: No

** **SMALL ENTITY** **

Title

BATTERY PERFORMANCE ASSESSMENT METHOD AND APPARATUS

Preliminary Class

Statement under 37 CFR 1.55 or 1.78 for AIA (First Inventor to File) Transition Applications: No

PROTECTING YOUR INVENTION OUTSIDE THE UNITED STATES

Since the rights granted by a U.S. patent extend only throughout the territory of the United States and have no effect in a foreign country, an inventor who wishes patent protection in another country must apply for a patent in a specific country or in regional patent offices. Applicants may wish to consider the filing of an international application under the Patent Cooperation Treaty (PCT). An international (PCT) application generally has the same effect as a regular national patent application in each PCT-member country. The PCT process **simplifies** the filing of patent applications on the same invention in member countries, but **does not result** in a grant of "an international patent" and does not eliminate the need of applicants to file additional documents and fees in countries where patent protection is desired.

Almost every country has its own patent law, and a person desiring a patent in a particular country must make an application for patent in that country in accordance with its particular laws. Since the laws of many countries differ in various respects from the patent law of the United States, applicants are advised to seek guidance from specific foreign countries to ensure that patent rights are not lost prematurely.

Applicants also are advised that in the case of inventions made in the United States, the Director of the USPTO must issue a license before applicants can apply for a patent in a foreign country. The filing of a U.S. patent application serves as a request for a foreign filing license. The application's filing receipt contains further information and guidance as to the status of applicant's license for foreign filing.

Applicants may wish to consult the USPTO booklet, "General Information Concerning Patents" (specifically, the section entitled "Treaties and Foreign Patents") for more information on timeframes and deadlines for filing foreign patent applications. The guide is available either by contacting the USPTO Contact Center at 800-786-9199, or it can be viewed on the USPTO website at http://www.uspto.gov/web/offices/pac/doc/general/index.html.

For information on preventing theft of your intellectual property (patents, trademarks and copyrights), you may wish to consult the U.S. Government website, http://www.stopfakes.gov. Part of a Department of Commerce initiative, this website includes self-help "toolkits" giving innovators guidance on how to protect intellectual property in specific countries such as China, Korea and Mexico. For questions regarding patent enforcement issues, applicants may call the U.S. Government hotline at 1-866-999-HALT (1-866-999-4258).

LICENSE FOR FOREIGN FILING UNDER

Title 35, United States Code, Section 184

Title 37, Code of Federal Regulations, 5.11 & 5.15

GRANTED

The applicant has been granted a license under 35 U.S.C. 184, if the phrase "IF REQUIRED, FOREIGN FILING LICENSE GRANTED" followed by a date appears on this form. Such licenses are issued in all applications where the conditions for issuance of a license have been met, regardless of whether or not a license may be required as set forth in 37 CFR 5.15. The scope and limitations of this license are set forth in 37 CFR 5.15(a) unless an earlier license has been issued under 37 CFR 5.15(b). The license is subject to revocation upon written notification. The date indicated is the effective date of the license, unless an earlier license of similar scope has been granted under 37 CFR 5.13 or 5.14.

This license is to be retained by the licensee and may be used at any time on or after the effective date thereof unless it is revoked. This license is automatically transferred to any related applications(s) filed under 37 CFR 1.53(d). This license is not retroactive.

The grant of a license does not in any way lessen the responsibility of a licensee for the security of the subject matter as imposed by any Government contract or the provisions of existing laws relating to espionage and the national security or the export of technical data. Licensees should apprise themselves of current regulations especially with respect to certain countries, of other agencies, particularly the Office of Defense Trade Controls, Department of State (with respect to Arms, Munitions and Implements of War (22 CFR 121-128)); the Bureau of Industry and Security, Department of Commerce (15 CFR parts 730-774); the Office of Foreign AssetsControl, Department of Treasury (31 CFR Parts 500+) and the Department of Energy.

NOT GRANTED

No license under 35 U.S.C. 184 has been granted at this time, if the phrase "IF REQUIRED, FOREIGN FILING LICENSE GRANTED" DOES NOT appear on this form. Applicant may still petition for a license under 37 CFR 5.12, if a license is desired before the expiration of 6 months from the filing date of the application. If 6 months has lapsed from the filing date of this application and the licensee has not received any indication of a secrecy order under 35 U.S.C. 181, the licensee may foreign file the application pursuant to 37 CFR 5.15(b).

SelectUSA

The United States represents the largest, most dynamic marketplace in the world and is an unparalleled location for business investment, innovation, and commercialization of new technologies. The U.S. offers tremendous resources and advantages for those who invest and manufacture goods here. Through SelectUSA, our nation works to promote and facilitate business investment. SelectUSA provides information assistance to the international investor

community; serves as an ombudsman for existing and potential investors; advocates on behalf of U.S. cities, states, and regions competing for global investment; and counsels U.S. economic development organizations on investment attraction best practices. To learn more about why the United States is the best country in the world to develop technology, manufacture products, deliver services, and grow your business, visit http://www.SelectUSA.gov or call +1-202-482-6800.

BATTERY PERFORMANCE ASSESSMENT METHOD AND APPARATUS

Field of the Invention

This invention relates to a battery performance and quality assessment method and apparatus. In preferred embodiments the invention may be used to provide a battery state of health assessment.

Background of the Invention

It is increasingly common for electrical devices and systems to use power supplies which incorporate batteries. Batteries are used in a wide range of applications, from communications and entertainment electronics through to electric vehicles and satellite power systems.

Over time the performance of a battery will degrade as it completes a large number of charge and discharge cycles. The performance of the battery can also be impacted by exposure to excessive heat or cold, humid conditions or by being overcharged or severely discharged. In many applications it is important to know what the condition or state of health of a battery is to potentially forecast how long a battery can continue to operate at a desired level of performance.

For example, in the case of uninterruptible power supplies batteries are used to prevent the failure of computer systems disconnected from mains power electrical supplies. It is critical to ensure that the batteries used have a robust state of health to be able to service loads which could be placed upon them at any time.

The terminal voltage of the battery can be measured, and an assessment made of the amount of charge held by the battery. However, this measurement requires the battery to be disconnected from the load it normally services, and terminal voltage in isolation does not provide a useful picture of battery state of health.

For this reason, prior art battery performance assessment methods use testing procedures to investigate battery impedance, which provides a better

indicator of the physical state of the battery cells and hence its state of health. For example, in some prior art assessment techniques it is a common practice to apply a 1 kHz stimulation signal to a battery to attempt to measure its impedance.

However again one or more battery impedance measurements recorded at the same time will not provide an effective indicator of battery state of health. Standard practice with current state-of-the-art health assessment methods is to record multiple battery impedance measurements over a long period of time in an attempt to identify a baseline impedance and to identify trends in the change of this baseline impedance.

Unfortunately, while results obtained from current state-of-the art assessment methods are reasonable, the accuracy of the actual assessment result itself is questionable. This is indicated by the failure of some batteries well prior to their predicted end dates.

It would therefore be of advantage to have an improved method and apparatus for assessing the performance of a battery (and possibly doing so with an increased sensitivity or accuracy) which addressed any or all the above issues, or at least that provided an alternative choice to the prior art. In particular it would be of advantage to have a technology available for assessing the performance and quality of the battery which did not require multiple independent measurements to be recorded at different times over an extended period of time, and/or which did not require the battery to be disconnected from the load normally serviced. Improvements over the prior art which provided more accurate performance assessments would also be of advantage.

Disclosure of the Invention

According to one aspect of the present invention there is provided a battery performance assessment apparatus which includes
two terminal connectors configured to electrically connect the assessment apparatus to the positive and negative terminals of a battery being assessed, and

a response measurement system configured to measure the terminal voltage and current of the battery when supplied with at least one alternating test current having a frequency less than 1 Hz and/or less than an impedance transition frequency associated with the battery being assessed, and
a processor in communication with the response measurement system and being configured to output a performance assessment indicator for the battery being assessed by calculating at least one impedance for the battery using terminal voltage and current measurements communicated by the response measurement system.

According to another aspect of the present invention there is provided a battery performance assessment apparatus which includes
two terminal connectors configured to electrically connect the assessment apparatus to the positive and negative terminals of a battery being assessed, and
a test current source configured to supply at least one alternating test current to the battery being assessed, said at least one alternating test current having a frequency less than 1 Hz and/or less than an impedance transition frequency associated with the battery being assessed, and
a response measurement system configured to measure the terminal voltage and current of the battery when supplied with said at least one alternating test current, and
a processor in communication with the response measurement system and being configured to output a performance assessment indicator for the battery being assessed by calculating at least one impedance for the battery using terminal voltage and current measurements communicated by the response measurement system.

According to a further aspect of the present invention there is provided a battery performance assessment apparatus substantially as described above wherein the processor is programmed to implement a circuit simulation model which uses the terminal voltage and current measurements communicated to the processor as input parameters to define at least one constant phase element fractional capacitor to simulate the battery being assessed.

According to another aspect of the present invention there is provided a battery performance assessment apparatus substantially as described above wherein the processor is programmed to implement a circuit simulation model which uses the terminal voltage and current measurements communicated to the processor as input parameters to define a plurality of fractionally arranged constant phase element fractional capacitor components to simulate the battery being assessed.

The present invention provides a battery performance assessment apparatus, in addition to a method of assessing the performance of a battery. Additional aspects of the invention encompass the provision of an improved circuit simulation model implemented through computer executable instructions run on a processor or similar programmable computer system utilised by the invention.

Reference in general throughout this specification will also be made to the invention being used primarily to assess the performance of a battery. Those skilled in the art will appreciate that references made to batteries throughout this specification encompasses both the assessment of the performance of a single electrical cell, or an array of cells connected together. Those skilled in the art will therefore appreciate that references made to the invention working with a battery also encompasses the invention assessing the performance of a single electrical cell.

Furthermore, reference will also be made to the provision of a test current source which is used to supply one or more alternating test currents in association with the present invention. Those skilled in the art will appreciate that this test current source may be formed by dedicated stand-alone components in some embodiments, and/or where the normal electrical load or load is connected to the battery in other embodiments.

The assessment apparatus provided by the invention employs terminal connectors to engage at least a test current source and a response measurement system to a battery being assessed. Those skilled in the art will appreciate that any appropriate form of connector may be used to form terminal conductors which can allow electrical current flows to and from the

battery and which allow for the measurement of various electrical parameters of the battery.

The assessment apparatus provided by the invention also incorporates a processor in communication with a response measurement system.

In some embodiments this processor may be physically connected to other elements of the apparatus, potentially being enclosed within a single common housing with these components.

In other embodiments the processor may be located remotely from the battery, test current source and response measurement system, and may be configured to receive information from, or transmit operational commands to various other components of the invention.

In yet other embodiments the processor may be implemented with a distributed architecture where a number of separate hardware components are connected together to form the processor, these components potentially being located remote from one another or from the battery being assessed.

Those skilled in the art will appreciate that well-known information technology systems may be used to implement this remote processor architecture, and furthermore the processor itself may be implemented across or by several separate microprocessors or integrated circuits.

Reference throughout this specification will however be made to a processor being implemented by a microprocessor or microcontroller physically connected to at least the response measurement system of the apparatus. Again those skilled in the art will appreciate that other circuit architectures are also envisioned and within the scope of the present invention.

The processor integrated into the assessment apparatus is configured to output a performance assessment indicator for a battery being assessed. Those skilled in the art will appreciate that the form, format or information incorporated within this indicator may vary over different embodiments of the invention. The specific performance criteria defined for a battery may differ depending on the application in which the battery is used – for

example, performance may be assessed in some embodiments by the maximum current which can be supplied, or alternatively by the maximum charge storage capacity.

In one embodiment a performance assessment indicator may be provided by a simple Boolean yes - no, good - bad output, whereas in other embodiments this indicator may take the form of a percentage estimated lifespan time period or estimated number of charge/discharge cycles remaining before the battery is unable to meet a set performance criteria requirement. An indicator may also take the form of a measured or derived value for an electrical parameter of the battery, for example being battery fractional capacitance. In yet other embodiments an indicator may take the form of a percentage achieved for a target performance criteria, such as – for example – assessed battery fractional capacitance compared to a target fractional capacitance, or maximum current delivered compared to a target current value. An indicator or indicators may also take the form of a graphical representation, plot or graph making a comparison between performance assessments undertaken at different times.

Those skilled in the art will also appreciate that a performance assessment indicator may be determined using voltage and current measurements recorded during a single continuous measurement period in response to several different frequencies of test currents, or multiple measurements recorded at during different measurement periods, again in response to the same test current. Those skilled in the art will appreciate that a single measurement period may span a variable length of time depending on the number of and frequencies of test currents applied during this period. A performance assessment indicator may also be determined using voltage and current measurements recorded in response to the use of several different frequencies of test currents, be they applied at approximately the same or at different times.

Reference in general will be made throughout this specification to the performance indicator generated by the invention identifying the state of health of a battery. Those skilled in the art will however appreciate that other metrics for battery performance may also be assessed in other

embodiments and may include an assessment of the quality of the battery being assessed.

In a variety of embodiments battery impedance may be calculated from voltage and current measurements recorded in response to the use of several different frequencies to test currents, and these impedance values can be used to calculate, or determine one or more performance assessment indicators.

For example in one particular embodiment a performance assessment indicator may be calculated using the rate of change of calculated impedance values with frequency. This rate of change of impedance values recorded using test currents below the impedance transition frequency or the less than 1 Hz can be used to indicate the efficiency of a battery, being the ratio of charging energy supply to the battery compared to stored energy available from the battery. A relatively high rate of change may be associated with a battery that has a higher efficiency than a battery with a lower rate of change value.

In another embodiment a performance assessment indicator may be calculated using the lower-frequency impedance values plotted with frequency coupled to the high-frequency impedance values. The values of impedance values recorded using test currents below the impedance transition frequency suggest a straight line. Where this straight line crosses the value measured at high frequencies is an estimate of the impedance transition frequency. A relatively high impedance transition frequency may indicate that a battery has a reduced ability to sustain high power energy delivery.

In yet another embodiment a performance assessment indicator may be calculated using at least one impedance zero offset value. These values can represent the magnitude of impedances recorded for a battery using test currents below the impedance transition frequency. In such embodiments a performance assessment indicator representative of the maximum charge capacity of the battery may be evaluated by, for example, extrapolating a y-axis intercept value for plotted impedance measurements against test current frequency, or alternatively comparing impedance values at a

selected predetermined frequency value below the impedance transition frequency. A relatively low impedance zero offset value or values may indicate that at battery has a greater storage capacity than a battery associated with a higher zero offset value or values.

In yet another embodiment a performance assessment indicator may be calculated using a transition bandwidth value. This impedance transition frequency bandwidth value can be found by identifying the frequency range where a relatively constant rate of change of the impedance of the battery at low frequencies transitions to an alternative or different rate of change of impedance at higher frequencies. The bandwidth of this transition zone can in some embodiments provide a general indication of the quality of the manufacture of the battery being assessed, the precision or tolerances used in the components making of the battery and/or the purity of the compounds employed to form the battery. In such embodiments a better quality battery may exhibit a smaller transition bandwidth value than a lower quality battery.

Those skilled in the art will appreciate that in various embodiments performance indicators may also be derived from combinations of rates of impedance change, transition frequency values, zero offset values and transition bandwidth values. This information can be used as parameters to a range of models or calibrations developed for specific battery constructions and may provide performance indicators appropriate to a variety of different battery performance characteristics.

In a preferred embodiment a battery performance assessment apparatus may also include a temperature sensor which in use is placed in close proximity to the battery being assessed. In such embodiments this temperature sensor may provide a measurement of the battery temperature to the processor to improve the accuracy of calculations undertaken to assess the performance of the battery. This temperature information can also be used in combination with a calibration undertaken for the form or type of the battery being assessed to apply corrections to measurements undertaken by the response measurement system.

The assessment apparatus provided by the invention includes a response measurement system which is used to measure the terminal voltage and current of the battery being assessed. These measurements are made when the battery responds to a test current.

In a preferred embodiment the response measurement system may record a plurality of measurements of both terminal voltage and current over the time period when a particular test current is applied to the battery. Those skilled in the art will appreciate that a range of prior art voltage and current measurement technologies may be employed with a required accuracy, resolution and precision depending on the application in which the invention is employed.

In one embodiment, the assessment apparatus provided by the invention preferably includes a test current source configured to stimulate the battery being assessed with at least one alternating test current.

In other embodiments the application of at least one single cycle of the alternating test current ensures that the battery experiences both charging and discharging.

In yet another embodiment, the application of at least one single cycle of the alternating test current ensures that the battery experiences either charging or discharging depending on the 'at use' charging or discharging operation of the battery.

Those skilled in the art will appreciate that a test current source may be provided by a number of different arrangements of components in various embodiments.

In a preferred embodiment a test current source may be provided by a dedicated alternating current generation circuit. Existing technology in this field may be readily utilised to implement this form of component.

In an alternative embodiment a test current source may be formed by or incorporates switching electronics connected across two or more batteries. In such embodiments two or more of these batteries may have their state of

health assessed concurrently, where current supplied from one battery can be used to charge the other battery and vice versa.

In yet other alternative embodiments the regular load and charging circuits normally connected to a battery during its usual application may be utilised as a test current source. Again these existing circuits can be connected to the battery using switching technology to charge and discharge the battery being assessed at the frequency required of an alternating test current.

In a preferred embodiment the processor incorporated within the assessment apparatus may be configured to control the operation of the test current source, and in particular the magnitude and frequency of the alternating test current applied to a battery. The processor may also control the time period over which a particular test current is applied. Furthermore, in various embodiments a processor may be configured to ensure that a plurality of alternating test currents with different frequencies are applied to the battery being assessed.

Reference throughout this specification will also be made to the processor being used to control the operation of the test current source and specifically being used to apply a number of alternating test currents with different frequencies. However those skilled in the art will appreciate that in other embodiments the processor integrated with the assessment apparatus need not necessarily function in this way. For example, in some alternative embodiments the test current source may include internal control systems configured to apply one or potentially a number of predetermined alternating test currents at selected frequencies.

In a preferred embodiment the assessment apparatus may undertake a test procedure which applies a plurality of alternating test currents with different frequencies. For example, in some embodiments the test current source may sequentially apply a set of alternating test currents one after the other while the response measurement system records battery terminal voltage and current. However, in one or more alternative embodiments a test current source may apply a composite test current signal. This composite test current can be formed from the summation of two or more separate

alternating test currents at particular frequencies of interest in the operation of the invention.

In a preferred embodiment the assessment apparatus may apply a test current for at least one cycle or period of the frequency of the test current. Applying these currents for a full cycle allows measurements to be captured across the entire range of charging and discharging operations experienced by the battery. In additional embodiments test currents may also be applied over many cycles to allow detailed measurements to be captured and to potentially mitigate errors in such measurements. In yet other embodiments a full cycle of measurements related to a particular test current may be provided from the merger of two or more measurements undertaken at different times, but which together show the batteries response to the entire period of the test current waveform.

The assessment apparatus provided by the invention is used to apply alternating test currents that have frequencies less than 1Hz or less than an impedance transition frequency associated with the battery being assessed.

This impedance transition frequency or frequencies can be determined experimentally for the form, construction or type of the battery being assessed. A plot can be made of measurements completed of battery impedance over a range of frequencies, preferably extending to below 1 μHz and up to at least 1-10 Hz. This impedance transition frequency zone can be found by identifying the frequency range where a relatively constant rate of change of the impedance of the battery at low frequencies transitions to an alternative or different rate of change of impedance at higher frequencies. By identifying the impedance transition frequency or frequencies of the battery the invention can then apply test currents with lower frequencies. These low frequency test currents are used by the invention to assess the performance of the battery.

In a preferred embodiment the magnitude of the peak or RMS current of the alternating test current may be varied based on the frequency of the alternating test current. In various embodiments an alternating test current may be applied for at least one cycle, which at low frequency values may result in relatively long charge and discharge times. The invention may

therefore manage the magnitude of the alternating current applied to a battery during the assessment process to ensure that it is not overcharged or severely discharged and damaged during assessment. Furthermore, this approach also ensures that measurements are not made of a response to a test current when the battery has an extremely low or high state of charge.

In a preferred embodiment the magnitude or amplitude of an alternating test current may be set based on the frequency of the signal being applied and the capacity of the battery being assessed. For example in some embodiments the test current applied may only deliver or remove approximately 10 percent of the charge capacity of the battery. In yet other embodiments only 1 percent of the charge capacity of the battery may be delivered or removed by a test current.

In some embodiments the assessment apparatus may be configured to execute a preliminary charge state fixing process prior to applying an alternating test current to a battery. In such embodiments the apparatus may be configured to apply a charging current at a voltage which provides a predictable state of charge in the battery. Charge may be supplied to the battery to preferably charge it to approximately the mid-point of its capacity, thereby minimising the potential for the battery being overcharged or over-discharged by the application of an alternating test current.

Preferably the processor provided with the assessment apparatus may be used to calculate a plurality of impedance values for the battery, each of these impedances being associated with a particular frequency alternating test current. These impedance values can be used in some embodiments by the processor as input parameters to a circuit simulation model run by the processor which aims to model and predict the characteristics of the battery. However in other embodiments performance indicators may be determined using these impedance values without the use of a circuit simulation model, as discussed above.

In a preferred embodiment the processor may be used to implement a circuit simulation model which uses these impedance values to define at least one constant phase element fractional capacitor to simulate the characteristics of the battery. Those skilled in the art will also appreciate

that this component can be described as a fractional capacitor or a constant phase element. In a further embodiment the circuit simulation model may define or model the battery using a single constant phase element fractional capacitor - also known as a 'CPE' - in combination with a single series resistance.

In such embodiments the parameters of the CPE component of this model may be defined using the rate of change of calculated impedance values with frequency, and the zero offset of calculated impedance values applied against frequency. Preferably the additional series resistance of this model may be defined by the resistance of the battery, determined through a measurement of the terminal voltage and current exhibited when a direct current signal is applied to the battery.

In a further embodiment the accuracy of the simulation model run by the processor may be improved by substituting the above-referenced single constant phase element fractional capacitor for an equivalent set of fractionally arranged constant phase element fractional capacitor components. In such embodiments the characteristics determined for the above referenced single CPE component may be substituted into a replacement split assembly which defines 'n' smaller CPE components, each of which has the same phase but an 'n' times lower admittance characteristic. This equivalent split assembly may be used to replace a single CPE component with n smaller CPE components, CPE/n, connected in parallel with an intervening resistance Rx/n.

The present invention may provide many potential advantages over the prior art.

In various embodiments the present invention can provide improvements in the assessment of the performance of batteries through utilising at set of measurements captured over a single continuous time period. Existing technology may be used in the implementation of the method of the invention to capture these measurements and to calculate a performance indicator.

Furthermore in some embodiments existing battery charging and discharging infrastructure may be utilised to stimulate the battery with a test current or currents at appropriate frequencies from which the invention can derive such performance information.

In various embodiments the invention may facilitate a method of assessment which may not require a battery to be disconnected from its normal load environment.

In yet further embodiments, the measurements made have improved sensitivity to small changes. This sensitivity can be utilised to provide more accurate performance metrics of the battery being measured. The increased sensitivity of the measurements obtained over time should enable someone skilled in the art to obtain a more reliable prediction of battery failure within a given time window of monitoring.

While performance is one metric by which state of health is measured, quality may also be a valuable metric that could be measured using the present invention. The measurements taken can provide an indication of the true efficiency of the return power and power density of a battery in operation. Accordingly, along with other performance metrics such as fractional capacitance, someone skilled in the art could utilise this method to determine the quality of a battery.

Brief description of the drawings

Additional and further aspects of the present invention will be apparent to the reader from the following description of embodiments, given in by way of example only, with reference to the accompanying drawings in which:

- Figure 1a shows a schematic circuit diagram of a battery performance assessment apparatus as provided in accordance with one embodiment of the invention,
- Figure 1b shows a further schematic circuit diagram of a battery performance assessment apparatus as provided in accordance with another embodiment of the invention,

- Figure 2 shows a flowchart of operational steps executed by the assessment apparatus illustrated with respect to figures 1a and 1b,
- Figure 3a shows a plot of impedance against frequency for a generic battery and the identification of at least one impedance transition frequency for this battery,
- Figure 3b shows a plot of impedance against frequency for both a Lithium-ion battery (triangle symbol) and a Lead-acid battery (inverted triangle symbol),
- Figure 3c shows a plot of impedance against frequency and phase for a generic battery where the temperature has been varied (indicated by solid symbols),
- Figure 4a shows a flowchart of calculation steps performed by the processor shown with respect to figure 1a to determine a state of health-based performance assessment indicator, and
- Figure 4b shows a flowchart of calculation steps performed by the processor shown with respect to figure 1b to determine a state of health-based performance assessment indicator, and
- Figures 5a and 5b show exemplary representations of equivalent circuit models used in a circuit simulation model implemented in a further aspect of the invention, and
- Figure 6 provides an indicative comparative plot of current against time for different frequencies of test current provided in accordance with another aspect of the invention, and
- Figure 7 provides an indicative plot of impedance against frequency as used to identify a transition frequency value in various embodiments, and
- Figure 8 provides an indicative plot of impedance against frequency comparing measurements from two different batteries exhibiting different zero offset values.

Further aspects of the invention will become apparent from the following description of the invention which is given by way of example only of particular embodiments.

Best modes for carrying out the invention

Figure 1a shows a schematic circuit diagram of a battery performance assessment apparatus 1 as provided in accordance with one embodiment of the invention. The apparatus 1 is connected to a battery 2 by a pair of terminal connectors 3. These terminal connectors provide positive and negative terminal connections to a test current source 4 and a response measurement system 5.

The test current source 4 is configured to supply a set of alternating test currents to the battery, where each of these test currents have a frequency less than an impedance transition frequency, as discussed in more detail with respect to figure 3. Each of these alternating test currents is supplied to the battery over several cycles of the frequency selected for the current and current magnitudes are fixed to prevent overcharging or over discharging of the battery.

The response measurement system 5 is configured to measure the terminal voltage and current of the battery when supplied a test current

Each of the test current source and response measurement systems are connected to and housed in combination with a processor 6. The processor 6 controls the operation of the test current source 4 and receives voltage and current measurements from the response measurement system 5. The processor 6 is also connected to a temperature sensor 7 which is located close to the battery 2 and is used to provide an indication of the temperature of the battery.

The processor is configured to output a state of health assessment indicator for the battery by calculating at least one impedance for the battery using the received terminal voltage and current measurements. The steps undertaken in this process are discussed in more detail with respect to the flowchart of figure 4a.

Figure 1b shows a further schematic circuit diagram of a battery performance assessment apparatus as provided in accordance with another embodiment of the invention. This circuit is similar in many respects to that

shown with respect to figure 1a and also incorporates terminal connectors 3 engaged with a battery 2 in addition to a test current source 4.

In the embodiment shown a voltage measurement circuit 5 is connected across the terminals 3 in addition to being connected through to a current measurement circuit 8. A processor 6 is provided with input and output connections to these components, as illustrated by the communications arrows shown. The processor can issue operational commands to the current source 4, while receiving current and voltage measurements from the voltage and current measurement circuits 5, 8 - as well as temperature measurements from a temperature sensor 7.

Figure 2 shows a flowchart of operational steps executed by the assessment apparatus illustrated with respect to both figures 1a and 1b.

In the embodiment shown the first step A of this method is implemented by an activation command being received from a user.

At step B the temperature sensor connected to the housing of a battery being assessed is polled and temperature information received in reply is sent to the processor memory.

At step C the processor commands the current source to apply the first of a series of alternating test currents to the battery, each current having a specific frequency and peak current amplitude. The processor also controls the time period each test current is applied over.

At step D the response measurement system is used to record a series of battery terminal voltage and current measurements while this test current is being applied. This set of measurements is sent to the processor memory.

At step E a test is applied to determine if the test current which was just used is the last in the series of test currents to be applied to the battery. If this is not true step F is executed to increment through a list of alternating test currents and to read from the processor memory the particulars of the next test current to be applied at step C.

If the recently applied test current is the last in the sequence of test currents step G is executed where the processor calculates a state of health indicator, as discussed in more detail with respect to figure 4.

Figure 3a shows a plot of impedance against frequency for a generic battery and the identification of at least one impedance transition frequency for this battery.

As can be seen from figure 3a the rate of change of the battery impedance drops substantially from low frequencies to high frequencies. This behavioural change occurs in the transitional zone centred around 10^{-3} Hz. The form of plot shown with respect to figure 3 can be used to identify a band of frequencies which define this transitional zone so the invention can supply lower frequency alternating test currents.

Figure 3b shows a plot of impedance against frequency for both a Lithium-ion battery (indicated by the triangle symbol) and a Lead-acid battery (indicated by the inverted triangle symbol).

As can be seen from figure 3b different types of battery will show different transition frequency characteristics and the transition points may shift dependent on battery type, size and quality.

Figure 3b also highlights the slope of the curve below the transition frequency. The slope indicates loss in a battery, with a smaller slope being associated with lower efficiency of returned power and lower power density. It could therefore be inferred from Figure 3b that the Lead-acid battery featured therein is of a lesser quality than that the Lithium-ion battery shown.

Figure 3c shows a plot of impedance against frequency and phase for a generic battery where the temperature has been varied. As can be seen from Figure 3c, a change in temperature results in a shift in the slope, which is constant with the understanding that battery performance can be dependent on temperature.

Figure 4a shows a flowchart of calculation steps performed by the processor shown with respect to figure 1a to determine a state of health based performance assessment indicator.

The first step A of this method a set of current and voltage measurements are loaded into the processor memory.

Next at step B a pre-processing operation is undertaken to improve the accuracy of the results obtained by the processor. The voltage and current data is subjected to a windowing pre-processing algorithm and is filtered to have a linear ramp component removed at this step.

Next at step C a computation is completed to compute magnitude and phase of the voltage and the current at selected test current frequencies. In the embodiment shown a discrete Fourier transform is applied to the data to resolve this information.

At step D a computation is executed to compute the complex impedance Z for particular frequencies of test currents by dividing voltage values by current values.

At step E the processor instantiates a circuit simulation model for the battery by defining the parameters of a sequence of fractionally arranged constant phase elements.

At step F the circuit simulation model generated is used to make a comparison to a maximum charge storage capacity target to indicate the state of health of the battery being assessed. At this stage a comparison is also made with stored state of health indications generated at prior times to identify any trends in the state of health of the battery.

Figure 4b shows a flowchart of calculation steps performed by the processor shown with respect to figure 1ab to determine a state of health based performance assessment indicator.

In the embodiment shown steps A, B, C and D are the same as discussed above with respect to figure 4a, with voltage and current measurements

being loaded to memory, undergoing a pre-processing operation, and voltage and current magnitude and phase being computed at selected test current frequencies. Step D is an executed to compute the complex impedance Z for particular frequencies of test currents by dividing voltage values by current values.

At step E computed values of impedance associated with different frequencies of test currents are applied as cross-referencing parameters to a lookup table loaded to processor memory. The stored entries of this table are pre-calculated to provide a numerical metric indication of battery state of health using previously prepared calibration data for the specific type of battery being assessed. Therefore in this embodiment a circuit simulation model does not need to be instantiated and run by a processor at this stage.

At step F the identified table entry isolated by the input impedance and frequency values is retrieved and displayed to a user to indicate the state of health performance of the battery. Again at this stage a comparison is also made of stored state of health indications generated at prior times to identify any trends in the state of health battery.

Figures 5a and 5b show exemplary representations of equivalent circuit models used in a circuit simulation model implemented in a further aspect of the invention.

In various embodiments the processor can be used to calculate a series of impedance values for the battery, each of these impedances being associated with a particular frequency of alternating test current. These impedances can then be used as input parameters to define each of the components shown in these two equivalent circuit models.

Figure 5a illustrates an equivalent circuit model for a battery which is composed from a single CPE constant phase element provided in combination with a single series resistance Rs.

The parameters of the CPE component are defined using the rate of change of calculated impedance values with frequency, and the zero offset of calculated impedance values applied against frequency. The additional series

resistance Rs is defined by a measurement of the terminal voltage and current exhibited when a direct current signal is applied to the battery.

Figure 5b shows an alternative circuit model where the single CPE component of figure 5b is substituted for an equivalent set of n fractionally arranged constant phase element fractional capacitor components – CPE/n. This equivalent split assembly replaces the single CPE component with n smaller CPE components, CPE/n, connected in parallel with an intervening resistance Rx/n to the same series resistance as before, Rs.

Figure 6 provides an indicative comparative plot of current against time for different frequencies of test current provided in accordance with another aspect of the invention.

In the embodiment shown the processor is configured to control the amplitude and frequency of the alternating test current applied to a battery. These controls are applied to avoid overcharging the battery during a measurement period as test currents are supplied to the battery.

As can be seen from figure 6 the amplitude of an alternating test current is set based on the frequency of the signal being applied and the capacity of the battery being assessed. The 188 μHz test current has the shortest wavelength shown, so is allowed to exhibit the highest current peak. Comparatively the 71 and 27 μHz test currents have increasingly longer wavelengths and need to be applied for longer times, so the current peak of each is progressively limited by the operation of the processor. In this way the test currents applied can deliver or remove approximately 10 percent or less of the charge capacity of the battery.

Figure 7 provides an indicative plot of impedance against frequency as used to identify a transition frequency value in various embodiments. In such embodiments a performance assessment indicator may be calculated using the lower-frequency impedance values plotted with frequency coupled to the high-frequency impedance values. As shown by figure 7 the values of impedance recorded using test currents below the impedance transition frequency suggest a straight line. Where this straight line crosses the value measured at high frequencies is an estimate of the impedance transition

frequency. This value is identified in figure 7 at the frequency where the two fitted lines intersect. In various embodiments a relatively high impedance transition frequency can indicate that a battery has a reduced ability to sustain high power energy delivery.

Figure 8 provides an indicative plot of impedance against frequency comparing measurements from two different batteries exhibiting different zero offset values.

In such embodiments a performance assessment indicator representative of the maximum charge capacity of the battery may be evaluated by, for example, extrapolating a y-axis intercept value for plotted impedance measurements against test current frequency, or alternatively comparing impedance values at a selected predetermined frequency value below the impedance transition frequency.

As can be seen from figure 8 the lower triangle data point plot has an anticipated lower y-axis intercept when compared with the anticipated y-axis intercept of the upper square data point plot. Similarly the low frequency impedance measurements of the triangle data point plot all exhibit small zero offset values when compared with the square data point plot. This indicates that the battery associated with the triangle data point measurements has a greater storage capacity when compared with the battery associated with the square data point measurements.

In the preceding description and the following claims the word “comprise” or equivalent variations thereof is used in an inclusive sense to specify the presence of the stated feature or features. This term does not preclude the presence or addition of further features in various embodiments.

It is to be understood that the present invention is not limited to the embodiments described herein and further and additional embodiments within the spirit and scope of the invention will be apparent to the skilled reader from the examples illustrated with reference to the drawings. In particular, the invention may reside in any combination of features described herein, or may reside in alternative embodiments or combinations of these features with known equivalents to given features. Modifications and

variations of the example embodiments of the invention discussed above will be apparent to those skilled in the art and may be made without departure of the scope of the invention as defined in the appended claims.

What we claim is:

1. A battery performance assessment apparatus which includes two terminal connectors configured to electrically connect the assessment apparatus to the positive and negative terminals of a battery being assessed, and
a response measurement system configured to measure the terminal voltage and current of the battery when supplied with at least one alternating test current having a frequency less than 1 Hz and/or less than an impedance transition frequency associated with the battery being assessed, and
a processor in communication with the response measurement system and being configured to output a performance assessment indicator for the battery being assessed by calculating at least one impedance for the battery using terminal voltage and current measurements communicated by the response measurement system.

2. A battery performance assessment apparatus as claimed in claim 1 which includes a test current source configured to supply at least one alternating test current to the battery being assessed, said at least one alternating test current having a frequency less than 1 Hz and/or less than an impedance transition frequency associated with the battery being assessed.

3. A battery performance assessment apparatus as claimed in claim 1 or 2 wherein the test current source is provided by a dedicated alternating current generation circuit.

4. A battery performance assessment apparatus as claimed in claim 1 or 2 wherein the test current source incorporates switching electronics connected across two or more batteries.

5. A battery performance assessment apparatus as claimed in claim 1 or 2 wherein the test current source is provided by regular load and charging circuits.

6. A battery performance assessment apparatus as claimed in any one of claims 1 to 5 wherein the processor is programmed to implement a circuit simulation model which uses the terminal voltage and current measurements communicated to the processor as input parameters to define at least one constant phase element fractional capacitor to simulate the battery being assessed.

7. A battery performance assessment apparatus as claimed in any one of claims 1 to 5 wherein the processor is programmed to implement a circuit simulation model which uses the terminal voltage and current measurements communicated to the processor as input parameters to define a plurality of fractionally arranged constant phase element fractional capacitor components to simulate the battery being assessed.

8. A battery performance assessment apparatus as claimed in any one of claims 1 to 7 wherein a performance assessment indicator is determined using voltage and current measurements recorded during a single measurement period in response to several different frequencies of test currents.

9. A battery performance assessment apparatus as claimed in any one of claims 1 to 7 wherein a performance assessment indicator is determined using multiple voltage and current measurements recorded during different measurement periods in response to the same test current.

10. A battery performance assessment apparatus as claimed in any one of claims 1 to 9 wherein the test current source applies a composite test current signal formed from the summation of two or more alternating test currents with different frequencies.

11. A battery performance assessment apparatus as claimed in any one of claims 1 to 10 wherein a performance assessment indicator is calculated using the rate of change of calculated impedance values with frequency.

12. A battery performance assessment apparatus as claimed in any one of claims 1 to 10 wherein a performance assessment indicator is calculated using the transition frequency value.

13. A battery performance assessment as claimed in any one of claims 1 to 10 wherein a performance assessment indicator is calculated using at least one impedance zero offset value.

14. A battery performance assessment apparatus as claimed in any one of claims 1 to 10 wherein a performance assessment indicator is calculated using a transition bandwidth value.

15. A battery performance assessment apparatus as claimed in any one of claims 1 to 14 wherein the assessment apparatus applies a test current for at least one cycle of the frequency of the test current.

16. A battery performance assessment apparatus as claimed in any one of claims 1 to 15 which includes a temperature sensor placed in close proximity to the battery being assessed.

17. A battery performance assessment apparatus as claimed in any one of claims 1 to 16 wherein at least one component of the processor is located remotely from the terminal connectors and response measurement system.

18. A battery performance assessment apparatus as claimed in any one of claims 1 to 17 wherein the processor is configured to control the amplitude and frequency of the alternating test current applied to a battery.

19. A battery performance assessment apparatus as claimed in claim 18 wherein the amplitude of an alternating test current is set based on the frequency of the signal being applied and the capacity of the battery being assessed.

20. A battery performance assessment apparatus as claimed in any one of claims 1 to 19 wherein the test current applied delivers or removes approximately 10 percent or less of the charge capacity of the battery.

21. A battery performance assessment apparatus as claimed in any one of claims 1 to 20 wherein the processor is configured to execute a preliminary charge state fixing process prior to applying an alternating test current to a battery.

Abstract:

In one aspect the invention provides an assessment apparatus which includes two terminal connectors configured to electrically connect the assessment apparatus to the positive and negative terminals of a battery being assessed. The apparatus also includes a response measurement system configured to measure the terminal voltage and current of the battery when supplied with at least one alternating test current having a frequency less than 1 Hz and/or less than an impedance transition frequency associated with the battery being assessed. Also provided is a processor in communication with the response measurement system and being configured to output a performance assessment indicator for the battery being assessed by calculating at least one impedance for the battery using terminal voltage and current measurements communicated by the response measurement system.

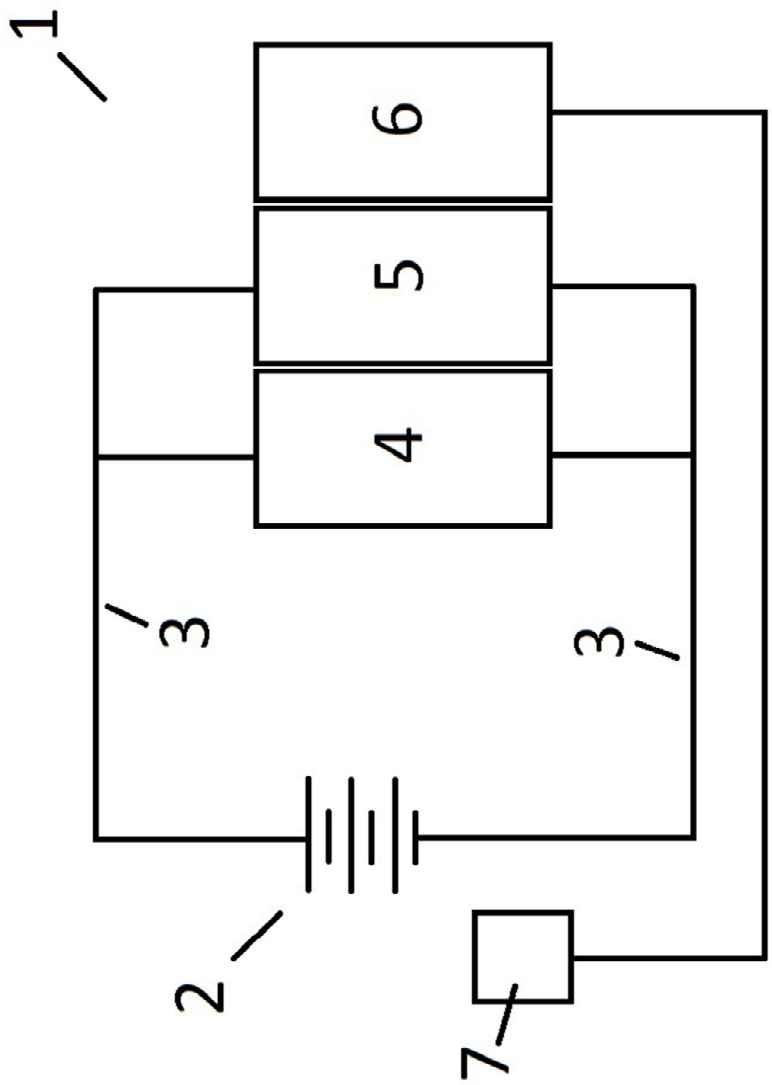

Figure 1a

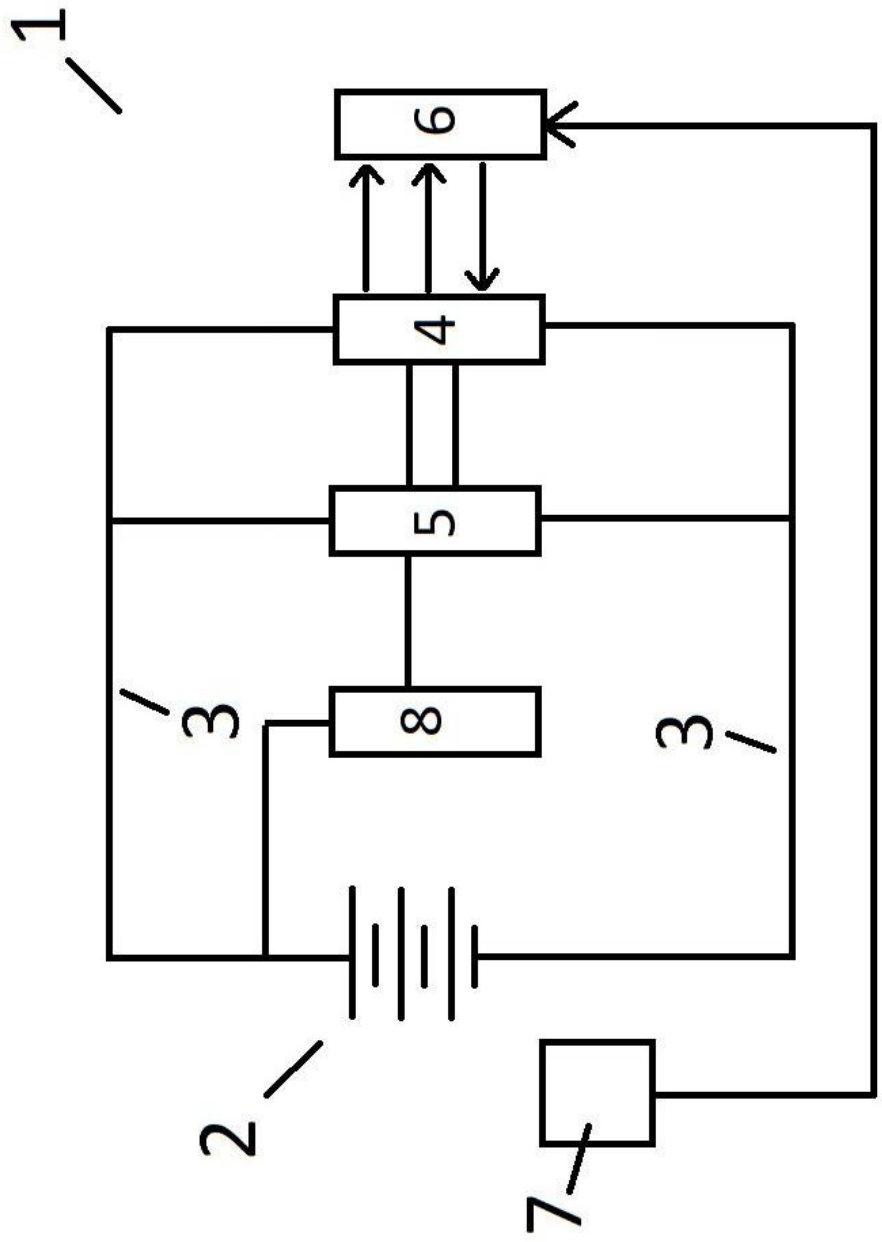

Figure 1b

Figure 2

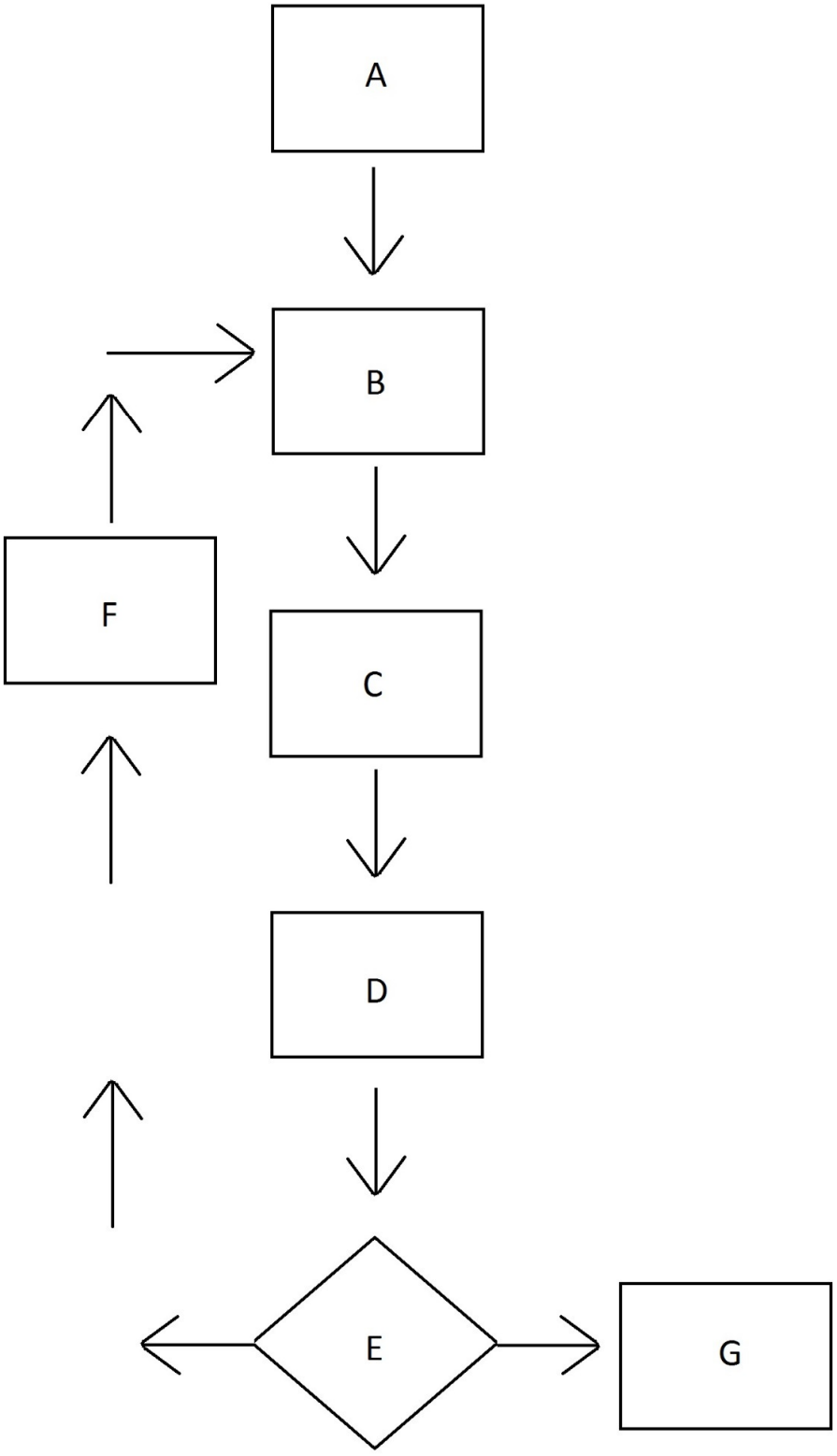

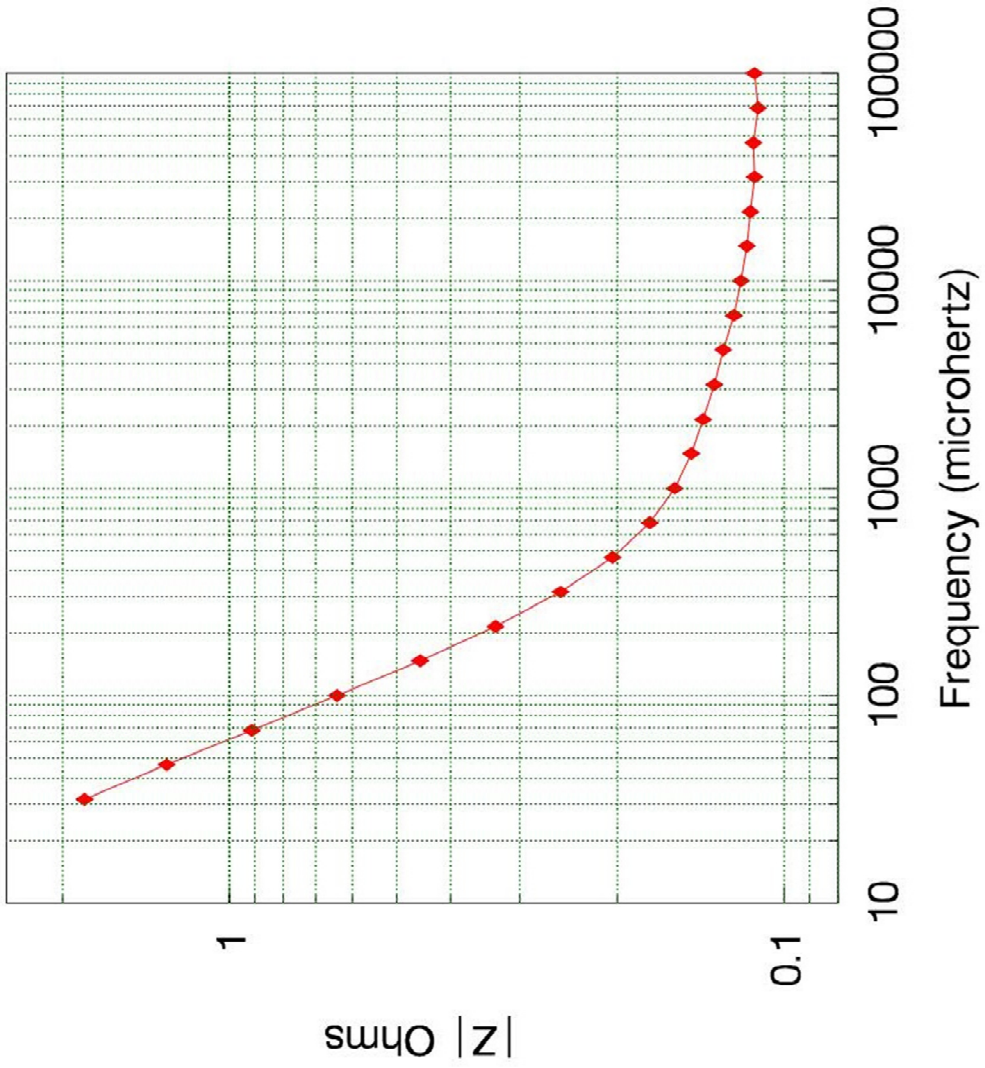

Figure 3a

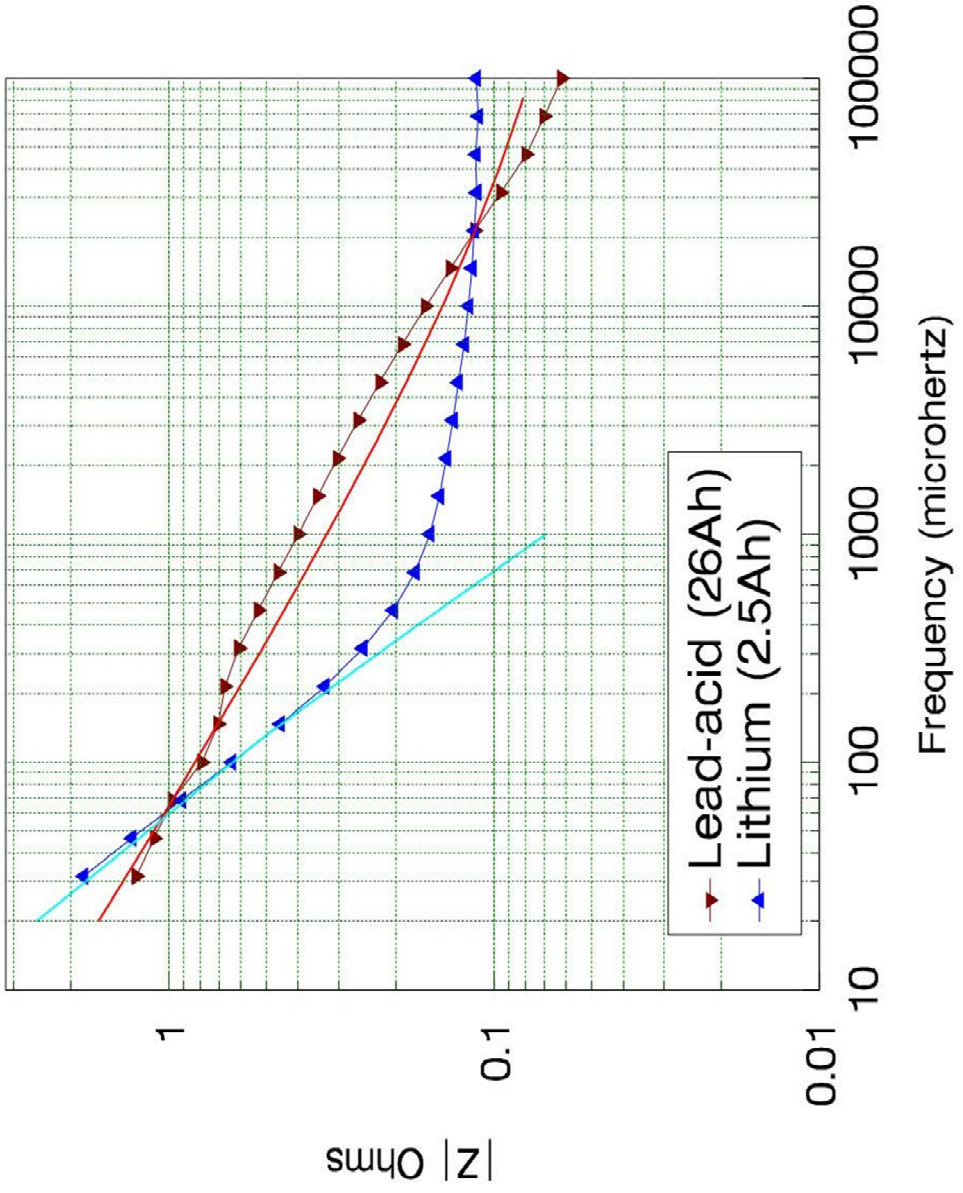
|Z| Ohms
1
0.1
0.01
10
100
1000
10000
100000
Frequency (microhertz)
Lead-acid (26Ah)
Lithium (2.5Ah)

Figure 3b

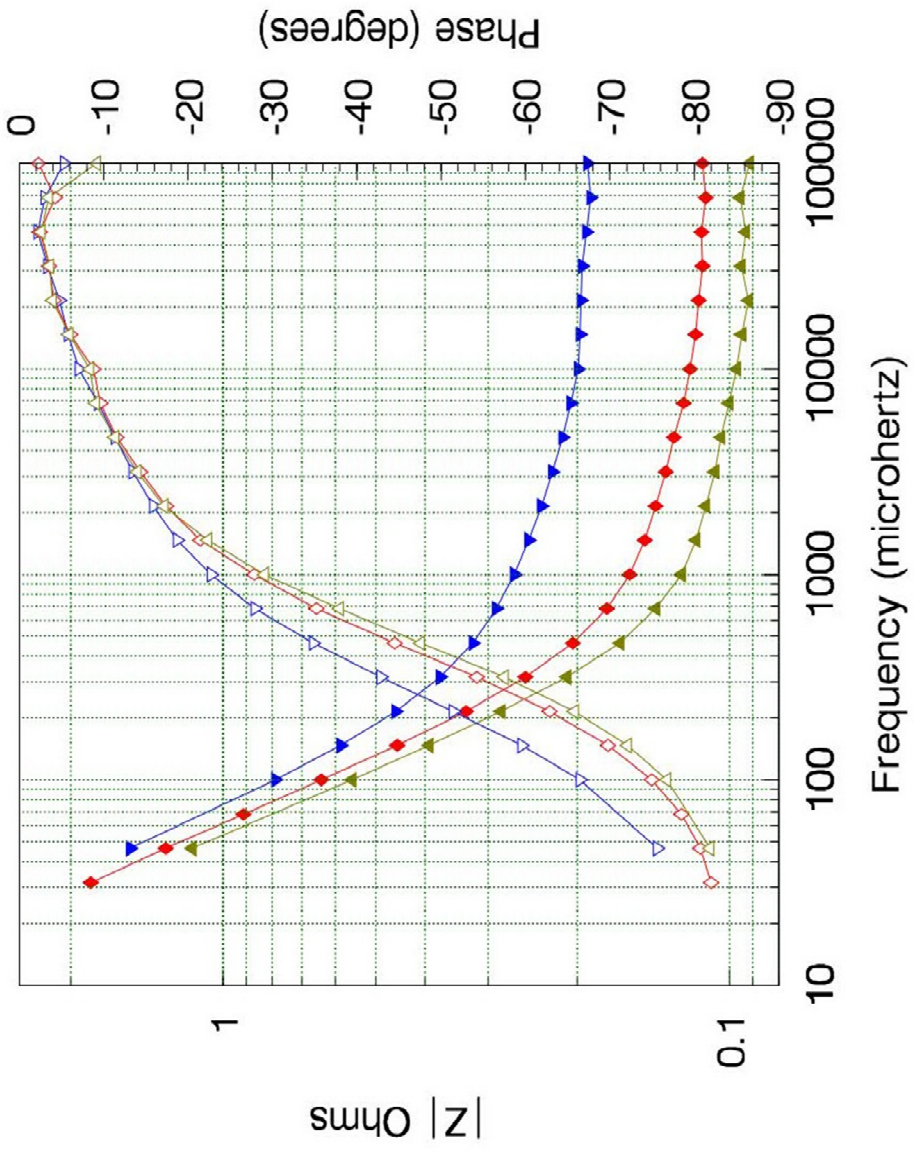
Phase (degrees)
0
-10
-20
-30
-40
-50
-60
-70
-80
-90
|Z| Ohms
1
0.1
10
100
1000
10000
100000
Frequency (microhertz)

Figure 3c

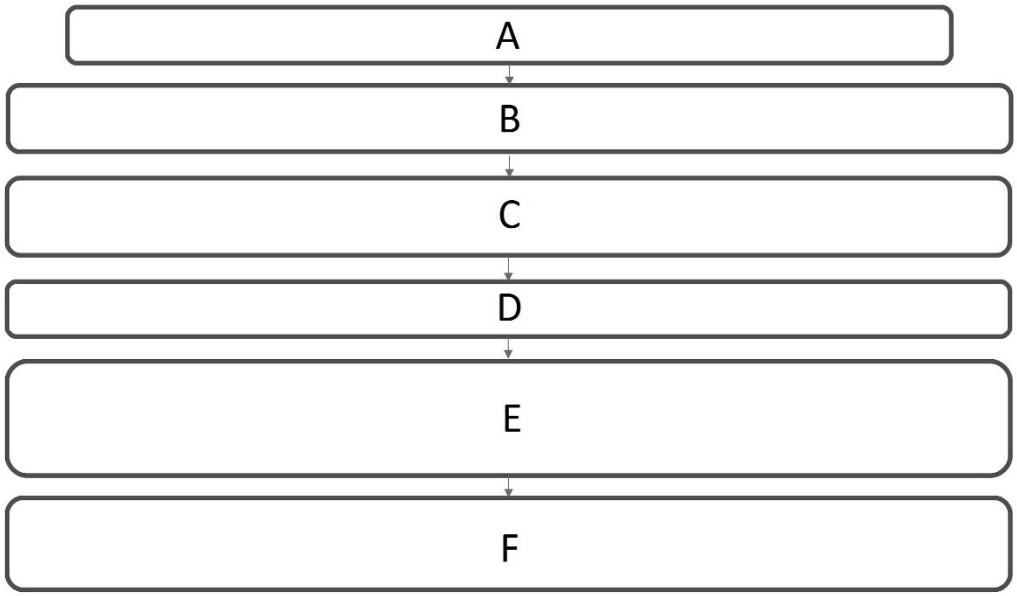

Figure 4a

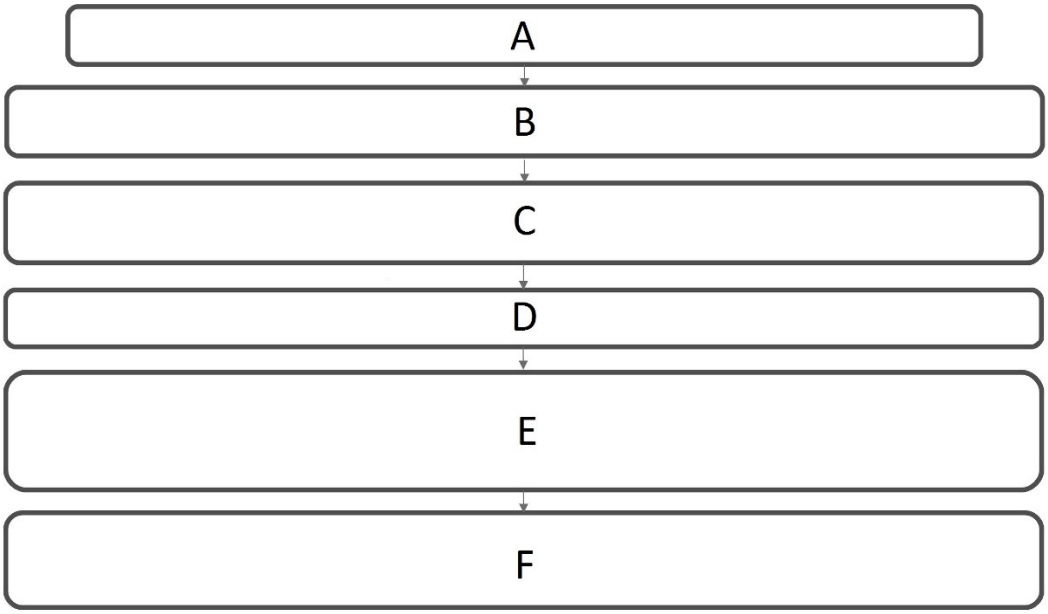

Figure 4b

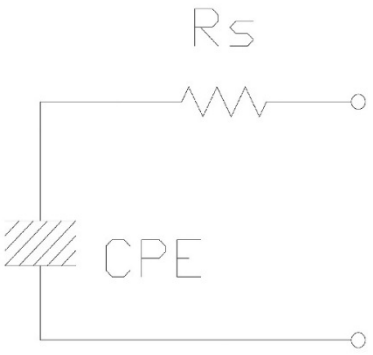

Figure 5a

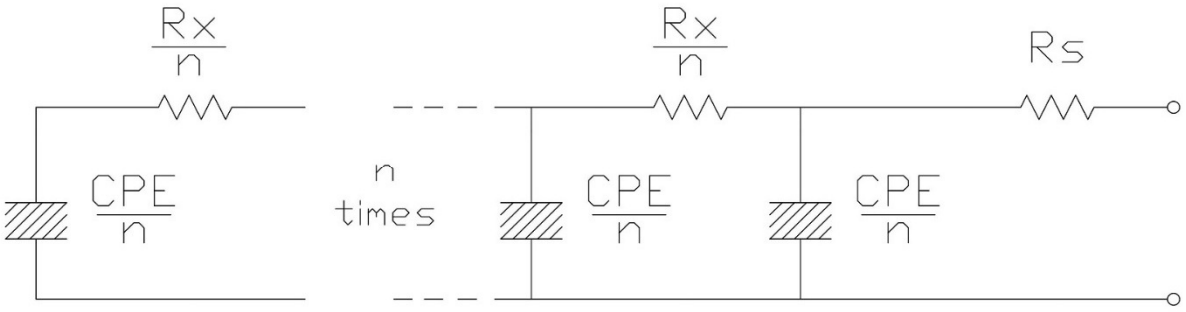

Figure 5b

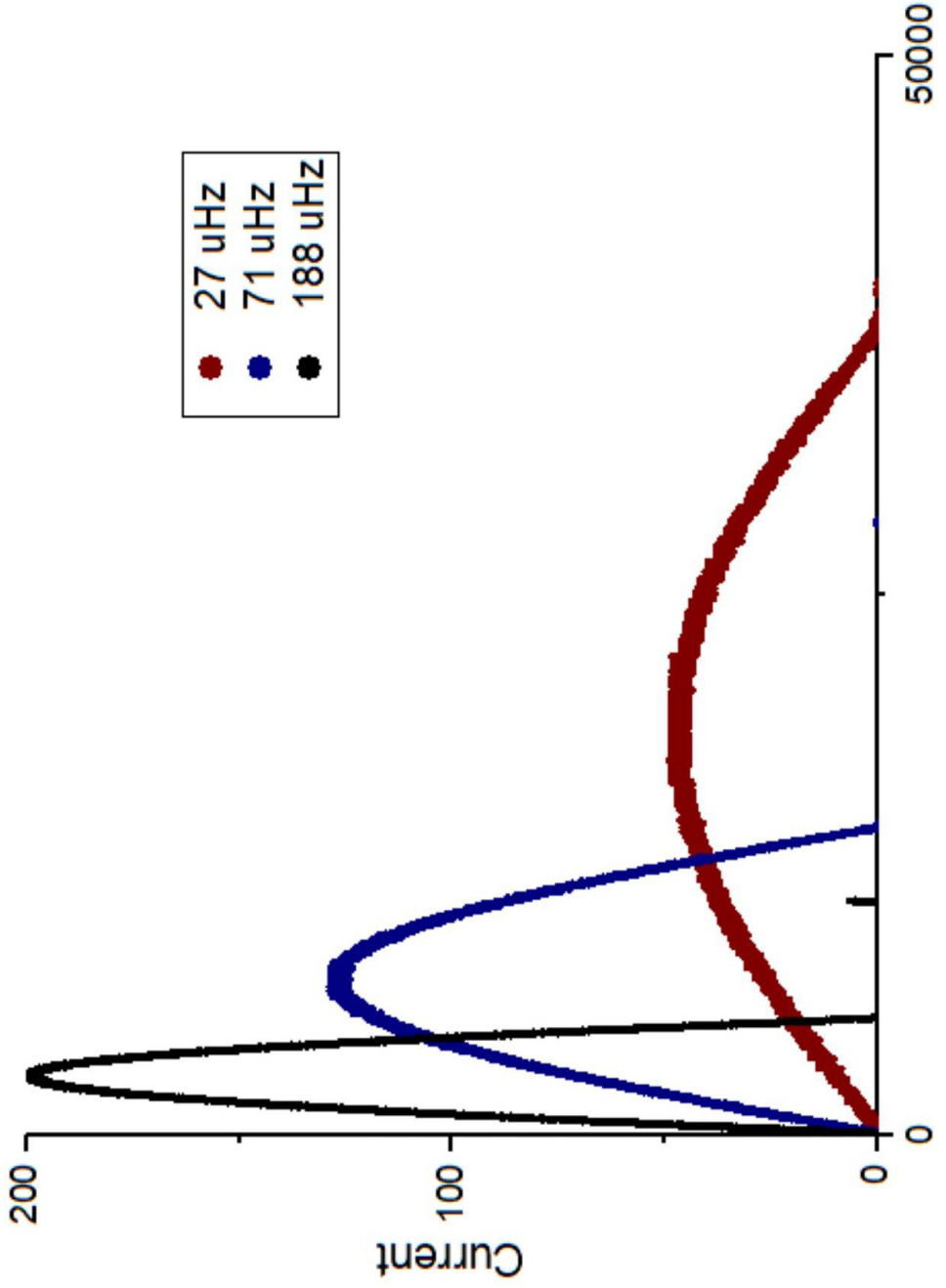

Figure 6

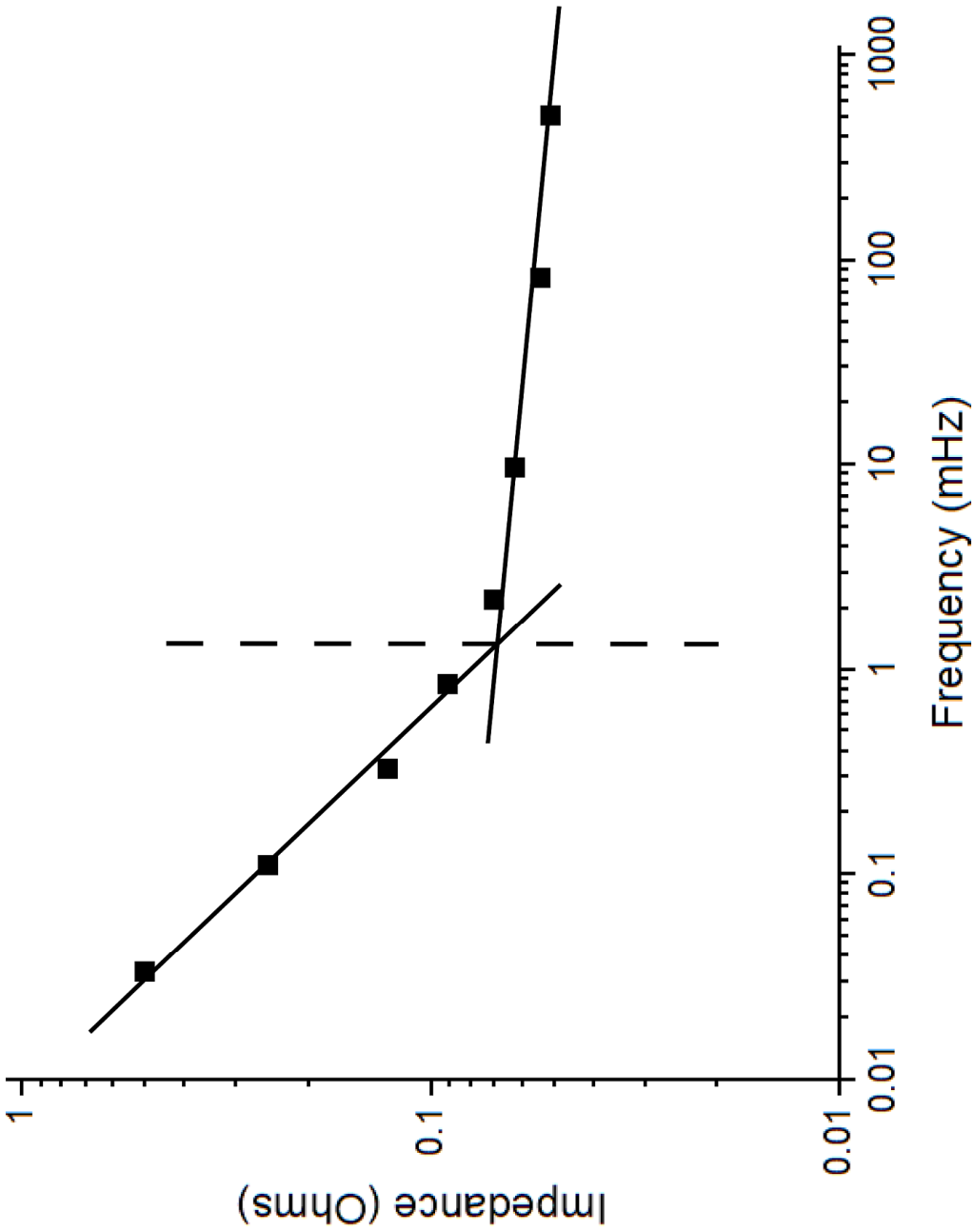

Figure 7

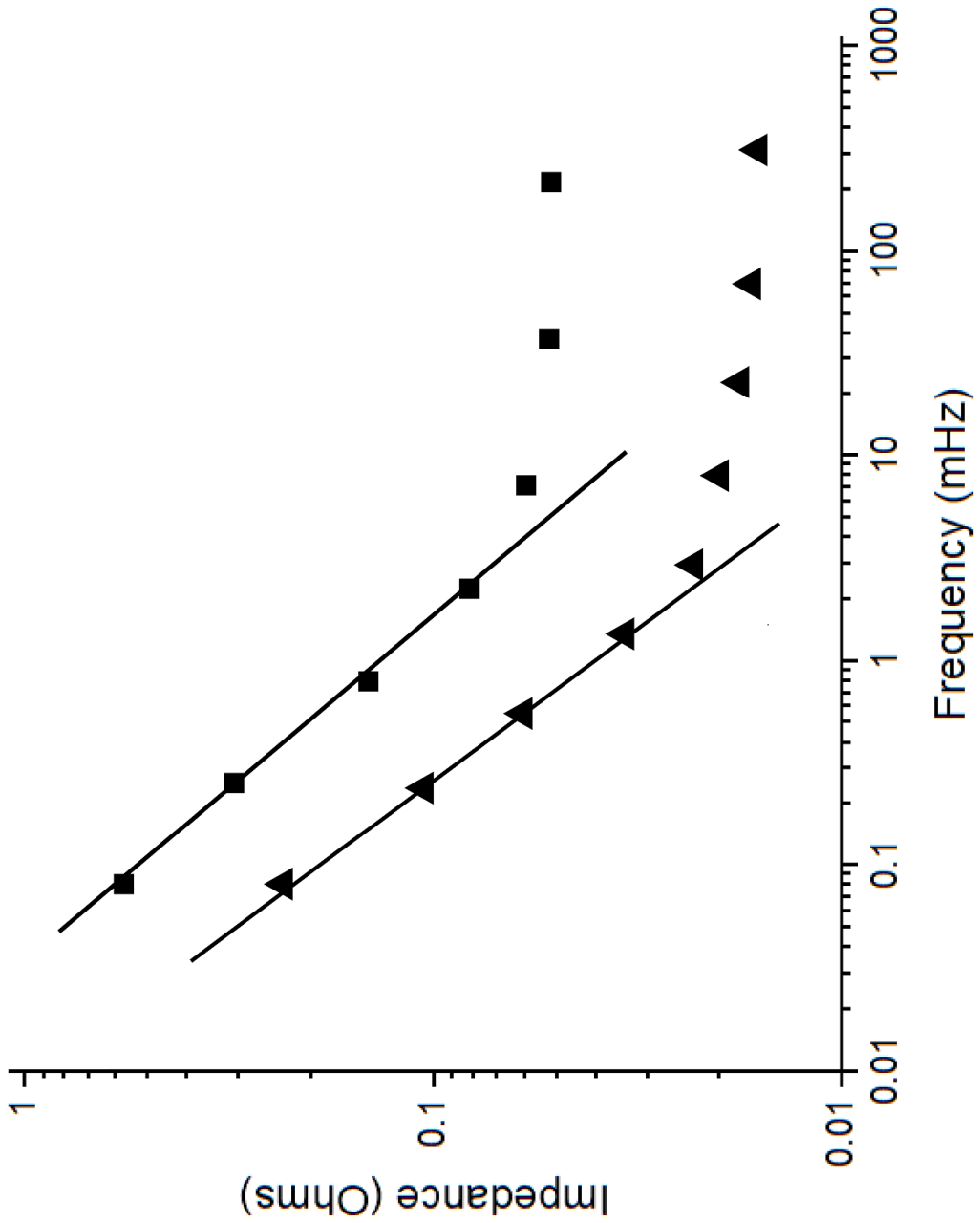

Figure 8

Appendix C

Equipment Datasheets

1260A

Impedance/gain-phase Analyzer

The 1260A Impedance/gain-phase Analyzer is - without doubt - the most powerful, accurate and flexible Frequency Response Analyzer available today.

In daily use by leading researchers wherever measurement integrity and experimental reliability are of paramount importance, 1260A's solid reputation is frequently endorsed in published research papers in fields such as:

- Corrosion studies
- Battery research and fuel cells
- Solar cells
- LCDs
- Bio-materials
- Ceramics / composites
- Electronic component development
- Civil engineering

Part of Solartron Analytical's extensive range of precision products designed to provide cost effective solutions for dc and ac analysis in electrochemical and materials research, 1260A offers an outstanding measurement specification for impedance spectroscopy:

Huge frequency range

Spanning 10µHz to 32MHz with 0.015ppm resolution, 1260A provides excellent coverage for virtually all chemical and molecular mechanisms - all in a single instrument.

Unbeatable accuracy

With an accuracy of 0.1%, 0.1°, measurements can be made with complete confidence, and even the most subtle changes in sample behavior detected and quantized.

Noise free Analysis

1260A uses Solartron Analytical's patented single-sine correlation technique, which inherently removes the noise and harmonic distortion which plagues lesser instruments.

- Frequency resolution: 1 in 65 million (0.015ppm)
- 0.1%, 0.1° accuracy -
- Resolution to 0.001dB, 0.01°
- Measures impedances >100MΩ
- 2-, 3- and 4-terminal measurement configurations
- Polarization voltage up to ±40.95V
- Renowned ZPlot software package simplifies experiments and optimizes throughput

Systems

When combined with other products from Solartron Analytical's range, including well-proven application software, 1260A can form the heart of an advanced electrochemical and materials measurement system, to provide superb accuracy, flexibility and reliability - even for the most complex research problems.

Impedance measurement

Virtually every liquid and solid is able to pass current when a voltage is applied to it. If a variable (ac) voltage is applied to the material, the ratio of voltage to current is known as the impedance. The measured impedance varies with the frequency of the applied voltage in a way that is related to the properties of the liquid or solid. This may be due to the physical structure of the material, to chemical processes within it or a combination of both.

The advantages of impedance measurement over other techniques include:

- Rapid aquisition of data
- Accurate, repeatable measurements
- Non-destructive
- Highly adaptable to a wide variety of different applications
- Ability to differentiate effects due to electrodes, diffusion, mass/charge transfer by analysis over different frequency ranges
- Equivalent circuit/modelling techniques for detailed analysis of results

1260A Impedance/Gain-Phase Analyzer Specification

Generator	Voltage mode	Current mode
AC Amplitude <10MHz >10MHz	0 to 3 V rms 0 to 1 V rms	0 to 60 mA rms 0 to 20 mA rms
Maximum ac resolution	5 mV	100 µA
DC bias range	±40.95 V	±100 mA
Maximum DC resolution	10 mV	200 µA
Output impedance	50 Ω±1%	>200 kΩ <1 kHz
Frequency	Range: 10 µHz to 32 MHz, max resolution: 10 µHz Error: ±100ppm, stability, 24hrs ±1°C: ±10ppm	
Sweep types	Frequency (log or lin), AC/DC voltage, AC/DC current	
Maximum voltage	Hi to lo: ±46 V peak, lo to ground: ±0.4 V peak	
Maximum current	±100 mA peak	
Impedance	Lo to ground: 100 kΩ, <10 nF	
Connection	Single BNC, floating shield	
Output disable	Contact closure or TTL logic 0	

Input System	Voltage (2x)	Current
3 independent analyzers operating in parallel		
Ranges	30 mV, 300 mV, 3 V	6 µA, 60 µA, 600 µA, 6 mA, 60 mA
Maximum resolution	1 µV	200 pA
Full scale peak	±5 V	±100 mA
Inputs protected to	±46 V	±250 mA
Connections	Single/differential BNC	single BNC
Shields	Floating/grounded	
Coupling	DC or AC (-3dB at 1Hz)	DC or AC (-3dB at Hz)
Input Impedance		
Hi to shield	1 MΩ, <35 pF	>600 µA range, 1 Ω
Shield to ground	10 kΩ, 330 pF	
Limits of error	Ambient temperature 20±10°C, integration time >200 ms. Data valid for one year after calibration.	

Results	
Variable	Frequency, AC amplitude, DC bias
Measured parameters	Voltage gain, phase, real, imaginary, Z, R, X, Y, G, B, V, I group delay, C, L, Q, D
Power supply	90 to 126 V, 198 to 252 V, 48 to 65 Hz
Power consumption	230 VA
Dimensions (w x h x d)	432 mm x 176 mm x 573 mm (17 in x 6.93 in x 22.56 in)
Weight	18 kg (40 lbs)
Operating temp. range	0 to 50°C (32 to 122 °F)

Limit of error Gain-phase measurements
Applies to all ranges at >10% full scale

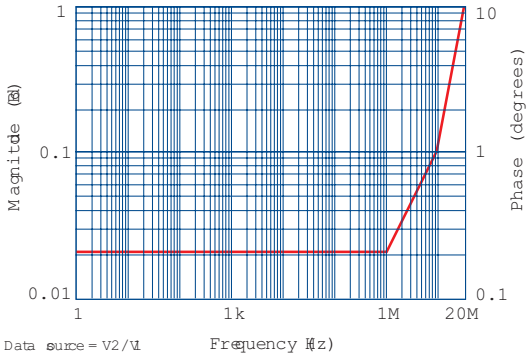

Impedance Measurements
Applies for stimulation level of 1 V for impedances >50 Ω or 20 mA for impedances <50 Ω

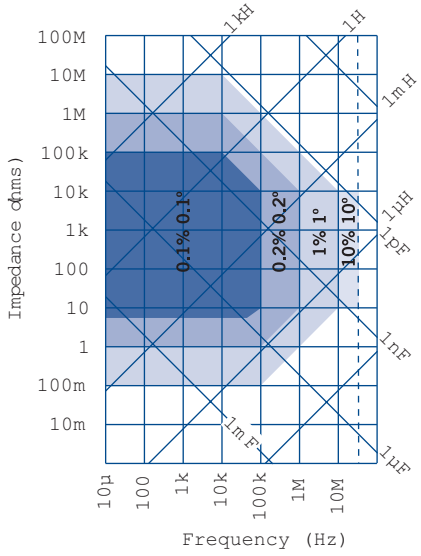

Princeton Applied Research
solartron analytical

www.ameteksi.com si.info@ametek.com

USA

Tel: (865) 425-1289
Fax: (865) 481-2410

Europe

Tel: +44 (0)1252 556800
Fax: +44 (0)1252 556899

Please see our website for a complete list of our global offices and authorized agents

0817A

Keysight Technologies E5260/E5270 Precision IV Analyzer

KEYSIGHT TECHNOLOGIES

Configuration and Connection Guide

Notices

Manual Part Number

E5260-90090

Edition

Edition 1, July 2003
Edition 2, July 2009
Edition 3, July 2015

Published by:
Keysight Technologies, Inc.
1400 Fountaingrove Parkway
Santa Rosa, CA 95403 USA

Warranty

The material contained in this document is provided “as is,” and is subject to being changed, without notice, in future editions. Further, to the maximum extent permitted by applicable law, Keysight disclaims all warranties, either express or implied, with regard to this manual and any information contained herein, including but not limited to the implied warranties of merchantability and fitness for a particular purpose. Keysight shall not be liable for errors or for incidental or consequential damages in connection with the furnishing, use, or performance of this document or of any information contained herein. Should Keysight and the user have a separate written agreement with warranty terms covering the material in this document that conflict with these terms, the warranty terms in the separate agreement shall control.

Technology Licenses

The hardware and/or software described in this document are furnished under a license and may be used or copied only in accordance with the terms of such license.

Restricted Rights Legend

If software is for use in the performance of a U.S. Government prime contract or subcontract, Software is delivered and licensed as “Commercial computer software” as defined in DFAR 252.227-7014 (June 1995), or as a “commercial item” as defined in FAR 2.101(a) or as “Restricted computer software” as defined in FAR 52.227-19 (June 1987) or any equivalent agency regulation or contract clause. Use, duplication or disclosure of Software is subject to Keysight Technologies’ standard commercial license terms, and non-DOD Departments and Agencies of the U.S. Government will receive no greater than Restricted Rights as defined in FAR 52.227-19(c)(1-2) (June 1987). U.S. Government users will receive no greater than Limited Rights as defined in FAR 52.227-14 (June 1987) or DFAR 252.227-7015 (b)(2) (November 1995), as applicable in any technical data.

NOTICE: This document contains references to Agilent Technologies. Agilent's former Test and Measurement business has become Keysight Technologies. For more information, go to **www.keysight.com.**

In This Document

This document provides the following information about Keysight E5260/E5270 Precision IV Analyzer.

1. E5260/E5270 series Product Configuration

   Describes the product configuration of the E5260/E5270.

2. Accessories for E5260/E5270

   Describes the available accessories for the E5260/E5270.

3. Connection Guide for Wafer Prober

   Describes how to connect the E5260/E5270, accessories, and a DUT interface such as wafer prober and your own test fixture.

4. Connection and Ordering Examples

   Describes fixture/prober connection and ordering examples.

Contents

Contents

1 E5260/E5270 series Product Configuration

KEYSIGHT TECHNOLOGIES

1.1 Product line up of the E5260/E5270 series

The Keysight E5260/E5270 Precision IV analyzer offers very accurate IV characterization solution. Using the powerful characterization software, EasyEXPERT group+ and integrated source and measurement units (SMUs), Precision IV analyzer can quickly enable highly accurate current-voltage measurement. This high performance IV analyzer with current measurement capability as low as 0.1 fA, along with SMU scalability, meets the requirements of advanced IV characterization, with the lowest pricing range.

With its intuitive graphical user interface, Keysight's EasyEXPERT group+ software which is included in the Precision IV analyzer, supports all of the characterization tasks from measurement setup through to data analysis and protection.

This complete device characterization platform, tailored for the Precision IV analyzer, can be installed on any PC and can quickly and efficiently accelerate the IV characterization of various materials and devices without the need for configuring instruments and programing. The EasyEXPERT group+ also offers robust analysis capabilities, reporting functions, and can be installed on multiple PCs to allow for cross-departmental group work.

The Precision IV analyzer series offers four product models. Two channel models offer fixed configuration at an affordable price. Eight slot models provide scalability and flexibility of configurable SMU modules. Any model contains triaxial cables for GNDU and SMU, GNDU to Kelvin adapter, USB-GPIB interface and EasyEXPERT group+ install media.

- **E5260A/E5270B Precision IV Analyzer (configurable up to 8 channels)**

  The E5260A/E5270B mainframe that provides the ground unit (GNDU) and eight empty slots for the measurement facilities can be controlled by external PC with the Keysight EasyEXPERT group+ software. The EasyEXPERT group+ is the GUI based measurement control and analysis software runs on the Windows operation system.

- **HPSMU module (E5260A-A10 / E5270B-A10)**

  High power source/monitor unit module. Occupies two slots.

- **MPSMU module (E5260A-A11 / E5270B-A11)**

  Medium power source/monitor unit module. Occupies one slot.

- **HRSMU module (E5270B-A17)**

High resolution source/monitor unit module. Occupies one slot. It is only available in the E5270B Precision IV Analyzer / 8 Slot Precision Measurement Mainframe. Needs Keysight E5288A ASU (option A28) to perform atto level current measurement or automatic switching of the measurement resources connection.

- **Atto sense and Switch Unit (E5270B-A28)**

  Atto sense and switch unit (ASU). Used to enable the 1 pA range for the atto level current measurement, also switch the measurement resource connected to the DUT. The measurement resource can be HRSMU or the instrument connected to the AUX terminal.

Figure 1-1 **E5260A IV analyzer Front View**

Figure 1-2 **E5262A/E5263A 2 channel IV analyzer Front View**

Figure 1-3 E5270B Precision IV analyzer Front View

Table 1-1 Mainframe Specification

Available Slots	**8 (8 slot model)**
Ground Unit (GNDU) sink capability	**4 A (2.2A for 2ch model)**
Instrument control	**GPIB**
External trigger inputs / outputs	**1 BNC Trigger in, 1 BNC Trigger out, 8 Programmable Trigger In/Out**

Table 1-2 SMU Module Variation (E5260A/E5262A/E5263A)

Module	Key specification				
	Max. Current	Max. Voltage	Current means. Resolu-tion	Voltage means. Resolu-tion	Req'd slots
HPSMU (High Power SMU)	±1 A	±200 V	5 pA	100 µV	2
MPSMU (Medium Power SMU)	±200 mA	±100 V	5 pA	100 µV	1

Table 1-3 SMU Module Variation (E5270B)

Module	Key specification				
	Max. Current	Max. Voltage	Current means. Resolu-tion	Voltage means. Resolu-tion	Req'd slots
HPSMU (High Power SMU)	±1 A	±200 V	10 fA	2 µV	2
MPSMU (Medium Power SMU)	±100 mA	±100 V	10 fA	0.5 µV	1
HRSMU (High Resolution SMU)	±100 mA	±100 V	1 fA	0.5 µV	1
ASU (Atto Sense and Switch Unit)	±100 mA	±100 V	0.1 fA	0.5 µV	NA

1.2 Options of E5270B Precision IV analyzer

This section describes Option items of the Keysight E5270B Precision IV Analyzer / 8 Slot Precision Measurement Mainframe.

Table 1-4 B1500A Options

Model/ Option	Description	OP Instruction
Mainframe		
E5270B	Precision IV Analyzer / 8 Slot Precision Measurement Mainframe	• Select option 015 or 030 to specify cable length. • Select option 050 or 060 to specify Power line frequency. • The following accessories are included. See Table 1-8, for more details of furnished accessories. One Interlock cable (1.5 m or 3.0 m) One GNDU cable (1.5 m or 3.0 m) One Triaxial cable (1.5 m or 3.0 m) GNDU to Kelvin adapter CD media for user's guide CD media for EasyEXPERT group+ SWS License To Use (LTU) for EasyEXPERT group+ software USB-GPIB interface
Select pre-configured package options (optional)		
E5270B-A01	Mid Power Source/Monitor Unit (4ea), Cables	• This package contains four MPSMU and eight Triaxial cables. • Cable length 1.5 m or 3.0 m is specified by option 015 or 030.
E5270B-A02	Mid power Source/Monitor unit (2ea), High Resolution Unit (2ea), Cables	• This package contains two MPSMU, two HRSMU and eight triaxial cables. • Cable length 1.5 m or 3.0 m is specified by option 015 or 030.
E5270B-A03	High Resolution Source/Monitor Unit (4ea), Cables	• This package contains four HRSMU and eight triaxial cables. • Cable length 1.5 m or 3.0 m is specified by option 015 or 030.
Select add-on packages (optional)		
E5270B-A10	Add High Power Source/Monitor Unit (E5280B) 1ea, Cables	• HPSMU add-on package adds one HPSMU and two triaxial cables. • Cable length 1.5 m or 3.0 m is specified by option 015 or 030.

Model/ Option	Description	OP Instruction
E5270B-A11	Add Mid Power Source/Monitor Unit (E5281B) 1ea, Cables	• MPSMU add-on package adds one MPSMU and two triaxial cables. • Cable length 1.5 m or 3.0 m is specified by option 015 or 030.
E5270B-A17	Add High Resolution Source/Monitor Unit (E5287A) 1ea, Cables	• HRSMU add-on package adds one HRSMU and two triaxial cables. • Cable length 1.5 m or 3.0 m is specified by option 015 or 030.
E5270B-A28	Add Atto Sense and Switch Unit (E5288A ASU) 1ea	• ASU add-on package adds one ASU, one D-sub cable, and one triaxial cable. • It requires option A17 Add HRSMU. • Cable length 1.5 m or 3.0 m is specified by option 015 or 030.
Specify the cable length (mandatory)		
E5270B-015	1.5 m cable length	• 1.5 m cable length (for bundled cables and for package options)
E5270B-030	3.0 m cable length	• 3.0 m cable length (for bundled cables and for package options)
Specify the power line frequency (mandatory)		
E5270B-050	50Hz line frequency	
E5270B-060	60Hz line frequency	
Select rack mount kit (optional)		
E5270B-1CM	Rack mount kit for E5270B	• Rack mount kit for the E5270B. • 5U height EIA
Specify the language of the paper manuals if you need (optional)		
E5270B-ABA	Printed Manuals (English)	• Printed manuals are optional. Order this option to get the paper manuals. Contains E5260/E5270 user guide, Plug & Play driver user guide, self-paced training manual, EasyEXPERT user guide, and programming guide.
E5270B-ABJ	Printed Manuals (Japanese)	
Bundled accessories delete option (optional)		
E5270B-DLA	Delete Accessories Bundled for Analyzer Use	• This option deletes USB-GPIB interface, CD Media for EasyEXPERT group+, and LTU for EasyEXPERT group+ software.
Select calibration options (optional)		

Model/ Option	Description	OP Instruction
E5270B-A6J	ANSI Z540-1-1994 Calibration	• Test Data for ISO 9001/2 Commercial Calibration. This option provides measurement test data for the standard commercial calibration and test equipment trace information.
E5270B-UK6	Commercial calibration certificate with test data	
Refurbished product		
E5270B -RMKT	Keysight Refurbished products	• Shipment of used product from factory.
Startup assistance		
PS-S20-01	Keysight 1 day startup assistance	• Startup assistance & product training.

1.3 Options of E5260A IV analyzer

This section describes Option items of the Keysight E5260A IV Analyzer / 8 Slot High speed Measurement Mainframe.

Table 1-5 B1500A Options

Model/ Option	Description	OP Instruction
Mainframe		
E5260A	IV Analyzer / 8 Slot High speed Measurement Mainframe	• Select option 015 or 030 to specify cable length. • Select option 050 or 060 to specify Power line frequency. • The following accessories are included. See Table 1-8, for more details of furnished accessories. One Interlock cable (1.5 m or 3.0 m) One GNDU cable (1.5 m or 3.0 m) One Triaxial cable (1.5 m or 3.0 m) GNDU to Kelvin adapter CD media for user's guide CD media for EasyEXPERT group+ SWS License To Use (LTU) for EasyEXPERT group+ software USB-GPIB interface
Select pre-configured package options (optional)		
E5260A-A01	Mid Power Source/Monitor Unit (4ea), Cables	• This package contains four MPSMU and eight Triaxial cables. • Cable length 1.5 m or 3.0 m is specified by option 015 or 030.
Select add-on packages (optional)		
E5260A-A10	Add High Power Source/Monitor Unit (E5290A) 1ea, Cables	• HPSMU add-on package adds one HPSMU and two triaxial cables. • Cable length 1.5 m or 3.0 m is specified by option 015 or 030.
E5260A-A11	Add Mid Power Source/Monitor Unit (E5291A) 1ea, Cables	• MPSMU add-on package adds one MPSMU and two triaxial cables. • Cable length 1.5 m or 3.0 m is specified by option 015 or 030.
Specify the cable length (mandatory)		
E5260A-015	1.5 m cable length	• 1.5 m cable length (for bundled cables and for package options)

Model/ Option	Description	OP Instruction
E5260A-030	3.0 m cable length	• 3.0 m cable length (for bundled cables and for package options)
Specify the power line frequency (mandatory)		
E5260A-050	50Hz line frequency	
E5260A-060	60Hz line frequency	
Select rack mount kit (optional)		
E5260A-1CM	Rack mount kit for E5260A	• Rack mount kit for the E5260A. • 5U height EIA
Specify the language of the paper manuals if you need (optional)		
E5260A-ABA	Printed Manuals (English)	• Printed manuals are optional. Order this option to get the paper manuals. Contains E5260/E5270 user guide, Plug & Play driver user guide, self-paced training manual, EasyEXPERT user guide, and programming guide.
E5260A-ABJ	Printed Manuals (Japanese)	
Bundled accessories delete option (optional)		
E5260A-DLA	Delete Accessories Bundled for Analyzer Use	• This option delete USB-GPIB interface, CD Media for EasyEXPERT group+, and LTU for EasyEXPERT group+ software.
Select calibration options (optional)		
E5260A-A6J	ANSI Z540-1-1994 Calibration	• Test Data for ISO 9001/2 Commercial Calibration. This option provides measurement test data for the standard commercial calibration and test equipment trace information.
E5260A-UK6	Commercial calibration certificate with test data	
Refurbished product		
E5260A -RMKT	Keysight Refurbished products	• Shipment of used product from factory.
Startup assistance		
PS-S20-01	Keysight 1 day startup assistance	• Startup assistance & product training.

1.4 Options of E5262A 2 channel IV analyzer

This section describes Option items of the Keysight E5262A 2 Channel IV Analyzer / Source Monitor Unit (Two Medium Power SMUs).

Table 1-6 B1500A Options

Model/ Option	Description	OP Instruction
Mainframe		
E5262A	2 Channel IV Analyzer / Source Monitor Unit (Two Medium Power SMUs)	• This model includes two MPSMUs and GNDU (2.2A). • Select option 015 or 030 to specify cable length. • Select option 050 or 060 to specify Power line frequency. • The following accessories are included. See Table 1-8, for more details of furnished accessories. One Interlock cable (1.5 m or 3.0 m) One GNDU cable (1.5 m or 3.0 m) Five Triaxial cables (1.5 m or 3.0 m) GNDU to Kelvin adapter CD media for user's guide CD media for EasyEXPERT group+ SWS License To Use (LTU) for EasyEXPERT group+ software USB-GPIB interface
Specify the cable length (mandatory)		
E5262A-015	1.5 m cable length	• 1.5 m cable length (for bundled cables)
E5262A-030	3.0 m cable length	• 3.0 m cable length (for bundled cables)
Specify the power line frequency (mandatory)		
E5262A-050	50Hz line frequency	
E5262A-060	60Hz line frequency	
Select rack mount kit (optional)		
E5262A-1CM	Rack mount kit for E5262A	• Rack mount kit for the E5262A. • 3U height EIA
Specify the language of the paper manuals if you need (optional)		

Model/ Option	Description	OP Instruction
E5262A-ABA	Printed Manuals (English)	• Printed manuals are optional. Order this option to get the paper manuals. Contains E5260/E5270 user guide, Plug & Play driver user guide, self-paced training manual, EasyEXPERT user guide, and programming guide.
E5262A-ABJ	Printed Manuals (Japanese)	
Bundled accessories delete option (optional)		
E5262A-DLA	Delete Accessories Bundled for Analyzer Use	• This option delete USB-GPIB interface, CD Media for EasyEXPERT group+, and LTU for EasyEXPERT group+ software.
Select calibration options (optional)		
E5262A-A6J	ANSI Z540-1-1994 Calibration	• Test Data for ISO 9001/2 Commercial Calibration. This option provides measurement test data for the standard commercial calibration and test equipment trace information.
E5262A-UK6	Commercial calibration certificate with test data	
Refurbished product		
E5262A -RMKT	Keysight Refurbished products	• Shipment of used product from factory.
Startup assistance		
PS-S20-01	Keysight 1 day startup assistance	• Startup assistance & product training.

1.5 Options of E5263A 2 channel IV analyzer

This section describes Option items of the Keysight E5262A 2 Channel IV Analyzer / Source Monitor Unit (High Power SMU, Medium Power SMU).

Table 1-7 B1500A Options

Model/ Option	Description	OP Instruction
Mainframe		
E5263A	2 Channel IV Analyzer / Source Monitor Unit (High Power SMU, Medium Power SMU)	• This model includes one HPSMU, one MPSMU and GNDU (2.2A). • Select option 015 or 030 to specify cable length. • Select option 050 or 060 to specify Power line frequency. • The following accessories are included. See Table 1-8, for more details of furnished accessories. One Interlock cable (1.5 m or 3.0 m) One GNDU cable (1.5 m or 3.0 m) Five Triaxial cables (1.5 m or 3.0 m) GNDU to Kelvin adapter CD media for user's guide CD media for EasyEXPERT group+ SWS License To Use (LTU) for EasyEXPERT group+ software USB-GPIB interface
Specify the cable length (mandatory)		
E5263A-015	1.5 m cable length	• 1.5 m cable length (for bundled cables)
E5263A-030	3.0 m cable length	• 3.0 m cable length (for bundled cables)
Specify the power line frequency (mandatory)		
E5263A-050	50Hz line frequency	
E5263A-060	60Hz line frequency	
Select rack mount kit (optional)		
E5263A-1CM	Rack mount kit for E5263A	• Rack mount kit for the E5263A. • 3U height EIA
Specify the language of the paper manuals if you need (optional)		

Model/ Option	Description	OP Instruction
E5263A-ABA	Printed Manuals (English)	• Printed manuals are optional. Order this option to get the paper manuals. Contains E5260/E5270 user guide, Plug & Play driver user guide, self-paced training manual, EasyEXPERT user guide, and programming guide.
E5263A-ABJ	Printed Manuals (Japanese)	
Bundled accessories delete option (optional)		
E5263A-DLA	Delete Accessories Bundled for Analyzer Use	• This option delete USB-GPIB interface, CD Media for EasyEXPERT group+, and LTU for EasyEXPERT group+ software.
Select calibration options (optional)		
E5263A-A6J	ANSI Z540-1-1994 Calibration	• Test Data for ISO 9001/2 Commercial Calibration. This option provides measurement test data for the standard commercial calibration and test equipment trace information.
E5263A-UK6	Commercial calibration certificate with test data	
Refurbished product		
E5263A -RMKT	Keysight Refurbished products	• Shipment of used product from factory.
Startup assistance		
PS-S20-01	Keysight 1 day startup assistance	• Startup assistance & product training.

1.6 Furnished accessories

Furnished accessories of the E5260/E5270 series Precision IV analyzer and furnished accessories of package options are described in this chapter.

Table 1-8 Furnished accessories on the B1500A semiconductor device analyzer mainframe

Description	Qty.	Note
Interlock cable	1	Cable length 1.5 m or 3.0 m is specified by the option 015 or 030. 
GNDU cable	1	Cable length 1.5 m or 3.0 m is specified by the option 015 or 030. 
GNDU Kelvin adapter	1	GNDU Kelvin adapter must be directly connected to the E5260/E5270 GNDU connector for taking out the GNDU Force and Sense to the individual connectors. Then the GNDU cable must be used for extending the GNDU Force. And the triaxial cable must be used for the Sense. 
Triaxial cable	1	Cable length 1.5 m or 3.0 m is specified by the option 015 or 030. 
Power cable	1	Power cable for the E5260/E5270

Description	Qty.	Note
Software CD	1	Media for EasyEXPERT group+ software
License Sheet	1	SWS License-to-use for EasyEXPERT group+ software.
Driver/Tools CD	1	VXIplug&play driver.

The EasyEXPERT group+ software includes the following utility program. For more details, see Keysight EasyEXPERT User's Guide.

- Prober control program
- sleep.exe program
- 4155/4156 setup file converter
- MDM file converter for IC-CAP users

Table 1-9 E5260A/E5270B-A01 Mid Power Source/Monitor Unit (4ea), Cables

Description	Qty.	Note
MPSMU	4	Installed Medium power source/monitor unit (MPSMU)
Triaxial cable	8	Cable length 1.5 m or 3.0 m is specified by the option 015 or 030.

Table 1-10 E5270B-A02 Mid power Source/Monitor unit (2ea), High Resolution Unit (2ea), Cables

Description	Qty.	Note
MPSMU	2	Installed Medium power source/monitor unit (MPSMU)
HRSMU	2	Installed High resolution source/monitor unit (HRSMU)
Triaxial cable	8	Cable length 1.5 m or 3.0 m is specified by the option E5270B-015 or E5270B-030.

Table 1-11 E5270B-A03 High Resolution Source/Monitor Unit (4ea), Cables

Description	Qty.	Note
HRSMU	4	Installed High resolution source/monitor unit (HRSMU)
Triaxial cable	8	Cable length 1.5 m or 3.0 m is specified by the option E5270B-015 or E5270B-030.

Table 1-12 E5260A/E5270B-A10 Add High Power Source/Monitor Unit 1ea, Cables

Description	Qty.	Note
HPSMU	1	Installed High power source/monitor unit (HPSMU)
Triaxial cable	2	Cable length 1.5 m or 3.0 m is specified by the option 015 or 030.

Table 1-13 E5260A/E5270B-A11 Add Mid Power Source/Monitor Unit 1ea, Cables

Description	Qty.	Note
MPSMU	1	Installed Medium power source/monitor unit (MPSMU)
Triaxial cable	2	Cable length 1.5 m or 3.0 m is specified by the option 015 or 030.

Table 1-14 E5270B-A17 Add High Resolution Source/Monitor Unit (E5287A) 1ea, Cables

Description	Qty.	Note
HRSMU	1	Installed High resolution source/monitor unit (HRSMU)
Triaxial cable	2	Cable length 1.5 m or 3.0 m is specified by the option E5270B-015 or E5270B-030.

Table 1-15 E5270B-A28 Add Atto Sense and Switch Unit (E5288A ASU) 1ea

Description	Qty.	Note
ASU	1	Atto sense switch unit (E5288A ASU), 1 ea. 
Triaxial and D-sub cable for ASU	1	Triaxial/D-sub Cable for ASU (16493M). Cable length 1.5 m or 3.0 m is specified by the option E5270B-015 or E5270B-030.  

1.7 Upgrade products for the E5260/E5270 series

The Keysight E5260A and E5270B have 8 slots so that users can install appropriate modules into mainframe. The upgrade/retrofit product is available to add more modules. These modules should be installed in Keysight Technologies service center to meet the specifications.

1.7.1 Option of E5270BU upgrade kit

The following table lists the upgrade products and related accessories for the E5270 series.

NOTE Keysight Technologies service center is responsible for module installation. Contact Keysight Technologies to get an estimation and order.

Table 1-16 Keysight E5270BU Upgrade kit for E5270B

Model/Option	Description	OP Instruction
Module upgrade		
E5270BU-080	Precision High Power Source/Monitor Unit Module (E5280B) / No cable included	Max. 1 A/200 V, 10 fA/2 µV resolution High power source/monitor unit module for use in the E5270B mainframe. This module consumes 2 slots.
E5270BU-081	Precision Medium Power Source/Monitor Unit Module (E5281B) / No cable included	Max. 100 mA/100 V, 10 fA/0.5 µV resolution Medium power source/monitor unit module for use in the E5270B mainframe. SMU has Kelvin connection port (Force / Sense terminal). This module consumes 1 slot.
E5270BU-087	High Resolution Source/Monitor Unit Module (E5287A) / No cable included	Max. 100 mA/100 V, 1 fA/0.5 µV resolution High resolution source/monitor unit module for use in the E5270B mainframe. SMU has Kelvin connection port (Force / Sense terminal) and the ASU D-sub connector. This module consumes 1 slot.
E5270BU-88A	Atto Sense And Switch Unit (E5288A ASU) with 1.5 m Triaxial and Dsub Cable. (HRSMU is required.)	0.1 fA (100 aA) resolution which is used with HRSMU. 1 Triaxial, 2 BNC input ports and 1 communication D-sub input between ASU and SMU. BNC inputs terminal can be used for external LCR meter, Pulse Generator or other instrument. Cables for DUT is not included.
E5270BU-88B	Atto Sense And Switch Unit (E5288A ASU) with 3 m Triaxial and Dsub Cable. (HRSMU is required.)	
EasyEXPERT extension support		

Model/Option	Description	OP Instruction
E5270BU-SWS	EasyEXPERT upgrade, extension support and subscription	EasyEXPERT upgrade, extension support and subscription includes the license to use (LTU) of EasyEXPERT group+ software. If you do not have the LTU, it is required to order option SWS when you use EasyEXPERT group+ software with E5270B.
E5270BU-SWD	EasyEXPERT upgrade, extension support and subscription (price adjustment)	If you quote or order the hardware upgrade and the S/N of E5270B is less than MY55250101, option SWS and option SWD for price adjustment are bundled in the order.
Manual and media option		
E5270BU-ABA	Printed Manuals (English)	Printed manuals are optional. Order this option to get the paper manuals. Contains E5260/E5270 user guide, Plug & Play driver user guide, self-paced training manual, EasyEXPERT user guide, and programming guide.
E5270BU-ABJ	Printed Manuals (Japanese)	
Cable option		
16494A	Triaxial cable	The E5270BU module option does not include any triaxial cables. If you need any triaxial cables for instrument or switches, please specify the following optional cables.
16494A-001	Triaxial cable (1.5 m)	Need to specify cable option and quantity.
16494A-002	Triaxial cable (3 m)	
16494A-003	Triaxial cable (80 cm)	
16494A-004	Triaxial cable (40 cm)	
16494A-005	Triaxial cable (4 m)	
Refurbished product		
E5270BU-RMKT	Keysight refurbished product	Shipment of used product from factory.
Startup assistance		
PS-S20-01	Keysight 1 day startup assistance	Startup assistance and product training.

1.7.2 Option of E5260AU upgrade kit

The following table lists the upgrade products and related accessories for the E5260 series.

NOTE Keysight Technologies service center is responsible for module installation. Contact Keysight Technologies to get an estimation and order.

Table 1-17 Keysight E5260AU Upgrade kit for E5260A/E5262A/E5263A

Model/Option	Description	OP Instruction
Module upgrade		
E5260AU-090	High Speed High Power Source/Monitor Unit Module (E5290A) / No cable included	Max. 1 A/200 V, 5 pA/100 µV resolution High power source/monitor unit module for use in the E5260A mainframe. This module consumes 2 slots. Module upgrade is not available for the E5262A and E5263A.
E5260AU-091	High Speed Medium Power Source/Monitor Unit Module (E5291A) / No cable included	Max. 200 mA/100 V, 5 pA/100 µV resolution Medium power source/monitor unit module for use in the E5260A mainframe. SMU has Kelvin connection port (Force / Sense terminal). This module consumes 1 slot. Module upgrade is not available for the E5262A and E5263A.
EasyEXPERT extension support		
E5260AU-SWS	EasyEXPERT upgrade, extension support and subscription	EasyEXPERT upgrade, extension support and subscription includes the license to use (LTU) of EasyEXPERT group+ software. If you do not have the LTU, it is required to order option SWS when you use EasyEXPERT group+ software with the Keysight E5260A/E5262A/E5263A.
E5260AU-SWD	EasyEXPERT upgrade, extension support and subscription (price adjustment)	If you quote or order the hardware upgrade and the S/N of E5260A is less than MY55250101, option SWS and option SWD for price adjustment are bundled in the order.
Cable option		
16494A	Triaxial cable	The E5260AU module option does not include any triaxial cables. If you need any triaxial cables for instrument or switches, please specify the following optional cables.
16494A-001	Triaxial cable (1.5 m)	Need to specify cable option and quantity.
16494A-002	Triaxial cable (3 m)	
16494A-003	Triaxial cable (80 cm)	
16494A-004	Triaxial cable (40 cm)	
16494A-005	Triaxial cable (4 m)	

Model/Option	Description	OP Instruction
Refurbished product		
E5260AU-RMKT	Keysight refurbished product	Shipment of used product from factory.
Startup assistance		
PS-S20-01	Keysight 1 day startup assistance	Startup assistance and product training.

1.7.3 About Plug-in modules

Keysight Technologies is responsible for the module installation of Keysight E5260A / E5270B. Contact Keysight Technologies for the module installation. Then send the following equipment and accessories to Keysight Technologies.

- E5260A / E5270B
- Plug-in modules to be installed
- ASU, for installing the exclusive SMU or retrofitting ASU only
- Connection cable between ASU and SMU, for installing the exclusive SMU or retrofitting ASU only

For returning ASU, do not forget to notify the combination of the unit, connection cable, and module channel.

WARNING **To prevent electrical shock, turn off Keysight E5260/E5270 and remove the power cable before removing the connection cables.**

NOTE Connect ASU to dedicated SMU

The specifications are satisfied and guaranteed for the exclusive combination of the ASU and the HRSMU. So confirm the serial number of the ASU and connect it to the dedicated SMU properly.

NOTE About warranty of E5270BU/E5260AU upgrade kit

The warranty term of E5270BU/E5260AU upgrade kit is 90 days as independent module. The warranty for E5260/E5270 mainframe covers upgraded modules also. If the warranty term of E5260/E5270 mainframe is not long enough, some custom extended warranty products (Return to Keysight) are available. Contact Keysight Technologies to extend warranty support.

1.7.4 Maximum Module Configuration

The E5260/E5270 mainframe can contain any combination of the supported module. However, the total power consumption of all SMU modules cannot exceed 80 W. Using the HPSMU, MPSMU, and HRSMU, it is impossible to create a combination that exceeds the 80 Watt limit. For the E5262A/E5263A, there are no power restrictions. Both mainframes support having both of their modules simultaneously output maximum voltage or current.

- Up to 8 MPSMU
- Up to 8 HRSMU
- Up to 4 HPSMU

1.7.5 Module type and locations

Module locations when the E5260/E5270 is shipped from the factory are shown in Table 1-18. This table shows the relative locations by the module types.

The medium power source/monitor unit (MPSMU) and high resolution source/monitor unit (HRSMU) occupy one slot. Hence, the MPSMU/HRSMU can be installed in any slot. Also, the channel number is the same as the slot number. The HRSMU is only available for E5270B mainframe.

The high power source/monitor unit (HPSMU) occupies two slots. Thus, the HPSMU can be installed in slots 1 to 2, 2 to 3, 3 to 4, 5 to 6, 6 to 7, or 7 to 8. The channel number is the larger slot number for the slots the HPSMU occupies. For example, if a HPSMU occupies slots 5 and 6, the channel number for the module must be 6. Channel numbers 1 and 5 are not available for the HPSMU.

Table 1-18 Module Installation Rule in the Factory

<table>
<tr><th colspan="2">Slot Number and Location</th><th>SMU type and port number</th></tr>
<tr><td>0</td><td>Frame</td><td>GNDU/ADC (Always installed)</td></tr>
<tr><td>1</td><td>top/left</td><td>High Resolution SMU (HRSMU, E5270B only)</td></tr>
<tr><td rowspan="3">:
:
:
:
:
:
:
:</td><td rowspan="3">:
:
:
:
:
:
:
:
:</td><td>Medium Power SMU (MPSMU)</td></tr>
<tr><td>High Power SMU (HPSMU, occupies 2 slots.)</td></tr>
<tr><td></td></tr>
<tr><td>7</td><td></td></tr>
<tr><td>8</td><td>bottom/right</td><td></td></tr>
</table>

NOTE About E5262A/E5263A

The Keysight E5262A and E5263A are fixed-configuration dual SMU instruments. The E5262A has two MPSMUs. The E5263A has one HPSMU and one MPSMU. These SMU configurations cannot be modified.

NOTE About E5260A and E5270B

The E5260A mainframe only support E5290A HPSMU and E5291A MPSMU. The E5280B, E5281B and E5287A cannot be used with the E5260A mainframe.

The E5270B mainframe only support E5280B HPSMU, E5281B MPSMU and E5287A HRSMU. The E5290A and E5291A cannot be used with the E5270B mainframe.

1.8 EasyEXPERT group+ software

This section describes Keysight EasyEXPERT group+ software and related functions. For technical details of EasyEXPERT group+ software, refer to data sheet of E5260/E5270 or www.keysight.com/find/easyexpert web site.

NOTE The EasyEXPERT group+ is upgradeable from the previous generation of EasyEXPERT/Desktop EasyEXPERT software.

1.8.1 Functions and capabilities

Keysight EasyEXPERT group+ software is a specially-designed Windows application program for controlling Keysight Precision Current-Voltage Analyzer series. The EasyEXPERT group+ provides the easy and effective measurement and analysis environment with intuitive graphical user interface (GUI). In addition, the EasyEXPERT group+ for PC supports Offline mode and control capability of the other instrument through GPIB interface. Some of the functions are listed below.

- Single measurement, repeat measurement, and append measurement
- Switching matrix control
- Measurement/setup data management by workspace
- Graph display and analysis with markers, cursors, and lines; and auto analysis
- Password protection and user level access control to protect the data and measurement setup
- Data import/export capability, data output by CSV/XML format, and graph output by EMF/BMP/GIF/PNG format
- Maintenance; self-test and self-calibration

The E5260/E5270 supports the following functionality in the EasyEXPERT group+.

- I/V sweep
- Multi-ch I/V sweep
- I/V list sweep
- Switching matrix control

NOTE To control E5260/E5270 by EasyEXPERT group+, the following firmware is required.

E5260A/E5262A/E5263A: B.01.10 or later
E5270B: B.01.10 or later

NOTE The EasyEXPERT group+ for PC supports most EasyEXPERT group+ functions. However, some functions are not supported on an external computer due to differences in hardware and so on.

Operation mode

The EasyEXPERT group+ has the following measurement operation environments.

- **Application test mode** - The EasyEXPERT group+ contains an application library that supports typical measurements for CMOS devices, TFT, BJT, memory, nanotechnology devices such as CNT FET, and so on. The application library includes more than three hundred test definitions. This mode realizes application oriented point-and-click test setup and execution.
- **Classic test mode** - You can perform measurements by using the user interface similar to the semiconductor parameter analyzers such as Keysight 4155/4156 series. The setup can be made by entering values into the setup tables used for the measurement module control. And it can be saved and recalled as your setup (*My Favorite Setup*).
- **Tracer test mode** - Curve tracer test mode. This test allows you to perform the high speed I-V measurement on one screen. The Tracer test screen provides GUI for selecting the used channels, setting the sweep output, and displaying the measurement result (tracing the I-V curve). Range of the sweep output and measurement can be changed by the rotary knob on the front panel. Test setups can be saved, and used in the classic test mode for further detailed measurement and analysis.
- **Quick test mode** - A GUI-based quick test mode enables you to perform test sequencing without programming. You can select, copy, rearrange, and cut-and-paste any test setups with a few simple mouse clicks. Once you have selected and arranged your tests, simply click on the measurement button to begin running an automated test sequence.

Application library

Contains many pre-defined application test conveniently organized by device type, application, and technology. You can easily edit and customize the furnished application tests to fit your specific needs.

The following table shows a part of tests included in the library. They are subject to change without notice.

Table 1-19 Application library, Category list

Category	Test items
CMOS	Id-Vg, Id-Vd, Vth, breakdown, etc.
BJT	Ic-Vc, diode, Gummel plot, breakdown, hfe, capacitance, etc.
Discrete	Id-Vg, Id-Vd, Ic-Vc, diode, etc.
Memory	Vth, capacitance, endurance test, etc.
Power Device	Pulsed Id-Vg, pulsed Id-Vd, breakdown, etc.
NanoTech	Resistance, Id-Vg, Id-Vd, Ic-Vc, etc.
Reliability	NBTI/PBTI, charge pumping, electromigration, hot carrier injection, J-Ramp, TDDB, etc.

Workspace and data management

EasyEXPERT group+ has separate work environment (Workspace). Every workspace supports the following features.

- Measurement setup and execution
- Save/Recall My Favorite (preset group) setup
- Save/Recall measurement data and settings
- Import/Export device definition, measurement settings, My Favorite setup, measurement data, and application library
- Test result data management
- Access authority (private/public) setting

The EasyEXPERT has the ability to import/export a workspace for back-up and portability.

External instrument control

EasyEXPERT group+ supports all aspects of parametric test, from basic manual measurements to test automation across a wafer in conjunction with a semiautomatic wafer prober. The following shows supported equipment list.

- Switching matrix operation panel (GUI)

  Keysight B2200A, B2201A, and E5250A with E5252A cards.

- External instruments supported by application tests

  Keysight 4284A/E4980A, 81110A, and 3458A

- Wafer prober control

  Scripts to perform chuck move/up/down and subsite move for major semiautomatic probers are furnished. The wafer prober control can be performed in the repeat measurement process.

Furnished Software

The EasyEXPERT group+ also furnishes the following software.

- Prober control scripts
- 4155/56 setup file converter

  Converts the measurement setup file (extension MES or DAT) for Keysight 4155 and 4156 into the equivalent setup file for EasyEXPERT classic test mode.

- MDM file converter

  Converts the EasyEXPERT test result data file (extension XTR or ZTR) to Keysight IC-CAP MDM file. Supports the data of the following classic tests

  - I/V Sweep
  - Multi Channel I/V Sweep
  - C-V Sweep

1.8.2 System requirements

The following table shows the minimum requirements to run the EasyEXPERT group+ software for PC furnished with the E5260/E5270. They are effective as of June 2015. For the latest information, go to www.keysight.com and type in EasyEXPERT in the Search field at the top of the page.

Table 1-20 System requirements

Operating System	Microsoft Windows Vista Business SP2 or later (32 bit)	Microsoft Windows 7 Professional SP1 or later (32 bit/64 bit)	Microsoft Windows 8.1 Professional SP1 or later (32 bit/64 bit)
Language	English (US)		
.NET Framework	Microsoft .NET Framework version 3.5 SP1		
Processor	Vista certified PC	Windows 7 certified PC	Windows 8.1 certified PC
Memory	2 GB	2 GB	2 GB
Display	XGA 1024 x 768 (SXGA 1280 x 1024 recommended)		
HDD	1 GB free space on the C drive, 30 GB free space on a drive for test setup / result data storage		
LAN interface	EasyEXPERT remote control function using socket service. (100BASE-TX/10BASE-T)		
GPIB interface	The Keysight Connection Expert is required.		
IO libraries	Keysight IO libraries Suite 16.2 or later (Keysight Connection Expert)		

NOTE

If your computer does not install a software, install the software in the above order. For example, if your computer does not install Microsoft .NET Framework 3.5 SP1, install it and Keysight IO Libraries in this order.

Prepare the Keysight IO Libraries software for Keysight GPIB interface. The latest IO library is available in “www.keysight.com/find/io” web site.

Open the EasyEXPERT group+ Prerequisites folder to get installation packages for the other required software.

NOTE

About socket services

The EasyEXPERT remote control interface is a software interface usable from the VISA/SICL library. And it is used via LAN using the socket service. Keysight instruments are standardized on using port 5025 for socket services. A data socket on this port can be used to send and receive commands, queries, and query responses. All commands must be terminated with a newline for the message to be parsed. All query responses will also be terminated with a newline.

1.8.3 License Management Tool

The license management tool is the program used to install the license of the software listed below. Before using Online mode, install SWS license into your PC by the license management tool.

- Keysight E5270BU-SWS EasyEXPERT Extension
- Keysight E5260AU-SWS EasyEXPERT Extension

Figure 1-4 License management tool in the computer

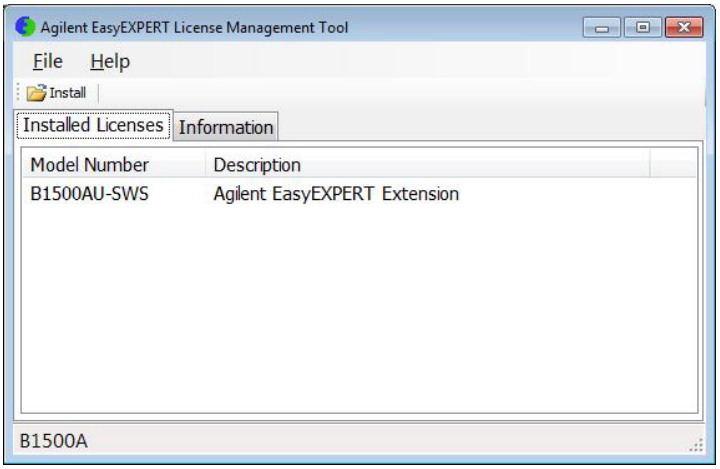

NOTE The EasyEXPERT software revision 5.5 or later requires license of Keysight EasyEXPERT Extension (SWS License To Use).

- **To launch program**

  Click Start > All Programs > (Keysight EasyEXPERT >) License Management Tool.

- **To check licenses already installed**

  Click Installed Licenses tab on the License Management Tool. The installed licenses will be displayed.

- **To check host ID**

  Click Information tab on the License Management Tool. The host ID of the computer will be displayed.

- **To install license**

  The following procedure installs the license.

  1. Click Install icon, or click File > Install License File to open a dialog box.
  2. Specify the license file (.lic file).
  3. Click open.

NOTE How to get the SWS Extension.

The latest E5260/E5270 includes the license for SWS Extension. However, if you use old revision of EasyEXPERT and upgrade to revision 5.5 or later, the E5260AU/E5270BU upgrade kit with SWS option is required. Contact Keysight Technologies to upgrade the software.

NOTE How to get the license file (.lic file) for SWS Extension.

The license file (.lic file) for SWS Extension can be gotten on the following web site with order number, certificate number and Host ID in EasyEXPERT group+ software. Please make sure order number and certificate number on LTU sheet. Keysight Software License (KSL) Redemption provides the license file for SWS Extension.
https://asl.software.keysight.com/license/login.asp

NOTE The latest revision of the EasyEXPERT update package can be obtained from Keysight Technologies web site.

2 Accessories for E5260/E5270

2.1 Accessories for the E5260/E5270 series

This section describes cables, adapters and accessories for the E5260/E5270 Precision IV analyzers.

2.1.1 SMU cables

- **Triaxial cables** - have three leads - a central conductor for the signal, an encapsulating conductor that shields the center signal by employing the same voltage thus decreasing a possible leakage current - and an outer conductor that serves as Common.
- **Kelvin Triaxial cables** - consist of two central twisted parallel leads that are connected to Force and Sense terminals of a SMU. A common guard and an outer conductor that is connected to Common further shield the two leads. By Kelvin connection it is possible to limit the influence of the connection leads on a lower resistively measurement to a minimum. Kelvin Triaxial cables should be employed when performing very sophisticated measurements.
- **GNDU cables** - have a very similar face to Triaxial cables. However the configuration of signal path is different from Triaxial cable. A central conductor for the Sense of GND voltage, outer conductor is used as GND signal, and the outermost conductor is for Common. In addition to that, the current capability of 16493L GND unit cable for mainframe is 4.2 Amps.
- **BNC cables** - Co-axial type cables. Central signal line is surrounded by shield potential. However, this is not suitable for ultra low current measurement below nA level. For these low current measurements, we recommend the Triaxial cables.

Table 2-1 SMU cables for E5260/E5270 series

Model/Option	Description	Additional Information
Triaxial cable		
16494A-001	Triaxial cable, 1.5 m	
16494A-002	Triaxial cable, 3 m	
16494A-003	Triaxial cable, 80 cm	
16494A-004	Triaxial cable, 40 cm	
16494A-005	Triaxial cable, 4 m	
Kelvin triaxial cable		
16493K-001	Kelvin triaxial cable, 1.5 m	
16493K-002	Kelvin triaxial cable, 3 m	

Model/Option	Description	Additional Information
16494B-001	Kelvin triaxial cable to E5250A switching matrix input port, 1.5 m	
16494B-002	Kelvin triaxial cable to E5250A switching matrix input port, 3 m	
16494B-003	Kelvin triaxial cable to E5250A switching matrix input port, 80 cm	
GNDU cable		
16493L-001	GNDU cable, 1.5 m	
16493L-002	GNDU cable, 3 m	
16493L-003	GNDU cable, 5 m	
16493N-001	GNDU cable for B2200A/B2201A switching matrix input port, 2 m (2.0 m cable length only)	
ASU cable		
16493M-001	Triaxial and D-sub cable for ASU(E5288A), 1.5 m	 
16493M-002	Triaxial and D-sub cable for ASU(E5288A), 3 m	
BNC cable		
16493B-001	Coaxial cable, BNC(m) to BNC(m), 1.5 m	
16493B-002	Coaxial cable, BNC(m) to BNC(m), 3.0 m	
The maximum voltage is 40 V, and Maximum current is 200 mA. The Keysight 16493B Coaxial Cable is designed for use with VSU (Voltage Source Unit), VMU (Voltage Measurement Unit) or PGU (Pulse Generator Unit) on the Keysight 4155 series Semiconductor Parameter Analyzer.		

WARNING **There are potentially hazardous voltages, up to ± 100 V (MPSMU/HRSMU) or ± 200 V (HPSMU) at the Force, Sense, and Guard terminals.**

To prevent electrical shock, do *not* expose these lines.

WARNING **To prevent electrical shock during use, install an interlock circuit and connect the Interlock cable (See chapter 2.1.3 Other I/F and interlock).**

CAUTION Never connect the Guard terminal to any output, including circuit common, chassis ground, or any other guard terminal. Doing so will damage the SMU.

CAUTION

The GNDU can sink current of up to 4.0 A. Use the Keysight 16493L GNDU cable to connect the GNDU to a test fixture or a connector plate.

Do not use normal triaxial cable (Keysight 16494A), because the maximum current rating of the cable is 1 A.

NOTE

For the lower current measurement, use the 16494A Triaxial cable with low-noise environment. This cable can maximize the guard effects and minimize the impression of the external noise.

2.1.2 Test fixture

Keysight 16442B test fixture is designed for testing packaged devices and electronic components. You can mount the suitable socket module on the 16442B, which allows you to easily connect various devices to measurement units.

The 16442B has the following input ports.

- 6 SMU channels (Triaxial connector. It can be used either for 6 non-Kelvin or 3 Kelvin connectors.)
- 2 VSU channels (BNC connector)
- 2 VMU channels (BNC connector)
- 2 PGU channels (BNC connector)
- 1 GNDU channel (Triaxial connector. It requires the Keysight 16493L GNDU cable.)
- 1 interlock 6-pin connector

Table 2-2 16442B Test Fixture

Model/Option	Description	Additional Information
16442B	Test Fixture for Semiconductor Devices The following items are shipped as standard with the 16442B test fixture. • Blank PTFE board • 28-pin dual-in-package (DIP) socket module • 0.075-inch universal socket module • 0.5-inch universal socket module • Miniature banana to pin plug cables, black (4 pcs) • Miniature banana to pin plug cables, red (4 pcs) • Miniature banana to pin plug cables, blue (4 pcs) • Pin plug to pin plug cables, black (3 pcs) • Pin plug to pin plug cables, red (3 pcs) • Pin plug to pin plug cables, blue (3 pcs) • Miniature banana to miniature clip cables, black (3 pcs) • Miniature banana to miniature clip cables, red (3 pcs) • Miniature banana to miniature clip cables, blue(3 pcs) • Miniature banana to miniature banana, black (3 pcs) • Miniature banana to miniature banana, red (3 pcs) • Miniature banana to miniature banana, blue(3 pcs) • Connection pin set (10 ea) • Accessory case	
Options for extra accessories		
16442B-010	Add four 1.5 m Triaxial cables (16494A-001)	If triaxial cables are required, select either 16442B-001 or 16442B-011.
16442B-011	Add four 3.0 m Triaxial cables (16494A-002)	

Model/Option	Description	Additional Information
16442B-800	Extra blank PTFE board	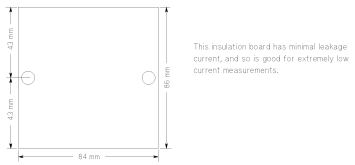
16442B-801	Add Universal socked module, 0.1 inch pitch, with 10 pins	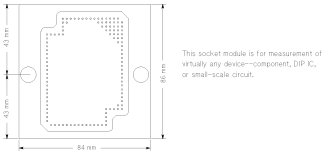
16442B-802	Extra Universal socked module, 0.075 inch pitch, with 10 pins	
16442B-803	Extra Universal socked module, 0.05 inch pitch, with 10 pins	
16442B-810	Extra pin set (for universal socket module, 10 pins.)	
16442B-811	Extra wire set (mini banana to pin plug, 6 ea)	
16442B-812	Extra wire set (pin plug to pin plug, 6 ea)	
16442B-813	Extra wire set (mini banana to pin clip, 6 ea)	
16442B-814	Extra wire set (mini banana to mini banana, 6 ea)	
16442B-821	Add socket module, 4-pin TO package	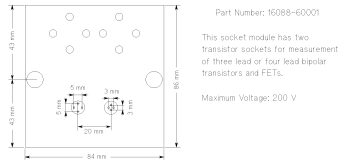
16442B-822	Add socket module, 18-pin DIP package	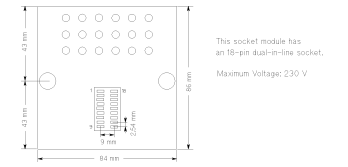
16442B-823	Extra socket module, 28-pin DIP package	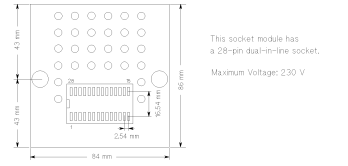
16442B-890	Extra accessories case	

2.1.3 Other accessories and interlock

The following table lists the options and accessories available for the E5260/E5270.

Table 2-3 Other accessories for E5260/E5270 series

Model/Option	Description	Additional Information
Interlock cable		
16493J-001	Interlock cable, 1.5 m	
16493J-002	Interlock cable, 3 m	
16493J-003	Interlock cable, 5 m	
GNDU cable		
16493L-001	GNDU cable, 1.5 m	
16493L-002	GNDU cable, 3 m	
16493L-003	GNDU cable, 5 m	
16493N-001	GNDU cable for B2200A/B2201A switching matrix input, 2 m	
Digital I/O cable		
16493G-001	Digital I/O control cable, 1.5 m	
16493G-002	Digital I/O control cable, 3 m	

Table 2-4 Adapter and connectors

Model/Option	Description	Additional Information
Digital I/O accessories		
N1253A-100	Digital I/O T-cable	Digital I/O T-cable has 2 male and 1 female connectors in order to connect more than two units. In order to connect three units, order one N1253A-100 and one 16493G cable.
N1253A-200	Digital I/O BNC box	Adapter for connecting Digital I/O port with BNC trigger port of other instruments. Box which has 8 BNC connectors for connecting with BNC trigger port of other instruments and 25 pin D-sub connector for connecting this box to B1500A. In order to use this box for connection, need D-sub 25 pin straight cable (16493G) and BNC cable.  
Adapters/Accessories for DC parametric measurement instrument		
N1254A-100	GNDU to Kelvin adapter Adapter for converting GNDU connector to Kelvin connector used only for E5260/E5270 series. The adapter which converts the GNDU connector to 2 triaxial connectors like connectors of SMU output. This adapter can be used with only E5260/E5270 Series. It does not fit with GNDU of 41501A/B.	 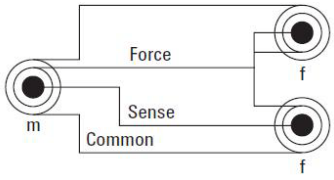

Model/Option	Description	Additional Information
N1254A-101	Triaxial (m) to Coaxial (f) adapter (1250-2648)	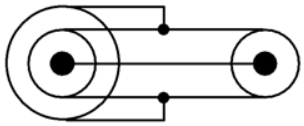
N1254A-102	Triaxial (f) to Coaxial (m) adapter (1250-2649)	
N1254A-103	Triaxial (m) to Coaxial (f) adapter (1250-2650)	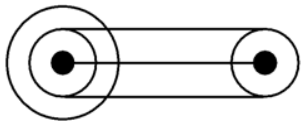
N1254A-104	Triaxial (f) to Coaxial (m) adapter (1250-2651)	
N1254A-105	Triaxial (f) to Coaxial (m) adapter (1250-2652)	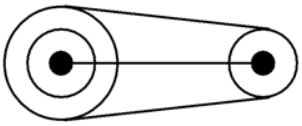
N1254A-106	Triaxial (m) to Coaxial (f) adapter (1250-2653)	
N1254A-107	Triaxial (m) to Triaxial (m) adapter (1250-2654)	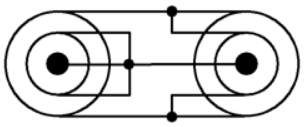
N/A	Triaxial (f) to Triaxial (f) adapter (1250-2618)	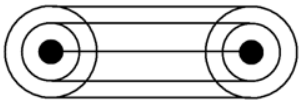
N1258A-108	Magnet Stand for ASU (E5288A)	
Accessories for 16442B test fixture		
N1254A-200	Transistor socket module in 16442B-821	4-pin TO package
N1254A-201	28pin DIP socket module in 16442B-823	
N1254A-202	18pin DIP socket module in 16442B-823	
N1254A-204	Universal socket module in 16442B-801	0.1 inch pitch
N1254A-205	Universal socket module in 16442B-802	0.075 inch pitch
N1254A-206	Universal socket module in 16442B-803	0.05 inch pitch
N1254A-207	Blank PTFE board module in 16442B-800	Blank PTFE board for measuring high resistance devices
N1254A-300	Contact Pins (10 ea)	Connection pins (10 ea) included in 16442B-801, 802 and 803
N1254A-301	Mini banana - pin plug (black, 1 ea)	Mini banana - pin plug included in 16442B-811

Model/Option	Description	Additional Information
N1254A-302	Mini banana - pin plug (red, 1 ea)	Mini banana - pin plug included in 16442B-811
N1254A-303	Mini banana - pin plug (blue, 1 ea)	Mini banana - pin plug included in 16442B-811
N1254A-304	Pin plug - pin plug (black, 1 ea)	Pin plug - pin plug included in 16442B-812
N1254A-305	Pin plug - pin plug (red, 1 ea)	Pin plug - pin plug included in 16442B-812
N1254A-306	Pin plug - pin plug (blue, 1 ea)	Pin plug - pin plug included in 16442B-812
N1254A-307	Mini banana - mini clip (black, 1 ea)	Mini banana - mini clip included in 16442B-813
N1254A-308	Mini banana - mini clip (red, 1 ea)	Mini banana - mini clip included in 16442B-813
N1254A-309	Mini banana - mini clip (blue, 1 ea)	Mini banana - mini clip included in 16442B-813
N1254A-310	Mini banana - mini banana (black, 1 ea)	Mini banana - mini banana included in 16442B-814
N1254A-311	Mini banana - mini banana (red, 1 ea)	Mini banana - mini banana included in 16442B-814
N1254A-312	Mini banana - mini banana (blue, 1 ea)	Mini banana - mini banana included in 16442B-814
Accessories		
N1254A-400	Coaxial cable between connector plate and probe card, black 1 m	Coaxial cable (50 ohm) between connector plate and probe card, black 1 m
N1254A-401	Triaxial connector for SMU and HCU (female)	
N1254A-402	Interlock micro switch (3101-0302)	

2.1.4 Rack mount kit for Keysight standard cabinet

Keysight E5260/E5270 mainframe can be mounted in a 19-inch EIA rack cabinet. It is designed to fit in five rack-units (5U) of space. 2 channel model has 3U size.

Table 2-5 Rack mount parts for B1500A

Model	Height EIA	Handle & Flange Kit	Std. slide	Support rail	D (mm)	Weight (kg)	Power Max. (VA)	Cooling & Vending
E5270B	5	5063-9223	1494-0059	E3663AC	575	25	600	Rear
E5260A	5	5063-9223	1494-0059	E3663AC	575	25	600	Rear
E5262A	3	5063-9221	1494-0059	E3663AC	575	16	400	Rear
E5263A	3	5063-9221	1494-0059	E3663AC	575	16	400	Rear

2.2 Accessories for the wafer prober / connector plate

When connecting the Keysight E5260/E5270 series to a prober, a connector interface may be required to feed the test leads through a shielding box. A connector plate fulfills the requirement of such an interface.

Keysight provides 2 types of Connector Plate.

- Connector (front) to connector (rear)
- Connector (front) to contacts for soldering (rear)

Figure 2-1 **Difference between “connector to connector” and “connector to contact for soldering”**

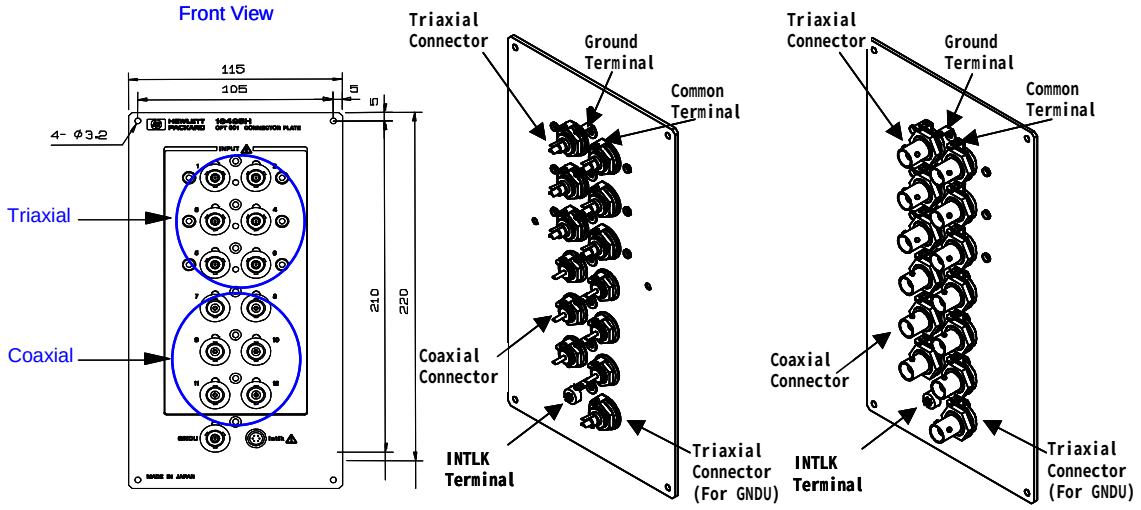

Table 2-6 **Item number information of 16495F Connector Plate with 12 Triaxial Interlock and GNDU connectors**

Item.	Description	OP Instruction
16495F	Connector plate with 12 triaxial, interlock and GNDU connectors	Half size connector plate with 12 triaxial, interlock and ground unit connectors. Common terminals are connected to plate. **ATTENTION**: Must specify either 16495F-001 or 16495F-002
16495F-001	Bulkhead feedthru connectors	Connection type is "Connector-Connector"
16495F-002	Connectors to contacts for soldering	Connection type is "Connector-Solder"

Table 2-7 Item number information of 16495G Connector Plate with 24 Triaxial, Interlock and GNDU connectors

Item.	Description	OP Instruction
16495G	Connector plate with 24 triaxial, interlock and GNDU connectors	Full size connector plate with 24 triaxial, interlock and ground unit connectors. Common terminals are connected to plate. **ATTENTION**: Must specify either 16495G-001 or 16495G-002
16495G-001	Bulkhead feedthru connectors	Connection type is "Connector-Connector"
16495G-002	Connectors to contacts for soldering	Connection type is "Connector-Solder"

Table 2-8 Item number information of 16495H Connector Plate with 6 Triax., 6 BNC, Intlk, GNDU

Item.	Description	OP Instruction
16495H	Connector plate with 6 triax., 6 BNC, intlk, GNDU	Half size connector plate with 6 triaxial, 6 BNC, interlock and ground unit connectors. Common terminals are floating. **ATTENTION**: Must specify either 16495H-001 or 16495H-002
16495H-001	Bulkhead feedthru connectors	Connection type is "Connector-Connector"
16495H-002	Connectors to contacts for soldering	Connection type is "Connector-Solder"

Table 2-9 Item number information of 16495J Connector Plate with 8 Triax., 4 BNC, Intlk, GNDU

Item.	Description	OP Instruction
16495J	Connector plate with 8 triax., 4 BNC, intlk, GNDU	Half size connector plate with 8 triaxial, 4 BNC, interlock and ground unit connectors. Common terminals are floating. **ATTENTION**: Must specify either 16495J-001 or 16495J-002
16495J-001	Bulkhead feedthru connectors	Connection type is "Connector-Connector"
16495J-002	Connectors to contacts for soldering	Connection type is "Connector-Solder"

Table 2-10 Item number information of 16495K Connector Plate with Universal Cable Holder

Item.	Description	OP Instruction
16495K	Connector plate with universal cable holder	16495K does not have any connections. This plate provides the cable hole and the cover with rubber used to block the light from the cable hole. This plate will be used with the E5288A ASU that will be installed in the shielding box. **ATTENTION**: Must specify 16495K-001
16495K-001	Connector plate with rubber holder	The cable hole is to pass the cables from the ASU to the instrument and so on. And the cables will be fixed to the shielding box by using the cover with rubber that will close the opening of the cable hole.

Table 2-11 Connector plate overview

		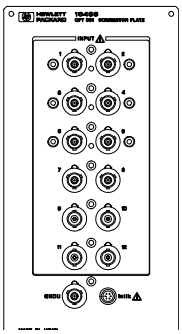
16495F (12 triax., Intlk, GNDU)	**16495G (24 triax., Intlk, GNDU)**	**16495H (6 triax. 6coax., Intlk, GNDU)**
		
16495J (8 triax. 4 coax., Intlk, GNDU)	**16495K Connector Plate with Universal Cable Holder for ASU**	**16495K inside**

3 Connection Guide for Wafer Prober

3.1 SMU/GNDU connection with prober

This section describes how to connect a wafer prober to the Keysight E5260/E5270 series.

Table 3-1 **Semi automated prober with Analyzers. (These pictures show B1500A semiconductor device analyzer.)**

B1500A with Cascade Prober	B1500A with Vector Prober
	
B1500A with Cascade (Suss) Prober	**ASUs on the probe station**
	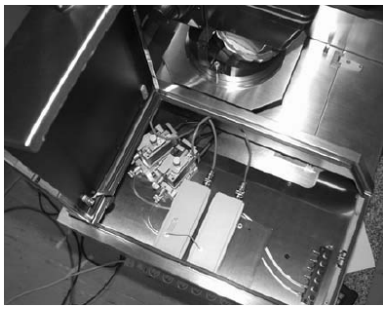

3.1.1 GNDU connections

An SMU has FORCE (SENSE), GUARD, and COMMON, but a GNDU has SENSE, FORCE, and COMMON as shown in Figure 3-1. User needs some sort of GNDU to Kelvin adapter when connecting the GNDU to standard triaxial connections.

CAUTION User should use the Keysight 16493L GNDU cable to connect the GNDU to the connector plate; do not use a standard triaxial cable. The GNDU cable can handle the maximum GNDU current of 4.2 A, but standard triaxial cables (16494A) are only rated to 1 A.

Figure 3-1 GNDU terminal

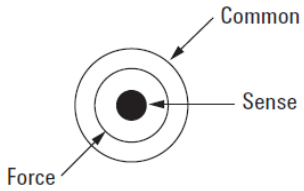

Non-Kelvin connection

Connect the triaxial connector using an adapter for GNDU (N1254A-107) as shown in Figure 3-2. For parts information for this connection, see Table 3-2.

Figure 3-2 Example of a GNDU non-Kelvin connection

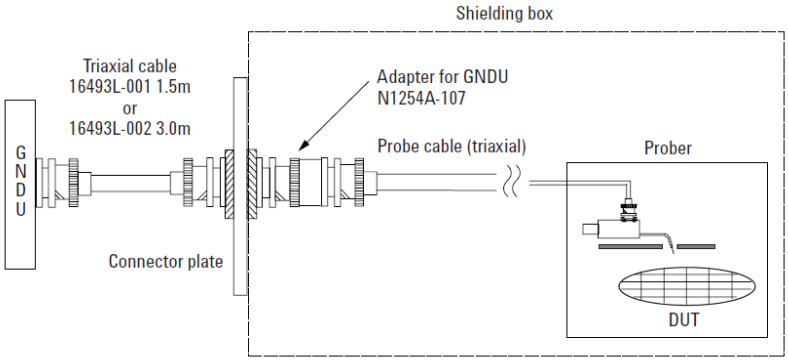

Table 3-2 Item number information for GNDU non-Kelvin connection with B1500A

Description	Qty	Product Number	Part number
Ground unit cable (1.5 m) - max 4.2 A	1	16493L-001	N/A
Ground unit cable (3.0 m) - max 4.2 A	1	16493L-002	N/A
Triaxial (m) to triaxial (f) adapter	1	N1254A-107	1250-2654

Kelvin connection

Connect the dual triaxial connector using a GNDU to Kelvin Adapter (N1254A-100) as shown in Figure 3-3. For parts information, see Table 3-3. Maximum current is restricted when the Kelvin triaxial cable is used.

Figure 3-3 Example of a GNDU Kelvin connection

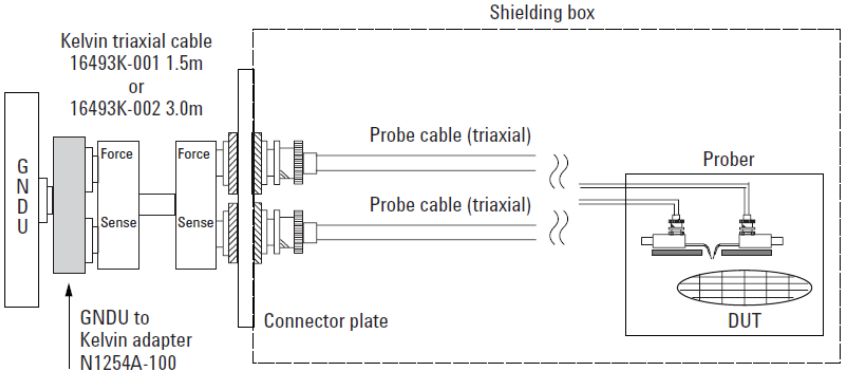

Table 3-3 Item number information for GNDU Kelvin connection with B1500A

Description	Qty	Product Number	Part number
Kelvin triaxial cable (1.5 m) - Max 3.0 A	1	16493K-001	N/A
Kelvin triaxial cable (3.0 m) - Max 2.6 A	1	16493K-002	N/A
GNDU to Kelvin adapter	1	N1254A-100	N/A

3.1.2 SMU connections

An SMU terminal is shown in Figure 3-4.

CAUTION Never connect the Guard terminal to any output, including circuit common, chassis ground, or any other guard terminal. Doing so will damage the SMU.

Figure 3-4 SMU terminal

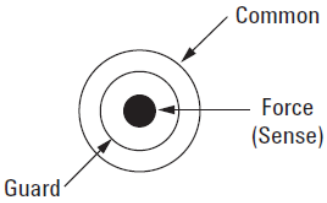

Non-Kelvin connection

These instructions apply when all connections are non-Kelvin. Connect the Keysight 16494A triaxial cables between the SMU and the Connector plate. Connect the triaxial connector on the probe cable as shown in Figure 3-5. For parts information, see Table 3-4.

NOTE Making non-kelvin connection

The Force terminals can be used to force and measure DC voltage or current. If you want to simplify the cable connections, open the Sense terminals and connect the Force terminals only to the connector plate by using the triaxial cables. If user makes the Kelvin connection, use both Force and Sense terminals. Connecting the Force and Sense lines together at the terminal of the device under test minimizes the measurement error caused by the residual resistance of the connection cables. The Kelvin connection is effective for the low resistance measurement and the high current measurement.

Figure 3-5 Example of an SMU non-Kelvin connection

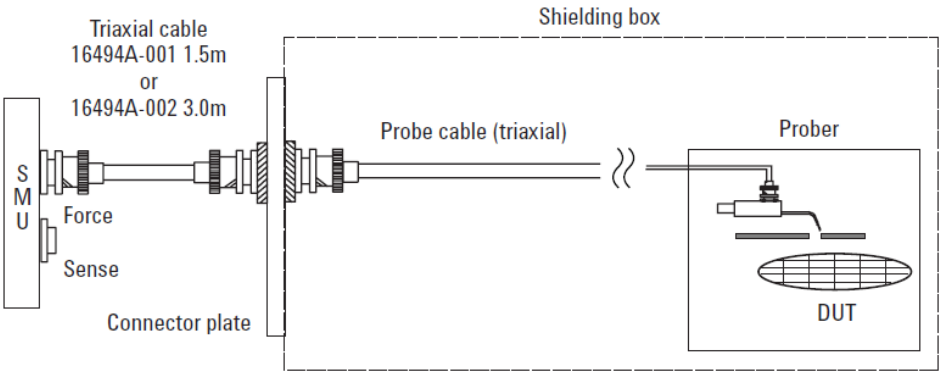

Table 3-4 Item number information for GNDU non-Kelvin connection with B1500A

Description	Qty	Product Number	Part number
Triaxial cable (1.5 m)	1	16494A-001	N/A
Triaxial cable (3.0 m)	1	16494A-002	N/A

Kelvin connection

These instructions apply when all connections are Kelvin. Two probes must contact the wafer in this connection. Connect an Keysight 16493K Kelvin triaxial cable (or two Keysight 16494A triaxial cables) between the SMU and the connector plate. Connect the FORCE and SENSE lines to probes separately. Connect the triaxial connector on the probe cable as shown in Figure 3-6. For parts information, see Table 3-5.

NOTE To prevent oscillations, do not use cables longer than 1.5 m, if you use two 16494A triaxial cables with Kelvin connections.

Figure 3-6 Example of an SMU Kelvin connection

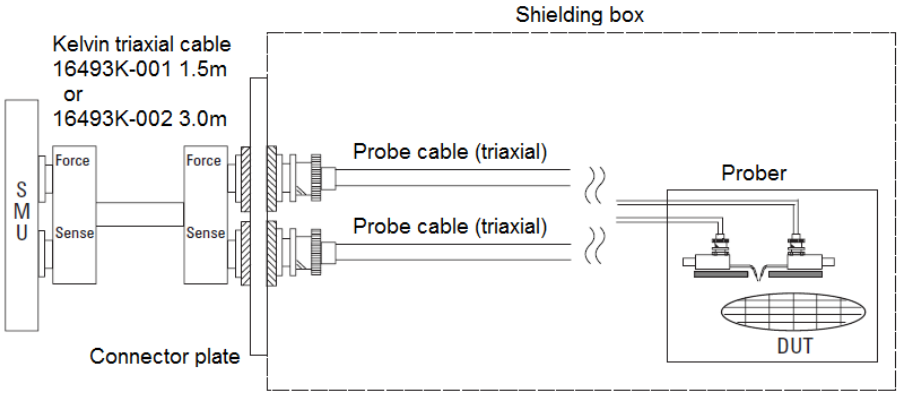

Table 3-5 Item number information for SMU Kelvin connection with B1500A

Description	Qty	Product Number	Part number
Kelvin triaxial cable (1.5 m) - max 3.0 A	1	16493K-001	N/A
Kelvin triaxial cable (3.0 m) - max 2.6 A	1	16493K-002	N/A

Kelvin to non-Kelvin connection

These instructions apply when the connections up to the Connector Plate are Kelvin, but the probe is a non-Kelvin connection. Connect an Keysight 16493K Kelvin triaxial cable (or two Keysight 16494A triaxial cables) between the SMU and the Connector plate. Connect the triaxial connector on the probe cable as shown in Figure 3-7. Connect the FORCE and SENSE lines on this side of the probe input terminal. A Triaxial tee connector can be used. For parts information, see Table 3-6.

NOTE To prevent oscillations, do not use longer than 1.5m, if user uses two 16494A triaxial cables with Kelvin connections.

NOTE When connecting the cable and tee connector as shown in Figure 3-7, space restrictions make an adjacent connector unusable. Since three connectors are necessary for a Kelvin connection a connector plate must be used. Select the correct connector plate for your application. To make two Kelvin connections, use an Keysight 16495H. To make three Kelvin connections, use an Keysight 16495J.

Figure 3-7 Example of an SMU Kelvin to non-Kelvin connection

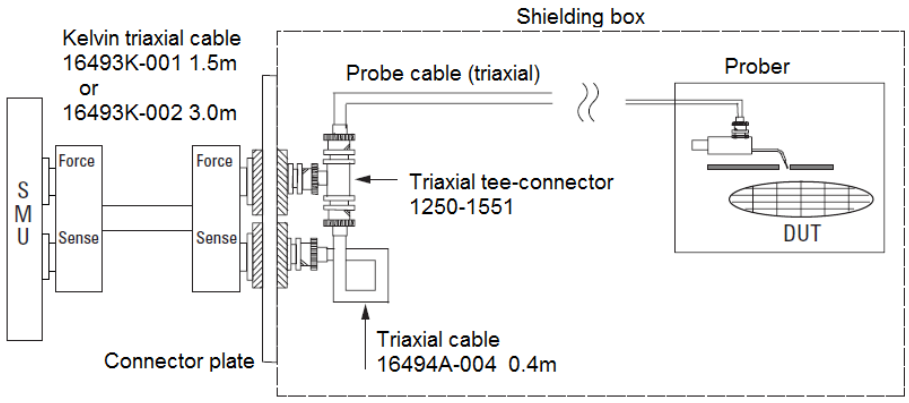

Table 3-6 Item number information for SMU Kelvin to non-Kelvin connection with B1500A

Description	Qty	Product Number	Part number
Kelvin triaxial cable (1.5 m) - max 3.0 A	1	16493K-001	N/A
Kelvin triaxial cable (3.0 m) - max 2.6 A	1	16493K-002	N/A
Triaxial cable (0.4 m)	1	16494A-004	N/A
Triaxial tee-connector	1	N/A	1250-1551

3.2 Connection for low current measurement

This section provides the information useful for connecting cables and probing needles to a connector plate.

3.2.1 To make connection to reduce leakage current

To reduce the leakage current caused by connection cables, the guard technique is effective. Connect the probing needles to the coaxial cables as shown below:

Guarding reduces the leakage current between the instrument and a DUT. This is important when you measure low current.

1. Cut and trim end of the coaxial cable so that the center conductor does not touch the outer conductor (connected to the guard terminal).
2. Connect the center conductor to tail of the probing needle. Never connect the outer conductor to the probing needle. However, the outer conductor should be extended as close as possible to the probing needle.
3. Connect the outer conductor to the outer conductor of the probing needle if it is a coaxial probing needle.

The following example connection can be used to reduce the leakage current. Extend the outer conductor as close as possible to the probing needle, This is also reduces the induced noise.

Figure 3-8 **Cable and Probing needle**

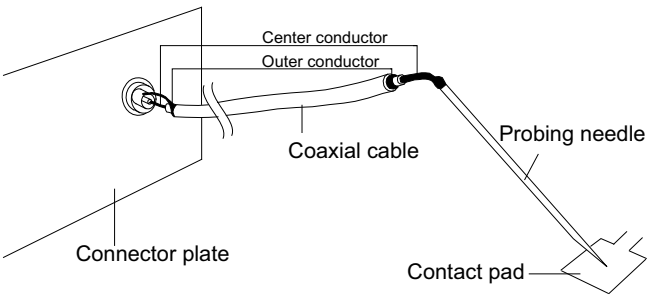

3.2.2 Guarding

Guarding reduces the leakage current between the instrument and the measurement point. This is important when you measure low current.

The following figure shows the theory of guarding. The buffer amplifier (×1) keeps the potential of the guard conductor at the same potential as the force conductor, so current does not flow between the force and guard conductors. Therefore, the current measured by the instrument is same as current at the DUT terminal because no current is leaked.

Figure 3-9 **Guarding**

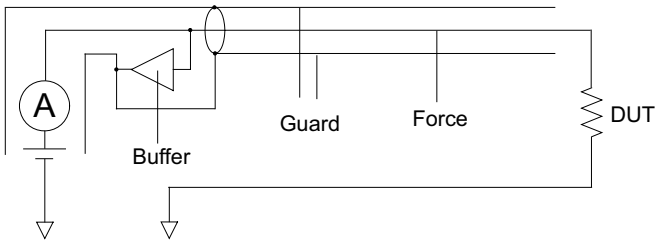

WARNING **Do not touch the guard terminal with bare hands because you may be shocked by high voltage. The potential of the guard terminal is equal to the output voltage.**

CAUTION Never connect the Guard terminal to any other output, including circuit common, chassis ground, or any other guard terminal. Doing so will damage the E5260/E5270.

3.3 Connection for low resistance measurement

This section provides the information useful for connecting cables and probing needles to a connector plate with Kelvin connections.

3.3.1 To make connection to measure low resistance

When you measure a low resistance, high current flows through the DUT. This high current increases the measurement error caused by the residual resistance of cables. To cancel the effect of this resistance, you can use Kelvin connections (4-wire, remote sensing), which means the Force and Sense lines are extended separately to the DUT.

Connect the probing needles to the terminals of the connector plate by using test leads or coaxial cables. Following instruction uses the coaxial cables:

1. Cut and trim end of the coaxial cable so that the center conductor does not touch the outer conductor (connected to the guard terminal).
2. Connect the center conductor to tail of the probing needle. Never connect the outer conductor to the probing needle. However, the outer conductor should be extended as close as possible to the probing needle.
3. Connect the outer conductor to the outer conductor of the probing needle if it is a coaxial probing needle.
4. Perform 1 to 3 for both Force and Sense lines.
5. Contact the probing needles for the Force and Sense lines as close as possible to the DUT.

The following example connection can be used to measure low resistance. The Sense line is extended to the probing pad, and contacts the Force line through the pad, so the voltage drop due to the residual resistance caused by cables and test leads is canceled.

Figure 3-10 **Cable and Probing needle**

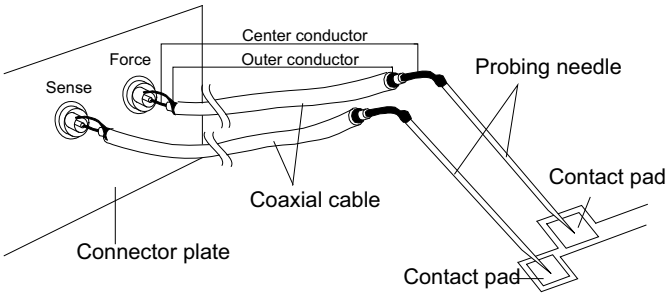

3.3.2 Kelvin connection

Kelvin connections give good measurement results when you force high-current. The following figure shows the equivalent circuits for Kelvin and non-Kelvin connections.

Figure 3-11 **Kelvin connection**

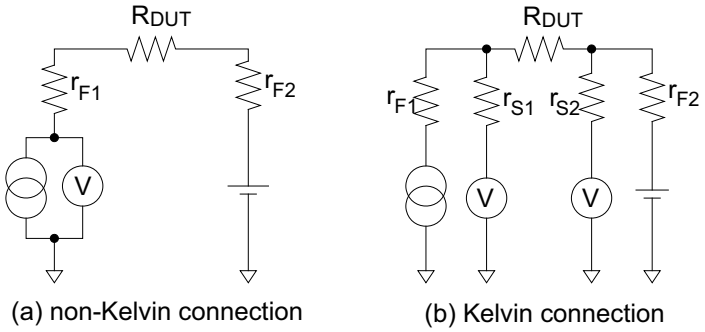

- For the non-Kelvin connection, the voltmeter measures the voltage drop of resistance r_{F1},R_{DUT}, and r_{F2}.
- For the Kelvin connection, the voltmeter measures the voltage drop of resistance R_{DUT} only. The impedance of the voltmeter is very high, so the voltage drop of resistances r_{S1} and r_{S2} can be ignored.

The Kelvin connection is effective even when forcing voltage. The voltage drop due to the residual resistance of the Force line wiring is fed back to the voltage source via a comparator in the Sense line. The input impedance of comparator is high, and current flow into the Sense line is very low. So output error is not significant if the Sense line wiring has a residual resistance of 10 Ω or less. Therefore, the specified voltage appears at the sense point (point where Sense line contacts Force line).

NOTE

Kelvin connection and non-Kelvin connection

To make the Kelvin connection, use both Force and Sense terminals. Connecting the Force and Sense lines together at the terminal of the DUT (device under test) minimizes the measurement error caused by the residual resistance of the connection cables. The Kelvin connection is effective for the low resistance measurement and the high current measurement.

If you want to simplify the cable connections, use the 2-wire connections by connecting the Force terminals only. Then open the Sense terminals. This is the non-Kelvin connection. The Force terminals can be used to force and measure dc voltage or current via R_s in Figure 3-12.

Figure 3-12 **Simplified SMU circuit diagram**

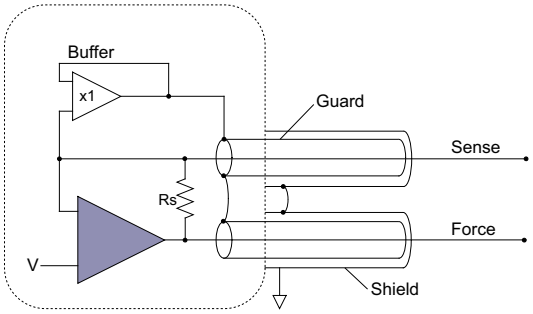

3.4 ASU

This section describes how to connect a wafer prober to the Keysight E5270B precision IV analyzer with ASU.

3.4.1 ASU connection

Each ASU has one D-sub control cable, one triaxial cable, and (optionally) two coaxial cables connected to it. The cables can be connected to the ASU inside the shielding box through the 16495K plate. The ASU outputs should be connected to the DUT by using triaxial cables as shown in Figure 3-13. When making IV measurements with the SMUs, all measurements are Kelvin. The SENSE line information is fed back to the SMU via the D-sub cable. When making CV measurements, the four-terminal pair (4TP) connections are correctly terminated inside of the ASUs. The ASUs also allow for a current return path between the outer conductors to stabilize the series inductance and improve accuracy. You must connect the furnished wire between the two ASUs to enable this feature.

Figure 3-13 Example of an ASU connection

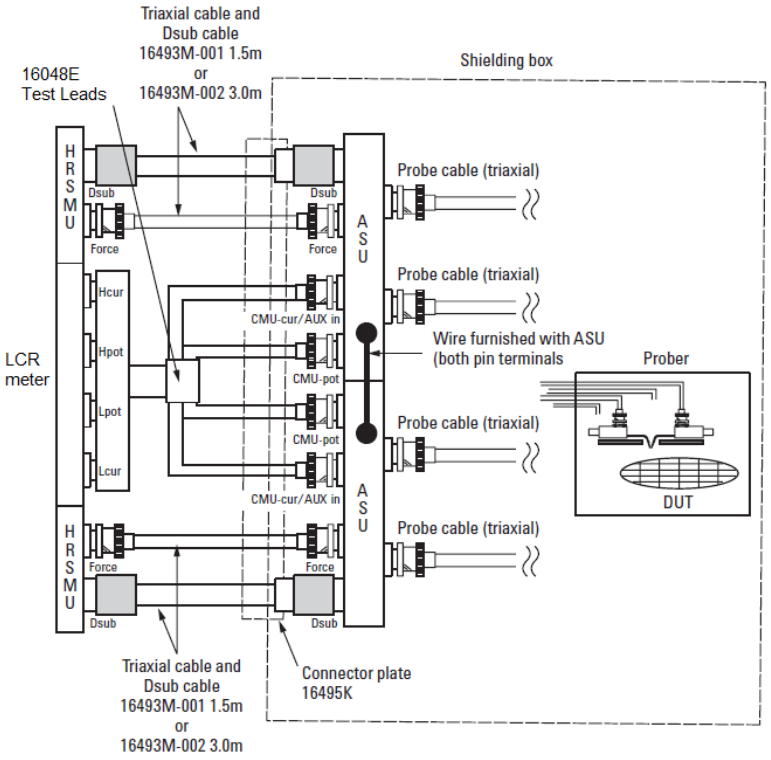

Table 3-7 Item number information for ASU connection with E5270B

Description	Qty	Product Number	Part number
Triaxial and D-sub cable for ASU (1.5 m)	2	16493M-001	N/A
Triaxial and D-sub cable for ASU (3.0 m)	2	16493M-002	N/A
Test leads for LCR meter (2.0 m)	1	16048D	N/A
Test leads for LCR meter (4.0 m)	1	16048E	N/A
Connector plate with universal cable holder	1	16495K	N/A

NOTE About ASU output cables

To perform capacitance measurement accurately, the cable length between DUT and the ASU output must be as short possible.

NOTE For the installation of the ASU and the connection to the DUT interface (probe card, manipulators, and so on), contact your favorite prober vendor. The prober vendor will have the solutions. Dimensions of the ASU are 132 mm (W) × 88.5 mm (H) × 50 mm (D) excluding the connectors.

3.5 Interlock circuit

The interlock circuit is designed to prevent electrical shock wen a user touches the measurement terminals.

CAUTION You must install an interlock circuit on a shielding box to prevent hazardous voltage when the door of the shielding box is open.

Figure 3-14 shows the pin assignments of the interlock connector that should be mounted on a connector plate or test fixture.

Figure 3-14 Interlock connector pin assignments

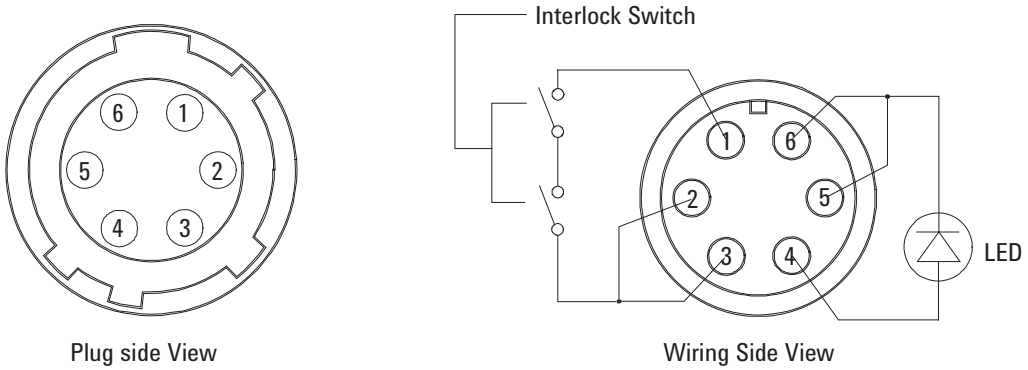

Table 3-8 Recommended parts for interlock circuit

Description	Qty	Product Number	Part number
Interlock connector (6 pin, female)	1	N/A	1252-1419
Interlock micro switch	1	N1254A-402	3101-0302 or 3131-3241
LED ($V_F \cong 2.1$ V@ $I_F = 10$ mA)	1	N/A	1450-0641
Wire (24 AWG, 600 V)	1	N/A	8150-5680

3.5.1 Installing the interlock circuit

Prepare the required parts listed in Table 3-8. And install the interlock circuit as shown below.

1. Make mounting hole for the interlock connector. See Figure 3-16 for dimensions.
2. Mount two mechanical switches on your shielding box, so that the switches close when the door of the shielding box is closed, and open when the door is opened. For the dimensions of the switch, see Figure 3-17 below.
3. Mount an LED on your shielding box. For the dimensions of the LED, see Figure 3-15.

4. Use wire to connect the two switches in series between pin number 1 and 2 (or 3) of the interlock connector. See Figure 3-14.
5. Use wire to connect the LED between pin number 4 and 5 (or 6) of the interlock connector. See Figure 3-14.
6. Attach the interlock connector to the mounting hole.

If Keysight E5260/E5270 Interlock connector is connected to the interlock circuit, Keysight E5260/E5270 SMU *cannot* force more than ± 42 V when the door is open. When the door is closed, it can force more than ± 42 V.

When more than ± 42 V is forced from an SMU, the LED lights to indicate *high voltage output*.

Figure 3-15 **Dimensions of the LED (Keysight part number 1450-0641)**

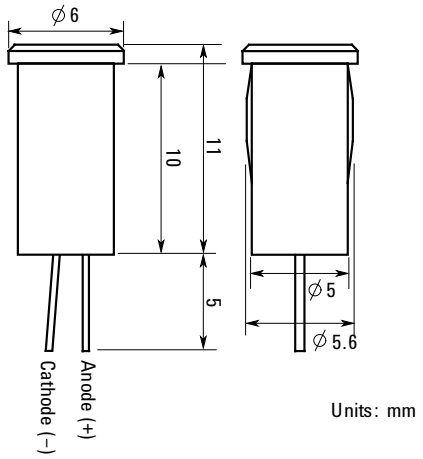

Figure 3-16 **Dimensions of Mounting Hole for the Interlock Connector**

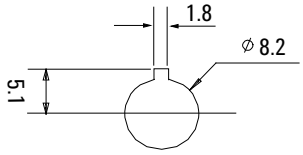

Figure 3-17 **Dimensions of the Interlock Switch (Keysight N1254A-402)**

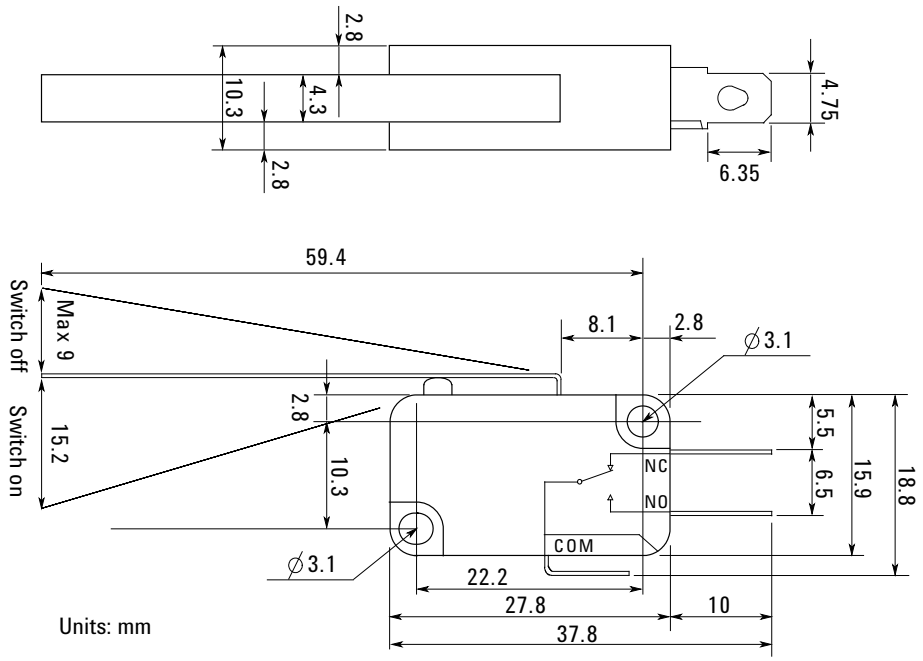

⚠ 3.5.2 To connect interlock circuit

The E5260/E5270 provides the Interlock connector to prevent you from receiving an electrical shock from high voltage (more than ± 42 V). If the interlock circuit is open, the E5260/E5270 *cannot* apply high voltage more than ± 42 V.

Before performing measurement, connect the 16493J interlock cable between the E5260/E5270 Interlock connector and the interlock connector which is a part of the interlock circuit installed in your DUT interface as described in the previous section.

4 Connection and Ordering Examples

4.1 Two terminal device

This chapter describes prober or Fixture connection and ordering example of Keysight E5260/E5270 series for 2 terminal devices.

4.1.1 General IV characterization

Figure 4-1 General IV configuration

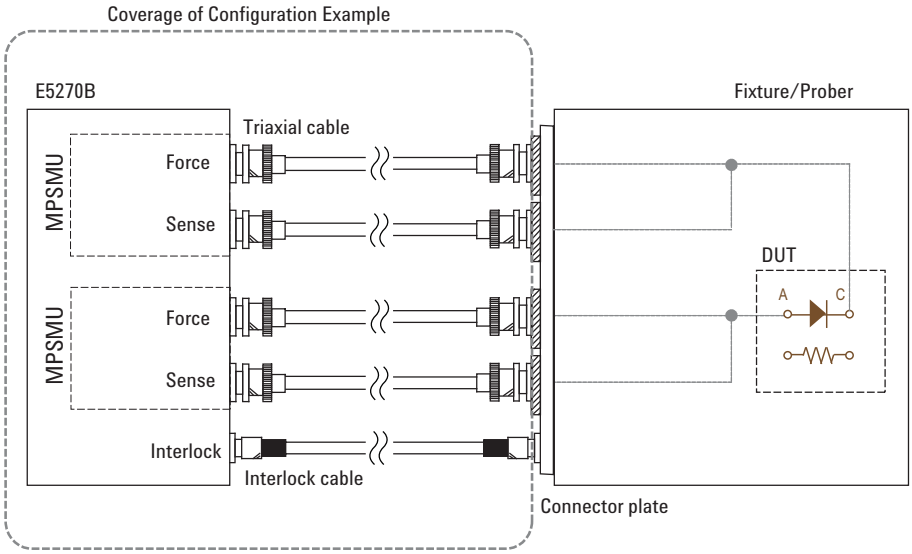

Table 4-1 Target device and application

Device	Application	Note
Diode	I_F-V_F, I_R-V_R, Breakdown	
Resister	R-I, R-V	2-wire or 4-wire

Table 4-2 Key specification

Item	Range	Note
Maximum I/V range	100 mA / 100 V	
Minimum I/V resolution	10 fA / 0.5 µV	

Table 4-3 Configuration Example

Model option	Description	Qty
E5270B	Precision IV Analyzer / 8 Slot Precision Measurement Mainframe	1
E5270B-015/030	1.5 m or 3 m length of bundled cables	1
E5270B-050/060	50 Hz or 60 Hz Line Frequency	1
E5270B-A11	Add Mid Power Source/Monitor Unit (E5281B) 1ea, Cables	2
16442B	Test fixture for packaged device measurement (Optional)	1

4.1.2 High resolution IV characterization

Figure 4-2 Precision IV configuration

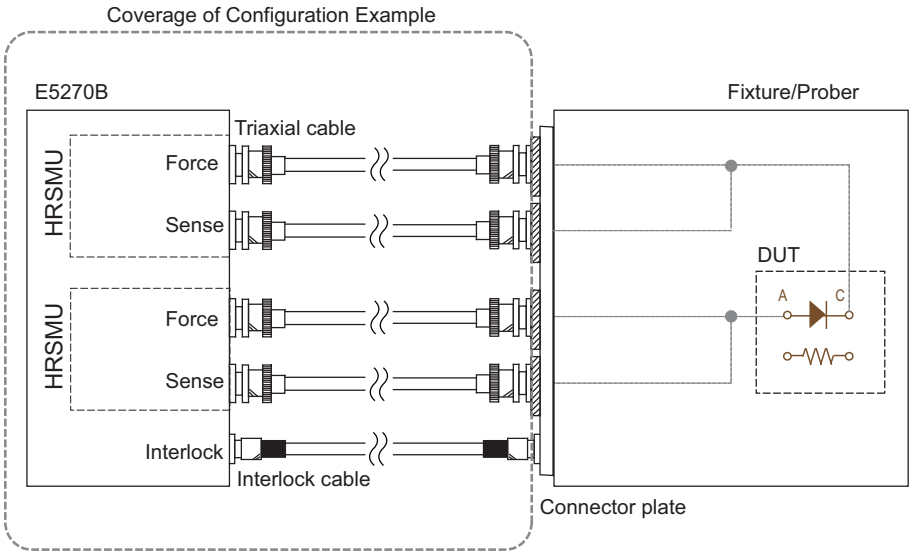

Table 4-4 Target device and application

Device	Application	Note
Diode	I_F-V_F, I_R-V_R, Breakdown	
Resister	R-I, R-V	2-wire or 4-wire

Table 4-5 Key specification

Item	Range	Note
Maximum I/V range	100 mA / 100 V	
Minimum I/V resolution	1 fA / 0.5 µV	

Table 4-6 Configuration Example

Model option	Description	Qty
E5270B	Precision IV Analyzer / 8 Slot Precision Measurement Mainframe	1
E5270B-015/030	1.5 m or 3 m length of bundled cables	1
E5270B-A17	Add High Resolution Source/Monitor Unit (E5287A) 1ea, Cables	2
16442B	Test fixture for packaged device measurement (Optional)	1

NOTE The low current level is around 1 nA with the 16442B test fixture.

4.1.3 High resolution IV/CV characterization

Figure 4-3 Precision IV/CV configuration

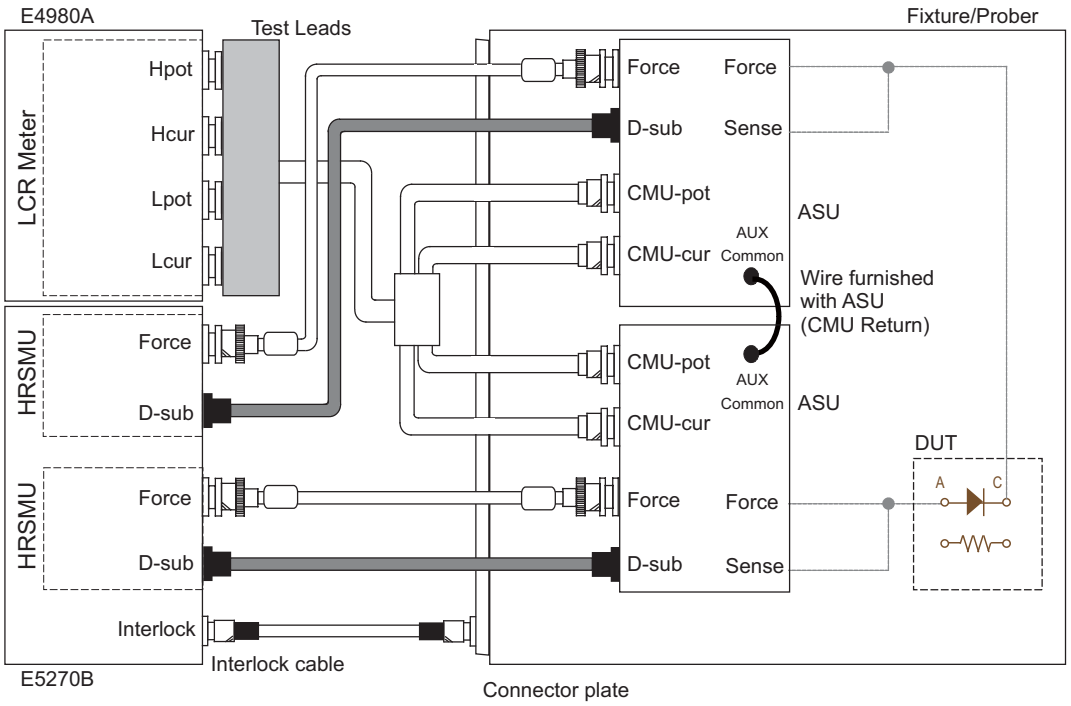

Table 4-7 Target device and application

Device	Application	Note
Diode	I_F-V_F, I_R-V_R, Breakdown, C-V, C-f, C-t	
Resister	R-I, R-V	2-wire or 4-wire

Table 4-8 Key specification

Item	Range	Note
Maximum I/V range	100 mA / 100 V	
Minimum I/V resolution	0.1 fA / 0.5 µV	
CV frequency range	20 Hz to 2 MHz	E4980A Precision LCR Meter
Maximum DC bias to CV	40 V	E4980A option 001is required.

Table 4-9 Configuration Example

Model option	Description	Qty
E5270B	Precision IV Analyzer / 8 Slot Precision Measurement Mainframe	1
E5270B-015/030	1.5 m or 3 m length of bundled cables	1
E5270B-A17	Add High Resolution Source/Monitor Unit (E5287A) 1ea, Cables	2
B1500A-A28	Add Atto Sense and Switch Unit (E5288A ASU) 1ea	2
E4980A	2 MHz Precision LCR Meter	1
E4980A-001	Output Power and DC Bias	1
16048E	Test leads (BNC), 4m	1
16442B	Test fixture for packaged device measurement (Optional)	1

NOTE The low current level is around 1 nA with the 16442B test fixture.

4.2 Four terminal device

This chapter describes prober or Fixture connection and ordering example of Keysight E5260/E5270 series for 4 terminal devices.

4.2.1 General IV characterization, Migration from 4155

Figure 4-4 General IV configuration

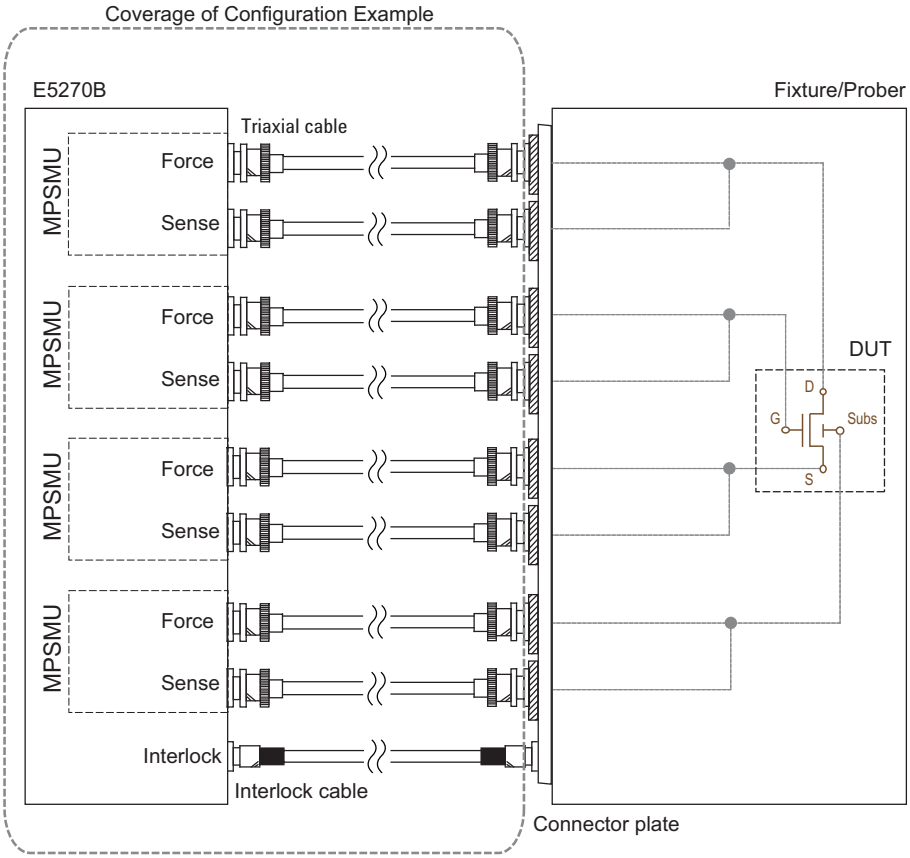

Table 4-10 Target device and application

Device	Application	Note
FET	I_d-V_d, V_{th}, BV_{dss}, I_d leak, I_g leak	

Table 4-11 Key specification

Item	Range	Note
Maximum I/V range	100 mA / 100 V	
Minimum I/V resolution	10 fA / 0.5 µV	

Table 4-12 Configuration Example

Model option	Description	Qty
E5270B	Precision IV Analyzer / 8 Slot Precision Measurement Mainframe	1
E5270B-015/030	1.5 m or 3 m length of bundled cables	1
E5270B-A01	Mid Power Source/Monitor Unit (4ea), Cables	1
16442B	Test fixture for packaged device measurement (Optional)	1

4.2.2 High resolution IV characterization, Migration from 4156

Figure 4-5 Precision IV configuration

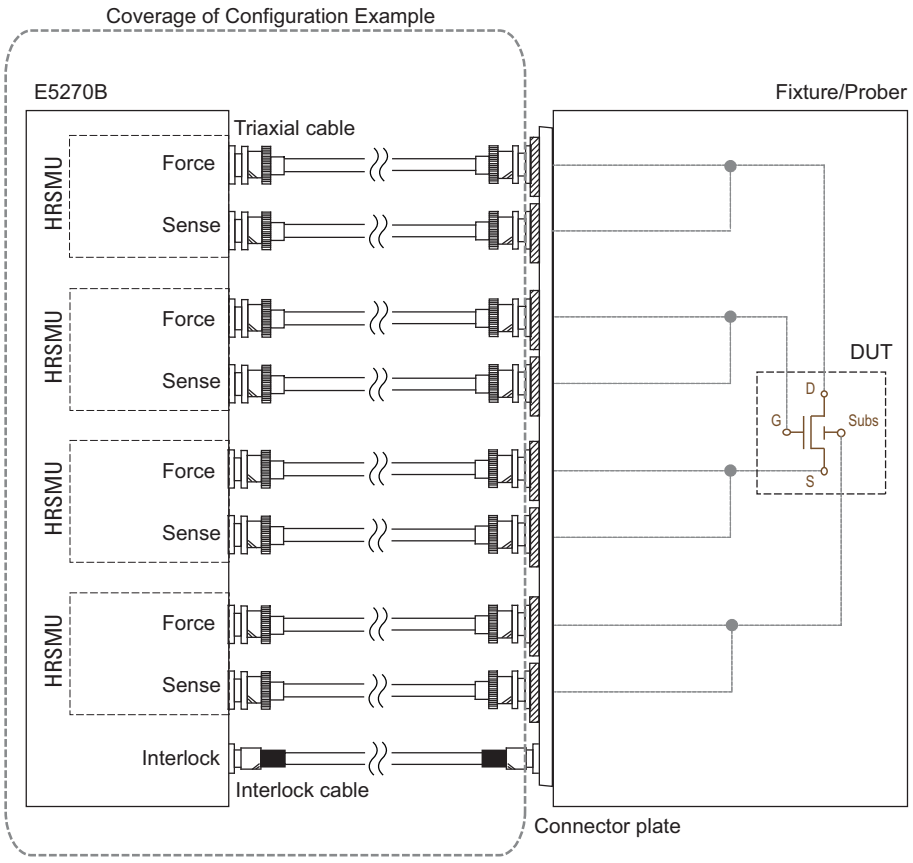

Table 4-13 Target device and application

Device	Application	Note
FET	I_d-V_d, V_{th}, BV_{dss}, I_d leak, I_g leak	

Table 4-14 Key specification

Item	Range	Note
Maximum I/V range	100 mA / 100 V	
Minimum I/V resolution	1 fA / 0.5 µV	

Table 4-15 Configuration Example

Model option	Description	Qty
E5270B	Precision IV Analyzer / 8 Slot Precision Measurement Mainframe	1
E5270B-015/030	1.5 m or 3 m length of bundled cables	1
E5270B-A03	High Resolution Source/Monitor Unit (4ea), Cables	1
16442B	Test fixture for packaged device measurement (Optional)	1

NOTE The low current level is around 1 nA with the 16442B test fixture.

4.2.3 High resolution IV characterization (ASU)

Figure 4-6 Precision IV configuration

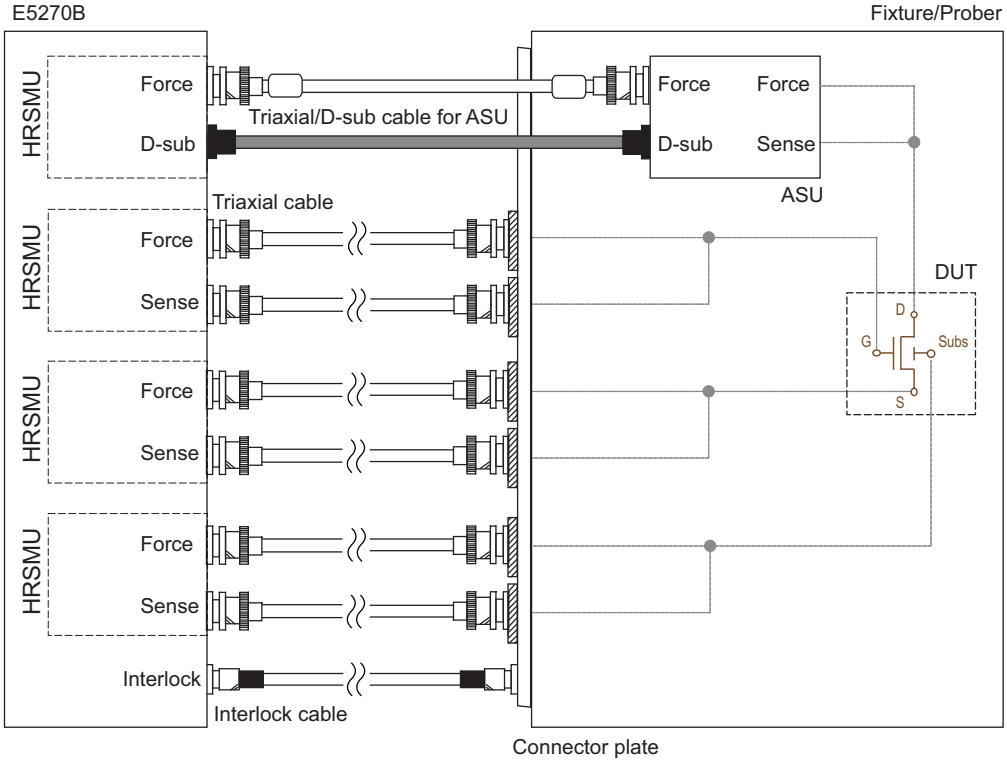

Table 4-16 Target device and application

Device	Application	Note
FET	I_d-V_d, V_{th}, BV_{dss}, I_d leak, I_g leak	

Table 4-17 Key specification

Item	Range	Note
Maximum I/V range	100 mA / 100 V	
Minimum I/V resolution	0.1 fA / 0.5 µV	

Table 4-18 Configuration Example

Model option	Description	Qty
E5270B	Precision IV Analyzer / 8 Slot Precision Measurement Mainframe	1
E5270B-015/030	1.5 m or 3 m length of bundled cables	1
E5270B-A03	High Resolution Source/Monitor Unit (4ea), Cables	1
E5270B-A28	Add Atto Sense and Switch Unit (E5288A ASU) 1ea	1
16442B	Test fixture for packaged device measurement (Optional)	1

NOTE The low current level is around 1 nA with the 16442B test fixture.

4.2.4 High resolution IV/CV characterization

Figure 4-7 Precision IV/CV configuration

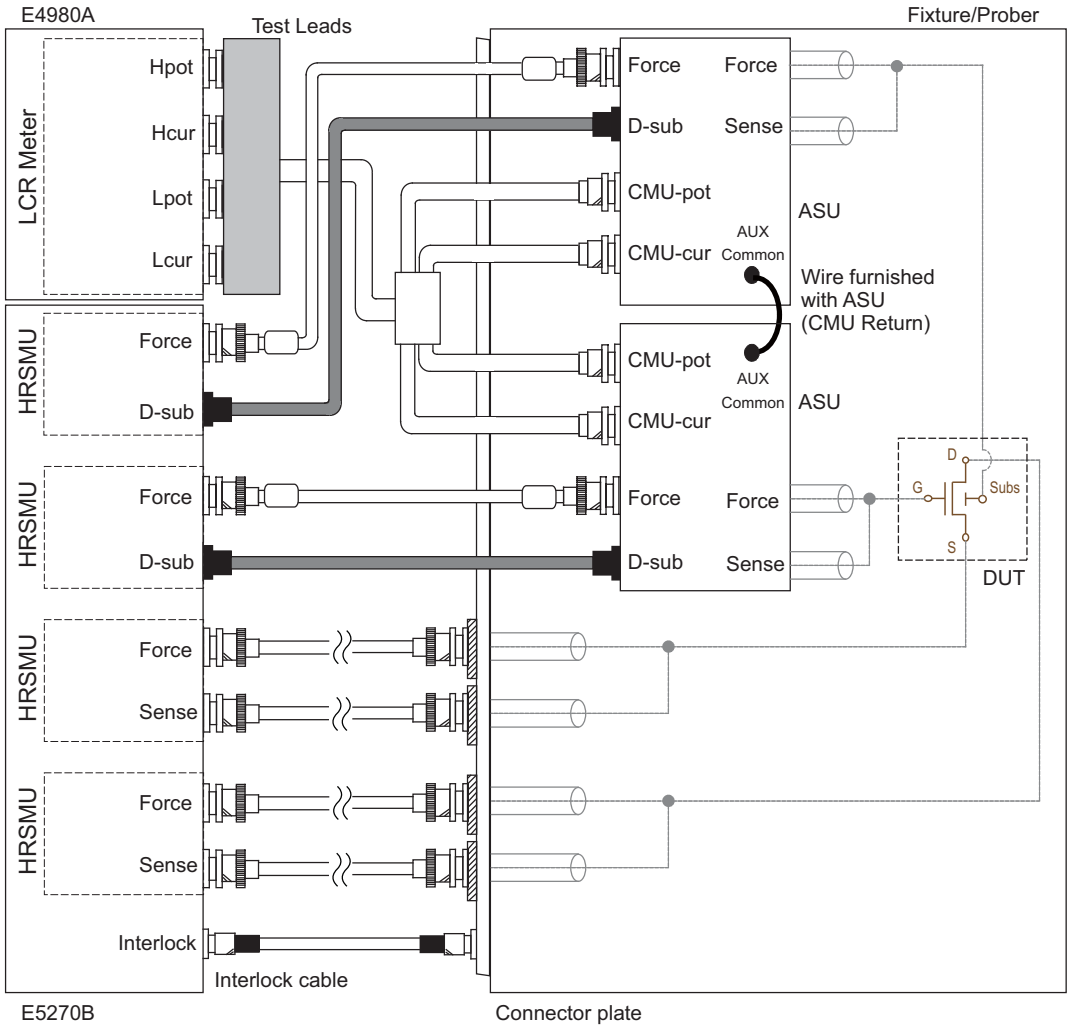

Table 4-19 Target device and application

Device	Application	Note
FET	I_d-V_d, V_{th}, BV_{dss}, I_d leak, I_g leak, C_{gb}	

Table 4-20 Key specification

Item	Range	Note
Maximum I/V range	100 mA / 100 V	
Minimum I/V resolution	10 fA / 0.5 µV	
CV frequency range	20 Hz to 2MHz	E4980A Precision LCR Meter
Maximum DC bias to CV	40 V	E4980A option 001 is required.

Table 4-21 Configuration Example

Model option	Description	Qty
E5270B	Precision IV Analyzer / 8 Slot Precision Measurement Mainframe	1
E5270B-015/030	1.5 m or 3 m length of bundled cables	1
E5270B-A03	High Resolution Source/Monitor Unit (4ea), Cables	1
E5270B-A28	Add Atto Sense and Switch Unit (E5288A ASU) 1ea	2
E4980A	2 MHz Precision LCR Meter	1
E4980A-001	Output Power and DC Bias	1
16048E	Test leads (BNC), 4m	1
16442B	Test fixture for packaged device measurement (Optional)	1

4.2.5 High power IV characterization

Figure 4-8 High power IV configuration

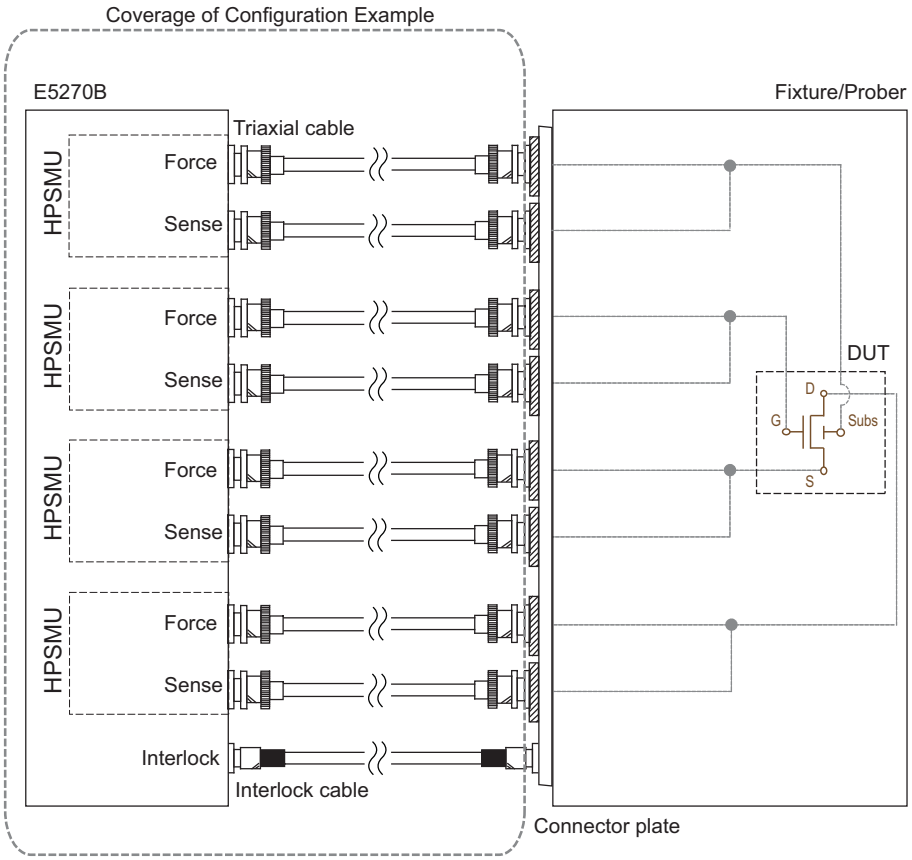

Table 4-22 Target device and application

Device	Application	Note
FET	I_d-V_d, V_{th}, BV_{dss}, I_d leak, I_g leak	

Table 4-23 Key specification

Item	Range	Note
Maximum I/V range	1 A / 200 V	
Minimum I/V resolution	10 fA / 2 µV	

Table 4-24 Configuration Example

Model option	Description	Qty
E5270B	Precision IV Analyzer / 8 Slot Precision Measurement Mainframe	1
E5270B-015/030	1.5 m or 3 m length of bundled cables	1
E5270B-A10	Add High Power Source/Monitor Unit (E5280B) 1ea, Cables	4
16442B	Test fixture for packaged device measurement (Optional)	1

Edition 3, July 2015

E5260-90090
www.keysight.com

Keysight 33220A
20 MHz Function/Arbitrary Waveform Generator

Data Sheet

LXI

Product Discontinuance Notice

The 33220A function generator and all associated options will be discontinued December 1, 2016. The last date this product can be ordered is November 30, 2016.

- For new product purchases, Keysight recommends the 33500B Trueform Series waveform generators.
- For more information, as well as to access to detailed migration guides, please visit **www.keysight.com/find/nextgenFGs**
- To contact a product selection expert, visit **www.keysight.com/find/contactus**

KEYSIGHT TECHNOLOGIES

Key Features

- Fully compliant to LXI Class C specification
- 20 MHz Sine and Square waveforms
- Pulse, Ramp, Triangle, Noise, and DC waveforms
- 14-bit, 50 MSa/s, 64 k-point arbitrary waveforms
- AM, FM, PM, FSK, and PWM modulation types
- Linear & logarithmic sweeps and burst operation
- 10 mV_{pp} to 10 V_{pp} amplitude range
- Graph mode for visual verification of signal settings
- Connect via USB, GPIB and LAN

Uncompromising performance for functions and waveforms

The Keysight Technologies 33220A function/arbitrary waveform generator uses direct digital synthesis (DDS) techniques to create a stable, accurate output signal for clean, low distortion sine waves. It also gives you square waves with fast rise and fall times up to 20 MHz and linear ramp waves up to 200 kHz.

Pulse generation

The 33220A can generate variable-edge-time pulses up to 5 MHz. With variable period, pulse width, and amplitude the 33220A is ideally suited to a wide variety of applications requiring a flexible pulse signal.

Custom waveform generation

Use the 33220A to generate complex custom waveforms. With 14-bit resolution, and a sampling rate of 50 MSa/s, the 33220A gives you the flexibility to create the waveforms you need. It also lets you store up to four waveforms in nonvolatile memory.

The Keysight IntuiLink arbitrary waveform software allows you to easily create, edit, and download complex waveforms using the waveform editor. Or you can capture a waveform using IntuiLink for Oscilloscope and send it to the 33220A for output. To find out more about IntuiLink, visit www.keysight.com/find/intuilink.

Easy-to-use functionality

Front-panel operation of the 33220A is straight-forward and user friendly. You can access all major functions with a single key or two. The knob or numeric keypad can be used to adjust frequency, amplitude, offset, and other parameters. You can even enter voltage values directly in V_{pp}, V_{rms}, dBm, or as high and low levels. Timing parameters can be entered in Hertz (Hz) or seconds.

Internal AM, FM, PM, FSK, and PWM modulation make it easy to modulate waveforms without the need for a separate modulation source. Linear and logarithmic sweeps are also built in, with sweep rates selectable from 1 ms to 500 s. Burst mode operation allows for a user-selected number of cycles per period of time. GPIB, LAN, and USB interfaces are all standard, plus you get full programmability using SCPI commands.

External frequency reference (Option 001)

The 33220A external frequency reference lets you synchronize to an external 10 MHz clock, to another 33220A, or to a Keysight 33250A. Phase adjustments can be made from the front panel or via a computer interface, allowing precise phase calibration and adjustment.

Measurement Characteristics

Waveforms	
Standard	Sine, Square, Ramp, Triangle, Pulse, Noise, DC
Built-in arbitrary	Exponential rise, Exponential fall, Negative ramp, Sin(x)/x, Cardiac

Waveforms Characteristics

Sine		
Frequency Range	1 µHz to 20 MHz	
Amplitude Flatness[1], [2] (relative to 1 kHz)		
	< 100 kHz	0.1 dB
	100 kHz to 5 MHz	0.15 dB
	5 MHz to 20 MHz	0.3 dB
Harmonic distortion[2], [3]		
	< 1 V_{PP}	≥ 1 V_{PP}
DC to 20 kHz	–70 dBc	–70 dBc
20 kHz to 100 kHz	–65 dBc	–60 dBc
100 kHz to 1 MHz	–50 dBc	–45 dBc
1 MHz to 20 MHz	–40 dBc	–35 dBc
Total harmonic distortion[2], [3]		
DC to 20 kHz	0.04%	
Spurious (non-harmonic)[2], [4]		
DC to 1 MHz	–70 dBc	
1 MHz to 20 MHz	–70 dBc + 6 dB/octave	
Phase noise (10 kHz offset)	–115 dBc / Hz, typical	
Square		
Frequency range	1 µHz to 20 MHz	
Rise/Fall time	< 13 ns	
Overshoot	< 2%	
Variable duty cycle	20% to 80% (to 10 MHz) 40% to 60% (to 20 MHz)	
Asymmetry (@ 50% duty)	1% of period + 5 ns	
Jitter (RMS)	1 ns + 100 ppm of period	
Ramp, Triangle		
Frequency range	1 µHz to 200 kHz	
Linearity	< 0.1% of peak output	
Variable Symmetry	0.0% to 100.0%	
Pulse		
Frequency range	500 µHz to 5 MHz	
Pulse width (period ≤ 10s)	20 ns minimum, 10 ns resolution	
Variable edge time	< 13 ns to 100 ns	
Overshoot	< 2%	
Jitter (RMS)	300 ps + 0.1 ppm of period	

Noise	
Bandwidth	9 MHz typical
Arbitrary	
Frequency range	1 µHz to 6 MHz
Waveform length	2 to 64 k points
Amplitude resolution	14 bits (including sign)
Sample rate	50 MSa/s
Min. Rise/Fall Time	35 ns typical
Linearity	< 0.1% of peak output
Settling Time	< 250 ns to 0.5% of final value
Jitter (RMS)	6 ns + 30 ppm
Non-volatile memory	four waveforms

Common Characteristics

Frequency	
Accuracy[5]	± (10 $_{ppm}$ + 3 pHz) in 90 days ± (20 $_{ppm}$ + 3 pHz) in 1 year
Resolution	1 µHz
Amplitude	
Range	10 mV_{PP} to 10 V_{PP} into 50 Ω 20 mV_{PP} to 20 V_{PP} into open circuit
Accuracy[1], [2] (at 1 kHz)	± 1% of setting ± 1 mV_{PP}
Units	V_{PP}, V_{rms}, dBm
Resolution	4 digits
DC Offset	
Range (peak AC + DC)	± 5 V into 50 Ω ± 10 V into open circuit
Accuracy[1], [2]	± 2% of offset setting ± 0.5% of amplitude ± 2 mV
Resolution	4 digits
Main Output	
Impedance	50 Ω typical
Isolation	42 Vpk maximum to earth
Protection	Short-circuit protected, overload automatically disables main output

External Frequency Reference (Option 001)

Rear Panel Input	
Lock Range	10 MHz ± 500 Hz
Level	100 mV_{PP} to 5 V_{PP}
Impedance	1 kΩ typical, AC coupled
Lock Time	< 2 seconds

Rear Panel Output	
Frequency	10 MHz
Level	632 mV_{PP} (0 dBm), typical
Impedance	50 Ω typical, AC coupled

Phase Offset	
Range	+ 360° to - 360°
Resolution	0.001°
Accuracy	20 ns

Modulation

AM	
Carrier waveforms	Sine, Square, Ramp, Arb
Source	Internal/External
Internal modulation	Sine, Square, Ramp, Triangle, Noise, Arb (2 mHz to 20 kHz)
Depth	0.0% to 120.0%
FM	
Carrier waveforms	Sine, Square, Ramp, Arb
Source	Internal/External
Internal modulation	Sine, Square, Ramp, Triangle, Noise, Arb (2 mHz to 20 kHz)
Deviation	DC to 10 MHz
PM	
Carrier waveforms	Sine, Square, Ramp, Arb
Source	Internal/External
Internal modulation	Sine, Square, Ramp, Triangle, Noise, Arb (2 mHz to 20 kHz)
Deviation	0.0 to 360.0 degrees
PWM	
Carrier waveform	Pulse
Source	Internal/External
Internal modulation	Sine, Square, Ramp, Triangle, Noise, Arb (2 mHz to 20 kHz)
Deviation	0% to 100% of pulse width
FSK	
Carrier waveforms	Sine, Square, Ramp, Arb
Source	Internal/External
Internal modulation	50% duty cycle square (2 mHz to 100 kHz)
External Modulation Input[6] (for AM, FM, PM, PWM)	
Voltage range	± 5 V full scale
Input impedance	5 kΩ typical
Bandwidth	DC to 20 kHz

Measurement Characteristics (Continued)

Sweep	
Waveforms	Sine, Square, Ramp, Arb
Type	Linear or Logarithmic
Direction	Up or Down
Sweep time	1 ms to 500 s
Trigger	Single, External, or Internal
Marker	falling edge of sync signal (programmable frequency)

Burst[7]	
Waveforms	Sine, Square, Ramp, Triangle, Pulse, Noise, Arb
Type	Counted (1 to 50,000 cycles), Infinite, Gated
Start/Stop Phase	–360° to +360°
Internal Period	1 µs to 500 s
Gate Source	External trigger
Trigger source	Single, External or Internal

Trigger Characteristics	
Trigger input	
Input level	TTL compatible
Slope	Rising or Falling, selectable
Pulse width	> 100 ns
Input impedance	>10 kΩ, DC coupled
Latency	< 500 ns
Jitter (rms)	6 ns (3.5 ns for pulse)
Trigger output	
Level	TTL compatible into ≥ 1 kΩ
Pulse width	> 400 ns
Output Impedance	50 Ω, typical
Maximum rate	1 MHz
Fanout	≤ 4 Keysight 33220As

Programming Times (typical)

Configuration times	USB	LAN	GPIB
Function Change	111 ms	111 ms	111 ms
Frequency Change	1.5 ms	2.7 ms	1.2 ms
Amplitude Change	30 ms	30 ms	30 ms
Select User Arb	124 ms	124 ms	123 ms
Arb Download Times (binary transfer)	**USB**	**LAN**	**GPIB**
64 k points	96.9 ms	191.7 ms	336.5 ms
16 k points	24.5 ms	48.4 ms	80.7 ms
4 k points	7.3 ms	14.6 ms	19.8 ms

General	
Power Supply	CAT II 100 - 240 V @ 50/60 Hz (–5%, +10%) 100 - 120 V @ 400 Hz (±10%)
Power Consumption	50 VA max
Operating Environment	IEC 61010 Pollution Degree 2 Indoor Location
Operating Temperature	0 to 55 °C
Operating Humidity	5% to 80% RH, non-condensing
Operating Altitude	Up to 3000 meters
Storage Temperature	–30 to 70 °C
State Storage Memory	Power off state automatically saved. Four user-configurable stored states
Interface	USB, GPIB, and LAN standard
Language	SCPI - 1993, IEEE-488.2
Dimensions (W x H x D)	
Bench top	261.1 mm x 103.8 mm x 303.2mm
Rack mount	212.8mm x 88.3mm x 272.3mm
Weight	3.4 kg (7.5 lbs)
Safety Designed to	UL-1244, CSA 1010, EN61010
EMC Tested to	MIL-461C, EN55011, EN50082-1
Vibration and Shock	MIL-T-28800, Type III, Class 5
Acoustic Noise	30 dBa
Warm-up Time	1 hour

Footnotes

1. Add 1/10th of output amplitude and offset spec per °C for operation outside the range of 18 to 28 °C

2. Autorange enabled

3. DC offset set to 0 V

4. Spurious output at low amplitude is –75 dBm typical

5. Add 1 ppm/°C average for operation outside the range of 18 to 28 °C

6. FSK uses trigger input (1 MHz maximum)

7. Sine and square waveforms above 6 MHz are allowed only with an "infinite" burst count

Ordering Information

Keysight 33220A

20 MHz function/arbitrary wavefrom generator

Accessories included

Operating manual, service manual, quick reference guide, IntuiLink waveform editor software, test data, USB cable, and power cord (see language option).

Options

Opt. 001	External timebase reference
Opt. A6J	ANSI Z540 calibration
Opt. AB0	Taiwan: Chinese manual
Opt. AB1	Korea: Korean manual
Opt. AB2	China: Chinese manual
Opt. ABA	English: English manual
Opt. ABD	Germany: German manual
Opt. ABF	France: French manual
Opt. ABJ	Japan: Japanese manual

Other Accessories

34131A	Carrying case
34161A	Accessory pouch
34190A	Rackmount kit
34191A	Dual flange kit, 2U
34194A	Dual lock link kit

myKeysight

myKeysight

www.keysight.com/find/mykeysight
A personalized view into the information most relevant to you.

www.lxistandard.org
LAN eXtensions for Instruments puts the power of Ethernet and the Web inside your test systems. Keysight is a founding member of the LXI consortium.

Keysight Assurance Plans
www.keysight.com/find/AssurancePlans
Up to five years of protection and no budgetary surprises to ensure your instruments are operating to specification so you can rely on accurate measurements.

www.keysight.com/quality
Keysight Electronic Measurement Group
DEKRA Certified ISO 9001:2008
Quality Management System

Keysight Channel Partners
www.keysight.com/find/channelpartners
Get the best of both worlds: Keysight's measurement expertise and product breadth, combined with channel partner convenience.

www.keysight.com/find/33220A

For more information on Keysight Technologies' products, applications or services, please contact your local Keysight office. The complete list is available at:
www.keysight.com/find/contactus

Americas

Canada	(877) 894 4414
Brazil	55 11 3351 7010
Mexico	001 800 254 2440
United States	(800) 829 4444

Asia Pacific

Australia	1 800 629 485
China	800 810 0189
Hong Kong	800 938 693
India	1 800 112 929
Japan	0120 (421) 345
Korea	080 769 0800
Malaysia	1 800 888 848
Singapore	1 800 375 8100
Taiwan	0800 047 866
Other AP Countries	(65) 6375 8100

Europe & Middle East

Austria	0800 001122
Belgium	0800 58580
Finland	0800 523252
France	0805 980333
Germany	0800 6270999
Ireland	1800 832700
Israel	1 809 343051
Italy	800 599100
Luxembourg	+32 800 58580
Netherlands	0800 0233200
Russia	8800 5009286
Spain	0800 000154
Sweden	0200 882255
Switzerland	0800 805353 Opt. 1 (DE) Opt. 2 (FR) Opt. 3 (IT)
United Kingdom	0800 0260637

For other unlisted countries:
www.keysight.com/find/contactus
(BP-05-29-14)

KEYSIGHT TECHNOLOGIES

Published in USA, May 21, 2015
5988-8544EN
www.keysight.com

Agilent 34401A Multimeter

Data Sheet

- Measure up to 1000 volts with 6½ digits resolution
- 0.0015% basic dcV accuracy (24 hour)
- 0.06% basic acV accuracy (1 year)
- 3 Hz to 300 kHz ac bandwidth
- 1000 readings/s direct to GPIB

See Agilent's Truevolt Series of DMMs

- Display DMM results in ways you never have before
- Measure with unquestioned Truevolt confidence
- Move to the next generation 34401A DMM with 100% assurance

www.agilent.com/find/dmm

Superior Performance

The Agilent Technologies 34401A multimeter gives you the performance you need for fast, accurate bench and system testing. The 34401A provides a combination of resolution, accuracy and speed that rivals DMMs costing many times more. $6\frac{1}{2}$ digits of resolution, 0.0015% basic 24-hr dcV accuracy and 1,000 readings/s direct to GPIB assure you of results that are accurate, fast, and repeatable.

Use It on Your Benchtop

The 34401A was designed with your bench needs in mind. Functions commonly associated with bench operation, like continuity and diode test, are built in. A Null feature allows you to remove lead resistance and other fixed offsets in your measurements. Other capabilities like min/max/avg readouts and direct dB and dBm measurements make checkout with the 34401A faster and easier.

The 34401A gives you the ability to store up to 512 readings in internal memory. For trouble-shooting, a reading hold feature lets you concentrate on placing your test leads without having to constantly glance at the display.

Use It for Systems Testing

For systems use, the 34401A gives you faster bus throughput than any other DMM in its class. The 34401A can send up to 1,000 readings/s directly across GPIB in user-friendly ASCII format.

You also get both GPIB and RS-232 interfaces as standard features. Voltmeter Complete and External Trigger signals are provided so you can synchronize to other instruments in your test system. In addition, a TTL output indicates Pass/Fail results when limit testing is used.

To ensure both forward and backward compatibility, the 34401A includes three command languages (SCPI, Agilent 3478A and Fluke8840A/42A), so you don't have to rewrite your existing test software. An optional rack mount kit is available.

Easy to Use

Commonly accessed attributes, such as functions, ranges, and resolution are selected with a single button press.

Advanced features are available using menu functions that let you optimize the 34401A for your applications.

The included Agilent IntuiLink software allows you to put your captured data to work easily, using PC applications such as Microsoft Excel or Word to analyze, interpret, display, print, and document the data you get from the 34401A. You can specify the meter setup and take a single reading or log data to the Excel spreadsheet in specified time intervals. Program-mers can use ActiveX components to control the DMM using SCPI commands. To find out more about IntuiLink, visit www.agilent.com/find/intuilink

1-Year Warranty

With your 34401A, you get full documentation, a high-quality test lead set, calibration certificate with test data, and a 1-year warranty, all for one low price.

Agilent Technologies

Accuracy Specifications ± (% of reading + % of range)[1]

Function	Range[3]	Frequency, etc.	24 Hour[2] 23°C ±1°C	90 Day 23°C ±5°C	1 Year 23°C ±5°C	Temperature Coefficient 0°C – 18°C 28°C – 55°C
DC voltage	100.0000 mV		0.0030 + 0.0030	0.0040 + 0.0035	0.0050 + 0.0035	0.0005 + 0.0005
	1.000000 V		0.0020 + 0.0006	0.0030 + 0.0007	0.0040 + 0.0007	0.0005 + 0.0001
	10.00000 V		0.0015 + 0.0004	0.0020 + 0.0005	0.0035 + 0.0005	0.0005 + 0.0001
	100.0000 V		0.0020 + 0.0006	0.0035 + 0.0006	0.0045 + 0.0006	0.0005 + 0.0001
	1000.000 V		0.0020 + 0.0006	0.0035 + 0.0010	0.0045 + 0.0010	0.0005 + 0.0001
True rms AC voltage[4]	100.0000 mV	3 Hz – 5 Hz	1.00 + 0.03	1.00 + 0.04	1.00 + 0.04	0.100 + 0.004
		5 Hz – 10 Hz	0.35 + 0.03	0.35 + 0.04	0.35 + 0.04	0.035 + 0.004
		10 Hz – 20 kHz	0.04 + 0.03	0.05 + 0.04	0.06 + 0.04	0.005 + 0.004
		20 kHz – 50 kHz	0.10 + 0.05	0.11 + 0.05	0.12 + 0.05	0.011 + 0.005
		50 kHz – 100 kHz	0.55 + 0.08	0.60 + 0.08	0.60 + 0.08	0.060 + 0.008
		100 kHz – 300 kHz[6]	4.00 + 0.50	4.00 + 0.50	4.00 + 0.50	0.20 + 0.02
	1.000000 V to 750.000 V	3 Hz – 5 Hz	1.00 + 0.02	1.00 + 0.03	1.00 + 0.03	0.100 + 0.003
		5 Hz –10 Hz	0.35 + 0.02	0.35 + 0.03	0.35 + 0.03	0.035 + 0.003
		10 Hz – 20 kHz	0.04 + 0.02	0.05 + 0.03	0.06 + 0.03	0.005 + 0.003
		20 kHz – 50 kHz	0.10 + 0.04	0.11 + 0.05	0.12 + 0.04	0.011 + 0.005
		50 kHz – 100 kHz[5]	0.55 + 0.08	0.60 + 0.08	0.60 + 0.08	0.060 + 0.008
		100 kHz – 300 kHz[6]	4.00 + 0.50	4.00 + 0.50	4.00 + 0.50	0.20 + 0.02
Resistance[7]	100.0000 Ω	1 mA Current Source	0.0030 + 0.0030	0.008 + 0.004	0.010 + 0.004	0.0006 + 0.0005
	1.000000 kΩ	1 mA	0.0020 + 0.0005	0.008 + 0.001	0.010 + 0.001	0.0006 + 0.0001
	10.00000 kΩ	100 µA	0.0020 + 0.0005	0.008 + 0.001	0.010 + 0.001	0.0006 + 0.0001
	100.0000 kΩ	10 µA	0.0020 + 0.0005	0.008 + 0.001	0.010 + 0.001	0.0006 + 0.0001
	1.000000 MΩ	5.0 µA	0.002 + 0.001	0.008 + 0.001	0.010 + 0.001	0.0010 + 0.0002
	10.00000 MΩ	500 nA	0.015 + 0.001	0.020 + 0.001	0.040 + 0.001	0.0030 + 0.0004
	100.0000 MΩ	500 nA || 10 MΩ	0.300 + 0.010	0.800 + 0.010	0.800 + 0.010	0.1500 + 0.0002
DC current	10.00000 mA	< 0.1 V Burden Voltage	0.005 + 0.010	0.030 + 0.020	0.050 + 0.020	0.0020 + 0.0020
	100.0000 mA	< 0.6 V	0.010 + 0.004	0.030 + 0.005	0.050 + 0.005	0.0020 + 0.0005
	1.000000 A	< 1.0 V	0.050 + 0.006	0.080 + 0.010	0.100 + 0.010	0.0050 + 0.0010
	3.00000 A	< 2.0 V	0.100 + 0.020	0.120 + 0.020	0.120 + 0.020	0.005 + 0.0020
True rms AC current[4]	1.000000 A	3 Hz – 5 Hz	1.00 + 0.04	1.00 + 0.04	1.00 + 0.04	0.100 + 0.006
		5 Hz – 10 Hz	0.30 + 0.04	0.30 + 0.04	0.30 + 0.04	0.035 + 0.006
		10 Hz – 5 kHz	0.10 + 0.04	0.10 + 0.04	0.10 + 0.04	0.015 + 0.006
	3.00000 A	3 Hz – 5 Hz	1.10 + 0.06	1.10 + 0.06	1.10 + 0.06	0.100 + 0.006
		5 Hz – 10 Hz	0.35 + 0.06	0.35 + 0.06	0.35 + 0.06	0.035 + 0.006
		10 Hz – 5 kHz	0.15 + 0.06	0.15 + 0.06	0.15 + 0.06	0.015 + 0.006
Frequency or period[8]	100 mV to 750 V	3 Hz – 5 Hz	0.10	0.10	0.10	0.005
		5 Hz – 10 Hz	0.05	0.05	0.05	0.005
		10 Hz – 40 Hz	0.03	0.03	0.03	0.001
		40 Hz – 300 kHz	0.006	0.01	0.01	0.001
Continuity	1000.0 Ω	1 mA test current	0.002 + 0.030	0.008 + 0.030	0.010 + 0.030	0.001 + 0.002
Diode test[9]	1.0000 V	1 mA test current	0.002 + 0.010	0.008 + 0.020	0.010 + 0.020	0.001 + 0.002

1. Specifications are for 1 hr warm-up and 6½ digits, slow ac filter.
2. Relative to calibration standards.
3. 20% over range on all ranges except 1000 Vdc and 750 Vac ranges.
4. For sinewave input > 5% of range. For inputs from 1% to 5% of range and < 50 kHz, add 0.1% of range additional error.
5. 750 V range limited to 100 kHz or 8 x 10^7 Volt-Hz.
6. Typically 30% of reading error at 1 MHz.
7. Specifications are for 4-wire ohms function or 2-wire ohms using Math Null. Without Math Null, add 0.2 Ω additional error in 2-wire ohms function.
8. Input >100 mV. For 10 mV to 100 mV inputs multiply % of reading error x10.
9. Accuracy specifications are for the voltage measured at the input terminals only. 1 mA test current is typical. Variation in the current source will create some variation in the voltage drop across a diode junction.

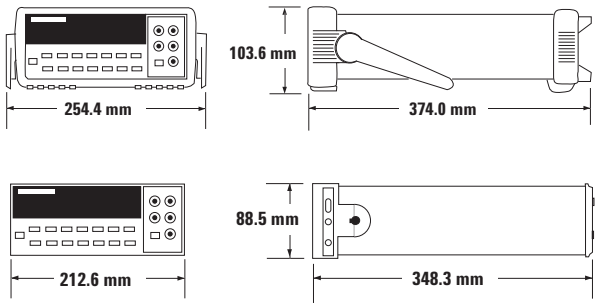

Measurement Characteristics

DC Voltage

Measurement Method:
Continuously integrating multi-slope III A-D converter

A-D Linearity: 0.0002% of reading + 0.0001% of range

Input Resistance:
10 MΩ or 0.1 V, 1 V, 10 V ranges: Selectable > 10,000 MΩ
100 V, 1000 V ranges: 10 MΩ ±1%
Input Bias Current: < 30 pA at 25°C

Input Protection: 1000 V all ranges

dcV:dcV ratio accuracy:
V_{input} Accuracy + $V_{relevance}$ Accuracy

True RMS AC Voltage

Measurement Method:
AC-coupled true rms-measures the ac component of the input with up to 400 Vdc of bias on any range.

Crest Factor:
Maximum of 5:1 at full scale.

Additional Crest Factor errors (non-sinewave):
Crest factor 1-2: 0.05% of reading
Crest factor 2-3: 0.15% of reading
Crest factor 3-4: 0.30% of reading
Crest factor 4-5: 0.40% of reading

Input Impedance:
1 MΩ ± 2% in parallel with 100 pF
Input Protection: 750 Vrms all ranges

Resistance

Measurement Method:
Selectable 4-wire or 2-wire Ohms.
Current source referenced to LO input.

Maximum Lead Resistance (4-wire):
10% of range per lead for 100 Ω, 1 kΩ ranges.
1 kΩ per lead on all other ranges.

Input Protection: 1000 V all ranges

DC Current

Shunt Resistance:
5 Ω for 10 mA, 100 mA
0.1 Ω for 1 A, 3 A

Input Protection:
Externally accessible 3 A 250 V fuse
Internal 7 A 250 V fuse

True RMS AC Current

Measurement Method:
Directly coupled to the fuse and shunt. ac coupled true rms measurement (measures the ac component only).

Shunt Resistance:
0.1 Ω for 1 A and 3 A ranges

Input Protection:
Externally accessible 3 A 250 V fuse
Internal 7 A 250 V fuse

Frequency and Period

Measurement Method:
Reciprocal counting technique

Voltage Ranges:
Same as ac voltage function

Gate Time: 1 s, 100 ms, or 10 ms

Continuity/Diode

Response Time:
300 samples/s with audible tone

Continuity Threshold:
Selectable from 1 Ω to 1000 Ω

Measurement Noise Rejection 60 (50) Hz[1]

dc CMRR: 140 dB
ac CMRR: 70 dB

Integration Time and Normal Mode Rejection[2]

100 plc/1.67 s (2 s): 60 dB[3]
10 plc/167 ms (200 ms): 60 dB[3]
1 plc/16.7 ms (20 ms): 60 dB
<1 plc/3 ms or 800 µs): 0 dB

Operating Characteristics[4]

Function	Digits	Reading/s
dcV, dcI, and Resistance	6½	0.6 (0.5)
	6½	6 (5)
	5½	60 (50)
	5½	300
	4½	1000
acV, acI	6½	0.15 slow (3 Hz)
	6½	1 medium (20 Hz)
	6½	10 fast (200 Hz)[5]
	6½	50
Frequency or Period	6½	1
	5½	9.8
	4½	80

System Speeds

Configuration rates:	26/s to 50/s
Autorange rate (dc Volts):	>30/s
ASCII readings to RS-232:	55/s
ASCII readings to RS-232:	1000/s
Maximum internal trig rate:	1000/s
Max. ext trig. rate to mem:	1000/s

Triggering and Memory

Reading HOLD Sensitivity:
10%, 1%, 0.1%, or 0.01% of range

Samples/Trigger: 1 to 50,000

Trigger Delay: 0 to 3600 s: 10 µs step size
External Trigger Delay: < 1 ms
External Trigger Jitter: < 500 µs
Memory: 512 readings

Math Functions

NULL, min/max/average, dBm, dB, limit test (with TTL output)

Standard Programming Languages

SCPI (IEEE-488.2), Agilent 3478A, Fluke 8840A/42A

Accessories Included

Test lead kit with probe, alligator and grabber attachments
Operating manual, service manual, test report and power cord

General Specifications

Power Supply:
100 V/120 V/220 V/240 V ±10%

Power Line Frequency:
45 Hz to 66 Hz and 360 Hz to 440 Hz, Automatically sensed at power-on

Power Consumption: 25 VA peak (10 W average)

Operating Environment:
Full accuracy for 0°C to 55°C,
Full accuracy to 80% R.H. at 40°C

Storage Temperature: -40°C to 70°C

Weight: 3.6 kg (8.0 lbs)

Safety: Designed to CSA, UL-1244, IEC-348

RFI and ESD: MIL-461C, FTZ 1046, FCC

Vibration & Shock: MIL-T-28800E, Type III, Class 5 (sine only)

Warranty: 1 year

1. For 1 kΩ unbalanced in LO lead, ± 500 V peak maximum.
2. For power line frequency ± 0.1%.
3. For power line frequency ± 1% use 40 dB or ± 3% use 30 dB.
4. Reading speeds for 60 Hz and (50 Hz) operation.
5. Maximum useful limit with default settling delays defeated.
6. Speeds are for 4½ digits, delay 0, auto-zero and display OFF.

www.agilent.com
www.agilent.com/find/34401A

Ordering Information

Agilent 34401A multimeter accessories included: Test lead kit with probe, alligator, and grabber attachments, calibration certificate, test report, and power cord. Also includes CD with: IntuiLink software, IVI and VXI PnP drivers, Quick start tutorial, user's guide, command quick reference, service guide, and data sheet.

Options

34401A-A6J
ANSI Z540 compliant calibration

Accessories

Probes/Leads/Clip Accessories
11059A Kelvin probe set
11060A Surface mount device (SMD) test probes
11062A Kelvin clip set
34133A Precision electronic test leads
34134A DC coupled current probe
34136A High voltage probe
34138A Test lead set
34171B Input terminal connector (sold in pairs)
34172B Input calibration short (sold in pairs)
34330A 30 A current shunt
E2308A 5 k thermistor probe
Y1133A Low-thermal external digital multimeter scanning kit

Rack Mount Kits
34190A Rackmount kit: designed for use with only one instrument, mounted on either the left or the right side of the rack.
34191A 2U Dual flange kit: secures the instrument to the front of the rack. This kit can be used with the 34194A dual lock link kit to mount two half-width, 2U height instruments side-by side.
34194A Dual lock link kit: recommended for side-by-side combinations and includes links for instruments of different depths. This kit can be used with the 34191A 2U dual flange kit to mount two half-width, 2U height instruments side-by-side.

Other Accessories
34131A Hard transit case
34161A Accessory pouch
34398A RS-232 cable, 9 pin (f) to 9 pin (f)
E5810A LAN/GPIB gateway

Three-Year Warranty

www.agilent.com/find/ThreeYearWarranty
Agilent's combination of product reliability and three-year warranty coverage is another way we help you achieve your business goals: increased confidence in uptime, reduced cost of ownership and greater convenience.

Agilent Advantage Services

www.agilent.com/find/AdvantageServices
Accurate measurements throughout the life of your instruments.

www.agilent.com/quality

myAgilent

www.agilent.com/find/myagilent
A personalized view into the information most relevant to you.

www.lxistandard.org
LAN eXtensions for Instruments puts the power of Ethernet and the Web inside your test systems. Agilent is a founding member of the LXI consortium.

Agilent Channel Partners

www.agilent.com/find/channelpartners
Get the best of both worlds: Agilent's measurement expertise and product breadth, combined with channel partner convenience.

For more information on Agilent Technologies' products, applications or services, please contact your local Agilent office. The complete list is available at:
www.agilent.com/find/contactus

Americas

Canada	(877) 894 4414
Brazil	(11) 4197 3600
Mexico	01800 5064 800
United States	(800) 829 4444

Asia Pacific

Australia	1 800 629 485
China	800 810 0189
Hong Kong	800 938 693
India	1 800 112 929
Japan	0120 (421) 345
Korea	080 769 0800
Malaysia	1 800 888 848
Singapore	1 800 375 8100
Taiwan	0800 047 866
Other AP Countries	(65) 375 8100

Europe & Middle East

Belgium	32 (0) 2 404 93 40
Denmark	45 45 80 12 15
Finland	358 (0) 10 855 2100
France	0825 010 700* *0.125 €/minute
Germany	49 (0) 7031 464 6333
Ireland	1890 924 204
Israel	972-3-9288-504/544
Italy	39 02 92 60 8484
Netherlands	31 (0) 20 547 2111
Spain	34 (91) 631 3300
Sweden	0200-88 22 55
United Kingdom	44 (0) 118 927 6201

For other unlisted countries:
www.agilent.com/find/contactus
(BP-3-1-13)

Product specifications and descriptions in this document subject to change without notice.

Published in USA, June 17, 2013
5968-0162EN

Agilent Technologies

References

[1] Pew Research Center.org. (2009). "Global Warming Seen as a Major Problem Around the World Less Concern in the U.S., China and Russia". [online] Available at: https://www.pewresearch.org/global/2009/12/02/global-warming-seen-as-a-major-problem-around-the-world-less-concern-in-the-us-china-and-russia/ [Accessed 30 April 2020]

[2] Leblanc, Rick. (2019). "The Importance of Battery Storage for Sustainable Energy". The balance small business. [online] Available at: https://www.thebalancesmb.com/importance-of-battery-storage-for-sustainable-energy-4163010 [Accessed 30 April 2020]

[3] Stevens, Pippa. (2019). "The battery decade: How energy storage could revolutionize industries in the next 10 years". CNBC. [online] Available at: https://www.cnbc.com/2019/12/30/battery-developments-in-the-last-decade-created-a-seismic-shift-that-will-play-out-in-the-next-10-years.html [Accessed 3 May 2020]

[4] Batteryuniversity.com. (2019). "Global Battery Markets Information – Battery University". [online] Available at: https://batteryuniversity.com/learn/article/global_battery_markets [Accessed 3 May 2020].

[5] Grand View Research. (2020). "Battery Market Size, Share & Trends Analysis Report By Product (Lead Acid, Li-ion, Nickle Metal Hydride, Ni-cd), By Application (Automotive, Industrial, Portable), By Region, And Segment Forecasts, 2020 - 2027". [online] Available at: https://www.grandviewresearch.com/industry-analysis/battery-market [Accessed 23 June 2021].

[6] Shunmugasundaram, R., Francine Lagadec, M., Degnarain, N. and Wood, V. (2019). The future is battery-powered. But are we overcharging the planet?. [online] World Economic Forum. Available at: https://www.weforum.org/agenda/2017/09/lithium-ion-batteries-ethics-global-battery-alliance/ [Accessed 3 May 2020].

[7] Nugroho, A., Rijanto, E., Wijaya, F. D., & Nugroho, P., "Battery state of charge estimation by using a combination of Coulomb Counting and dynamic model with adjusted gain", *2015 International Conference on Sustainable Energy Engineering and Application (ICSEEA)*, 5-7 Oct. 2015, Bandung, Indonesia, pp. 54 - 58.

[8] Sangwan, V., Sharma, A., Kumar, R., & Rathore, A. K., "Estimation of optimal li-ion battery parameters considering c-rate, SOC and temperature", *2016 7th India International Conference on Power Electronics (IICPE)*, 17-19 Nov. 2016, Patiala, India, pp. 1 - 6.

[9] Min Chen and Gabriel A. Rincón-Mora, "Accurate Electrical Battery Model Capable of Predicting Runtime and I/V Performance", IEEE Transactions on Energy Conversion, Vol. 21, No. 2, June 2006.

[10] Hasan, R., & Scott, J. B., "Application of Swingler's Method for Analysis of Multicomponent Exponentials with Special Attention to Non-equispaced Data", *IEEE 12th International Colloquium on Signal Processing & Its Applications (CSPA)*, 4-6 March 2016, Melaysia, pp. 12–15.

[11] J. E. B. Randles, "Kinetics of rapid electrode reactions," *Discussions Faraday Soc.*, vol. 1, pp. 11–19, Mar. 1947.

[12] S. Grimnes and O. Martinsen, "Bioimpedance and Bioelectricity Basics". New York, NY, USA: Academic, 2008.

[13] Jonathan Scott and Peter Single, "Compact Nonlinear Model of an Implantable Electrode Array for Spinal Cord Stimulation (SCS)", *IEEE Transactions on Biomedical Circuits and Systems*, vol.8, no.3, pp.382–390, 2014.

[14] R. Morrison, "RC constant-argument driving-point admittances", *IRE Transactions on Circuit Theory*, vol. 6, no. 3, pp. 310–317, September 1959.

[15] Mark H. Jones and Jonathan Scott, "Scaling of Electrode-Electrolyte Interface Model Parameters in Phosphate Buffered Saline", *IEEE Transactions on Biomedical Circuits and Systems*, November 2013, pp. 1-8.

[16] P.Single, J.Scott, "Cause of pulse Artefacts inherent to the electrodes of neuro modulation implants", *IEEE Trans. Neural Syst. Rehabil. Eng.*, vol. 26, no. 10, pp. 2078–2083, Oct. 2018.

[17] P. Mauracher and E. Karden, "Dynamic modelling of lead/acid batteries using impedance spectroscopy for parameter identification," *J. Power Sources*, vol. 67, nos. 1–2, pp. 69–84, 1997.

[18] Hasan, R., Scott, J. B., "Extending Randles's battery model to predict impedance, charge-voltage, and runtime characteristics", *IEEE Access*, 2020, vol 8, pp. 1–8.

[19] Dr. Jurgen Fricke, "The World of Batteries- Functions, Systems, Disposal", GRS Batteries, Hamburg, Germany, December 2007.

[20] Bobby. (2014). "History Of Batteries: A Timeline". [online] Available at: https://www.upsbatterycenter.com/blog/history-batteries-timeline/ [Accessed 1 May 2020]

[21] Paulo Santos. 2019. "Anatomy of a battery". [online] Available at: https://medium.com/@devpro/anatomy-of-a-battery-d528e7696124 [Accessed 1 May 2020].

[22] Batteryuniversity.com. (2020). "What's the Best Battery?" [online] Available at: https://batteryuniversity.com/learn/archive/whats_the_best_battery [Accessed 1 May 2020].

[23] Battery University. (2015). "Secondary (Rechargeable) Batteries". [online] Available at: https://wecanfigurethisout.org/ENERGY/Lecture_notes/Electrification_of_Tranportation_Supporting_Materials%20/Secondary%20(Rechargeable)%20Batteries%20%E2%80%93%20Battery%20University.pdf [Accessed 24 June 2021].

[24] Honsberg, C., and Bowden, S. (2019). "Battery Capacity". PVEducation.org. [online] Available at: https://www.pveducation.org/pvcdrom/battery-characteristics/battery-capacity [Accessed 3 May 2020]

[25] Hasan, R., & Scott, J. B. (2019). Measurement for fractional characteristic of lithium batteries. Presented at the 2019 IEEE International Instrumentation and Measurement Technology Conference, Conference held Auckland, New Zealand.

[26] Batteryuniversity.com. (2020). "BU-903: How to Measure State-of-charge". [online] Available at: https://batteryuniversity.com/learn/article/how_to_measure_state_of_charge [Accessed 3 May 2020].

[27] Honsberg, C., and Bowden, S. (2019). "Battery Efficiency". PVEducation.org. [online] Available at: https://www.pveducation.org/pvcdrom/battery-characteristics/battery-efficiency [Accessed 4 May 2020]

[28] Electropaedia (2005). "State of Health (SOH) Determination". [online] Available at: https://www.mpoweruk.com/soh.htm [Accessed 20 May 2020]

[29] *Solatron 1260A Impedance/Gain-Phase Analyzer*, Ametek Scientific Instruments. Accessed July, 2018. [Online]. Available: `https://www.ameteksi.com/products/frequency-response-analyzers/1260a-impedance-analyzer`.

[30] Hicham Chaoui, Navid Golbon, Imad Hmouz, Ridha Souissi, Sofiène Tahar, "Lyapunov-Based Adaptive State of Charge and State of Health Estimation for Lithium-Ion Batteries", *IEEE Transactions on Industrial Electronics*, Volume: 62, Issue: 3, 2015, pp.1610–1618.

[31] Bhaskar Saha, Kai Goebel, Scott Poll, and Jon Christophersen, "Prognostics Methods for Battery Health Monitoring Using a Bayesian Framework," *IEEE Transactions on Instrumentation and Measurement*, Vol. 58, No. 2, February 2009, pp 291–296.

[32] Gadoue, S., Chen, K.W., Mitcheson, P., Yufit, V., Brandon, N., "Electrochemical impedance spectroscopy state of charge measurement for batteries using power converter modulation". *9th International Renewable Energy Congress (IREC)*, 20-22 March 2018, Hammamet, Tunisia, pp 1–5.

[33] X. Wang, X. Wei, H. Dai and Q. Wu, "State Estimation of Lithium Ion Battery Based on Electrochemical Impedance Spectroscopy with On-Board Impedance Measurement System", 2015 IEEE Vehicle Power and Propulsion Conference (VPPC), 19-22 Oct. 2015, Montreal, QC, Canada.

[34] Li Ran, Wu Junfeng, Wang Haiying and Li Gechen, "Prediction of state of charge of Lithium-ion rechargeable battery with electrochemical impedance spectroscopy theory", 2010 5th IEEE Conference on Industrial Electronics and Applications, 15-17 June 2010, Taichung, Taiwan.

[35] Arijit Guha, Amit Patra, "Online Estimation of the Electrochemical Impedance Spectrum and Remaining Useful Life of Lithium-Ion Batteries", *IEEE Transactions on Instrumentation and Measurement*, 2018, Vol. 67, Issue. 8, pp. 1836 - 1849.

[36] Luc H. J. Raijmakers, Dmitri L. Danilov, Joop P. M. van Lammeren, Thieu J. G. Lammers, Henk Jan Bergveld, Peter H. L. Notten, "Non-Zero Intercept Frequency: An Accurate Method to Determine the Integral Temperature of Li-Ion Batteries", *IEEE Transactions on Industrial Electronics*, 2016, Volume: 63, Issue: 5, pp: 3168–3178.

[37] Hioki E.E. Corporation, *Chemical Impedance Analyzer IM3590*, `https://www.hioki.com/en/products/detail/?product_key=5749` and Battery Impedance Meter BT4560 `https://www.hioki.com/en/products/detail/?product_key=5664`. Downloaded October 2018.

[38] Zurich Instruments, *MFIA 500 kHz Impedance Analyzer*, `https://www.zhinst.com/products/impedance` Downloaded October 2018.

[39] Ferrero, R., Wu, C., Carboni, A., Toscani, S., De Angelis, M., George-Williams, H., Patelli, E., and Pegoraro, P. A. "Low-Cost Battery Monitoring by Converter-Based Electrochemical Impedance Spectroscopy". *IEEE International Workshop on Applied Measurements for Power Systems (AMPS)*, 20–22 September 2017.

[40] Bliss G. Carkhuff, Plamen A. Demirev, Rengaswamy Srinivasan, "Impedance-Based Battery Management System for Safety Monitoring of Lithium-Ion Batteries", *IEEE Transactions on Industrial Electronics*, Volume: 65, Issue: 8, Aug. 2018, pp. 6497 - 6504.

[41] Alessio Carullo, Franco Ferraris, Marco Parvis, Alberto Vallan, Emma Angelini, and Paolo Spinelli, "Low-Cost Electrochemical Impedance Spectroscopy System for Corrosion Monitoring of Metallic Antiquities and Works of Art," *IEEE Transactions on Instrumentation and Measurement*, Vol. 49, No. 2, April 2000, pp 371–375.

[42] Shimul Kumar Dam, Vinod John, "High-Resolution Converter for Battery Impedance Spectroscopy", *IEEE Transactions on Industry Applications*, 2018, Volume: 54, Issue: 2, pp. 1502 - 1512.

[43] Md. Kamal Hossain, S.M. Rakiul Islam,"Battery Impedance Measurement Using Electrochemical Impedance Spectroscopy Board", *2nd International Conference on Electrical and Electronic Engineering* (ICEEE), Rajshahi, Bangladesh, Dec. 2017.

[44] Roberto E. Serrano-Finetti, "Output Impedance Measurement in Low-Power Sources and Conditioners", *IEEE Transactions on Instrumentation and Measurement*, Vol. 58, No. 1, January 2009, pp 180–186.

[45] Roberto E Serrano-Finetti and Ramon Pallas-Areny, "Output Impedance Measurement in Power Sources and Conditioners", *IEEE Instrumentation & Measurement Technology Conference (IMTC)*, 1–3 May, 2007, pp1–5.

[46] Jaber A. Abu Qahouq, "Online battery impedance spectrum measurement method", *IEEE Applied Power Electronics Conference and Exposition* (APEC), 2016, pp. 3611–3615.

[47] Jaber A. Abu Qahouq , Zhiyong Xia, "Single-Perturbation-Cycle Online Battery Impedance Spectrum Measurement Method With Closed-Loop Control of Power Converter", *IEEE Transactions on Industrial Electronics*, 2017, Volume: 64, Issue: 9 Pages: 7019–7029.

[48] Yong-Duk Lee, Sung-Yeul Park, Soo-Bin Han, "Online Embedded Impedance Measurement Using High-Power Battery Charger", *IEEE Transactions on Industry Applications*, 2015, Volume: 51, Issue: 1, pp: 498–508.

[49] Hasan, R., and Scott, J., "Fractional behaviour of rechargeable batteries", Proceedings of the 2016 Electronics New Zealand Conference, November 17-18, 2016, Victoria University of Wellington, pp111–114. `https://ecs.victoria.ac.nz/foswiki/pub/Events/ENZCon2016/WebHome/ENZCon 2016 Proceedings.pdf`

[50] Qian-Kun Wang, Yi-Jun He, Jia-Ni Shen, Xiao-Song Hu, Zi-Feng Ma, "State of Charge-Dependent Polynomial Equivalent Circuit Modeling for Electrochemical Impedance Spectroscopy of Lithium-Ion Batteries", *IEEE Transactions on Power Electronics*, 2018, Volume: 33, Issue: 10, Pages: 8449–8460.

[51] Gmez-Aguilar Jos Francisco, Rosales-Garca Juan, Razo-Hernndez Jos Roberto, Gua-Caldern Manuel, "Fractional RC and LC Electrical Circuits", *Ingeniera Investigacin y Tecnologa*, Vol XV, April 2014, pp. 311–319.

[52] David MacCallum (2017), *Automatic Measurement of Implantable Electrode Characteristics using a Single Impedance Analyser*. University of Waikato, Waikato, New Zealand.

[53] Nagaoka, N., & Ametani, A., "An estimation method of Li-ion battery impedance using z-transform", *2012 IEEE 13th Workshop on Control and Modeling for Power Electronics (COMPEL)*, 10-13 June 2012, Kyoto, Japan, pp. 1 - 6.

[54] Nejad, S., Gladwin, D. T., & Stone, D. A., "Sensitivity of lumped parameter battery models to constituent parallel-RC element parameterisation error", *IECON 2014 - 40th Annual Conference of the IEEE Industrial Electronics Society*, 29 Oct.-1 Nov. 2014, Dallas, TX, USA, pp. 5660 - 5665.

[55] Shin-Young Cho ; Il-Oun Lee ; Jae-Il Baek ; Gun-Woo Moon, "Battery Impedance Analysis Considering DC Component in Sinusoidal Ripple-

Current Charging", *IEEE Transactions on Industrial Electronics*, 2016, Volume: 63, Issue: 3, pp. 1561 - 1573.

[56] L. Song, J.W. Evans, "Electrochemical-thermal model of lithium polymer batteries", *Journal of Electrochemical Society*, 147 (2000) 2086–2095.

[57] P.M. Gomadam, J.W. Weidner, R.A. Dougal, R.E. White, "Mathematical modeling of lithium-ion and nickel battery systems", *Journal of Power Sources*, 110 (2) (2002) 267–284.

[58] D.W. Dennis, V.S. Battaglia, A. Belanger, "Electrochemical modeling of lithium polymer batteries", *Journal of Power Sources*, 110 (2) (2002) 310–320.

[59] M. Pedram, Q. Wu, Design considerations for battery-powered electronics, in: Proc. 36th Des. Autom. Conf., 1999, pp. 861–866.

[60] C.F. Chiasserini, R.R. Rao, "Energy efficient battery management", *IEEE Journal on Selected Areas Communication* 19 (7) (2001) 1235–1245.

[61] R. Rynkiewicz, "Discharge and charge modeling of lead acid batteries", in: Proc. Appl. Power Electron. Conf. Expo., vol. 2, 1999, pp. 707–710.

[62] H.L. Chan, D. Sutanto, "A new battery model for use with battery energy storage system and electrical vehicles power systems", in: Proc. IEEE PES Winter Meeting, January 23–27, vol. 1, 2000, pp. 470–475.

[63] Jean Paul CUN, Jean No FIORINA, Michael FRAISSE, Henri MABBOUX, "The Experience of a UPS Company in Advanced Battery Monitoring", MGE UPS Systems, Grenoble, France,'http://wwwmerlingerin.eunet.fr/news/techpap/tp02us.ht'

[64] Bing, D., Yantao, T., & Changjiu, Z., "One Estimating Method of the State of Charge of Power Battery for Electronic Vehicle", *2014 Sixth International Conference on Measuring Technology and Mechatronics Automation*, 10-11 Jan. 2014, Zhangjiajie, China, pp. 439 - 442.

[65] Haijun Ruan, Jiuchun Jiang, Bingxiang Sun, Ningning Wu, Wei Shi, & Yanru Zhang, "Stepwise segmented charging technique for lithium-ion battery to induce thermal management by low-temperature internal heating", *2014 IEEE Conference and Expo Transportation Electrification Asia-Pacific (ITEC Asia-Pacific)*, 31 Aug.-3 Sept. 2014, Beijing, China, pp. 1 - 6.

[66] Song, Y., Liu, W., Li, H., Zhou, Y., Huang, Z., & Jiang, F., "Robust and accurate state-of-charge estimation for lithium-ion batteries using generalized extended state observer", *2017 IEEE International Conference on Systems, Man, and Cybernetics (SMC)*, 5-8 Oct. 2017, Banff, AB, Canada, pp. 2146 - 2151.

[67] Feng, Y., Meng, C., Han, F., Yi, X., & Yu, X., "An Online Estimation Algorithm of State-of-Charge of Lithium-Ion Batteries", *IECON 2018 - 44th Annual Conference of the IEEE Industrial Electronics Society*, 21-23 Oct. 2018, Washington, DC, USA, pp. 3879 - 3882.

[68] Sangwan, V., Kumar, R., & Rathore, A. K., "State-of-charge estimation for li-ion battery using extended Kalman filter (EKF) and central difference Kalman filter (CDKF)", *2017 IEEE Industry Applications Society Annual Meeting*, 1-5 Oct. 2017, Cincinnati, OH, USA, pp. 1 - 6.

[69] Ma, Y., Li, B., Zhou, X., & Chen, H., "Battery state of charge estimation hardware-in-loop system design based on xPC target", *2016 12th World Congress on Intelligent Control and Automation (WCICA)*, 12-15 June 2016, Guilin, China, pp. 1338 - 1343.

[70] S. Nejad ; D. T. Gladwin ; M. P. Foster ; D. A. Stone, "Parameterisation and online states estimation of high-energy lithium-titanate cells", *IECON 2017 - 43rd Annual Conference of the IEEE Industrial Electronics Society*, 29 Oct.-1 Nov. 2017, Beijing, China, pp. 7660 - 7665.

[71] Xing Zhou ; Long Cheng ; Yanzhen Tang ; Zhengqiang Pan ; Quan Sun, "Model identification of lithium-ion batteries in the portable power system", *2016 IEEE International Conference on Prognostics and Health Management (ICPHM)*, 20-22 June 2016, Ottawa, ON, Canada, pp. 1 - 5.

[72] Tiansi Wang ; Lei Pei ; Rengui Lu ; Chunbo Zhu ; Guoliang Wu, "Online Parameter Identification for Lithium-Ion Cell in Battery Management System", *2014 IEEE Vehicle Power and Propulsion Conference (VPPC)*, 27-30 Oct. 2014, Coimbra, Portugal, pp. 1 - 6.

[73] Chung-Chun Kung ; Si-Xun Luo ; Sung-Hsun Liu, "Implementation of the State of Charge Estimation with Adaptive Extended Kalman Filter for Lithium-Ion Batteries by Arduino", *2018 International Conference on System Science and Engineering (ICSSE)*, 28-30 June 2018, New Taipei, Taiwan, pp. 1 - 6.

[74] G. Nobile, M. Cacciato, G. Scarcella, and G. Scelba, "Performance Assessment of Equivalent-Circuit Models for Electrochemical Energy Storage Systems", *43rd Annual Conference of the IEEE Industrial Electronics Society (IECON)*, 2017, pp2799–2806.

[75] Si Li, & Ximing Cheng, "A comparative study on RC models of lithium-ion battery", *2014 IEEE Conference and Expo Transportation Electrification Asia-Pacific (ITEC Asia-Pacific)*, 31 Aug.-3 Sept. 2014, Beijing, China, pp. 1 - 4.

[76] Sangwan, V., Sharma, A., Kumar, R., & Rathore, A. K,, "Estimation of battery parameters of the equivalent circuit models using meta-heuristic techniques", *2016 IEEE 1st International Conference on Power Electronics, Intelligent Control and Energy Systems (ICPEICES)*, 4-6 July 2016, Delhi, India, pp. 1 - 6.

[77] Qiao Zhu ; Meng'en Xu ; Meng'qian Zheng, "Iterative Learning Based Model Identification and State of Charge Estimation of Lithium-Ion Battery", *2018 IEEE 7th Data Driven Control and Learning Systems Conference (DDCLS)*, 25-27 May 2018, Enshi, China, pp. 222 - 228.

[78] Gholizadeh, M., & Salmasi, F. R., "Estimation of State of Charge, Unknown Nonlinearities, and State of Health of a Lithium-Ion Battery Based on a Comprehensive Unobservable Model", *IEEE Transactions on Industrial Electronics*, 61(3), March 2014, pp. 1335–1344.

[79] Tiezhou Wu, Lunan Liu, Qing Xiao, Quan Cao, and Xieyang Wang, "Research on SoC Estimation Based on Second-order RC Model", *Telkomnika*, vol. 10, no. 7, Nov 2012, pp. 1667–1672.

[80] Ze Cheng, Jikao Lv, Yanli Liu, and Zhihao Yan, "Estimation of State of Charge for Lithium-Ion Battery Based on Finite Difference Extended Kalman Filter", *Journal of Applied Mathematics*, 2014, Article ID 348537, Vol. 2014, pp.1–10.

[81] Kim, J.G., Ahn, J.H., & Lee, B.K., "Enhanced Li-ion battery modeling using recursive parameters correction", *2016 IEEE Applied Power Electronics Conference and Exposition (APEC).*, 20-24 March 2016, Long Beach, CA, USA, pp. 2161 - 2166.

[82] Peng Cheng ; Yimin Zhou ; Zhibin Song ; Yongsheng Ou, "Modeling and SOC estimation of LiFePO4 battery", *2016 IEEE International Conference on Robotics and Biomimetics (ROBIO)*, 3-7 Dec. 2016, Qingdao, China, pp. 2140 - 2144.

[83] Byungchul Kim ; Younggeun Kim ; Chulho Shin ; Ross Baldick, "Adaptive Energy Management System with a BESS through Experimental-Based Cell Modeling and Adaptive Model Predictive Control", *2018 IEEE Innovative Smart Grid Technologies - Asia (ISGT Asia)*, 22-25 May 2018, Singapore, Singapore, pp. 1062 - 1067.

[84] Bao Qiang ; Cheng Yan ; Wu Zhongjian, "The dynamic impedance modeling and simulation analysis of lithium battery cell in micro power grid", *2017 12th IEEE Conference on Industrial Electronics and Applications (ICIEA)*, 18-20 June 2017, Siem Reap, Cambodia, pp. 1613 - 1618.

[85] Qiao Zhu ; Liang Li ; Xiaosong Hu ; Neng Xiong ; Guang-Di Hu, "H_∞-Based Nonlinear Observer Design for State of Charge Estimation of Lithium-Ion Battery With Polynomial Parameters", *IEEE Transactions on Vehicular Technology*, 2017, Volume: 66, Issue: 12, pp. 10853 - 10865.

[86] Qi Guo ; Wei Qu ; Haoran Deng ; Xueyuan Zhang ; Yi Li ; Xiaowei Wang ; Xiangwu Yan, "Estimation of electric vehicle battery state of health based on relative state of health evaluation", *2017 IEEE 2nd Advanced Information Technology, Electronic and Automation Control Conference (IAEAC)*, 25-26 March 2017, Chongqing, China, pp. 1998 - 2002.

[87] Jufeng Yang ; Bing Xia ; Yunlong Shang ; Wenxin Huang ; Chunting Chris Mi, "Adaptive State-of-Charge Estimation Based on a Split Battery Model for Electric Vehicle Applications", *IEEE Transactions on Vehicular Technology*, 2017, Volume: 66, Issue: 12, pp. 10889 - 10898.

[88] Brando, G., Dannier, A., Spina, I., & Piegari, L., "Comparison of accuracy of different LiFePO4 battery circuital models", *2014 International Symposium on Power Electronics, Electrical Drives, Automation and Motion*, 18-20 June 2014, Ischia, Italy, doi:10.1109/speedam.2014.6872021.

[89] Wijewardana, S., Vepa, R., & Shaheed, M. H., "Dynamic battery cell model and state of charge estimation". *Journal of Power Sources*, 2016, 308, pp. 109–120.

[90] Swingler, D. N., "A Differential Technique for the Fourier Transform Processing of Multicomponent Exponential Functions", *IEEE Transactions on Biomedical Engineering*, 1977, BME-24(4), pp. 408–410.

[91] S. C. Hageman, "Simple PSpice models let you simulate common battery types," Electronic Design News, vol. 38, pp. 117 – 129, 1993.

[92] Sabatier, J., Aoun, M., Oustaloup, A., Grégoire, G., Ragot, F., & Roy, P., "Fractional system identification for lead acid battery state of charge estimation", Signal Processing, 2006, 86(10), pp. 2645–2657.

[93] Cugnet, M., Sabatier, J., Laruelle, S., Grugeon, S., Sahut, B., Oustaloup, A., & Tarascon, J.-M., "On Lead-Acid-Battery Resistance and Cranking-Capability Estimation", *IEEE Transactions on Industrial Electronics*, 2010, 57(3), 909–917.

[94] Cheng Zhang, Kang Li, Sean Mcloone, and Zhile Yang, "Battery Modelling Methods for Electric Vehicles — A Review", *European Control Conference (ECC)*, Strasbourg, France, June 24–27, 2014.

[95] Yan Ma, Xiuwen Zhou, and Hong Chen, "Fractional Modeling and SOC Estimation of Lithium-ion Battery", *IEEE/CAA Journal of Automatica Sinica*, Vol 3, No. 3, July 2016, pp. 281-287.

[96] Kollmeyer, P., Hackl, A., & Emadi, A., "Li-ion battery model performance for automotive drive cycles with current pulse and EIS parameterization", *2017 IEEE Transportation Electrification Conference and Expo (ITEC).*, 22-24 June 2017, Chicago, IL, USA, pp. 486 - 492.

[97] Xiaoqiang Zhang, Weiping Zhang, and Geyang Lei, "A Review of Li-ion Battery Equivalent Circuit Models", *TRANSACTIONS ON ELECTRICAL AND ELECTRONIC MATERIALS*, December 25, 2016, Vol. 17, No. 6, pp. 311-316.

[98] R. Xiong and J. Tian, "A Comparative Study on Fractional Order Models for Voltage Simulation of Lithium Ion Batteries", *2019 IEEE 89th Vehicular Technology Conference (VTC2019-Spring)*, Kuala Lumpur, Malaysia, 2019, pp. 1-5.

[99] Jones, M. H., & Scott, J. B., "Scaling of Electrode-Electrolyte Interface Model Parameters In Phosphate Buffered Saline", *IEEE Transactions on Biomedical Circuits and Systems*, 2014, 9(3), 441–448.

[100] D. R. Merrill, M. Bikson, and J. G. R. Jefferys, "Electrical stimulation of excitable tissue: Design of efficacious and safe protocols", *J. Neurosci. Methods*, vol. 141, no. 2, pp. 171–198, Feb. 2005.

[101] J. Scott, Research Topics, 03-Oct-2020. [Online]. Available: https://www.waikato.ac.nz/staff-profiles/people/scottj/ResearchTopics-Mar20.png. [Accessed: 19-Nov-2020].

[102] J. Scott, personal communication, 23 November 2020.

[103] C. Dunn, personal communication, 17 November 2020.